



THÈSE

En vue de l'obtention du

DOCTORAT DE L'UNIVERSITÉ DE TOULOUSE

Délivré par *l'Université Toulouse III - Paul Sabatier*
Discipline ou spécialité : *Génie Mécanique, Mécanique des Matériaux*

Présentée et soutenue par *Sayyid Masoodur Rahman SHAH*
Le *09/11/2010*

Titre : *Investigation of crack propagation in X38CrMoV5 tool steel at room temperature and 600°C on small scale specimens*

JURY

<i>Président :</i>	<i>Pr. Roland FORTUNIER, Ecole des Mines St. Etienne</i>
<i>Examineur:</i>	<i>Pr. Walter RUBIO, Université Paul Sabatier, Toulouse</i>
<i>Directeurs:</i>	<i>Pr. Farhad REZAÏ-ARIA, EMAC - Albi</i> <i>Dr. Catherine MABRU, ISAE, Toulouse</i>
<i>Rapporteurs:</i>	<i>Pr. Abderrahim ZEGHLOUL, UPV Metz, Université Int. Rabat</i> <i>DdR. Christine SARRAZIN-BAUDOUX, LMPM, Futuroscope</i>

Ecole doctorale : *MEGeP*

Unité de recherche : *Université de Toulouse; INSA, UPS, Mines Albi, ISAE; ICA (Institut Clément Ader), Campus Jarlard, Route de Teillet, F-81013 Albi - France*

Directeur(s) de Thèse : *Pr. Farhad REZAÏ-ARIA, Dr. Catherine MABRU*

à Nuzhat

Dedication

The work on this thesis was carried out at SUMO (Research group on surface, machining, materials and tools) of the Institut Clément Ader – Albi which is a part of the Ecole des Mines d’Albi – Carmaux, France. Here I had the pleasure of working for almost four and a half years; three and a half years as a PhD laureate as well as doing masters in Mechanical Engineering from the same school.

First of all I would like to thank Messrs Roland Fortunier, Walter Rubio, Abderrahim Zegloul and Madam Christine Sarrazin-Baudoux for participating as jury members for my thesis defence. I was greatly encouraged by their remarks and observation on my work. I would especially like to thank them for their efforts in finding a convenient defence date, which was difficult to come by due to the industrial action at that time in France.

Obviously this work could not have been possible without the sea of knowledge and innovative ideas of Professor Farhad Rezaï-Aria, director of my PhD thesis and the omnipresent guidance of Dr Catherine Mabru, co-director of the thesis. I was especially honoured by the confidence shown by my directors in allowing me to carry out the research work more or less independently. I thank Professor Rezaï for the long discussions we had, not necessarily related to science, around a cup of coffee in the morning and in his office all day long.

I would equally like to thank other people, with whom I had the honour of making an acquaintance. Souleymane Ramde and Mehdi Salem are two people who provided motivation, company and support throughout my stay in France, on a personal as well as a professional level. Many people call Souleymane my twin brother although I always failed to see the resemblance. I would always remember Emile, Zeeshan, Max, Nicolas Pirc, Abdullah Tayyibi, Serekan, Fabio, Alvine, Sebastian and Jacques and hold close to my heart Valentina, Laura, Sawsane, Claire, Alvine, Elodie, Nathalie, Ines and Manel. I was will always be especially touched by the affection of our secretaries Esther and Cathy and their unending help in administrative matters. Serge, Thomas, Didier, Vincent, Sabine and Jean-Michel, George and Jean-Paul were always present to help me with technical issues in my experiments. We had good times telling each other jokes and stories also.

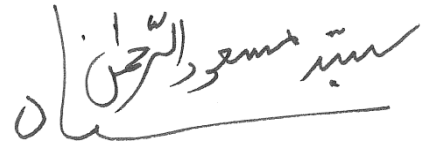
I would like to thank a few people for their hidden support in many matters. Dr Christine Boher, Michel Pavageau (Director of international relations at EMAC) and Mme Sandie Favier (Scientific attaché of the French embassy in Pakistan) were instrumental in solving many administrative issues. Mme Somia Ashraf and Mme Anna Maneta of the SFERE were always very helpful and forthcoming in solving all matters related to our scholarship and legal documents in France.

Special thank to a great visionary Professor Atta-ur-Rahman of the Higher Education Commission of Pakistan for having the audacity and vision to conceive our scholarship program in spite of the many criticisms and hurdles. I also thank the people of Pakistan for sponsoring our studies, despite of our limited resources. I hope to be able, one day, to give back some part of it to the nation.

Most importantly, this effort is the tip of the iceberg created by my father and mother; investing all their lives into our studies and training. My father always proved to be very far sighted, and sometimes very convincing in his advice, especially related to our careers. To quote his advice that actually motivated me to leave my comfortable life in Pakistan come to France, many thousand miles away from family to study was:

“Son you will understand the worth of what I say when your old man is in his grave”.

The choice after this was not very difficult.



Dr. Sayyid Masoodur Rahman SHAH

Contents

Preface	1
Chapter 1: Introduction	3
Résumé en Français	5
A. Contexte Industriel.....	5
B. Stratégie de Modélisation de l'Endommagement des Surfaces	7
C. Objectifs Scientifiques	9
I. Industrial Context	10
II. Surface Damage Modelling Strategy	13
III. Scientific Objectives	15
III.1 Isothermal fatigue crack propagation.....	17
III.2 Thin specimen testing	18
III.3 Crack driving force	19
IV. Organisation of the Manuscript	20
V. References	22
Chapter 2: Experimental Setup	23
Résumé en Français	25
A. Matériau	25
B. Moyens Expérimentaux.....	25
C. Procédure Expérimentale	26
I. X38CrMoV5 / AISI H11 Hot Work Tool Steel	27
I.1 Applications.....	27
I.2 Chemical Composition	27
I.3 Heat Treatment and Microstructure	28
I.4 Mechanical Properties	31
II. Experimental Setup	33
II.1 Universal testing machine	33
II.1.1 Modifications to the machine.....	33
II.2 Induction Heating	34
II.3 Specimens	36
II.4 Observations and Measurements	37
II.4.1 Long distance travelling microscope.....	37
II.4.2 Camera and recording	37
II.4.3 Post treatment of video	38
III. Experimental Procedure	39
III.1 Effect of load ratio (R) on crack propagation at ambient temperature.....	39
III.2 Effect of specimen thickness on crack propagation at ambient temperature.....	41
III.3 Crack propagation at elevated temperatures	42
III.4 Effect of oxidation on crack propagation.....	44
IV. Post Mortem Analysis	46
IV.1 Specimen preparation	46
IV.2 Chemical attacks for microstructure	47
V. Conclusion	48
VI. References	49

Chapter 3: Numerical Simulation	51
Résumé en Français	53
I. Introduction.....	55
I.1 Bibliography: Methods of SIF calculation.....	56
I.1.1 Extrapolation of displacements method	57
I.1.2 Singular finite elements method of SIF determination.....	58
I.1.3 Energetic approach of determining SIF.....	58
I.2 Conclusion	59
II. Numerical Simulation of SE(T)_c Specimens	60
II.1 Numerical model	60
II.2 Computational procedure	63
II.2.1 Material behaviour.....	63
II.2.2 Rectangular specimens and boundary conditions (linear elastic)	64
II.2.3 Dog bone specimens and boundary conditions.....	65
II.2.4 Sensitivity analysis of grip position	66
III. Results.....	66
III.1 J-Integral calculations	66
III.2 Rectangular Specimens	68
III.3 Dog bone specimen	70
III.3.1 Elastic and elastic-plastic analysis for tests performed at ambient temperature	70
III.3.2 Elastic and elastic-plastic analysis of material tested at elevated temperature (600°C)	72
III.3.3 Sensitivity analysis of the specimen grip position.....	73
IV. Conclusion	76
V. References.....	77
Chapter 4: Experimental Results	79
Résumé en Français	81
A. Propagation de Fissure en Fatigue à Température Ambiante	81
B. Détermination de K_{Ic} à la Température Ambiante.....	82
C. Propagation de Fissure en Fatigue à 600 °C.....	82
I. Fatigue Crack Propagation at Room Temperature.	83
I.1 Effect of R ratio on fatigue crack propagation	83
I.2 Effect of thickness “e” on fatigue crack propagation	86
I.3 Observation of fracture surface	88
I.3.1 Mechanism of fatigue crack propagation.....	89
I.3.2 Specimens of 2.5mm thickness.....	93
I.3.3 Specimens of 1.0mm, 0.60mm and 0.250mm thickness	96
II. Determination of K_{Ic} at Room Temperature	99
II.1 Dependence of K_{Ic} on a/W	99
II.2 Dependence of K_{Ic} on the specimen thickness e.....	100
III. Fatigue Crack Propagation at 600°C.	101
III.1 Effect of R ratio on fatigue crack propagation and comparison with ambient temperature results.	101
III.2 Effect of specimen thickness on the fatigue crack propagation rate at 600°C and comparison with ambient temperature	112
III.3 Observation of fracture surface	114
IV. Conclusion	120

V. References.....	121
Chapter 5: Modelling of Fatigue Crack Propagation Criteria	123
Résumé en Français	125
I. Introduction.....	127
II. Effect Of R Ratio.....	129
II.1 Data consolidation of R ratio effect based on crack closure.....	129
II.2 Consolidation of R ratio effect based on a “two parameter crack driving force”	135
II.2.1 Determining α for fatigue crack.....	136
II.2.2 Application on experimental data	137
III. Damage Parameter: Crack Opening Displacement.....	139
III.1 Use of J Integral as a damage parameter.....	139
III.2 Use of CTOD as a damage parameter	140
III.2.1 Bibliography: Relationship between J-integral and δ_t	140
III.2.2 Determination of parameters of $\delta_t = d_n(J/\sigma_0)$ for X38CrMoV5 at 20°C and 600°C.....	143
III.2.2.1 Test conditions.....	143
III.2.2.2 Determination of d_n	144
III.2.3 Adaptation of $\delta_t = d_n(J/\sigma_0)$ for fatigue crack propagation	144
IV. Application of Δ CTOD Criterion on Fatigue Crack Propagation	147
IV.1 Measurement of Δ CTOD	147
IV.1.1 Definition of terms.....	147
IV.1.2 Δ COD and Δ CTOD measurement.....	148
IV.2 $\Delta\delta_t$ and $\Delta\delta_{th}$ for specimens under different conditions.....	149
IV.3 Calculation of FCGR criterion based on $\Delta\delta_t$ and $\Delta\delta_{th}$	153
IV.3.1 Application of $\sqrt{\Delta J^{\delta_{th}} E}$ and $\sqrt{\Delta J^{\delta_t}}$ on specimens tested at 25°C at R = 0.1 and 0.7	154
IV.3.2 Comparison of $\sqrt{\Delta J^{\delta_{th}} E}$ and $\sqrt{\Delta J^{\delta_t}}$ FCGR curve at 600°C and 25°C tested at R = 0.1.....	156
IV.3.3 Use of $\sqrt{\Delta J^{\delta_{th}} E}$ and $\sqrt{\Delta J^{\delta_t}}$ as an R independent FCGR criterion	159
V. Critical Analysis Of The Crack Driving Force Models.....	162
V.1 Rationalisation of R ratio: $\bar{K}^* = (K_{max})^\alpha (\Delta K)^{1-\alpha}$	162
V.2 J-Integral as a damage parameter.....	162
V.3 Cyclic J – Integral calculated using $\delta_t = d_n(J/\sigma_0)$ as a damage parameter	164
V.3.1 Material properties.....	164
V.3.2 Large scale yielding in front of crack tip.....	164
V.3.2 Large scale yielding in front of crack tip.....	Erreur ! Signet non défini.
VI. Conclusion	167
VII. References.....	168
Chapter 6: Conclusions and Perspectives	171
Résumé en Français	173
A. Résumé	173
B. Principaux Résultats Obtenus	174
C. Perspectives	176
I. Resume.....	178
II. Principal results obtained	179
III. Future Perspectives.....	181
Appendices	183
Appendix A : Thermal Gradient In Specimens.....	185

Appendix B : Supplementary Paris Curves.....	187
I. Comparison of Paris curves of different specimen configurations SE(T) _c and C(T) at R = 0.1	187
II. Study of the effect of crack front oxidation on fatigue crack propagation.....	188
III. Effect of multicracking	189
Appendix C : Temperature Dependent Evolution of Crack Tip Plastic Zone.....	191
Appendix D : Procedure of K_c Determination.....	193
Appendix E : ΔCOD Measurements	195
Appendix F : ΔCTOD Measurements	199
Appendix G: Symbols and Abbreviations.....	203
Appendix H: Material Properties Used in Numerical Simulations.....	205

Preface

This study concerns an investigation of the surface damage of hot work tool steels. The experimental procedures, damage criteria, calculations etc. necessary for surface damage characterisation have been developed. It is a continuation of other works carried out at the Institute Clément Ader – Albi (ICAA), formerly known as Centre for Research on Tools, Materials and Processes (CROMeP). Hot work tool steels used in forging and high pressure die casting have been extensively studied in the laboratory. Most of the work has been carried out on X38CrMoV5 or AISI H11 steel. The previous PhD theses related to fatigue have been focussed on isothermal fatigue life by Delagnes 1998, Velay 2003, Daffos 2004, Ahmer (in progress) Souki (in progress), thermo mechanical fatigue by Oudin 2001 and thermal fatigue by Jean 1999, Medjedoub 2004 and Salem 2009. Interaction between fatigue, oxidation is addressed by Oudin 2001 and Daffos 2004. Jean 1999 and in particular Salem 2009 have worked on the rate of oxidation and corrosion (steam) in thermal fatigue whereas Bruckel 2003 has studied the stress free isothermal oxidation mechanisms. Wear and friction was studied by Barrau 2004.

Besides fatigue, microstructure stability and the relationship between composition, microstructure, precipitation, dislocations their effects on the behaviour were studied by Mebarki 2001, Michaud 2004, Mauriès 2008, and Bellot(in progress). Thermomechanical constitutive laws were studied by Velay 2003, and Ahmer (in progress).

In this study, mainly fatigue crack propagation is investigated on thin specimens. These specimens are machined directly from the bulk material. It is expected that the thin specimens will have damage properties similar to that of the surface of the tools. It is also expected that the thin specimens may show more clearly the effect of oxidation and its interaction with the crack tip due to greater effect of oxidation from the lateral surface instead of only the crack faces as in plane strain specimens.

Some mechanical modelling has been carried out to use the J integral and CTOD as a damage criterion. The numerical simulations and experimental measurements are compared. The validity of the J integral and the CTOD criteria has been explored to gain better understanding of the material behaviour. Image correlation has been extensively used to determine CTOD and crack closure in the fatigue crack propagation experiments.

This manuscript can be broken down into five major sections. Chapter I presents the industrial context of the study as well as the interest in developing the experimental capacity to test low thickness materials. Chapter II gives a breakdown of the experimental procedures used and developed for the testing of thin specimens. Chapter III relates to the numerical simulations carried out to determine the damage criterion to be used in characterising fatigue crack propagation. Chapter IV presents all the experimental results of the crack propagation experiments at ambient temperature (RT) as well as elevated temperature (600°C). Some fractography pertinent to the effects on the propagation experiments is also presented. Chapter V deals with modelling carried out to improve the characterisation of fatigue crack propagation and the exploitation of the fatigue crack propagation results. The crack opening displacement and its use as a fatigue crack propagation criterion is also

discussed in this chapter. The chapter VI presents the summary, some conclusions and suggestions for future works.

Although it may seem paradoxical, until now the fatigue crack propagation was studied basically under thermal fatigue and thermomechanical fatigue. A systematic investigation of the isothermal fatigue crack propagation was missing not only in the laboratory but even in the literature.

Chapter 1: Introduction

Résumé en Français	5
I. Industrial Context	10
II. Surface Damage Modelling Strategy	13
III. Scientific Objectives	15
IV. Organisation of the Manuscript	20
V. References.....	22

RESUME EN FRANÇAIS

Les outillages de mise en forme à chaud notamment en forgeage et fonderie sous pression sont soumis à des chargements thermiques et thermomécaniques très sévères. Ils sont généralement fabriqués avec des aciers à outils pour travailler à chaud qui se caractérisent par leur résistance et leur tenue mécanique à des températures élevées. Dans ce chapitre, le contexte industriel de cette étude en terme d'endommagement des outillages de fonderie est présenté. L'approche scientifique développée pour étudier l'endommagement de ces outillages est ensuite discutée.

A. CONTEXTE INDUSTRIEL

Forgeage : Le forgeage est un processus de fabrication de pièces métalliques par déformation. En effet, le métal situé entre les deux parties du moule est comprimé par la matrice sous l'effet de la pression. Dans le cas du forgeage à chaud, une partie du matériau est chauffée. L'interface entre l'outil et la pièce est alors le siège d'importants transferts thermiques et de chargements thermomécaniques. Des phénomènes thermiquement activés comme l'oxydation et l'évolution de la microstructure (précipitation des carbures dans les aciers à outil) sont provoqués par l'élévation de la température du moule. L'écoulement du métal lors de la déformation peut par ailleurs, entraîner l'usure de la surface du moule.

Fonderie Sous Pression : La fonderie sous pression est souvent utilisée dans la fabrication des pièces en alliages légers comme l'aluminium ou le magnésium. Elle consiste à refouler le métal liquide (en fusion) sous une forte pression dans l'empreinte d'un moule permanent. La chaleur est extraite de la pièce vers le moule qui est refroidi en permanence. La pièce est éjectée du moule après sa solidification. La surface du moule en fonderie sous pression est comme dans le cas du forgeage à chaud, soumise à des chargements thermiques et thermomécaniques très sévères. Elle est également exposée à la corrosion (ex. l'aluminisation) et l'oxydation lorsqu'elle n'est plus protégée (défaillance du poteyage ou du revêtement et contact direct avec le métal liquide et l'air). Le métal injecté à de grandes vitesses peut éventuellement entraîner l'érosion de l'outil lors du choc. Ce phénomène est connu sous le nom de lavage et se produit particulièrement dans les zones d'attaque.

En général les mécanismes d'endommagement des outillages sont [1, 2] :

- 1) Rupture brutale,
- 2) Endommagement par fatigue,
- 3) Fatigue thermique,
- 4) Choc thermique,

- 5) Usure à chaud due aux oxydes abrasifs,
- 6) Déformation par fluage,
- 7) Collage (étamage),
- 8) Oxydation et corrosion

Les six premiers mécanismes sont liés aux contraintes et déformations d'origines thermiques qui sont exercées sur la surface du moule. Les trois derniers sont liés à la déformation thermiquement activée ou à des réactions chimiques. Voici quelques micrographies illustrant les mécanismes d'endommagement des outillages de production. La figure 1 met en évidence la grande déformation de microstructure au niveau de la surface d'un outil de forgeage utilisé.

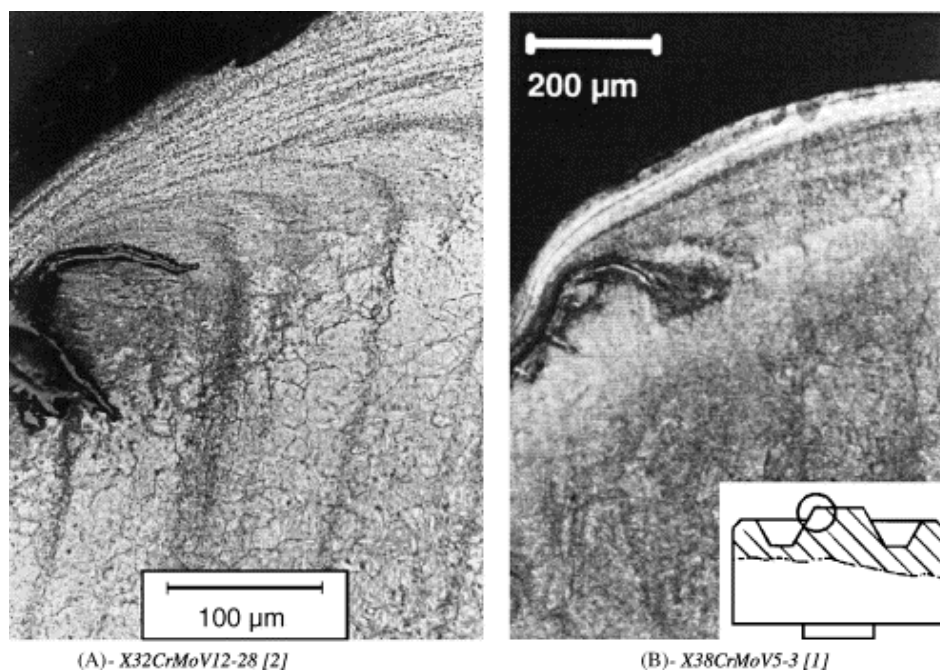


Figure 1. Usure par plasticité dans un moule de forgeage [3]

La figure 2 présente l'aspect de la fissuration par fatigue thermique dans le congé d'une broche d'un moule de fonderie sous pression d'aluminium.

Une vue en coupe réalisée au MEB à partir de la même broche est représentée en figure 3. Cette dernière met en évidence le mécanisme d'amorçage de fissure et la présence d'une fine couche d'oxyde.

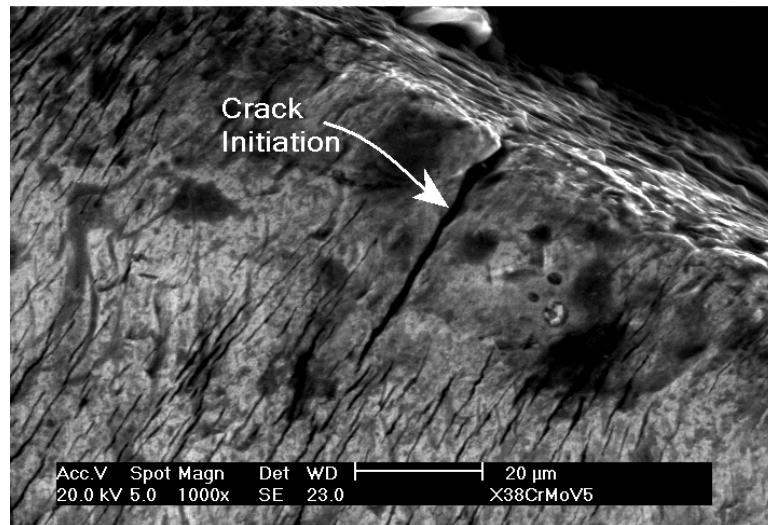


Figure 2. Fissuration uni-axiale dans une zone de concentration de contrainte (micrographie réalisée à partir d'une broche d'un moule de fonderie sous pression d'aluminium) [4]

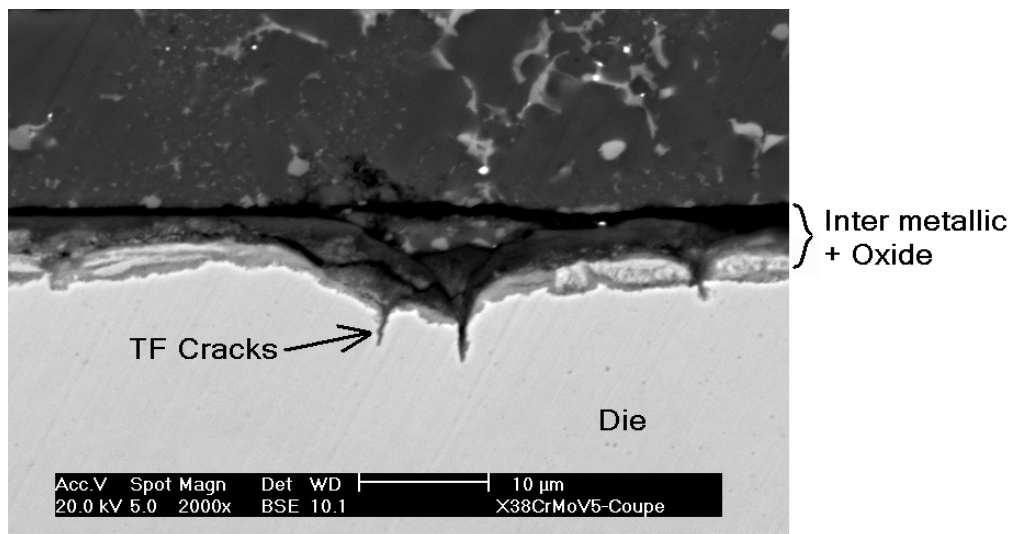


Figure 3. Fissuration par couplage entre la fatigue thermique et l'oxydation (vue en coupe à partir d'une broche d'un moule de fonderie sous pression d'aluminium) [4]

B. STRATEGIE DE LA MODELISATION DE L'ENDOMMAGEMENT DES SURFACES

L'endommagement des surfaces est une problématique majeure dans de nombreux procédés industriels comme le laminage, extrusion, usinage etc. L'endommagement se fait d'abord dans une fine couche superficielle qui est sollicitée dans des conditions complexes. L'endommagement du matériau de base qui n'est pas en contact direct avec l'environnement

externe diffère de celui de la couche superficielle. La stratégie de l'étude menée pour caractériser l'endommagement au niveau de cette zone critique (sub-surface) est schématisée en figure 4. L'idée consiste à réaliser des essais de fatigue thermomécanique à partir d'échantillons prélevés de la couche externe du matériau étudié. Les modèles d'endommagement ainsi déterminés sont complétés par l'étude de l'endommagement du matériau de base afin de décrire une durée de vie globale de l'outillage.. Cette approche peut être extrapolée pour l'étude des dépôts indépendamment du matériau de base comme les revêtements par nitruration.

L'objet de cette étude est de caractériser la durée de vie en fatigue de l'acier à outils pour travailler à chaud « X38CrMoV5 ». Les éprouvettes ont été prélevées par usinage à partir des blocs en acier vierge (non-endommagé) fournis par « Aubert & Duval ». Des essais de propagation de fissure en fatigue ont été réalisés dans différentes conditions. L'effet de l'épaisseur de l'éprouvette sur la propagation de fissure a été étudié en utilisant des éprouvettes de 0.12 à 2.5 mm d'épaisseur. L'effet des conditions de chargement a été également étudié en réalisant des essais avec différents rapports de charge ($R = 0.1, 0.2$ et 0.7). Des essais de propagation de fissures en fatigue isotherme ont été conduits à 600 °C ce qui correspond à la température maximale que peut atteindre les outillages de fonderie sous pression d'aluminium.

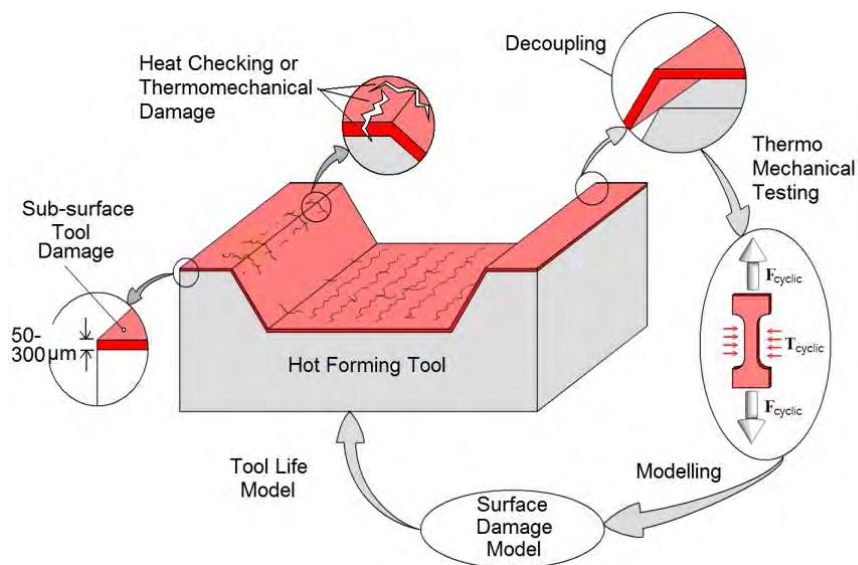


Figure 4. Stratégie d'étude de l'endommagement de surface des outillages

C. OBJECTIFS SCIENTIFIQUES

Les critères d'endommagement sont nécessaires pour caractériser le comportement en endommagement des matériaux. Dans le cas des essais de propagation de fissure en fatigue, les critères d'endommagement doivent prendre en compte :

- 1) la dépendance de K_I vis à vis du rapport entre la longueur et la largeur des éprouvettes ;
- 2) les effets de la plasticité et de l'état de contrainte en pointe de fissure ;
- 3) la forte plasticité en pointe de fissure à chaud ;
- 4) la possibilité d'avoir un paramètre d'endommagement mesurable directement sur la surface d'une éprouvette.

Les deux premières considérations peuvent être résolues en calculant les valeurs de K_I (ou facteur d'intensité de contrainte) par la simulation numérique . L'ouverture en pointe de fissure (CTOD) adaptée pour des matériaux de faible épaisseur a été utilisée comme paramètre pour décrire la propagation de fissure Les valeurs d'ouverture de fissure ont été déterminées par mesure in situ à l'aide d'un microscope optique en utilisant la méthode de corrélation d'images.

Forging and high pressure die casting processes impose heavy thermal and mechanical loads on die materials and tools. The dies are most often made of a class of tool steels called Hot Work Tool Steels. These steels retain their mechanical properties at elevated temperatures. In this chapter the industrial context of this study based on hot work tool steels damage is presented. It is followed by the discussion on the scientific approach necessary for adequately describing the damage behaviour of the tool material.

I. INDUSTRIAL CONTEXT

Forging: It is a process of shaping metals into a required shape by deformation. In hot forging process the work piece is heated and placed between two faces of a die having the negative impression of the required shape (die cavity), and a mechanical load is applied on the work piece which transfers heat and load to the dies. The heated work piece thus takes the shape of the die cavity. This process exposes the die faces to high mechanical and thermal stresses due to contact with the work piece. Sliding and flowing of the work piece material in the die cavity causes friction and wear of the die material as well. The high temperature on the die face may cause increased oxidation and microstructure evolution (e.g. precipitation of carbides in tool steels).

High Pressure Die Casting: The High Pressure Die Casting process HPDC is extensively used in creating net shape aluminium or magnesium (light alloys) parts. In the process, molten aluminium alloy is introduced in the die cavity. The molten aluminium cools and solidifies in the die. The solid part is later removed. As in forging, this process imposes high thermo mechanical stresses and strains on the die surface. The flow of the molten aluminium alloy also causes erosion of the die surface called washing out. Heat of the molten metal is conducted through the dies faces at their contact interface. This may cause oxidation and corrosion as well as microstructure evolution in the die material. In addition to this, a phenomenon called aluminisation may be caused, which is in fact a chemical reaction between the aluminium and the die steel.

In general the mechanisms involved in the damage of die materials are [1, 2]:

- 1) Sudden rupture
- 2) Fatigue damage
- 3) Thermal fatigue
- 4) Thermal shock breakage
- 5) Hot wear with the abrasive action of oxides
- 6) Creep deformation

7) Chemical adhesion

8) Oxidation and corrosion

The first six mechanisms are related to the exposure of the die surface to cyclic stresses and strains or temperature variations. The last three are basically due to effects of thermally activated deformation or chemical reactions or processes. Some case studies with their corresponding micrographs are presented here. Figure 1 shows the effect of wear on the microstructure of a forging die.

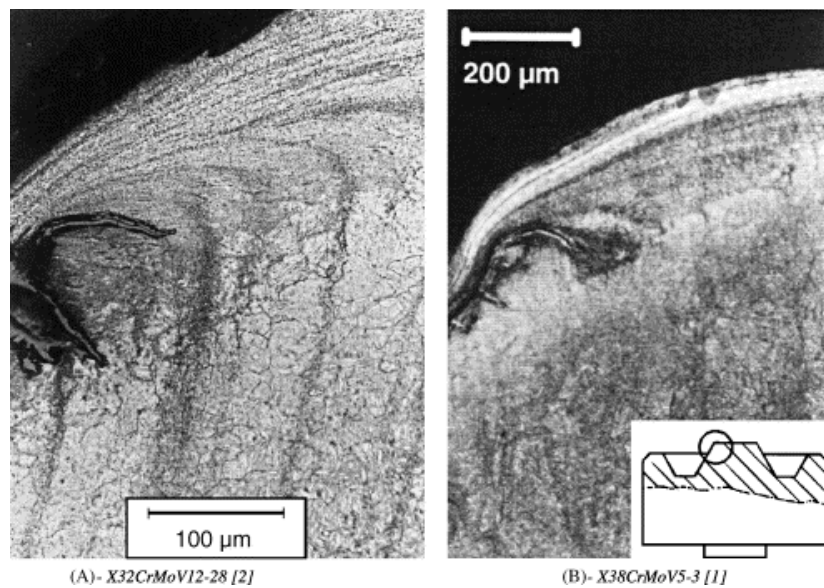


Figure 1: Wear plasticity in forging dies [3].

A high amount of plasticity deformation of the microstructure can be seen at the work surface. Figure 2 shows a surface crack in an HPDC die. This crack is found on a corner inside the die cavity.

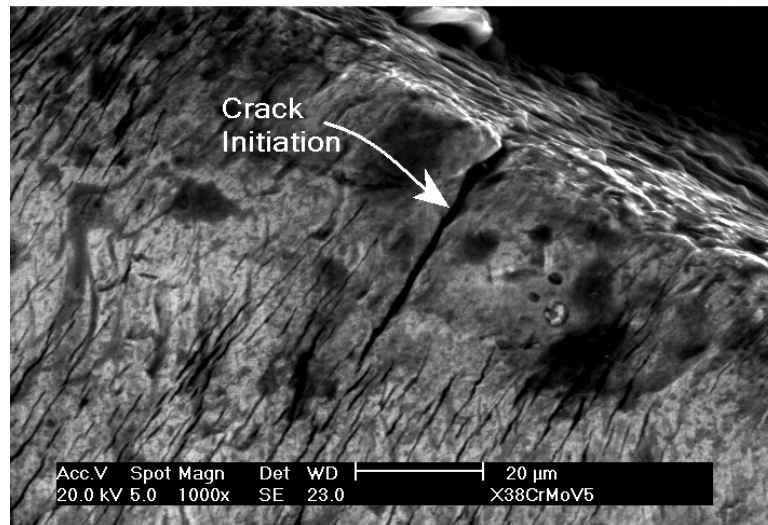


Figure 2: Surface cracking in an HPDC die [4]

In certain manufacturing processes, there may be surface alloying or adhesion between the material being formed and the die cavity. One such example of aluminisation is shown in figure 3. Here, an inter-metallic compound is formed between the steel die and the aluminium casting alloy. One can observe the initiation of cracks at the inter metallic / oxide layer, which extend into the main die body.

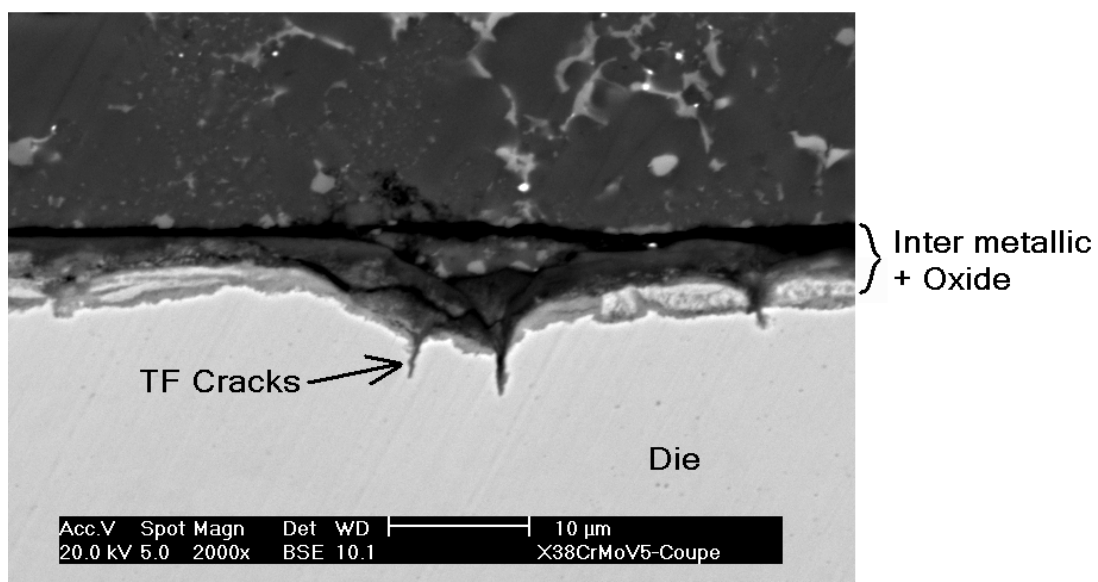


Figure 3: Aluminisation and surface cracking in an HPDC die [4]

II. SURFACE DAMAGE MODELLING STRATEGY

Many other examples of surface damage may be found in the industry, like in rolling, extrusion, machining, bearing surfaces etc. One thing to note in all the above examples is that a very thin layer of material near the surface is exposed to high cyclic pressure, wear, oxidation or chemical attack under transient temperature. The damage behaviour of this thin layer of exposed material may be different from that of the bulk. To study the behaviour of this layer a strategy is proposed as shown in figure 4. The material near the tool surface; very prone to damage, will henceforth be referred to as “surface”. The idea is to machine this thin layer of modified / damaged material (surface) off the bulk material of real dies. In fact the heat treatment of dies; in particular large dies result in a gradient in properties. Discrepancies may be found in material behaviour if one studied the real condition material (with specimens extracted from a real die) as opposed to the well controlled laboratory heat treated specimens.

This “surface” will then be studied and characterised with the help of thermal and mechanical testing. In light of the experimental data obtained, a surface damage model might be obtained. This surface damage model may then be coupled to the original bulk material damage models to get the complete tool life.

The decoupling of the surface from the bulk material may also provide the means to study the damage of coated surfaces of the tools (nitriding or other coatings etc) separate from the bulk material. However, in this study thin specimens were machined from the bulk material for testing. No processes that may cause microstructural modification prior to testing were performed. The experiments are designed in such a way that in addition to the above requirements, the fatigue behaviour and life of the specimens should be addressed.

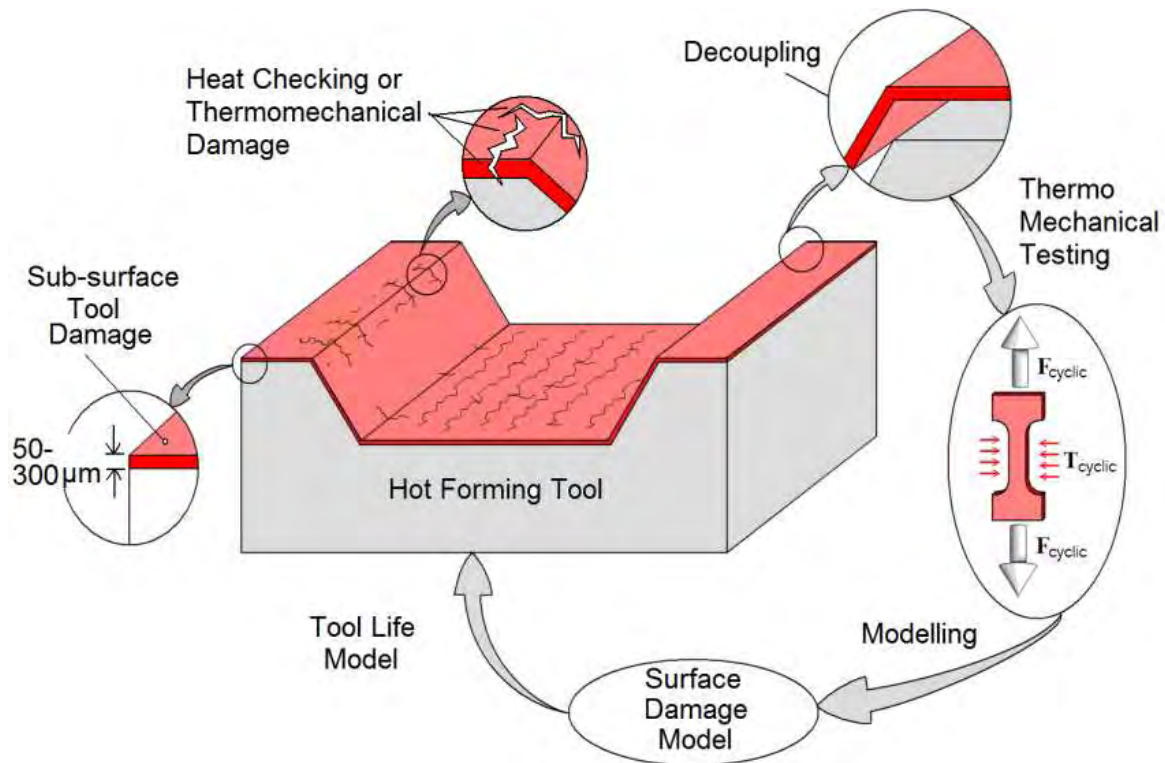


Figure 4. Tool surface damage characterisation and modelling strategy.

In this study the difference of damage properties between the bulk material and a thin material is studied. Fatigue crack propagation experiments are carried out on specimens of different thicknesses ranging from 2.5mm down to 120µm.

Tool steels are generally tested in tension compression LCF testing [5-7] or thermal fatigue [8, 9]. In this study fatigue crack propagation was chosen for three reasons. The first is the technical difficulty of applying compressive loads on thin specimens due to the problem of buckling. The second interest is that there exists no coherent study of fatigue crack propagation under different conditions of loading and temperature for the X38CrMoV5 steel. The data generated as a result of this study combined with the other theses carried out in the centre (ICAA) would provide complete data on the damage properties of this steel.

The third reason is the development of a capacity (and characterisation techniques) of testing very thin materials. The applications of such testing may be extended beyond tools to, for example, microelectronic components, thin foils etc. MEMS devices suffer from cyclic thermal and mechanical fatigue causing failure. The techniques developed in this work may be used to characterise their damage properties as well.

III. SCIENTIFIC OBJECTIVES

As described in the preface, this study is carried out in continuation to the other research carried out in the ICAA. The fatigue life of a mechanical component can be divided into two distinct stages [10].

Initiation: This involves the substructural and microstructural changes which cause nucleation of permanent damage. This is followed by the creation of microscopic cracks. The coalescence of these microscopic cracks forms a dominant macrocrack. The environmental conditions may strongly influence this part of the total life.

Propagation: The stable propagation of the dominant macrocrack which could be followed by structural instability or complete failure.

The relative importance of the initiation and propagation stage depends on the material being tested and the testing conditions. For example tests carried out on this material for Thermal Fatigue resistance (Salem 2009 [9]) show that for 650°C maximum temperature the crack initiation stage is at 10,000 cycles while the propagation stage is at 20,000 cycles for 5mm crack length propagation. Thus the initiation life is 1/3 and the propagation life 2/3 of the total fatigue life. However, with a reduction of 50°C in the maximum test temperature (600°C) in the same specimen, the crack initiation occurs at 90,000 cycles. The propagation for 5mm crack length is only 10,000 cycles. In this case the initiation stage becomes much more important than the propagation stage. The results are summarized in the table 1.

Table 1: Fraction of initiation and propagation stage in thermal fatigue tests [9]

Test	Max Temp °C	Min Temp °C	Initiation cycle N_i	Propagation cycles N_p	Fraction of fatigue life	
					Initiation	Propagation
1	650	100	10,000	20,000	1/3	2/3
2	600	100	90,000	10,000	2.7/3	0.3/3

In general for lower stresses and strains the dominant fatigue life is the initiation stage. An increase in the stresses causes the ratio of the initiation stage to propagation stage to diminish i.e. initiation life becomes less important while propagation life becomes dominant.

Die steels are most often tested using the **total-life approach**. The material fatigue life is characterised in terms of cyclic stress range (S-N curves) or the cyclic strain range (total or

plastic strain). The total-life approach assumes the material to be initially flawless. The flaw is then created by cyclic plastic strain at a geometric stress concentration, inclusions, microstructural flaws or preferential crystallographic directions.

Generally this type of crack initiation and early growth is characterised by **Low Cycle Fatigue** (LCF), where the stresses can be higher than the yield stress of the material. Smooth specimens are subjected to cyclic plastic deformations. The cycles may be symmetric (traction-compression) or asymmetric (traction-traction or compression-compression). An example of initiation of a macrocrack in this grade of steel in an LCF experiment taken from the work of Oudin 2001 [5] is presented in figure 5.

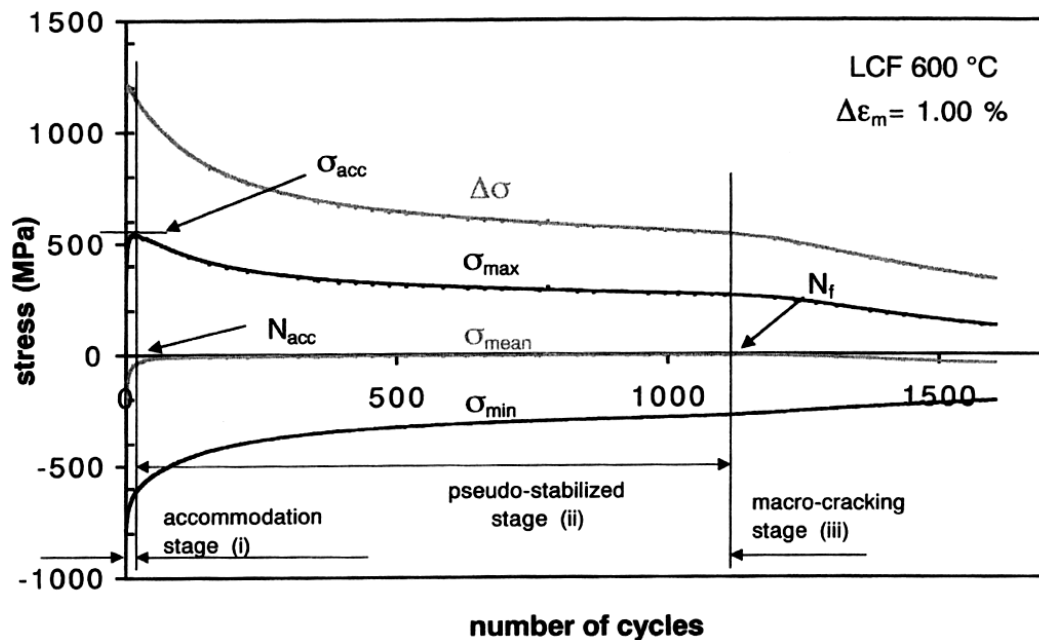


Figure 5. Different stages and the variation of the stress as a function of the number of cycles in an LCF test on X38CrMoV5-47HRC steel [5]

As soon as the macrocrack appears the compliance of the test specimen drops. Since this is a strain controlled test (1% mechanical strain), the drop in compliance is seen as a sharp drop in the stress range. One should however be careful while interpreting the LCF tests as a measure of initiation. The first accommodation stage and the pseudo stabilised stage consist of the cyclic softening of the material as well as the creation of microcracks or damage in the material. Oudin 2001 [5] has worked on the LCF and thermo-mechanical tests on this material up to 650°C. The thermo-mechanical tests consisted mostly of out of-phase heating with the applied strain cycles. Delagnes 1998 [6] had studied the isothermal LCF testing of this material up to

600°C. Daffos 2004 [7] has carried out LCF tests on nitrated and virgin X38CrMoV5-47HRC tool steel. This study has tried to establish the advantage of nitriding, if any, on increasing the total fatigue life of the steel. It was found that the effect of nitriding is mainly to increase the stabilised zone (figure 5) in the LCF test. It was shown that if the applied plastic strain $\Delta\varepsilon_p$ is smaller than a critical plastic strain $\Delta\varepsilon_p^{\text{crit}}$, then the total fatigue life N_f is increased. However if $\Delta\varepsilon_p > \Delta\varepsilon_p^{\text{crit}}$ the nitride steel has lower N_f than the virgin steel.

Thermal fatigue crack propagation was investigated by Jean [11] and Medjedoub [8, 12]. The work of Medjedoub was very systematic concerning the thermal fatigue crack propagation under different T_{max} and heating periods. However, these experiments were carried out in tubular specimens leading naturally to multi-axial loading. This also caused difficulties in following the evolution of “one” specific crack. Many specimens had to be used to establish any crack propagation curves. In addition to this the numerical modelling of such a multi-axial system was complicated and time consuming.

The only work done on the fatigue crack propagation under uniaxial conditions was by Salem 2009 [9]. Here the propagation was a result of a thermal gradient in a disc specimen of 1 mm thickness. The unequal expansion and contraction due to thermal gradient creates stresses and strains, that consequently causes crack propagation. The researchers have no access to the actual applied force and the stress intensity factors were calculated using numerical simulations via different methods. At the beginning a characteristic hardening due to damage accumulation was absent in this material and a continuous cyclic softening was observed.

III.1 Isothermal fatigue crack propagation

In this work isothermal fatigue crack propagation experiments are carried out in a systematic manner. This as explained above provides a continuity to the preceding work carried out in the laboratory. Generally the FCGR tests are carried out on C(T) specimens of 10 to 25 mm thickness on this material. However, here base thicknesses of 2.5mm, 1.0mm and 0.6mm were chosen with tests carried out on side edge notched (SENT) specimens (Also called $SE(T)_c$ = Side edge cracked, clamped specimens). The thicknesses follow other studies; Salem 2009 [9] (Thermal Fatigue on 1mm thickness discs), Oudin 2001 [5] (Thermomechanical Fatigue on 1mm wall thickness hollow cylindrical specimens). The second idea of using thin specimens is developing the capacity to do thermomechanical fatigue testing which requires rapid heating or cooling with induction heating systems with no drastic through thickness thermal gradients as in TMF specimens.

The next logical step in the study of this material is isothermal fatigue crack propagation. The FCGR experiments are carried out on SENT specimens having thickness between 2.5mm and

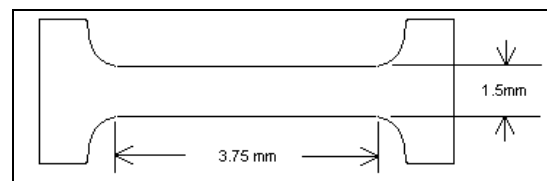
0.12mm. A group of experiments is also carried out to determine the critical stress intensity factor for rupture of these specimens at room temperature.

III.2 Thin specimen testing

One of the goals of this study was to develop the experimental capacity to be able to test thin specimens. Other researchers have developed methods for testing of thin specimens. A summary of some of the works is presented below.

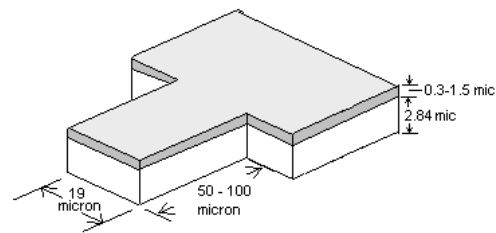
➤ **Copper Traction-Compression [13]**

1. Thickness 25 μ m.
2. Fatigue LCF traction-compression.
3. Grain size between 1.1 and 15 μ m



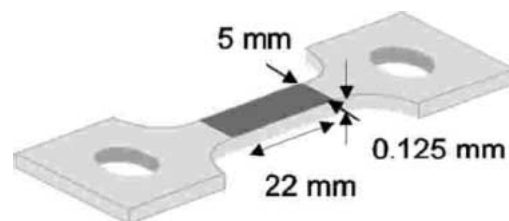
➤ **Silver Microbeam [14]**

1. Thickness 0.3-1.5 μ m.
2. Fatigue LCF traction-traction.
3. Grain size between 0.5 and 2.0 μ m.



➤ **Copper on Polyimide Substrate [15]**

1. Thickness 3.0 μ m.
2. Fatigue LCF traction-compression.
3. Grain size approximately 0.8 μ m.



All of these research works are basically designed for endurance testing of the thin films. The idea of using a substrate to accomplish compression testing of the films works only at lower temperatures. Also in FCGR experiments the crack opening should be unrestricted to be able to properly characterise the material behaviour. Metal supported by a substrate will act as a composite material. Most of the thin films are fabricated by vapour deposition or by successive rolling and annealing.

A systematic study of fatigue crack propagation on thin wires has been done Petit et al. [16]. They have carried out tests on a wire of 1.0mm thickness. Two sides of the wire are machined to make a micro SENT specimen with a nominal thickness between 0.3 – 0.35mm. A notch of 0.15 mm radius semicircle is machined. Fatigue crack propagation experiments at ambient temperatures with a load ratio between 0.4 and 0.9 have been performed, mainly to determine the fatigue threshold of the wire material. Δ CTOD is also used as a fatigue crack propagation criterion.

In this study the main idea is to test the unmodified material near the tool surface. The specimens thus have to be machined from the bulk material without causing excessive microstructural deformation. The details of the specimen fabrication are presented in chapter 2 of this manuscript.

III.3 Crack driving force

Classically fatigue crack growth experiments are carried out on thick C(T) specimens that present plane strain conditions at the crack tip. In such a case the mode I stress intensity factor K_I is used as a crack driving force. However, due to technical constraints in testing thin specimens, clamped SENT specimens ($SE(T)_c$) were used. To determine the crack driving force parameters the following considerations must be taken into account.

- 1) Height to width ratio dependence of K_I in clamped SENT specimens.
- 2) Effects of large plastic zone, and plane stress conditions.
- 3) Large scale plasticity in front of crack tip during elevated temperature testing.
- 4) Exploring the possibility of using a parameter measured directly on the specimen.

J-Integral and K_I : To take into account the first two considerations, numerical simulations were carried out in ABAQUS to determine the J-Integral. In Linear Elastic Fracture Mechanics (LEFM) conditions this can be used to interpret the K_I values as well. The advantage of J-Integral testing is that it can be used as an Elastic Plastic Fracture Mechanics (EPFM) parameter as well, especially when the plastic deformation model is used in the numerical solution. This was used as an EPFM parameter at high temperature testing.

Crack Tip Opening Displacement (CTOD): To be able to test thin specimens of tool steel, as well as other materials or composites it was decided to consider the Crack Tip Opening Displacement or CTOD as another criterion for crack driving force. The CTOD parameter is interesting in the manner that it also allows us to experimentally establish the J-Integral values. This is necessary for establishing coherent and comparable FCGR curves. The crack tip opening

displacement measurements were carried out using image correlation techniques on images obtained using a long distance optical microscope.

IV. ORGANISATION OF THE MANUSCRIPT

This manuscript is organised in 6 chapters, each covering a specific part of the thesis.

Chapter II describes the experimental methods. It describes the material tested, its microstructure, heat treatment, chemical composition and applications etc. The methods of specimen fabrication are detailed. The procedure and the FCGR testing strategies are discussed. Details of the equipment used and developed during the thesis work are shown. High temperature grips were designed and manufactured out of high temperature nickel alloys. The heating system is based on induction heating. Optical observation and the image correlation procedure is also described in this chapter.

Chapter III discusses the numerical simulations carried out on SENT specimens to determine the crack driving force parameters. The numerical modelling and methodology is described. The material models used and the experimental conditions and their effects on the results have been detailed. Some insight is also provided into different methods of numerical simulation used in this field as well as justifications for the use of the J-Integral based crack driving force parameter calculation.

Chapter IV relates to the experimental results. All the raw data results are presented. The effect of R (load ratio) and the effect of thickness on fatigue crack propagation is discussed. Experiments are carried out at ambient as well as at elevated temperatures. Extensive testing is done to determine the threshold values of FCG at 600°C. Monotonic crack propagation experiments have been carried out as well to determine the effects of thickness and crack length on the critical stress intensity factor K_C .

Chapter V is dedicated to modelling of the crack propagation X38CrMoV5. The main consideration in modelling is the data consolidation or rationalisation of FCGR curves obtained at different experimental conditions. FCGR experiments at different conditions of geometry, R, loading, temperature etc, give different crack propagation curves. To achieve data consolidation different approaches are considered. The first is based on crack closure correction to remove the difference between crack propagation curves of specimens tested at different R values. The second approach is purely mathematical and is based on the rationalisation of FCGR curve by using a “two parameter crack driving force” criterion (FCGR dependent on ΔK and K_{max}) coupled with a weight function calculated with the help of FCGR curves. The third approach, which makes the dominant part of the modelling study, is based on

Δ CTOD measurements. Δ CTOD measurements are then interpreted into the J-Integral which is subsequently used to establish consolidated FCGR curves for material tested at different temperatures. For practical use in an FCG law, a mathematical derivation is provided for its use in conjunction with R ratio.

Chapter VI gives the conclusions and some suggestions for future work in continuation to this thesis. Suggestions are made for further developing experimental procedures, improvements in the numerical simulation and modelling procedures.

V. REFERENCES

1. Mattavelli, D., *Die casting problems and possible solutions*. Die casting and technology, 1998: p. 42-51.
2. Reynoldson, R., *Die casting tools manufactured from H13 tool steel*. Die casting and technology, 1998: p. 39-50.
3. Barrau, O., et al., *Analysis of the friction and wear behaviour of hot work tool steel for forging*. Wear. **255**(7-12), 2003: p. 1444-1454.
4. Salem, M. and F. Rezaï-Aria, *Unpublished work*. 2010, ICA, Albi: Albi.
5. Oudin, A., *Thermo-mechanical fatigue of hot work tool steels*. 2001, Thesis Ecole des Mines de Paris, work performed at Ecole des Mines d'Albi - Carmaux.
6. Delagnes, D., *Comportement et tenue en fatigue isotherme d'aciers à outils Z38CrMoV5 autour de la transition oligocyclique-endurance*. 1998, Thesis Ecole des Mines de Paris work performed at Ecole des Mines d'Albi - Carmaux.
7. Daffos, C., *Endommagement des outillages de forgeage traités par nitruration : étude et modélisation*. 2004, Thesis l'Institut National des Sciences Appliquées de Toulouse, work performed at Ecole des Mines d'Albi - Carmaux (Confidential).
8. Medjedoub, F., *Détermination des paramètres influant sur le phénomène d'endommagement par fatigue thermique des moules en fonderie sous pression d'aluminium*. 2004, Thesis Ecole des Mines de Paris work performed at Ecole des Mines d'Albi - Carmaux.
9. Salem, M., *Etude d'endommagement par fatigue thermique des moules de fonderie sous pression d'aluminium: effet de l'interaction avec l'aluminisation et l'oxydation*. 2009, Thesis: Université de Toulouse work performed at Ecole des Mines d'Albi - Carmaux.
10. Suresh, S., *Fatigue of materials*. 1998: Cambridge Univ Pr.
11. Jean, S., *Méthodology d'exploitation mécanique et microstructurale d'un essai de fatigue thermique: Application à l'étude du faïençage d'un acier d'outil de forge à chaud*. 1999, Thesis: Institut National Polytechnique de Toulouse work performed at Ecole des Mines d'Albi - Carmaux.
12. Medjedoub, F., et al., *Experimental conditions and environment effects on thermal fatigue damage accumulation and life of die-casting steel X38CrMoV5 (AISI H11)*. International Journal of Microstructure and Materials Properties, 2008. **3**(2): p. 336-349.
13. Hong, S. and R. Weil, *Low cycle fatigue of thin copper foils*. Thin Solid Films, 1996. **283**(1-2): p. 175-181.
14. Schwaiger, R. and O. Kraft, *High cycle fatigue of thin silver films investigated by dynamic microbeam deflection*. Scripta Materialia(USA), 1999. **41**(8): p. 823-829.
15. Kraft, O., R. Schwaiger, and P. Wellner, *Fatigue in thin films: lifetime and damage formation*. Materials Science and Engineering A, 2001. **319**: p. 919-923.
16. Petit, J., C. Sarrazin-Baudoux, and F. Lorenzi, *Fatigue crack propagation in thin wires of ultra high strength steels*. Procedia Engineering. **2**(1): p. 2317-2326.

Chapter 2: Experimental Setup

Résumé en Français	25
A. Matériau	25
B. Moyens Expérimentaux	25
C. Procédure Expérimentale.....	26
I. X38CrMoV5 / AISI H11 Hot Work Tool Steel	27
II. Experimental Setup.....	33
III. Experimental Procedure.....	39
IV. Post Mortem Analysis	46
V. Conclusion	48
VI. References.....	49

RESUME EN FRANÇAIS

L'environnement expérimental et le matériau étudié sont présentés dans ce chapitre. Le banc d'essais qui se compose de la machine d'essais mécanique, du système de chauffage et des moyens d'observations optiques sont exposés. Les méthodes de préparation des éprouvettes ainsi que les techniques d'analyses et les moyens d'observations sont aussi décrits.

A. MATERIAU

Le matériau choisi pour cette étude est l'acier à outils pour travailler à chaud « X38CrMoV5 », désigné aussi par « AISI H11 ». Les familles des aciers AISI H11 et H13 ont fait l'objet de nombreuses études dans le laboratoire (ICAA), notamment dans le cadre du forgeage et de la fonderie sous pression d'aluminium [1-12]. La nuance utilisée est fournie en bloc par l'aciériste Aubert et Duval – France et contient 5% de Chrome et 0,36% de carbone. Elle présente une teneur très faible en particules non métalliques. Le traitement typique de cet acier pour l'obtention d'une dureté égale à 47 HRC comprend un recuit à 750°C suivi par une austénitisation à 990°C pendant 1h, une trempe à l'air et un double revenu. Le premier et le deuxième revenu sont effectués pendant 2h, respectivement à 550°C et 603°C. Ce traitement thermique confère à l'acier une microstructure martensitique revenu.

B. MOYENS EXPERIMENTAUX

Un banc d'essais de fatigue a été développé spécialement pour tester des éprouvettes très minces. Le système permet de réaliser des essais de fatigue LCF et HCF à différentes températures. Le système de chauffage a été conçu de manière à rendre accessible l'observation de la surface de l'éprouvette pendant le test permettant ainsi de suivre la propagation des fissures. Un microscope à longue portée a été utilisé à cet effet. La machine d'essais de fatigue, Walter et Bai (Suisse), travaille à une charge maximale de 40 kN avec une fréquence d'essai allant jusqu'à 20 Hz. Elle a été réadaptée pour réaliser des essais avec un signal de force stable à faible charge. Une cellule de charge de 2 kN et une servo-vanne de 4 l/min (au lieu de 40 l/min) ont été installées. Le système est actuellement capable d'effectuer des essais de fatigue à des fréquences allant de 0,2 Hz à 20 Hz avec une charge de 0,05 kN de façon stable.

Le système de chauffage choisi utilise l'induction électromagnétique. L'induction est un moyen de chauffage rapide et sans contact. La surface de l'éprouvette demeure visible pendant le test. La température maximale du système est de 750 °C. Les mors de la machine d'essai ont été pour cette étude. Ils ont été fabriqués avec les superalliages IN 718 et IN 100 pour pouvoir résister à haute température.

Les éprouvettes sont de type SENT conçues conformément aux normes ASTM E647-00, E606 et E399-90 ; avec quelques modifications (rapport entre la largeur et la longueur et le rayon d'épaulement) afin de les réadapter à nos contraintes d'essais (échantillons minces).

Un microscope à longue portée QUESTAR de 1,1 μm de résolution optique maximale a été utilisé pour observer la propagation de fissure. Il est équipé d'une caméra analogique reliée à un système d'enregistrement (magnétoscope) permettant l'enregistrement de l'évolution de la longueur de fissure. L'ouverture de fissure est déterminée par corrélation d'images issues des séquences enregistrées par un magnétoscope. Les films enregistrés sont en effet convertis en images avec le logiciel iMovie HD®. Ces images sont ensuite traitées avec un logiciel de corrélation d'images VIC 2D®. On utilise généralement cinq extensomètres virtuels de 200 μm qui sont placés sur l'image de base utilisée pour la corrélation.

C. PROCEDURE EXPERIMENTALE

Les essais ont été réalisés dans différentes conditions, afin d'étudier la propagation de fissure et les phénomènes suivants :

- 1) effet du rapport de charge (R),
- 2) effet de l'épaisseur de l'éprouvette,
- 3) effet de la température (20 °C et 600°C),
- 4) facteur d'intensité de contrainte de seuil de propagation à différents R,
- 5) effet de l'oxydation à chaud sur la propagation de fissure.

Les essais conduits à 20 et 600 °C sont réalisés respectivement à 10 et 2 Hz. Afin de mesurer l'ouverture de la fissure in situ, des essais à 0,2 Hz ont été réalisés.

Une analyse fractographique des faciès de rupture a été menée sur toutes les éprouvettes post mortem, à l'aide d'un microscope électronique à balayage (MEB). Cela a permis de mettre en évidence la présence de bandes de glissements au voisinage des zones de plasticité élevée. La microstructure des éprouvettes testées à chaud a également été caractérisée.

A chaud, une couche d'oxyde se forme sur les faciès de rupture. Cette couche a été décapée avec un mélange de HCl (agent décapant) et de HMTA « Héxaméthylène-Tetramine » qui permet de protéger la surface de métal ainsi mise à nue.

This chapter concerns the properties of the material chosen as well as the experimental techniques for this study. The fatigue testing equipment, heating system and the observation techniques are discussed in detail. All the design parameters and preparation techniques for the specimens are also discussed. A description for the post mortem observation techniques is also provided which includes chemical or electrochemical etching, deoxidation, recrystallisation etc.

I. X38CrMoV5 / AISI H11 HOT WORK TOOL STEEL

The alloy chosen for this study is an X38CrMoV5 or AISI H11 hot work tool steel. The material for the study has been provided by Aubert & Duval – France free of charge. The family of AISI H11 and H13 material has been studied extensively in the laboratory especially in the application of forging and HPDC [1-12]. The principal area of application for this class of steels is high temperature tooling. The material has been provided in the form of forged blocks as shown in fig 9. The commercial designation of the steel used in the study is ADC3. The predecessor to this steel was given the designation SMV3, which had higher silicon content. The microstructure of this steel may be best described as a tempered martensite microstructure.

I.1 Applications

The X38CrMoV5 steel is extensively used in making dies for the high pressure aluminium die casting and as well as for forging dies. The material has a high resistance to loading even at elevated temperatures. It exhibits a high tensile strength at elevated temperatures, good fracture toughness (40 - 57 MPa.m^{1/2} [13] for 47 HRC Hardness) and presents a good thermal conductivity ($\approx 26 - 29 \text{ W m}^{-1} \text{ K}^{-1}$ at 200 – 600°C [8, 11]). Other uses for this material include extrusion of light alloys, stamping dies, moulds and tools of the plastics processing industry.

I.2 Chemical Composition

The X38CrMoV5 steel is a 5% Chrome, low non metallic particle content tempered-martensitic steel. The chemical composition is given in table 1. The hot work tool steels generally have a medium carbon content associated with the alloying elements like nickel, chromium, molybdenum and vanadium. A brief discussion of the effects of these elements is presented below.

Table 1: Chemical composition Wt % of X38CrMoV5 / AISI H11 (Grade ADC3) Steel

Elements	C	Cr	Mo	V	Ni	Si	Mn	Fe
Wt %	0.35	5.11	1.21	0.47	0.06	0.28	0.35	bal

Chromium is an alpha-generators and a carbide forming element which has an essential role in improving the quench hardenability of the steel. Chrome combines with carbon to give carbides of the type $M_{23}C_6$ and M_7C_3 [4, 11, 12] which increase its resistance to abrasion and resistance to grain growth during austenisation. It is also responsible for the retardation of softening during tempering of the steel which in fact increases the resistance of the steel at high temperature. Another advantage of chromium is that it increases resistance to oxidation.

Molybdenum is a strong carbide former. It contributes in the solid solution strengthening of the steel and stabilizes the microstructure. During the tempering of the steel, molybdenum produces carbides of the type M_2C [3, 11].

Vanadium is important for the hot hardness and resistance to abrasion. It forms very hard, small carbide particles in the steel. Since it has very low solubility in the matrix, it easily forms carbides of the type MC [11, 12].

I.3 Heat Treatment and Microstructure

The material was received in "as heat treated condition" by Aubert & Duval. The typical heat treatment of this steel involves four steps; annealing, austenisation followed by double tempering. Each of these is explained in some detail as follows.

Annealing is done at a temperature of 750°C with a corresponding hardness range of 200 – 250 HV [3]. The aim of annealing is to relax the residual stresses created during manufacture and to obtain a uniform microstructure. Annealing is typically done below the AC_3 temperature to avoid the γ – phase and subsequent grain growth. The time depends on the thickness and temperature of the work piece and it may vary between 1 and 4 h [3]. The as annealed microstructure is made up of fine globular carbides embedded in a ferrite matrix fig 1.

Austenisation is done at 980°C (above the AC_3 temperature in the γ – phase) for 30 minutes followed by air quenching. It is done in order to dissolve most of the carbides into the matrix. The dissolved carbon (from carbide dissolution at 980°C) and the well distributed alloying elements can form secondary carbides during the tempering process later on. During the austenisation, grain growth is blocked by carbides of the type MC [12]. Austenisation is followed by air quenching, which gives a hard martensite structure. Since martensite formation is diffusion less, most the carbon dissolved during austenisation remains dissolved in the ferrite matrix which is available for carbide formation during tempering.

Tempering is done immediately after the austenisation. It is a two step process. The first tempering is done at 550°C for 2h and the second tempering at 603°C for 2h [1] to achieve a

hardness of 47 HRC. The tempering is done in order to remove the retained austenite (conversion to secondary martensite) after quenching, and the second tempering to precipitate the desired type of fine carbides. During tempering a secondary hardness peak can be seen in figure 2 which is due to the transformation of retained austenite into hard secondary martensite. During the second tempering, secondary carbides of the type MC (principally vanadium carbides) are created (2 nm [12]) which are instrumental in giving the alloy its hot hard properties. These carbides are extremely resistant to dissolution and coalescence at high temperatures. The whole heat treatment process is schematically presented in the figure 3. The quenched and tempered microstructure is shown in figure 4. Typically the martensite lathes are in the form of needles of 1 μm diameter and 10 μm length.

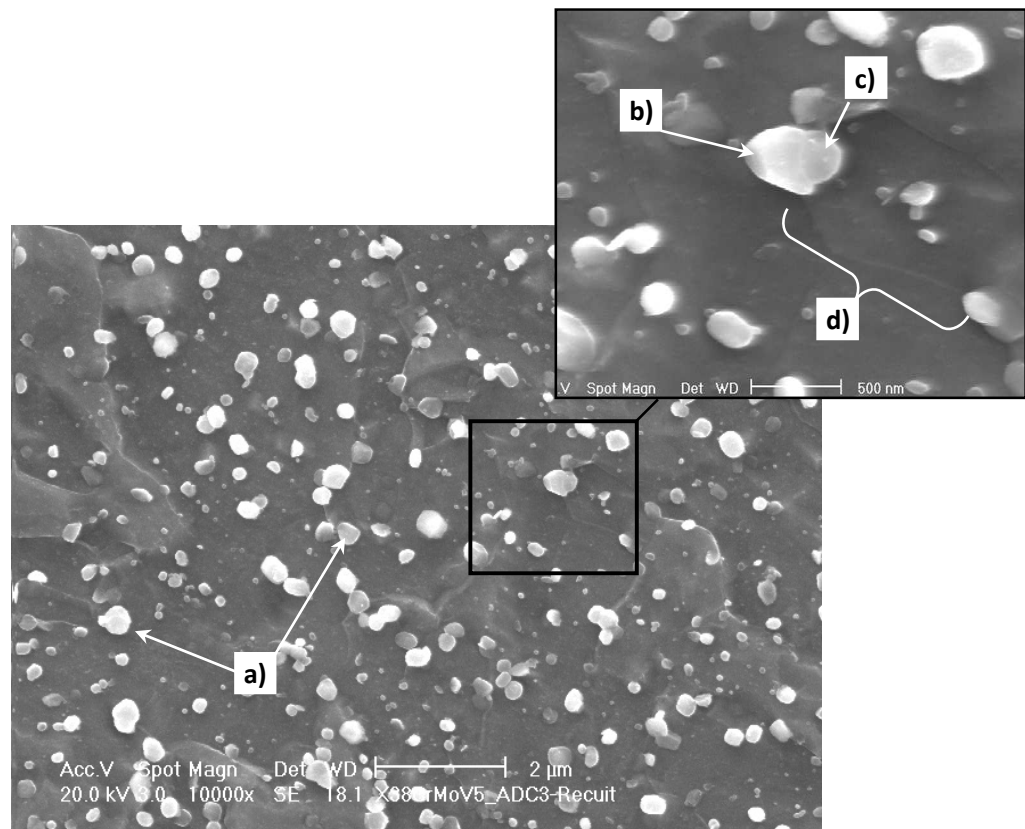


Fig 1. Microstructure of X38CrMoV5 in as annealed state. Revealed by Nital 3% for 15s electron microscope. : a) Globular carbides, b) et c) Polyhedric carbides, d) Ferrite grain [11]

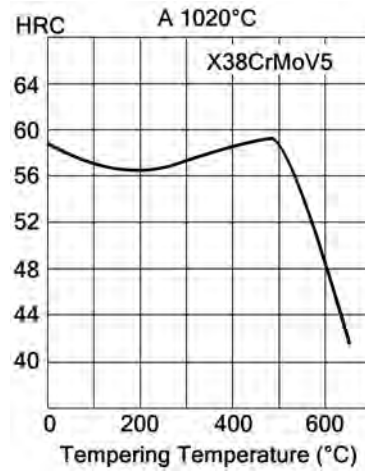


Fig 2. Evolution of hardness with respect to the increase in tempering temperature [3]

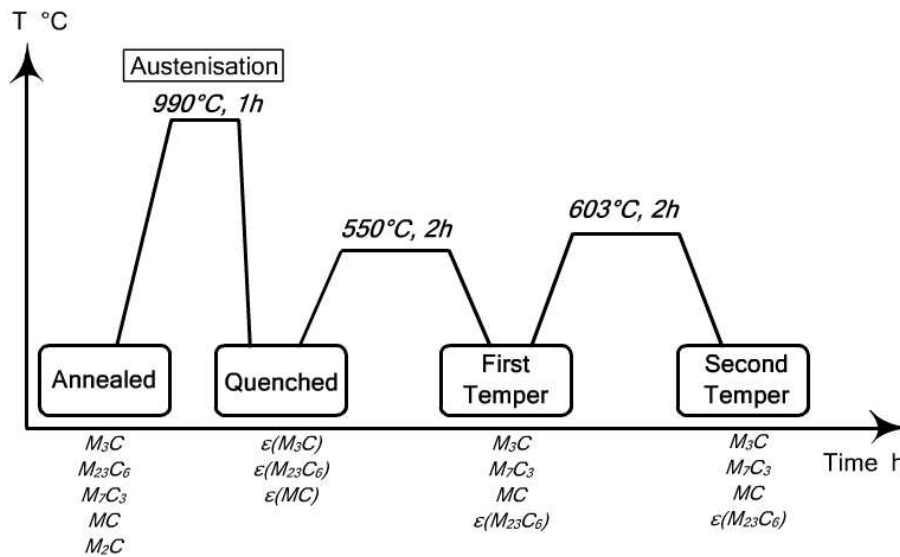


Fig 3. Schematic of the heat treatment for X38CrMoV5 steel with corresponding carbides formed at each stage of heat treatment [12]

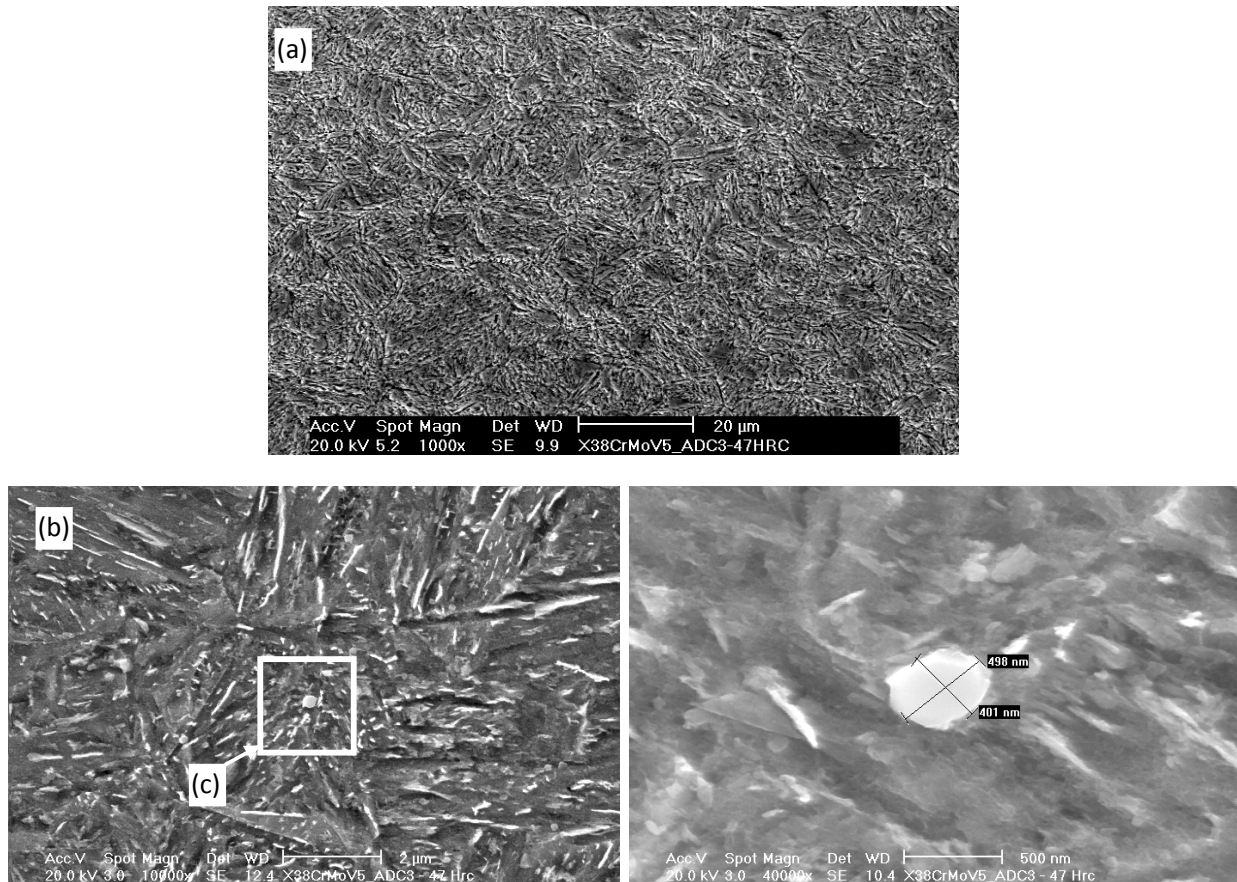


Fig 4. Microstructure of X38CrMoV5 quenched and tempered

a) Martensite lath structure (Nital at 3% for 20s), b) Elongated inter-lath carbides (Villela's reagent) and c) Morphology of a globular carbide [11]

I.4 Mechanical Properties

The X38CrMoV5 steel belongs to the class of hot work tool steels and is thus characterised by high mechanical, oxidation and corrosion resistance.

The steel is available in different grades based upon hardness. The 42 HRC and 47 HRC hardness grades are the most commonly used grades. The 42 HRC steel has a higher toughness value ($60 \sim 90 \text{ MPa}\cdot\text{m}^{1/2}$) as compared to the 47 HRC steel ($40 \sim 60 \text{ MPa}\cdot\text{m}^{1/2}$). In our work we have used only the 47 HRC grade. The mechanical properties derived from monotonic tensile tests have been presented in the figure 5 [11].

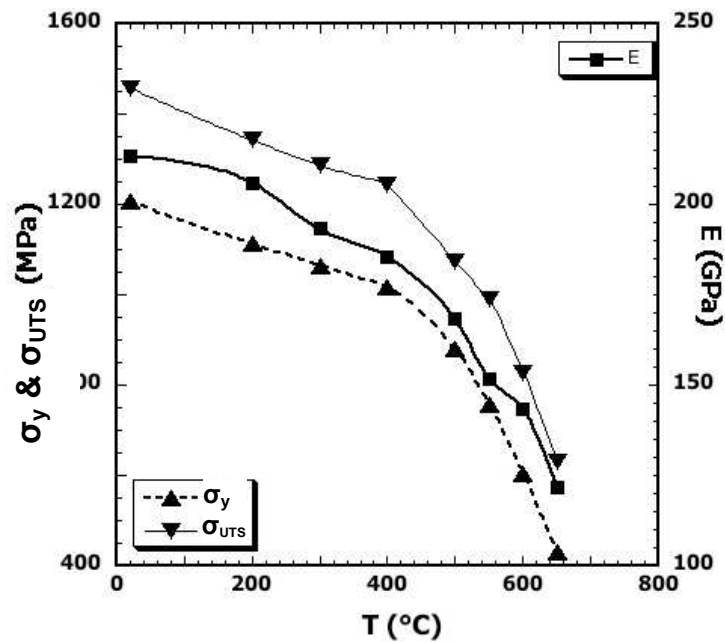


Fig 5. Mechanical properties of X38CrMoV5 steel from monotonic tensile tests at different temperatures: ultimate strength (σ_{UTS}), elastic limit (σ_y) and young's modulus (E) [11]

According to its application in the high pressure die casting and the forging industry, the material is expected to resist mechanical loading at the working temperatures imposed by its application. The reduction in the elastic limit and yield strength is not excessive until 400°C after which the drop in these properties becomes higher. However the safe temperature of use is considered to be up to 550°C (first tempering temperature) because the effects of thermal aging are not pronounced. However, beyond 550°C we can see a marked reduction in the mechanical resistance of the material [11].

II. EXPERIMENTAL SETUP

For the fatigue testing of very thin materials, a test facility was specifically designed and developed. The system is capable of carrying out HCF and LCF tests at different temperatures while giving visual access to the crack propagation through a high power long distance microscope.

II.1 Universal testing machine

All the HCF experiments are carried out on a 40 kN servo hydraulic universal testing machine manufactured by Walter + Bai of Switzerland. **The hydraulic system** has a working pressure of 250 bar, which feeds a linear 100mm stroke piston cylinder actuator. This is a very versatile machine which can be used in the classic vertical configuration or a horizontal configuration.

In its initial configuration the machine comes with a 40 l/min servo valve and a load cell of 40kN. **The controller**, EDC 120 is used to interface all the commands from the PC with the machine as shown in figure 6. There are three measurable inputs on the controller; deformation, force and piston displacement. The PC interface, DionPro™, is based on the DELPHI programming platform. All data transfer between the controller and the PC is done through serial cable. It is capable of working reliably at a minimum load of 1kN at a frequency range of 0.2Hz to 20Hz in the standard configuration.

II.1.1 Modifications to the machine

Control: Although in its standard configuration, the machine has high control and stability, the experiments on thin specimens demand higher precision and control. For this purpose, a new servo valve with a smaller flow rate 4 l/min was installed. Load cells of 2kN and 0.1kN were also installed to gain higher precision in force controlled experiments of thin specimens. In the modified configuration the machine can work reliably at 0.05kN at a frequency range between 0.2Hz to 20Hz.

Elevated temperature: Testing hot work tool steels requires the experiments to be carried out at elevated temperatures. It was decided that the specimen grips should be able to work for long durations at up to 750°C. For this purpose special grips were designed and fabricated, figure 7. They are internally cooled through the upper fixture or piston figure 7, which is made of stainless steel. The external collar is made of IN 718 super alloy which is cooled externally by a brass cooling jacket. The jaws of the grips are made of IN 100 which has a very high temperature resistance. This was necessary because the jaws cannot be cooled directly and are exposed to induction heating as well. The whole grips fixture is presented in figure 7.

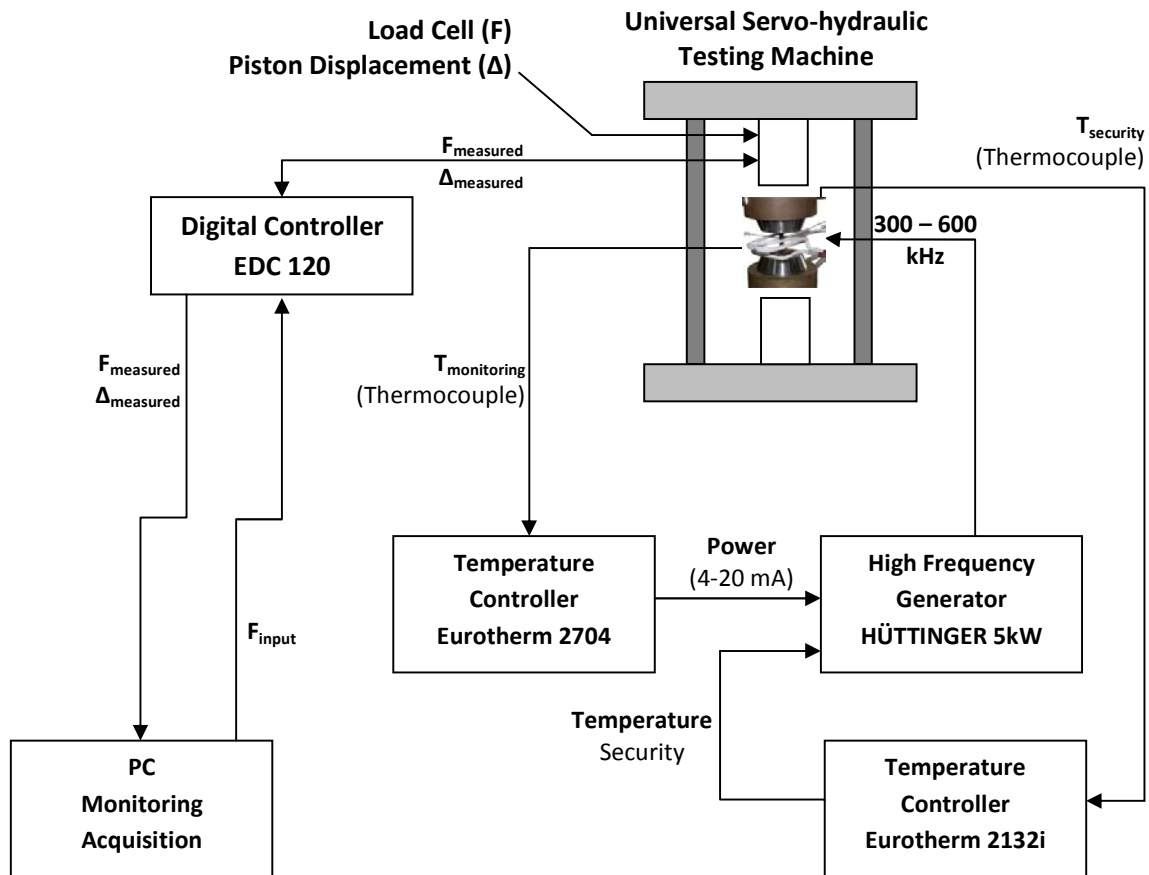


Fig 6. Schematic of the high cycle fatigue testing facility

II.2 Induction Heating

High temperature isothermal HCF experiments use a high frequency induction heating system AXIO 5kW manufactured by HÜTTINGER Elektronik. The induction heating system is chosen because it provides the capability of variable temperature thermo mechanical fatigue testing in addition to isothermal tests.

The heating is done at a slow ramp speed of 20°C/min up to 600°C in isothermal tests. The speed and temperature is maintained by the Eurotherm 2704 temperature controller. To avoid any accidents due to overheating a security temperature controller is also installed which cuts off all signal to the inductor generator in case of out of range values or thermocouple failure.

Three thermocouples are installed on each specimen, figure 8. They are placed in order to be able to effectively monitor the thermal gradient and the temperature for the whole length of the crack propagation.

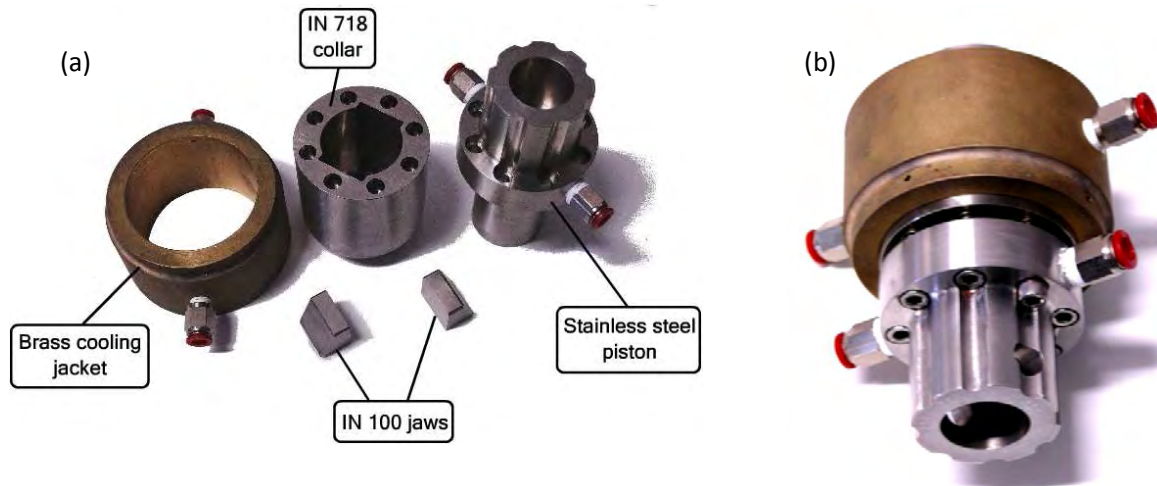


Fig 7. High temperature grip: (a) disassembled (b) assembled.

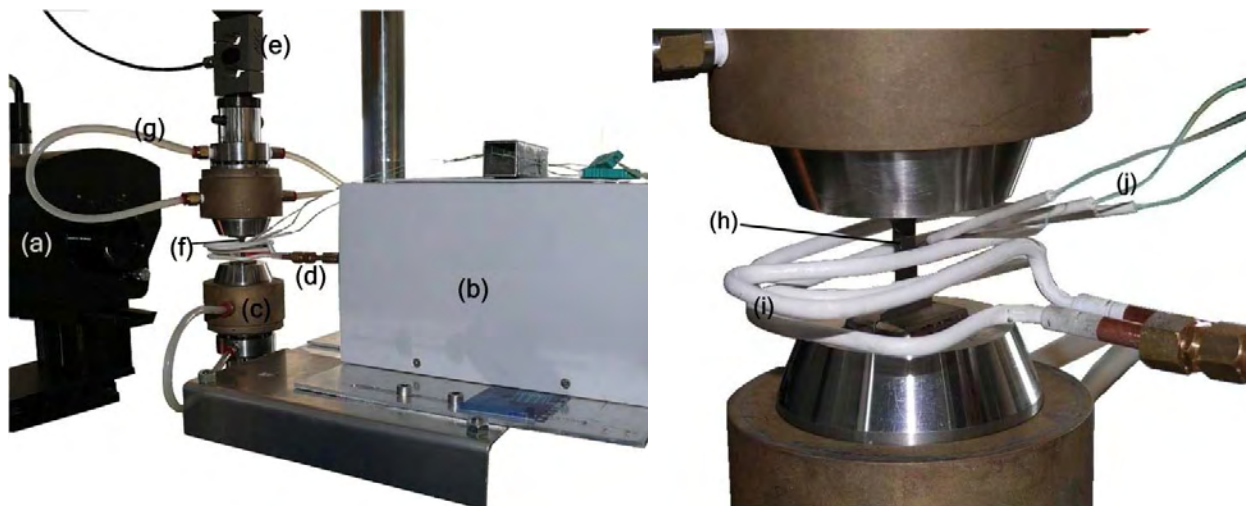


Fig 8. Detailed view of experimental setup: (a) microscope, (b) inductor generator, (c) grips, (d) inductor connection to generator, (e) load cell 2kN, (f) specimen, (g) cooling water, (h) specimen, (i) inductor and (j) thermocouples

Inductor: The inductor, figure 8 is of rectangular form designed in order to heat a strip specimen in a uniform manner and to provide adequate opening for optical observation of the crack propagation.

II.3 Specimens

The specimens are of unique form designed specifically to be used in the experiments of this study. Most design parameters were taken from the guidelines given in the ASTM E647-00, E606, E399-90 standards. However the experimentation imposes specific constraints on the specimen design thus some modifications were made which are not according to the ASTM guidelines. The main limitation comes from the design for the prevention of buckling during compression. The free length of the specimen (outside grips) has to be as short as possible. For this purpose the shoulders of the specimens have a radius smaller than the ASTM standard. This gives the specimen more rigidity but creates a slight stress concentration at the shoulders. This stress concentration has no real effect on crack propagation experiments since the charge never exceeds 25% of the elastic limit of the material.

All the specimens are of the SE(T) [side edge cracked tension] type, dog bone profile, traction specimens, figure 9(a). They were conceived from forged blocks provided by the manufacturer with the preparation procedure as follows (figure 9(c)):

- 1) Profile machining by wire cut electroerosion including the notch of 200 μ m radius.
- 2) Slicing into required thickness by wire cut electroerosion.
- 3) Parallel grinding of opposing surfaces to exact dimensions (2.5mm, 1.0mm and 0.6mm)
- 4) Reducing thickness of specimens by SiC paper of 80 grit size (down to 0.1mm; some specimens only).
- 5) Polishing of the flat surfaces successively by SiC paper of 180, 320, 600, 1200 grit size.
- 6) Polishing to mirror finish with 6, 3 and 1 μ m diamond paste on a metallographic polisher.
- 7) Engraving of grid on the flat surface (some specimens only), figure 9(b).

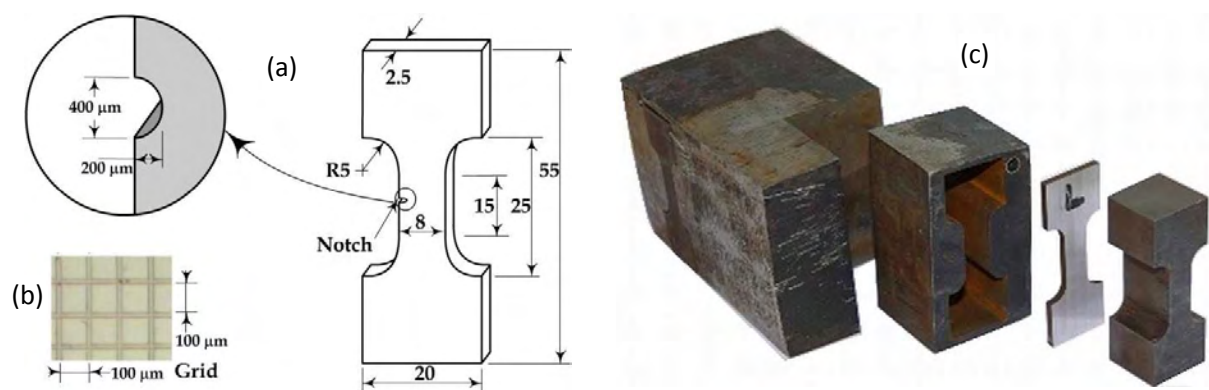


Fig 9. Specimen: (a) dimensions (b) engraved grid details and (c) different steps of manufacturing

All the specimens have been machined from the block in the same direction (longitudinal) for consistency in the properties of the material.

II.4 Observations and Measurements

II.4.1 Long distance travelling microscope

The crack propagation length is observed optically, in situ with a long distance microscope, without interruptions to the experiment. The microscope is a Questar Step Zoom 100 (SZM 100), figure 10(b), made in the USA. It has a maximum optical resolution of $1.1\mu\text{m}$. The field of view, depending on zoom, is between 0.375 and 8.0mm. Long distance microscope gives an advantage of observation from a distance of between 152 and 381mm. It should however be noted that the highest resolution is obtained when the distance between the specimen and the microscope is as low as possible. The microscope is installed directly in front of the specimen as shown in figure 8 and 10(a).

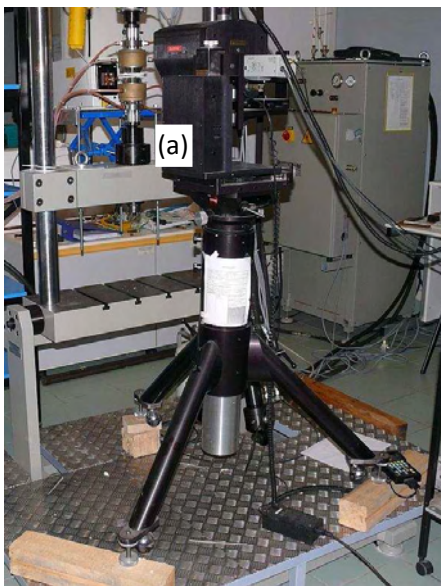


Fig 10. (a) Configuration of the experiment observation microscope, (b) Questar SMZ 100 and (c) CCD camera

II.4.2 Camera and recording

A CCD camera is connected to the microscope for recording the images. The camera is a Sony EXWAVE HAD[®] with a CCD sensor figure 10(c). The sensor is of $\frac{1}{2}$ inch size with a resolution of $470 * 300$ lines (horizontal * vertical). Theoretically, the microscope-camera combination

having 0.4mm field of view (max microscope zoom) and 400 horizontal lines on the CCD sensor we can have an image resolution of $1\mu\text{m}$. Practically, the resolution does not exceed about $4\mu\text{m}$ for the crack length. This is due to the errors induced by machine vibrations, camera sensor noise and video compression by the tape recorder that records the images from the camera.

All the images of the camera are recorded onto a tape recorder at 25fps (frames per second). This video can later be used for post experiment treatment of images.

II.4.3 Post treatment of video

The video recorded by the camera – recorder apparatus can be used for various analyses after the experiment has terminated. The most useful information that was gained by the post treatment was the crack opening displacement.

Traditionally crack opening is measured at the mouth of the crack. The optical system used in this work gave us the possibility of measuring crack opening behind the crack tip for different crack lengths. At the maximum resolution it has been observed that crack opening may be measured as close as $50\mu\text{m}$ behind the crack tip with increments of $100\mu\text{m}$. The figure 11 shows an example with 5 extensometers; the first extensometer is placed $200\mu\text{m}$ behind the crack tip while the others are placed at equal intervals of $200\mu\text{m}$. The different crack opening displacement (COD) values thus obtained may be extrapolated to get the crack tip opening (CTOD). For this purpose all the videos are downloaded to the software iMovie HD®. This software converts the video into images that can be used with image analyses softwares. The crack opening was calculated using image correlation software VIC 2D®.

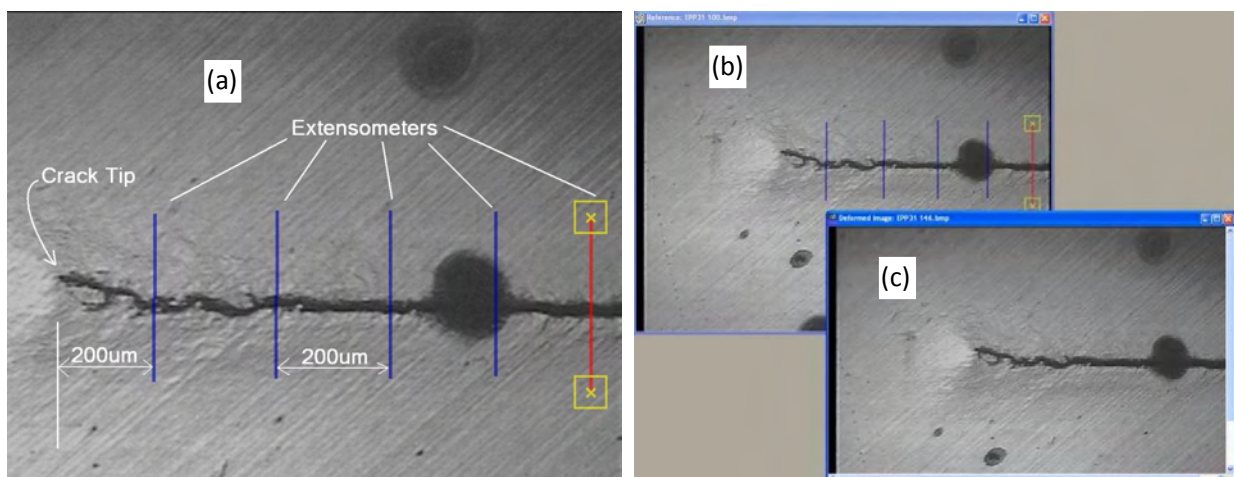


Fig 11. Image correlation for crack opening displacement (a) placement of virtual extensometers behind crack tip, (b) reference image (P_{min}) and (c) deformed image (P_{max}) for correlation

III. EXPERIMENTAL PROCEDURE

This study has been carried out to characterise the surface damage of hot work tool steel X38CrMoV5. For this purpose it was decided that crack propagation experiments will be carried out under different conditions to be able to get an insight of the metal damage process.

All experiments are traction-traction crack propagation experiments under load control. Crack opening data is recorded onto tape via the microscope and camera. Special consideration is given to the stability and smoothness of the load curve applied by the machine. The PID is carefully adjusted and continuously monitored during the experimentation.

Different testing conditions are applied on specimens. Some of the tests are quantitative while others are more qualitative to get an indication of the physical processes under loading especially at high temperatures.

III.1 Effect of load ratio (R) on crack propagation at ambient temperature

R ratio is defined as the ratio of the minimum load to the maximum load in fatigue experiment.

$$R = P_{min}/P_{max} = \sigma_{min}/\sigma_{max}$$

The effect of load ratio is important to be able to determine correctly the effects of crack closure and/or the mean load on the damage of the material. Three groups of experiments are carried out which are summarized in table 2.

Table 2: Tests for the effects of load ratios on fatigue crack propagation

Group of Tests	Thickness (mm) of specimens	<u>Applied max stress</u> Yield stress (%)	Load ratio R	Test Frequencies (Hz)
1	2.5	8.3	0.1	10
	2.5	25	0.1	
	2.5		0.7	
2	0.60	25	0.1	
	0.60		0.7	
3	0.12	25	0.1	
	0.12		0.6	

To determine the effect of maximum stress on FCGR, a test was carried out while keeping very low σ_{max} value: 8.3% of the yield stress. This would ensure good LEFM conditions by reducing the possibility of plastic yielding ahead of the crack tip.

For all the group 1 and 2 specimens two tests are carried out for each R whereas for the group 3 specimens only 1 experiment per condition has been carried out.

Each specimen has a 200 μ m notch. The crack initiation is started at 80% of the material σ_Y . The initiated crack is almost always of about 300 μ m length including the notch. The load is gradually reduced to 25% of the σ_Y to allow for the crack to exit the residual plastic zone at the crack front as for long crack propagation under LEFM conditions. This procedure brings the crack length to between 0.6mm and 1mm. The crack propagation experiment is then accounted from this crack length. The monotonic plastic zone maybe calculated using the following relationships of Irwin (1960) [14].

$$r_p = \frac{1}{3\pi} \left(\frac{K_I}{\sigma_Y} \right)^2, \text{ for plane strain}$$

$$r_p = \frac{1}{\pi} \left(\frac{K_I}{\sigma_Y} \right)^2, \text{ for plane stress}$$

Having a low thickness with respect to what is required by the LEFM analyses, the formula for plane stress is used to calculate the plastic zone.

There were two main goals of each experiment: find out the difference in crack propagation rate curves (Paris curves) and the threshold values of crack propagation at different R if any. The crack propagation or Paris regime experiments are carried out with a constant load and ascending K. The load signal is schematically presented in figure 12.

The determination of the threshold values requires descending K values strategy or the so called load shedding technique.

To test the thinner specimens a smaller load cell has to be installed. This load cell has a maximum capacity of 2kN and is suitable for testing specimens of 0.12mm thickness.

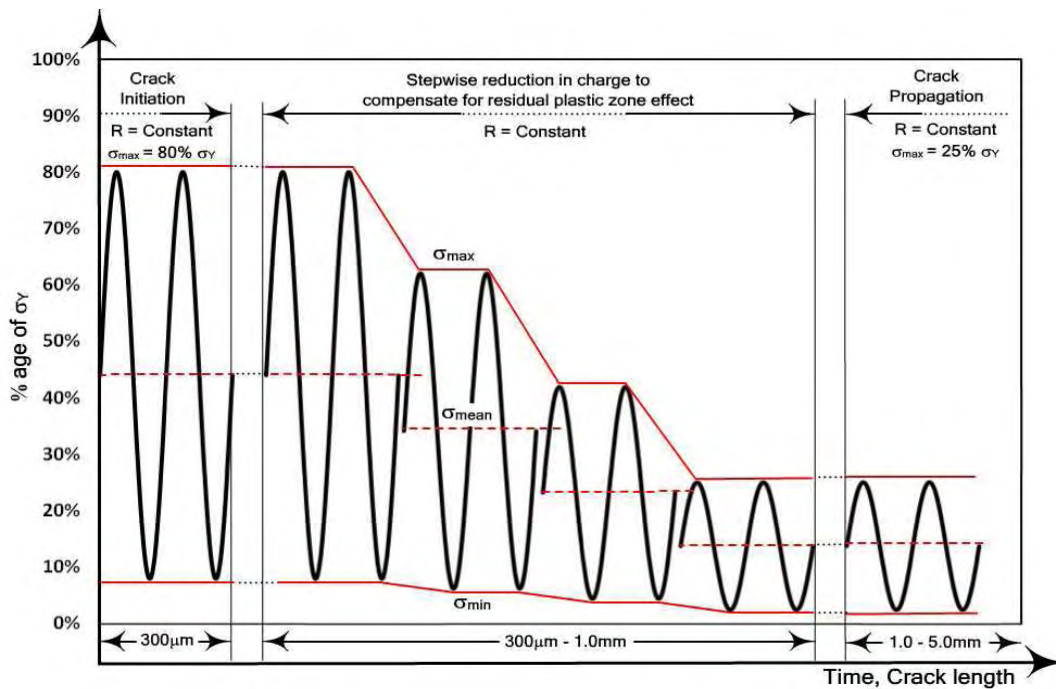


Fig 12. Force applied on the specimen during different stages of the fatigue crack propagation experiment

III.2 Effect of specimen thickness on crack propagation at ambient temperature

As described before the thickness of interest in tool surface damage is of the order of several micrometers. Tests thus have to be carried out on specimens which may have thicknesses as low as 50 μm . This thickness is outside the values recommended by ASTM standard (E399 and E647). We thus have to first establish if there exists any fundamental difference between the crack propagation behaviour of thick and thin materials. For this purpose fatigue crack propagation tests are carried out on specimens of different thicknesses, with same specimen profile. The tests are summarized in the table 3.

Table 3: Tests for the effects of specimen thickness on fatigue crack propagation

Group of Tests	Thickness (mm)	Applied max stress Yield stress (%)	Stress ratio $R = \sigma_{\min} / \sigma_{\max}$	Test Frequencies (Hz)
4	2.50	25	0.1	10
	1.00			
	0.60			
	0.25			
	0.12			

A constant R ratio of 0.1 is maintained for all the experiments.

For the specimens of 1mm and 0.6mm thickness the crack opening displacement (COD) was measured as well. Since the camera has a refresh rate of only 25 fps, not enough information is obtained at 10Hz test frequency. The test frequency is reduced to 0.2 Hz for every 0.5mm of propagation and the microscope images are recorded. The load signal form is changed as well from sine wave to triangular form. The advantage is that the load applied by the machine and COD measurements by video are easily and readily synchronised by calibrating the time base. The recorded video is then passed through the image analysis software to get the COD values. The signal and COD by image analysis is shown in the figure 13.

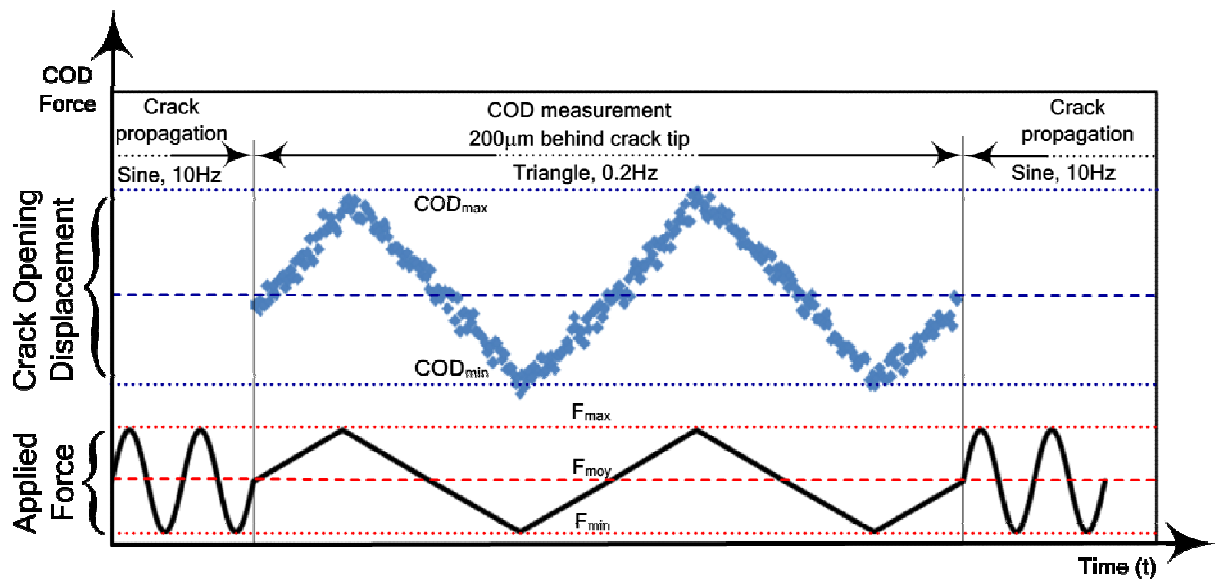


Fig 13. Illustration of applied force signal modification for COD measurements

III.3 Crack propagation at elevated temperatures

The real conditions of utilisation of the hot work tool steels are at elevated temperatures. The X38CrMoV5 is commonly used at 550°C for long periods [1-12]. At elevated temperature the damage to material may be due to many mechanisms working simultaneously. These include fatigue damage, increase in plasticity, creep, oxidation etc. Thus to correctly characterise the surface damage of hot work tools the tests on the material have to be carried out at elevated temperatures.

It should be emphasized here that the fatigue crack propagation data at elevated temperatures for this steel is not available in the literature to our knowledge.

The experiment consists of pre cracking the specimen at 20°C at a high frequency (10Hz). The interest in pre cracking at low temperature is to keep the plastic zone beyond the crack front to a limited size. The specimen is then heated at 20°C/min to a maximum temperature of 600°C in laboratory air. The specimens are held at this temperature for 30 minutes to stabilise the temperature of the grips thus controlling the temperature gradient in the specimen. This stabilisation technique presents certain problems. This 30 minute duration at elevated temperature may cause microstructural changes in the material. However, if the experiment is started without stabilisation, the young's modulus of the specimen will evolve with time as the specimen temperature gradient stabilises. Thus a material or mechanics choice has to be made; we have chosen to give priority to the mechanical conditions, thus introduction of the high temperature stabilisation step. The control of temperature gradient is discussed in appendix A.

At 600°C the tests are carried out for different specimen thicknesses, to see the effect of thickness on crack propagation, figure 14. The same strategy of reducing the testing speed for observation of crack opening displacement is also used for the specimens at elevated temperatures. The summary of all the tests performed is provided in the table 4. Experiments are carried out to establish the effect of R and specimen thickness on the fatigue crack propagation and the threshold values.

The effect of R and specimen thickness on the threshold propagation is studied in detail at elevated temperatures. A test is also carried out to determine the effect of transient temperature on the fatigue crack growth threshold, the details of which are presented in chapter 4.

Table 4: Tests for the effects of temperature on fatigue crack propagation

Group of Tests	Thickness (mm)	Applied max stress Yield stress 25°C	Stress ratio $R = \sigma_{\min} / \sigma_{\max}$	Test Frequencies (Hz)	Temperature °C
5	2.5	25 %	0.5	2	600
	2.5				
	1.0		0.1		
	0.6		0.7		
	0.6		0.3		
	0.4		0.1		
6	0.6	25 %	0.7		20°C – 300°C – 500°C – 600°C Temperature increased in steps during testing

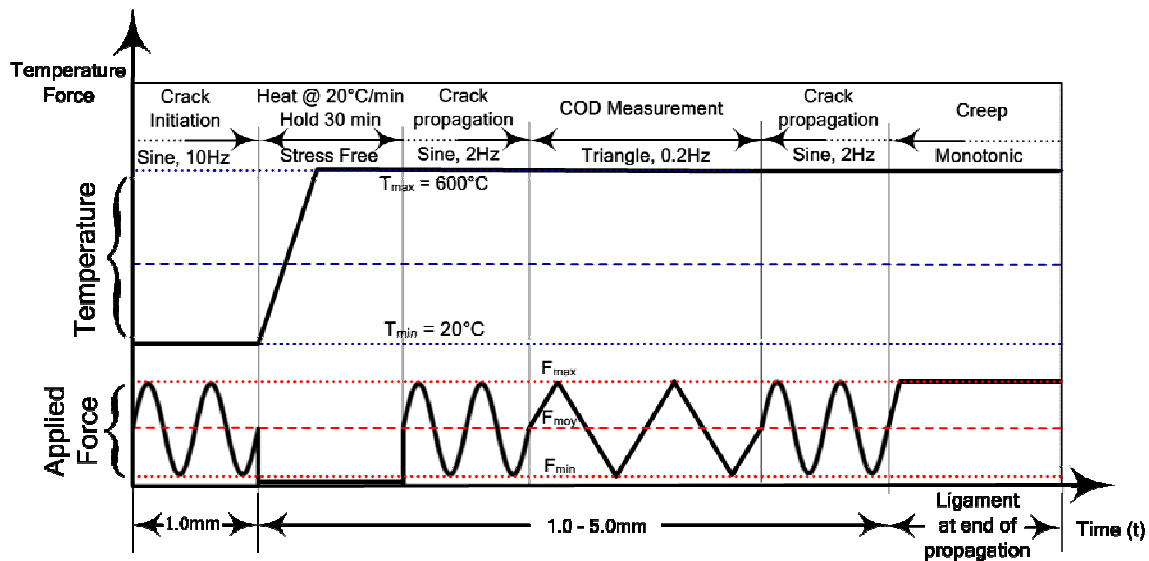


Fig 14. Illustration of the fatigue crack propagation at elevated temperatures, COD and creep

For the specimens of 1mm thickness a creep test was performed by holding the specimen under a monotonic traction load, figure 14. The idea was to determine qualitatively the presence, or absence of creep deformation at this temperature and load at the crack tip.

III.4 Effect of oxidation on crack propagation

Much research has been done on the effect of environment on the fatigue crack propagation. The X38CrMoV5 having 5% Chrome is considered to be oxidation resistant, especially at room temperature. At temperatures above 550°C and in humid air the speed of oxidation is rapid [3, 6, 7]. The effect of oxidation on crack propagation is studied.

A specimen of 0.6mm thickness is selected for the purpose of studying the effect of oxidation on the crack propagation behaviour. A specimen is pre cracked to a certain length; then oxidized at 600°C for five hours under stress free conditions in a tube furnace, figure 15. The specimen is then cooled (natural cooling) to room temperature and re-polished and the crack propagation experiment is continued for a prescribed crack length. This oxidation-polishing-crack propagation procedure is repeated several times. The idea behind this experiment was to establish if there exists an effect of oxygen penetrating beyond the visible oxide layer into the material or not i.e. if the apparently non oxidised material (in front of crack tip) is weakened under the effect of oxidation. The experimental conditions are schematically shown in figure 16.

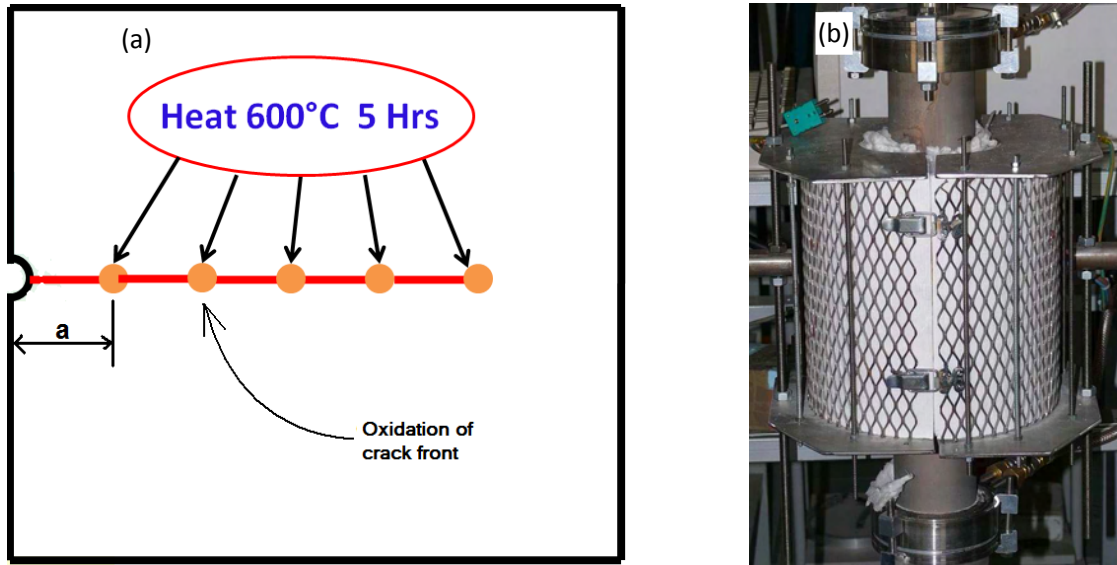


Fig 15. (a) Schematic representation of the experiment to study effects of oxidation on propagation and (b) tubular furnace used for oxidation of specimen

The tube furnace is an electric resistance furnace with the elements placed externally to a tube of tantalum. The advantage of this furnace is its short heating and cooling time and even temperature distribution. The furnace is controlled by a Eurotherm 2704 controller. The thermocouples are mounted directly on the specimen by spot welding. The thermocouples are connected to a data acquisition system which gives the whole thermal cycle during the experiment. This type of test is very long and takes about 5 – 7 days to complete.

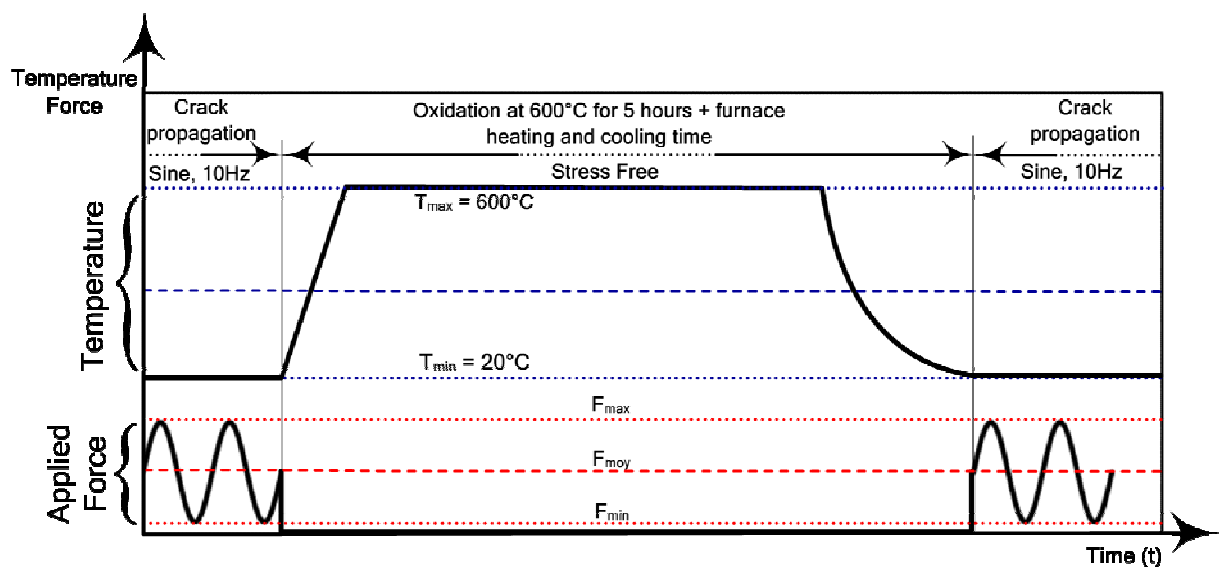


Fig 16. Illustration of the intermittent oxidation experiment parameters

IV. POST MORTEM ANALYSIS

The post mortem analysis in fatigue fracture gives important insights into the modes and mechanisms of fracture and damage of the material. At the end of each experiment the fracture surface as well as the profile of fracture is observed. Here, the preparation, orientation, equipment and the different techniques used are described.

IV.1 Specimen preparation

Generally at the end of a fatigue crack propagation experiment the specimen is fractured into two parts, figure 17. One of the fractured parts is generally conserved for further analysis, figure 17(1) while the other part is prepared for fractographic analysis, figure 17(2). The part cut for fractography is mounted on a double coil spring to keep it upright. It is then observed under binoculars for macroscopic analysis. Afterwards it is mounted on the stage of the SEM for microscopic analysis figure, 17.

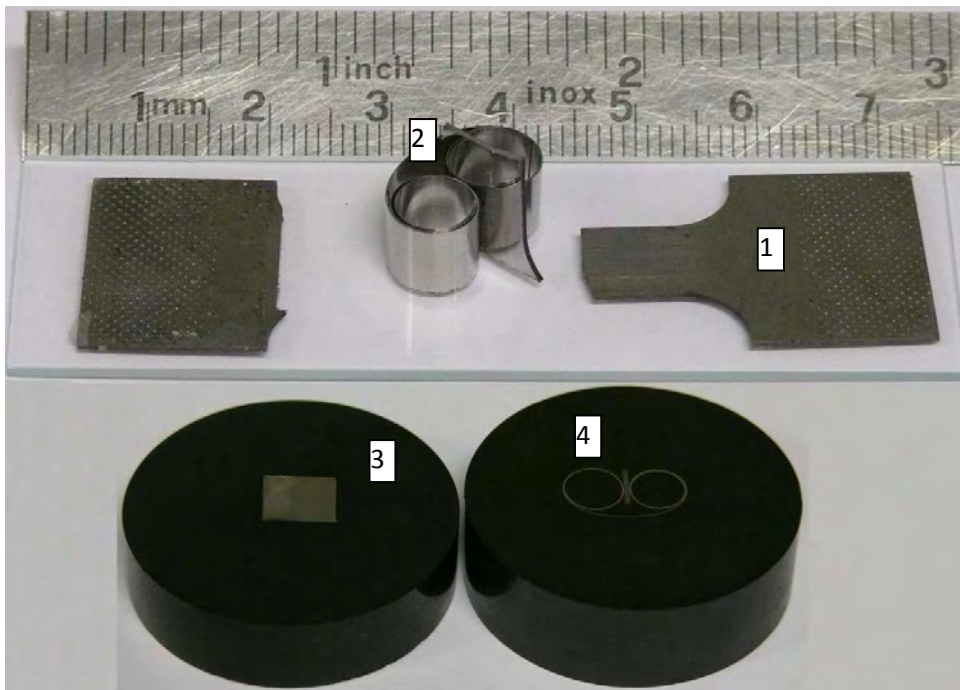


Fig 17. Specimen preparation for post mortem analysis of specimens

Under the SEM the crack initiation zone near the notch is observed. Afterwards the crack propagation for “long” crack is observed while looking for fatigue striations, propagation path and texture of the surface to try to interpret the presence of slip bands or other artefacts.

After this the specimen is mounted on its flat profile, figure 17(3) or edgewise, figure 17(4) in a conducting resin. Generally the configuration (3) is used for microstructure analysis or surface artefacts due to deformation. Initially the specimen is observed under SEM as is for presence of slip bands.

IV.2 Chemical attacks for microstructure

If there is an oxide layer on the crack surface it has to be removed chemically by a mixture of HCl (etchant) and HMTA (Hexamethylene-Tetramine inhibitor). The HCl removes the oxide layer but the underlying metal surface is protected by the HMTA.

Different chemical attacks may be used to reveal the microstructural properties or modifications during the test. Mostly the Nital (3% HNO₃ in Ethyl alcohol) is used to reveal the martensite microstructure. The crack path then can be traced in the microstructure of the material and the interaction of the two can be studied.

In some of the tests an electrolytic etching method using chromic acid is used to reveal the previous austenitic grain network. This method is used to find out if the crack propagation is intergranular or transgranular in nature.

During crack propagation considerable plastic deformation occurs beyond the crack tip. A method was devised to get an indication of the size of this large plastic deformation. The cracked specimens are heated, in air, up to 50°C above the AC₃ (950°C in this case) for 10 minutes and then cooled. This causes the recrystallisation of the deformed grains, wherein the severely deformed grains have smaller crystal structure as compared to the undeformed ones. The oxide of the air penetrates the grain boundaries more severely. After removal of the oxide layer the austenite structure can be easily seen under a microscope. However with this procedure the crack surface is completely destroyed and no information on crack path remains.

V. CONCLUSION

In this chapter the different experimental methods, procedures and conditions have been described. The metal chosen for this study is an X38CrMoV5 (AISI H11) hot work tool steel. The metal studied has been heat treated by air quenching followed by double tempering to obtain a tempered martensitic microstructure and a hardness of 47 HRC.

The specimen used is an SE(T) specimen with a dog bone profile. Fatigue crack propagation experiments are carried out at different temperatures. The effects of oxidation on crack propagation is also studied. All the observations during the experiment are carried out in-situ without interruptions to the experiments. Heating of the specimen is done by an internally water cooled induction heating system. High temperature grips were specifically developed for this purpose.

At the end of the experiments the data recorded on tape is analysed. The specimens undergo post mortem analysis. The preparation of the specimens differs with the testing conditions. Different etching techniques are used to get information on the interaction between the crack propagation and the microstructure of the metal.

VI. REFERENCES

1. Delagnes, D., *Comportement et tenue en fatigue isotherme d'aciers à outils Z38CrMoV5 autour de la transition oligocyclique-endurance*. 1998, Thesis Ecole des Mines de Paris.
2. Jean, S., *Méthodology d'exploitation mécanique et microstructurale d'un essai de fatigue thermique: Application à l'étude du faïençage d'un acier d'outil de forge à chaud*. 1999, Thesis: Institut National Polytechnique de Toulouse.
3. Oudin, A., *Thermo-mechanical fatigue of hot work tool steels*. 2001, Thesis Ecole des Mines de Paris.
4. Mebarki, N., *Relation Microstructures - Propriétés Mécaniques d'Aciers Martensitiques Revenues Destinés aux Outillages de Mise en Forme d'Alliages Légers*. 2001, Thesis; Ecole des Mines de Paris.
5. Velay, V., *Modélisation du comportement cyclique et de la durée de vie d'aciers à outils martensitiques*. 2003, Thesis Ecole des Mines de Paris.
6. Bruckel, P., *Oxydation de l'Acier à Outils X38CrMoV5 à 600-700°C et en présence de vapeur d'eau*. 2003, Thesis Ecole des Mines de Paris.
7. Daffos, C., *Endommagement des outillages de forgeage traités par nitruration : étude et modélisation*. 2004, Thesis l'Institut National des Sciences Appliquées de Toulouse.
8. Medjedoub, F., *Détermination des paramètres influant sur le phénomène d'endommagement par fatigue thermique des moules en fonderie sous pression d'aluminium*. 2004, Thesis Ecole des Mines de Paris.
9. Barrau, O., *Etude du frottement et de l'usure d'acier de l'outils de travail à chaud*. 2004, Thesis l'Institut National Polytechnique de Toulouse.
10. Michaud, P., *Influence des Elements d'Alliages sur la Relation entre les Précipitation et les Propriétés Mécanique Usuelles d'Acier à Outils à 5 % de Chrome*. 2006, Thesis Ecole des Mines de Paris.
11. Salem, M., *Etude d'endommagement par fatigue thermique des moules de fonderie sous pression d'aluminium: effet de l'interaction avec l'aluminisation et l'oxydation*. 2009, Thesis: Université de Toulouse.
12. Mauries, S., *Caractérisation et modélisation de la séquence de précipitation de carbures au cours du traitement thermique d'aciers martensitiques alliés*. 2008, MEGeP, Institut National Polytechnique de Toulouse, work performed at Ecole de Mines d'Albi - Carmaux.
13. Jespersen, H., *Influence of the heat treatment on the toughness of some hot-work tool steel grades*.
14. Irwin, G.R., *Plastic zone near a crack and fracture toughness*. Proceedings of the Seventh Sagamore Ordnance Materials Conference, 1960. **4**: p. 63-78.

Chapter 3: Numerical Simulation

Résumé en Français	53
I. Introduction.....	55
II. Numerical Simulation of SE(T)_c Specimens	60
III. Results	66
IV. Conclusion	76
V. References.....	77

RESUME EN FRANÇAIS

Les conditions expérimentales de cette étude imposent un dimensionnement spécifique des éprouvettes. La validité de la caractérisation de l'endommagement du matériau dépend de la détermination précise du paramètre d'endommagement. Cela permet aussi de comparer les résultats obtenus sur nos éprouvettes non normalisées avec d'autres travaux, concernant des éprouvettes normalisées. Ce chapitre est consacré à l'analyse numérique qui a permis de calculer les facteurs d'intensité de contrainte en mode I (FIC) ou K_I , ainsi que les valeurs d'intégrale J élasto-plastique à différentes longueurs de fissure.

La surface des outillages est très sensible à la fissuration et à l'usure. Afin d'avoir une meilleure caractérisation de l'endommagement de la surface des outillages, les essais sur des éprouvettes de faible épaisseur sont mieux adaptés par rapport à des éprouvettes C(T) massives normalisées. À cet effet, les essais réalisés sur les éprouvettes de type SENT encastées (ensuite appelée $SE(T)_C$) présentent une alternative très intéressante à des éprouvettes C(T). Les éprouvettes $SE(T)_C$ enlèvent complètement les problèmes de flambage ou flexion sous chargement en fatigue traction - traction. Les problèmes de flambage et de flexion existent aussi dans les éprouvettes de traction mises en place avec un système à goupilles. D'autre part, la surface en contact avec les goupilles est susceptible de s'endommager, en particulier pour les éprouvettes d'épaisseur voisine de 0.1 mm. Lorsque la surface est plate, caractéristique des éprouvettes $SE(T)_C$, des mesures précises (de l'ordre de 1 micromètre) d'ouverture de fissure à l'aide d'une caméra sont également réalisables. Un schéma d'une éprouvette $SE(T)_C$ est présenté dans la figure 1, sur laquelle la direction d'application de la charge est indiquée. Il est alors nécessaire d'utiliser une méthode de calcul de facteur d'intensité de contrainte adapté à ce type d'éprouvette.

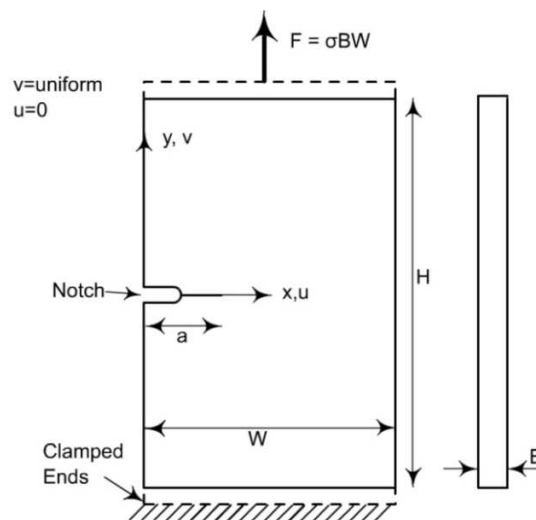


Fig 1. Schéma d'une éprouvette $SE(T)_C$

Le calcul du facteur d'intensité de contrainte utilisé dans cette étude est basé sur la méthode énergétique utilisant l'intégrale J. Le logiciel utilisé pour la simulation numérique est ABAQUS/Standard™. Les conditions aux limites considérées sont le déplacement uniforme imposé et la force uniforme imposée sur l'éprouvette. La comparaison des résultats d'analyse avec ceux qui sont répertoriés dans la littérature (réalisée sur des éprouvettes normalisées de forme rectangulaire avec différents rapports longueur/largeur) a permis la validation de la méthode numérique. On constate que la méthode donne des résultats suffisamment précis pour la condition aux limites de déplacement uniforme imposé.

Après cette vérification, la méthode d'analyse est appliquée sur les formes d'éprouvettes « réels » dont le profil est de type « Dog Bone ». Quatre types d'analyses ont été réalisés :

- 1) analyse élastique à 20 °C,
- 2) analyse élasto-plastique à 20 °C,
- 3) analyse élastique à 600 °C,
- 4) analyse élasto-plastique à 600 °C.

Les résultats obtenus pour l'analyse élastique et élasto-plastique à température ambiante sont identiques car l'effet de la plasticité en pointe de fissure sur les valeurs de l'intégrale J est insignifiant. Cependant, l'analyse élastique à 600°C et l'analyse élastique à température ambiante donnent des valeurs identiques de l'intégral J en revanche pour l'analyse élasto-plastique à 600°C l'effet de la plasticité (en pointe de fissure) influe considérablement sur la valeur de l'intégrale J, menant à des valeurs très différentes de celles obtenues à température ambiante.

En mécanique linéaire élastique de la rupture, l'application du facteur d'intensité de contrainte comme critère de propagation de fissure n'est plus justifiée lorsque la plasticité devient importante notamment à températures élevées. Un autre critère qui tient compte de la plasticité en pointe de fissure tel que : $\sqrt{J_{el,pl}E'}$ est alors introduit. Les critères K_I et $\sqrt{J_{el,pl}E'}$ sont utilisés dans le chapitre 4 « Experimental results ».

L'effet de la variation de la position des éprouvettes dans les mors a aussi été étudié. Des petites variations de l'écart entre les deux mors au cours de l'installation des éprouvettes peuvent exister. Ce sont des variations inévitables. Il a été constaté que cette variation d'écart n'a pas un effet important sur le facteur d'intensité de contrainte.

The testing conditions imposed on the experiments in this study require us to use non standard specimen profiles. The validity of the characterisation of damage behaviour of the material is dependent on the accurate determination of a damage criterion. The accurate determination is also required to able us to compare the experimental results with those of other researchers. This section describes the numerical analyses carried out in order to determine the mode I Stress Intensity Factors (SIF) or K_I and elastic-plastic J-Integral values at different crack lengths. The effects of variation in specimen installation, inherent to the experimental procedure, are also explored.

I. INTRODUCTION

The surface of forming tools is highly prone to cracking and wear. To get better insight into the behaviour and damage accumulation near the surface of the tools, testing on specimens with reduced thickness is more appropriate as compared to standard C(T) specimens. To test the surface damage of die steels, small specimens of very low thickness are needed[1, 2]. For this purpose clamped SE(T)_c specimens provide a good alternative to C(T) specimens because they completely remove the possibility of buckling or bending during tensile fatigue testing. The same problems of buckling and bending would be present in pin loaded specimens (effects of non symmetric rotation) as well as failure at the bearing surfaces since the specimen thicknesses can be as low as 0.10mm[1, 2]. Also the free standing surface keeps a flat view towards the camera throughout the test which is very important for making displacement measurements of the order of 1 micron accurately. A schematic for the single edge cracked specimen is shown in figure 1. The direction of the applied load is also shown. However a method is needed to calculate accurately the stress intensity factors generated in these specimens.

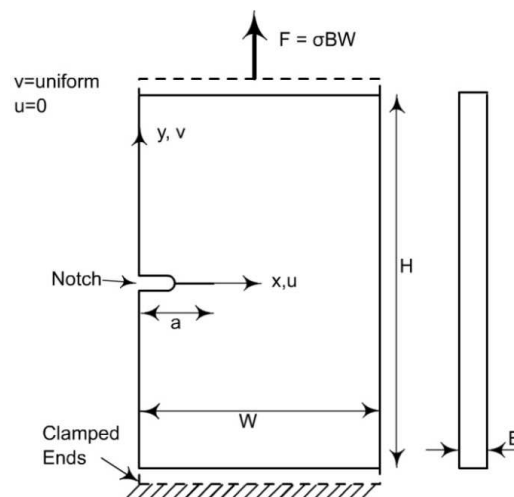


Fig 1. Schematic of the single edge cracked tensile specimen with clamped ends, SE(T)_c

Nomenclature

SE(T)	side edge cracked, tension specimen
SE(T) _c	side edge cracked, clamped tension specimen
a/W	crack length to specimen width ratio
C(T)	compact tension specimen
a	crack length
B	specimen thickness
W	specimen width inside gauge length
W ^e	specimen width at the specimen ends
H	specimen height
H/W	height to width ratio
s	length of the arc around the contour
y	direction perpendicular to crack plane
v,u	displacement parallel to y axis and x axis respectively
u*	displacement vector
w	deformation energy density
Γ	contour for J-Integral
T	traction vector
F	force perpendicular to crack plane
K	stress intensity factor
K _I	mode I stress intensity factor
E	Young's modulus
FEA	finite element analysis
ε	strain
r	distance from the crack tip
σ _y	yield stress
ν	Poisson's ratio
U _y	displacement applied at the end of a specimen
R _x , R _y , R _z	rotation of specimen ends along x, y and z axis respectively
f	reaction force on each node of an finite element model
f(a/W)	geometric correction factor for stress intensity factor
∅	ratio of in plane rigidity of gauge length to in plane rigidity of specimen ends

I.1 Bibliography: Methods of SIF calculation

Different strategies and calculation procedures have been employed by researchers over the years. Some of these methods are used to calculate the SIF directly by measuring displacement fields near the crack tip, while others use an indirect energetic approach (global). This section describes some of the methods used in the numerical simulation of SIF. This section is based largely on a review of the numerical simulation methods by S. Courtin et al[3].

I.1.1 Extrapolation of displacements method

This is a method often used to calculate the SIF. It is based on the extrapolation of displacements in the vicinity of the crack tip and the use of analytical expressions of LEFM (equation 1)[3, 4]:

$$K_I \begin{cases} (2\kappa - 1)\cos\frac{\theta}{2} - \cos\frac{3\theta}{2} \\ (2\kappa + 1)\sin\frac{\theta}{2} - \sin\frac{3\theta}{2} \end{cases} = 4G \sqrt{\frac{2\pi}{r}} \begin{cases} u_r \\ u_\theta \end{cases} \quad (1)$$

Where,

$$G = \frac{E}{2(1 + \nu)}$$

$$\kappa = \frac{3 - \nu}{1 + \nu} \quad \text{plane stress} \quad (2)$$

$$\kappa = 3 - 4\nu \quad \text{plane strain}$$

Considering a meshed two dimensional crack tip, figure 2:

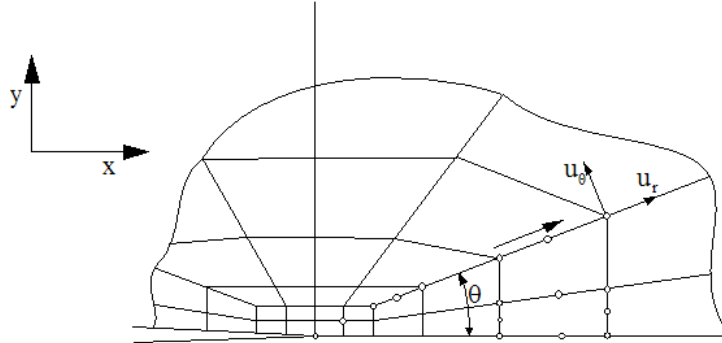


Fig. 2. 2D crack tip in a cylindrical reference

The finite element analysis can be used to get the displacement field in the vicinity of the crack. The expression (1) can be used at any point along the radial line emanating from the crack tip. In general, authors like to work on the crack faces (or lips) for which we have $\theta = \pi$. Thus the expression 1 becomes:

$$K_I = \frac{E}{4(1 - \nu^2)} \sqrt{\frac{2\pi}{r}} u_\theta \quad \text{Plane Strain} \quad (3)$$

$$K_I = \frac{E}{4} \sqrt{\frac{2\pi}{r}} u_\theta \quad \text{Plane Stress}$$

The expressions 3 can be used to plot the K values against a radial distance r from the crack tip figure 3. The values close to the crack tip may be discarded and the K value for the nodes near the tip may be extrapolated. Obviously the value of K at $r = 0$ is the stress intensity factor K_I .

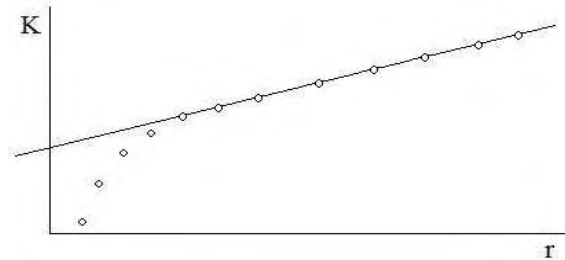


Fig 3. Obtaining K by displacement extrapolation method [3, 4]

I.1.2 Singular finite elements method of SIF determination

This method was introduced by Barsoum [5], wherein singular finite elements are used. It gives better results in the vicinity of the crack tip as compared to the displacement extrapolation method. The procedure consists of collapsing three nodes of an element on the same geometric point, figure 4. Then the mid-side nodes are then shifted to quarter point positions (figure 4), which exactly simulates the square root stress intensity factor predicted by LEFM.

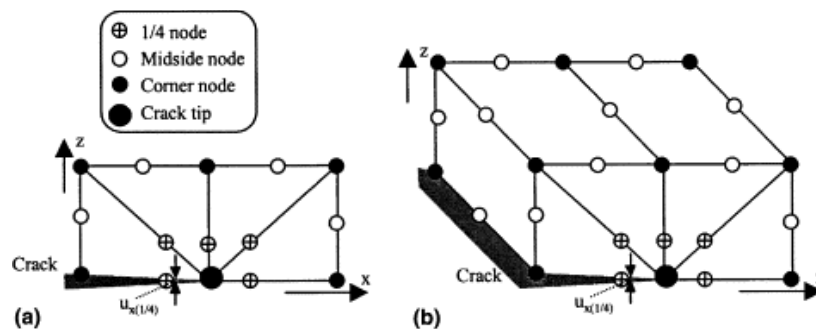


Fig 4. Quarter-point finite elements in (a) 2D and (b) 3D [6]

I.1.3 Energetic approach of determining SIF

The energetic approach involves determining the J-Integral value in the cracked body. The J-Integral introduced by Rice [7] is shown schematically in figure 5. Here a material with a crack is monotonically loaded by a force F in the direction perpendicular to the direction of crack propagation. Considering T as traction independent of the crack length on a contour Γ around the crack tip and assuming there is no load on the crack faces, the integral “ J ” around the contour Γ is given by the expression [7,11]:

$$J = \int_{\Gamma} \left(w \cdot dy - T \cdot \frac{\partial \vartheta^*}{\partial x} \cdot ds \right) \quad (4)$$

Where, w = deformation energy density

dy = displacement perpendicular to crack plane

T = traction vector

ds = differential length of arc around contour

v^* = displacement vector

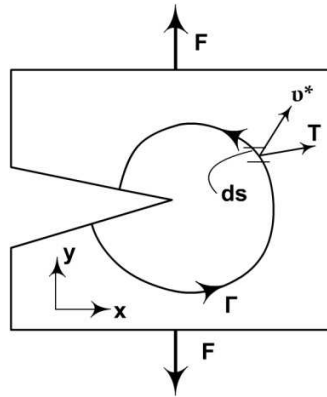


Fig 5. Schematic of a cracked body loaded for contour integral or “J-Integral” calculation

The elastic J-Integral calculated in this manner may be easily related to the elastic mode I stress intensity factor K_I which is directly calculated using the expression.

$$J = K_I^2 / E' \quad (5)$$

Where $E' = E$ for plane stress and $E' = E/(1-\nu^2)$ for plane strain.

The J-integral by definition is independent of the path or the contour on which the integral has been calculated as long as it represents a minimum volume which includes the deformation due to the presence of the crack. Due to this property the numerical simulation can be carried out for fairly coarse mesh without much problem [3].

I.2 Conclusion

A comparison of the different methods discussed here and the analytical expressions has been provided by Courtin et al. [3] for the C(T) specimens at a specific crack length (Table 1).

Table 1: Comparison of K-values (in $MPa\sqrt{m}$) obtained with various methods

Empirical Expressions	2D		3D	3D Coarse mesh		J-Integral
	Singular elements	Displacement extrapolation	Displacement extrapolation	Displacement extrapolation		
				In the crack plane	Perpendicular to the crack plane	
985-1015	1015	999	1045	1046	1057	1060

The different methods give similar results with a variation of upto 8% between different authors. In the laboratory we have access to the finite element code ABAQUS/Standard™ which is used to carry out all the calculations. This code uses the J-Integral method explained above to calculate the K_I values in the specimens.

II. NUMERICAL SIMULATION OF $SE(T)_C$ SPECIMENS

With reference to the figure 1, K_I is known to be dependent on the H/W ratio and the end conditions as shown in literature [8-10]. These variations are calculated for clamped $SE(T)_C$ specimens and compared with values found in the literature [8-10]. It is also observed that in practice the position of the specimens inside the grips may vary slightly from one experiment to another. The influence of these variations on the K_I values needs to be assessed to determine its effects on the interpretation of the results of the experiments. Thus a sensitivity study has been carried out to see the effects of this variation on the SIF values in the specimen.

II.1 Numerical model

Detailed finite element analyses are performed on plane strain models of three types of 1-T $SE(T)_C$ specimens, all having a thickness of 2.5mm using the software package ABAQUS/Standard™. The analysis is carried out on two rectangular specimens with height to width ratio (H/W) of 2 and 3 respectively as well as on one dog bone type specimen shown in Figure 6.

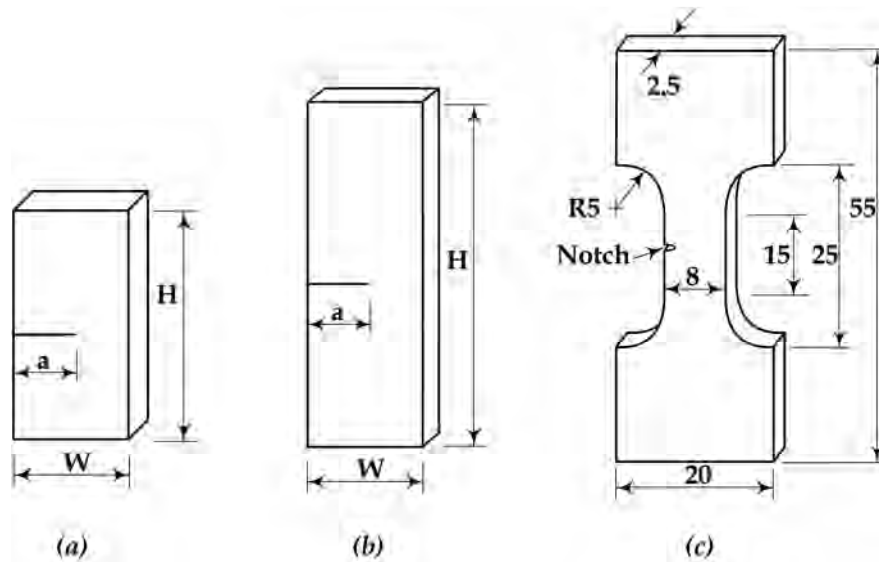


Fig 6. Schematic of the $SE(T)_C$ specimens used in finite element analyses: (a) Rectangular $H/W=2$ (b) Rectangular $H/W = 3$ (c) Dog bone used in FEA and experiments

As indicated above the K_I is dependent on the H/W ratios in rectangular specimens. This does not pose a problem as long as the test specimens are rectangular and the K_I values may be

obtained directly in the literature. However, when using a dog bone specimen as in this work, the situation is more complex. The specimen no longer represents a simple rectangular form. In this example, there are different H/W ratios; for gauge length it is 1.875 and that for the unconstrained length between grips is 3.125. It may also be noted that in the unconstrained length between grips there are shoulders which change the compliance of the specimen due to variable section along the length. This specimen thus has to be considered as a structure instead of a simple rectangular specimen. However since the two extreme H/W ratios possible are between ≈ 2 & 3 figure 6, the numerical analysis procedure is verified for these two H/W values.

Although the finite element analyses are carried out on all the specimens (rectangular and dog bone), the procedure is described only for the dog bone specimen whereas the procedure for other two geometries stays the same. Figure 7 shows the finite element model constructed for the $SE(T)_C$ specimen along with the finite element mesh. In the rectangular specimens, a is the crack size including the notch, W is the width of the specimens and H is the height. The rectangular specimens are analyzed with the intention of comparing the results obtained with those of other researchers [8-10]. The comparison will be presented in the results section.

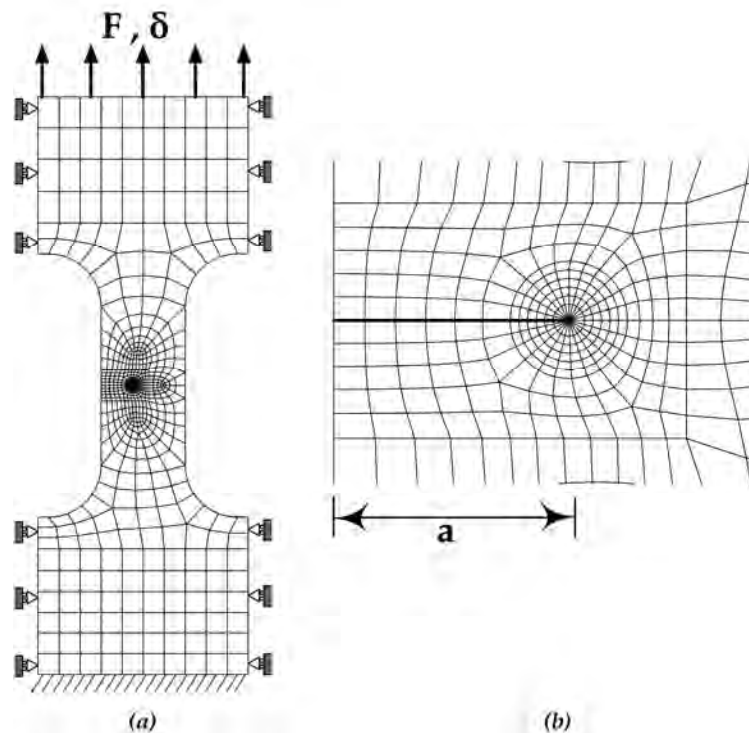


Fig 7. Finite element model used in plane strain analyses: (a) Complete specimen (b) region of interest around the crack tip

All the specimens are tested for $0.125 \leq a/W \leq 0.625$ which corresponds to crack lengths of 1mm to 5mm in a total width of 8mm. A conventional crack analysis mesh configuration is used with a focused ring of 15-node quadratic triangular prism (C3D15) elements around the crack tip, figure 8. Around this first cylinder of triangular elements five concentric rings of 20-node quadratic brick, reduced integration (C3D20R) elements are generated. These rings are subsequently used for calculation of the J-Integral wherein the values on the first ring are ignored [11]. There has to be convergence on all other element rings for results to be valid (see ABAQUS/Standard™ user's manual [11] for a detailed analysis). The position of the center of these rings defines the crack front. A typical 3D finite element mesh contains about 10000 elements. A transverse plane surface is then chosen from the center of the rings to the crack edge which is defined as the crack plane. In the analysis ABAQUS/Standard™ duplicates the nodes on the crack plane and then assigns one set of nodes to one face and the other set to the other. This creates a crack with no opening at initial condition (zero charge) and at the crack tip a singularity in terms of stresses and strains. However since the large strain zone is very localized at the singularity the problem can be overcome satisfactorily using small-strain analysis. The crack tip strain depends on the choice of the material model used. In this analysis an incremental plasticity isotropic hardening model is used. If r is the distance from the crack tip then the strain singularity valid for small strain is:

$$\varepsilon \propto 1/\sqrt{r} \quad (6)$$

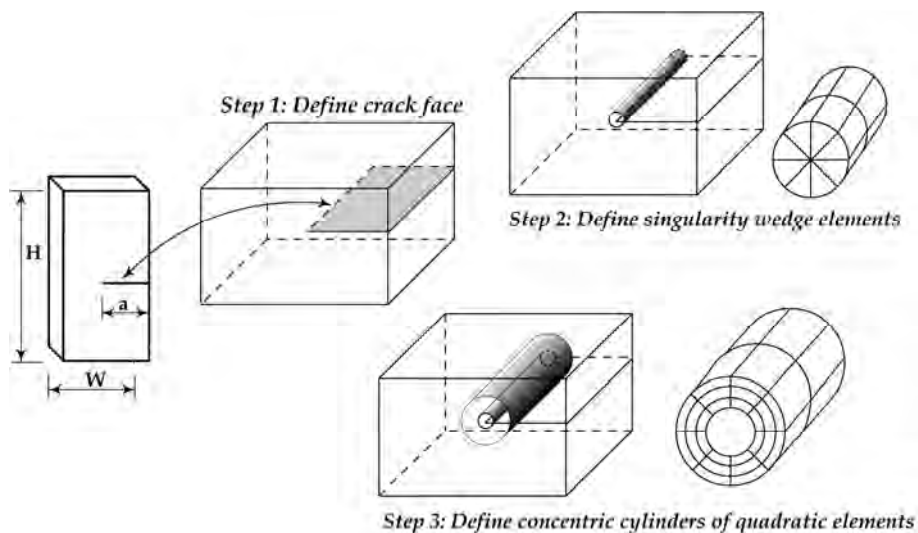


Fig 8. A schematic of stepwise procedure of meshing

This singularity is automatically built into the finite element model in ABAQUS/Standard™ with the help of the triangular prismatic elements which are used to represent collapsed quadratic elements. The need for creating “quarter point” nodes manually is essentially eliminated. The

0.25 stress singularity simulates the collapsing of quadratic elements at a distance of 0.25 points from the crack tip into a wedge element [11] figure 9.

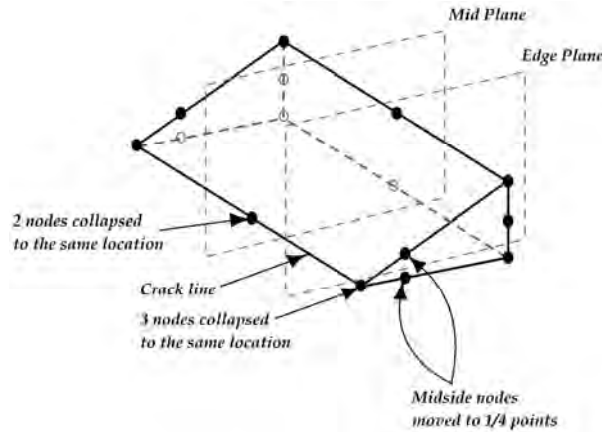


Fig. 9. C3D20R element collapsed on one side to create a singularity, the collapsed element can be simulated automatically by using a C3D15 element [11]

The finite element code ABAQUS/Standard™ provides the numerical solutions for plane strain analyses for 3D models as presented here. The plane stress analyses are usually treated using 2D models to reduce the time of calculation, however here only the 3D models are analysed. The evaluation of the J-integral is based on the domain integral procedure [7] which yields J values in excellent agreement with other methods of calculation [3]. The procedure is supposed to maintain strong path independence for domains outside the highly strained field near the crack tip. Such J values provide a convenient parameter to characterize the average intensity of far field loading on the crack front. The advantage being that we can directly calculate the K_I stress intensity factor values using the equation 5.

II.2 Computational procedure

II.2.1 Material behaviour

The material behaviour defined for all the analyses is an incremental plasticity isotropic hardening model using values for an X38CrMoV5-47HRC hot work tool steel (see appendix H for material properties). As indicated in table 2, two material property sets are chosen for the purpose of simulating material at ambient temperature and at 600°C.

Table 2: Tensile test data for X38CrMoV5 – 47HRC

Temperature	R_{p0} (MPa)	$R_{p0.2}$ (MPa)	E (MPa)	n	ν
20°C	913	1100	208000	12	0.3
600°C	213	600	147000	5.3	0.3

The charge in all the specimens never exceeds 250MPa in total thus giving a fairly accurate approximation to a linear elastic analysis with a confined plastic zone ahead of the crack tip specimens at ambient temperature. However, the material properties at 600°C are such that there may be generalised plasticity (monotonic) ahead of the crack tip or in the whole of the specimen. Therefore the analyses are carried out for linear elastic materials at different temperatures as well as elastic-plastic material model. Different types of analyses are performed at ambient temperature and at 600°C which are detailed separately as follows.

II.2.2 Rectangular specimens and boundary conditions (linear elastic)

The main purpose of testing the rectangular specimens is to compare the procedure of numerical analysis explained above with that of other researchers [8-10]. The analysis is also used to correctly identify the effect of different boundary conditions for the calculation of K_I ; (i) with one end fixed while a uniform force applied on the other end or (ii) one end fixed with a uniform displacement applied at the free end. Two different H/W values (figure 6a, 6b) are used because the final dog bone (figure 6c) specimen falls within this ratio as discussed above. Figure 10 shows the end conditions in detail.

In the first set of boundary conditions (figure 10a), one end of the specimen is fixed while at the other end a uniform force is applied such that the total force is equal to F , while the displacement of this face is kept completely free. In the second set of boundary conditions (figure 10b), one end is fixed as before while a fixed displacement U_y is applied on the other end. The magnitude of this displacement is adjusted in such a way that the sum of reaction forces f , on all the nodes of this face should be equal to the force F applied in the first case. This second set of boundary conditions follows more closely the real testing conditions inside the laboratory while using fixed end loading.

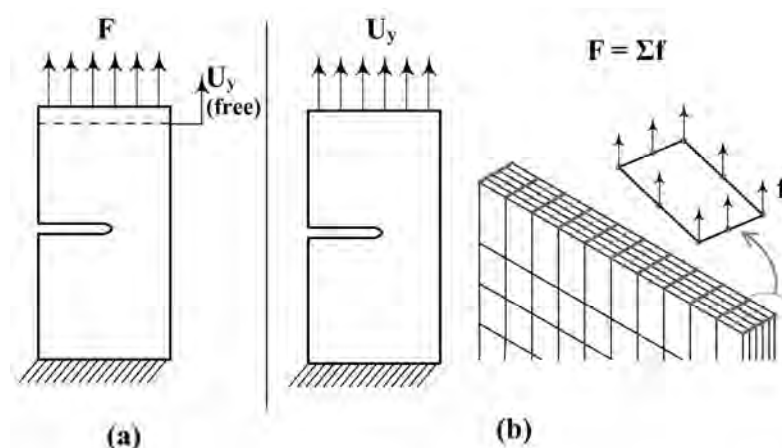


Fig 10. Boundary conditions: (a) Applied uniform force (b) Applied displacement

The K_I values are calculated for both boundary conditions to be compared with the work of Chiodo et al.[8, 10] and that of John et al.[9], both of whom use the applied displacement boundary condition in their analyses. John et al.[9] have used the singular elements method [5] of K_I calculation, which is a method based on the displacement of near crack-tip nodes. The software used is ADINATM. Whereas the method used by Chiodo et al. [8, 10] is similar to the one described in this work i.e., is an energetic solution based on the domain integral method (J – Integral) [3, 10]. They have carried out the simulation in WARP3DTM software. The results of the simulation comparison will be presented in the results section of this chapter.

II.2.3 Dog bone specimens and boundary conditions

With the help of the comparative study on rectangular specimens as described above it was concluded that the applied displacement method gives a better correlation for the K_I values. It is, in any case physically closer to the experimental configuration in the fixed grip loading. This point is discussed in more detail in paragraph III.2.

The dog bone specimen is completely constrained on one end where the ends of the specimen that go into the grips (represented by faces xy in figure 11a) are also constrained, figure 11a. On the free end of the specimen (hydraulic piston side on the machine) the displacement is applied on the top face (plane xz , figure 11b) with a magnitude adjusted to create a 250 MPa stress in the gauge length of the specimen. The side faces of this end (faces on xy plane figure 11b) also are constrained for axial displacement only, figure 11b.

Subsequently, finite element analyses are run for five different crack lengths that lie in the range $0.125 \leq a/W \leq 0.625$.

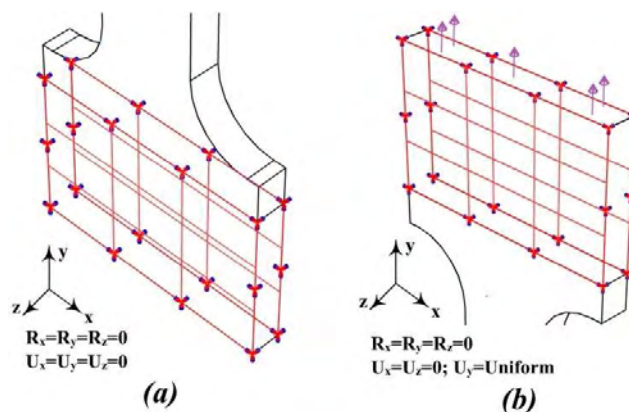


Fig 11. Boundary conditions of dog bone specimen: (a) Fixed end (b) Applied displacement end

For this configuration four different material models (mechanical behaviour models) are applied i.e. 1) Linear elastic at 25°C, 2) elastic – plastic at 25°C, 3) Linear elastic at 600°C and 4)

Elastic-plastic at 600°C. J-Integral values are obtained for all these conditions however the K_I values are calculated only for linear elastic models. For the elastic plastic models with incremental plasticity, a parameter is defined that takes into account the plasticity ahead of the crack tip $\sqrt{J_{el,pl}E'}$, described later in this chapter.

II.2.4 Sensitivity analysis of grip position

As will be seen in the results section, the values of K_I in the rectangular specimens are strongly dependent on the H/W ratio. During the installation of specimens in the machine grips, it was noted that there is usually some variation in the position of the grips on the specimen. This variation may be due to operator error or due to installation of an extensometer on some experiments and its absence on others. This requires more clearance between the grips, consequently pushing them apart. It follows from the H/W sensitivity, that the variation in position in the grips may be a source of errors during the experiment. Thus a sensitivity analysis of the grip position on the specimen is carried out to quantify the error, if any exists. Different grip positions are analyzed, from the extremity of the specimen to full coverage of specimen broad ends in the grip, figure 12. This analysis is carried out on linear elastic models at 25°C.

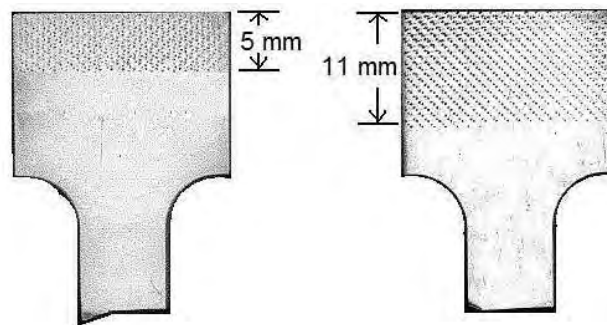


Fig 12. Variation in the position of the specimen in the grips

III. RESULTS

III.1 J-Integral calculations

After running the analysis in ABAQUS/Standard™ we get the K_I values for different concentric domains around the crack tip. The table 3 presents one such line (group of five contours) as an example from the ABAQUS/Standard™ output. These results verify the path independence of the J-integral obtained at the crack tip and in domains further away. Also, since the steel is a very high tensile stress material with a high hardening constant the plastic zone remains essentially confined near the crack tip and the plasticity effects on the far field domains are

minimal. The same has been found to be true for 600°C, the J-Integral simulation shows a strong path independence as shown in table 3.

Table 3: An example of J Integral values output by ABAQUS for one layer of contours.

Crack front node set	Temperature °C	Contour	-1-	-2-	-3-	-4-	-5-
-12-	20°C	J	1.288	1.290	1.291	1.292	1.292
-12-	600°C	J	1.927	1.978	1.985	1.988	1.989

Considering one element layer along the thickness, the analysis will calculate 10 values for five element contours on element faces and 5 values for midplane positions (Left of figure 13). These include the 5 rings of nodes of the quadratic element edges (Green) plus the 5 mid-side node rings (Red). However the output in the *.dat file is always for five contours averaged between mid-side nodes and edge nodes. The mid-side nodes are always present in 20 node quadratic brick elements (Lower right figure 13). The 3D model consists of five layers of elements that make up the thickness of the specimen (each layer being 0.5mm). The outer most layers gives lower values due to plane stress condition. There are 11 parallel sets of node rings making up the thickness of the specimen. Six contour rings on the element faces and five on the mid-plane positions. Thus we have a total of 55 J-integral values for each analysis carried out. Here, only the values of the last ring of nodes are considered. The 11 values (11 layers of elements) are then averaged to find out the desired J-integral. The value of J-integral at the first contour, closest to the singularity, is never considered because they may give erroneous results due to large strains [3, 11]. The contours are explained in detail in the figure 13.

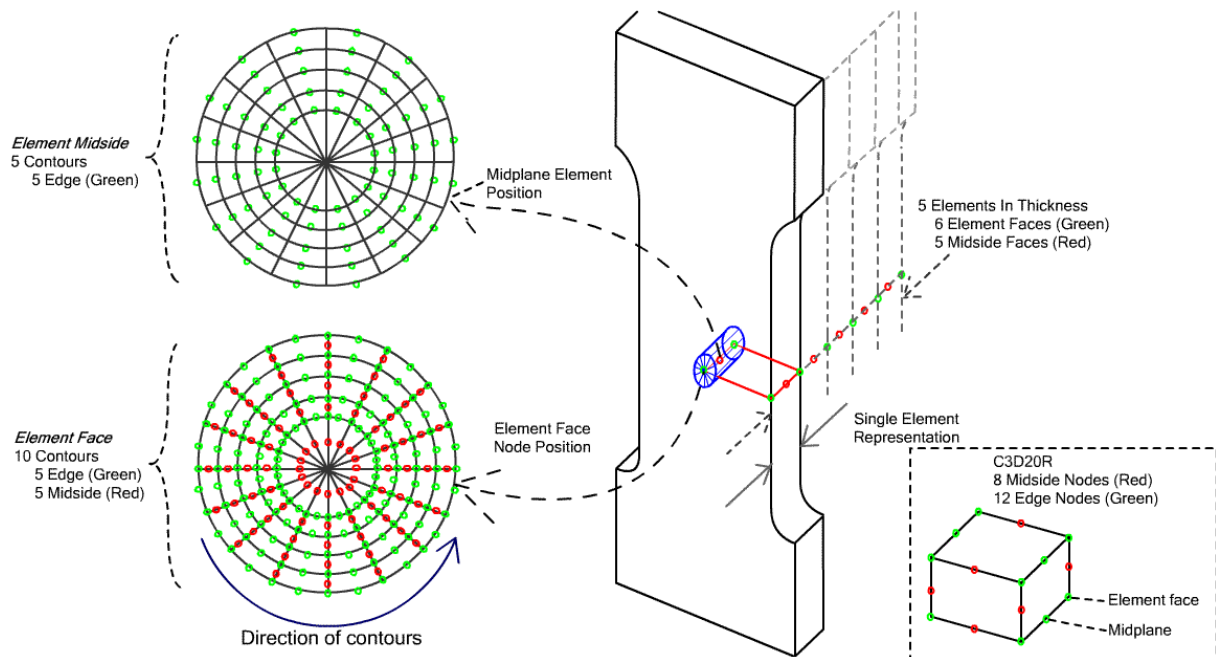


Fig 13. Positions of the contours in the specimen numerical model

The table 4 presents the summary of the conditions under which the analyses are carried out and the total number of analyses.

Table 4: Summary of the numerical analyses carried out in the study

Specimen Type	Material	Analyses
Rectangular	X38CrMoV5 20°C Linear-Elastic	5 (H/W=2)
		5 (H/W=3)
Dog Bone	X38CrMoV5 20°C Linear-Elastic	5
	X38CrMoV5 20°C Elastic-Plastic	5
	X38CrMoV5 600°C Linear-Elastic	5
	X38CrMoV5 600°C Elastic-Plastic	5
Sensitivity Analysis	X38CrMoV5 20°C Linear-Elastic	25

III.2 Rectangular Specimens

The rectangular specimens, as described previously are analyzed for verification and comparison of the method of FEA used in this analysis and by other researchers [8-10].

Table 5: Values of the correction factor $f(a/W)$, comparison with literature

H/W = 2 $f(a/W) = K_I / \sigma \sqrt{\pi a}$					
a/W	0.125	0.250	0.375	0.500	0.625
ABAQUS Force	1.1240	1.1869	1.2641	1.3806	1.5651
ABAQUS Displacement	1.1117	1.1457	1.1939	1.2855	1.4495
John et al [9]	1.1292	1.1555	1.2023	1.2875	1.4471
Chiodo et al [8, 10]	1.1243	1.1577	1.2099	1.3009	1.4605
H/W = 3 $f(a/W) = K_I / \sigma \sqrt{\pi a}$					
a/W	0.125	0.250	0.375	0.500	0.625
ABAQUS Force	1.1563	1.2657	1.4084	1.5931	1.8298
ABAQUS Displacement	1.1502	1.2445	1.3623	1.5199	1.7338
John et al [9]	1.1580	1.2470	1.3680	1.5211	1.7282
Chiodo [8, 10] et al	1.1493	1.2309	1.3451	1.5011	1.7165

The stress intensity factor in a body (Figure 1) loaded by a force F leading to a nominal stress $\sigma = F/BW$, is given by:

$$K_I = \sigma \sqrt{\pi \cdot a} \cdot f(a/W) \quad (7)$$

Where $f(a/W)$ is the geometric correction factor. During the numerical simulation the software gives an output of the K_I values. From these values the $f(a/W)$ can be deduced from the equation 7. The Table 5 presents all the values of the correction factors. The graph in the figure 14 represents the variation of the geometric correction factor as a function of the ratio of the crack length to the specimen width.

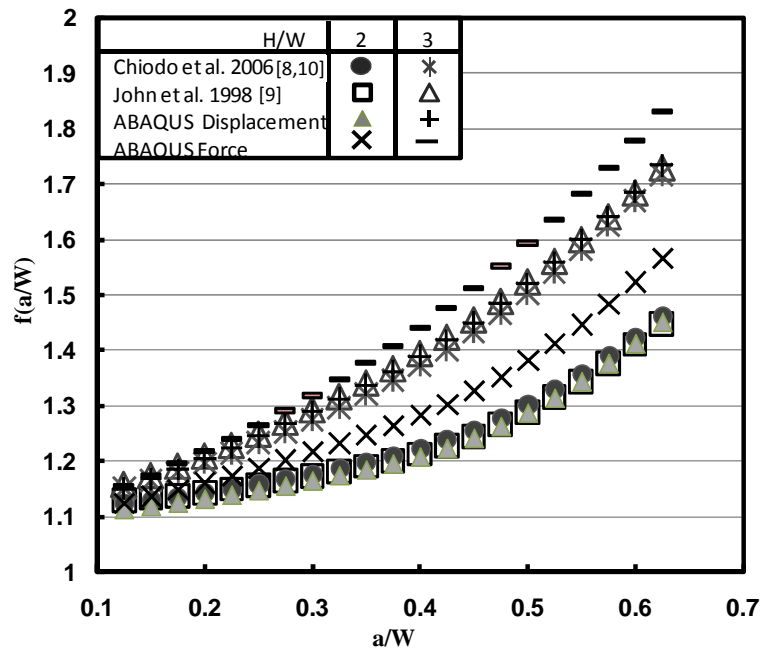


Fig 14. Verification of the numerical analysis method on standard rectangular $SE(T)_c$ specimens by comparing with other publications

The lower set of curves represents the correction factors for $H/W = 2$ and the upper set represents the curves for $H/W = 3$. The correction factors obtained under different conditions of applied uniform force and applied uniform displacement are represented by the names “ABAQUS Force” and “ABAQUS Displacement” on the graph (figure 14) respectively. These curves are subsequently compared with the calculations done by John et al. [9] and Chiodo et al. [8, 10] using procedures as mentioned previously. The two authors have used an applied uniform displacement boundary condition. The comparison of the graphs clearly shows that the applied displacement boundary condition correlates very well in comparison to these authors, with the error ranging from 0.25% for $a/W = 0.125$ to 1.5% for $a/W = 0.625$. Whereas the error in readings at the same positions goes up to 8% for applied force boundary conditions.

Being an asymmetric specimen with respect to the force axis, the applied force boundary condition tends to add a bending moment at the crack tip. This was analyzed in detail by S. Cravero et al. [10] for pin loaded $SE(T)$ specimens. In fixed grip specimens, the reaction of this moment is present on the grips which, being very rigid as compared to the specimen, do not deform considerably. This has an effect analogous to closing the crack, thus reducing the values of the correction factors.

In view of the above discussion and the experimental conditions analyzed in section II.2.3, it was decided to analyze the dog bone specimen with the applied displacement boundary condition only.

III.3 Dog bone specimen

III.3.1 Elastic and elastic-plastic analysis for tests performed at ambient temperature

The correction factors for the dog bone specimen are calculated in the same manner as above for crack lengths corresponding to $0.125 \leq a/W \leq 0.625$. The values obtained for this specimen are given in the Table 6 for elastic and elastic-plastic models.

Table 6: Correction factor $f(a/W)$ for dog bone specimens at 25°C

a/W		0.125	0.250	0.375	0.500	0.625
f(a/W)	Elastic	1.1428	1.2363	1.3568	1.5088	1.7119
	Elastic-Plastic	1.1463	1.2412	1.3623	1.5151	1.7272

$$f\left(\frac{a}{W}\right) = 1.0869 + 0.2383\left(\frac{a}{W}\right) + 1.9830\left(\frac{a}{W}\right)^2 - 2.8373\left(\frac{a}{W}\right)^3 + 2.5771\left(\frac{a}{W}\right)^4 \quad (8)$$

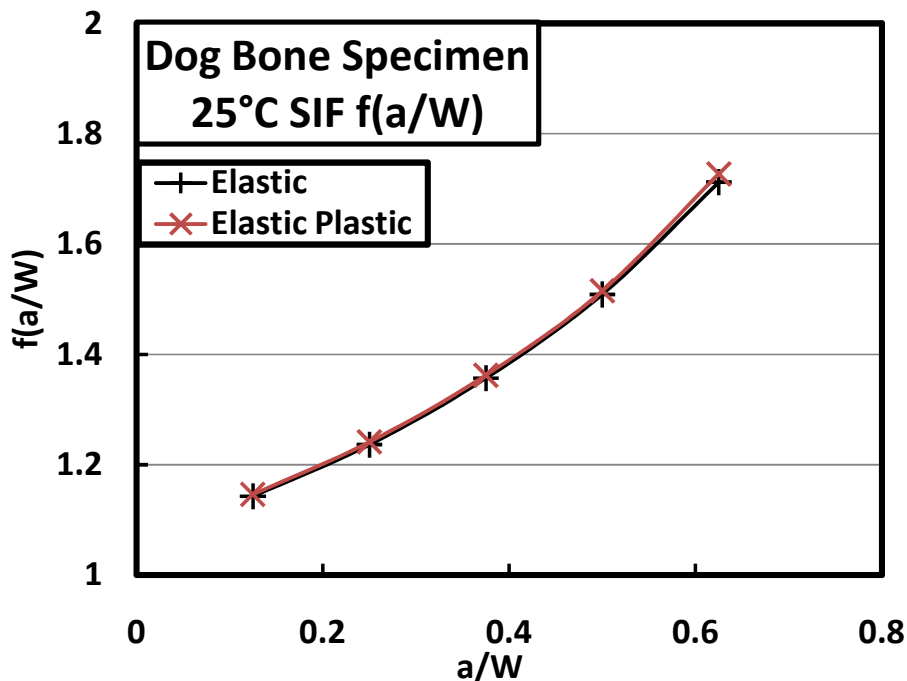


Fig 15. Comparison of correction factors of dog bone specimen for elastic and elastic-plastic material model at 25°C

We can see that for the experimental conditions and material properties presented here there is less than 1% difference between the elastic and elastic plastic material correction factors (see figure 15 and table 6). The expression calculated and the subsequently used in all the experiments for ambient temperature is based on the elastic solution, represented by the fourth order polynomial given in equation 8.

In figure 16 the values of $f(a/W)$ are compared for the dog bone specimen and the standard rectangular $SE(T)_C$ specimen with $H/W = 3$. It is interesting to note that the $f(a/W)$ values for the dog bone specimen approach those for the rectangular specimen. Considering figure 6c and the results in figure 16, one can thus see that the effective H of the specimen should be considered to be the length between the shoulder extremities (25 mm) and not the gauge length (15 mm). However, since the specimen is a structure (not a simple rectangle) it is considered prudent to make the proper numerical simulations for each type of specimen form, prior to coming to any conclusions about the effect of H/W .

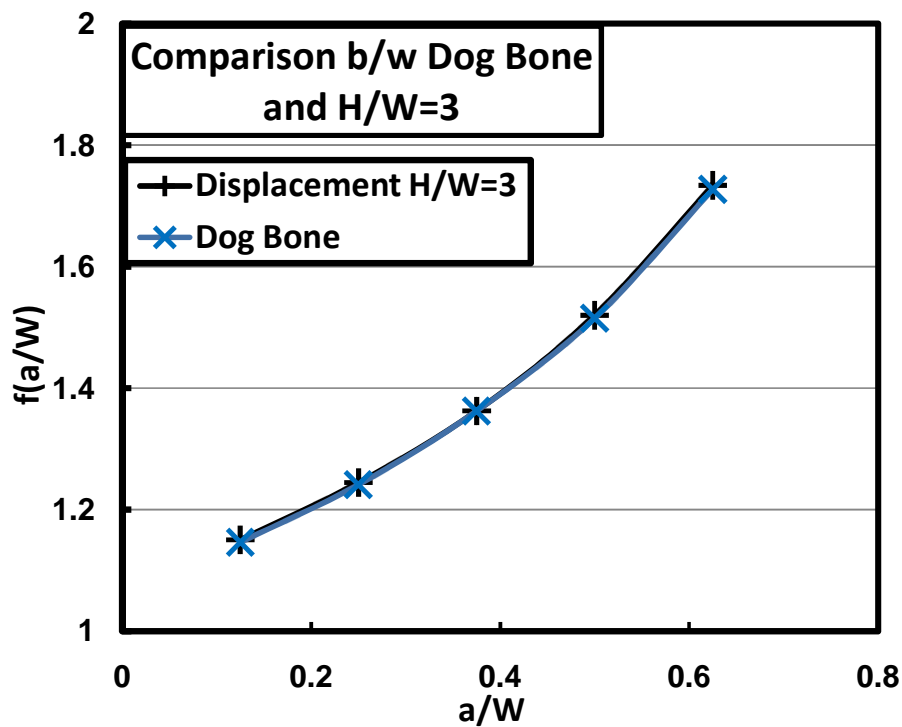


Fig 16. Comparison of correction factors of dog bone specimen and a rectangular specimen of $H/W = 3$ with applied displacement condition

III.3.2 Elastic and elastic-plastic analysis of material tested at elevated temperature (600°C)

The details presented for ambient temperature are satisfactory for a purely elastic material or material with high yield limit. However at higher temperatures the effects of plasticity are non negligible and thus the use of K_I may no longer be justified due to generalised or large scale yielding (LSY) in front of the crack tip. The use of K_I in this case may also give erroneous results on Paris law of fatigue crack propagation.

A new crack driving force parameter $\sqrt{J_{el,pl}E'}$ is defined. It was introduced by Sadanada[12] for characterising high temperature fatigue crack propagation of superalloys. The term $J_{el,pl}$ is the J-Integral calculated in the finite element model by using an elastic-plastic model. However, this parameter is a monotonic parameter (determined by monotonic tensile test simulation) and not to be confused with the cyclic J-Integral of Dowling [13]. E' is the young's modulus for plane deformation defined as:

$$E' = E(1/1 - \nu^2) \quad (9)$$

The advantage of this parameter is that at room temperature, it gives almost the same values as for an elastic analysis since the crack tip plasticity is of small scale. However at higher temperatures the parameter shows the effects of crack tip plasticity while keeping the same dimensions (and units) as the K_I parameter. A second important advantage is for comparison of fatigue crack propagation curves at room and elevated temperatures. In practice the parameter takes the form:

$$\sqrt{J_{el,pl}E'} = g\left(\frac{a}{W}\right) \sigma \sqrt{\pi a} \quad (10)$$

The values obtained for the correction factor $g(a/W)$ at 600°C are given in the table 7.

Table 7: Correction factor $g(a/W)$ for dog bone specimens at 600°C

a/W		0.125	0.250	0.375	0.500	0.625
g(a/W)	Elastic	1.1424	1.2363	1.3569	1.5091	1.7216
	Elastic-Plastic	1.1865	1.3163	1.4988	1.7403	2.0761

At room temperature the correction factor given by equation (8) is used because the effects of plasticity are negligible. However the expression of the correction factor at 600°C is presented in equation (11).

$$g\left(\frac{a}{W}\right) = 1.1321 + 0.0151\left(\frac{a}{W}\right) + 3.9899\left(\frac{a}{W}\right)^2 - 5.6491\left(\frac{a}{W}\right)^3 + 4.9493\left(\frac{a}{W}\right)^4 \quad (11)$$

All the results obtained for the elastic and elastic-plastic correction factor for different material models as a function of crack length are presented in figure 17 for comparison.

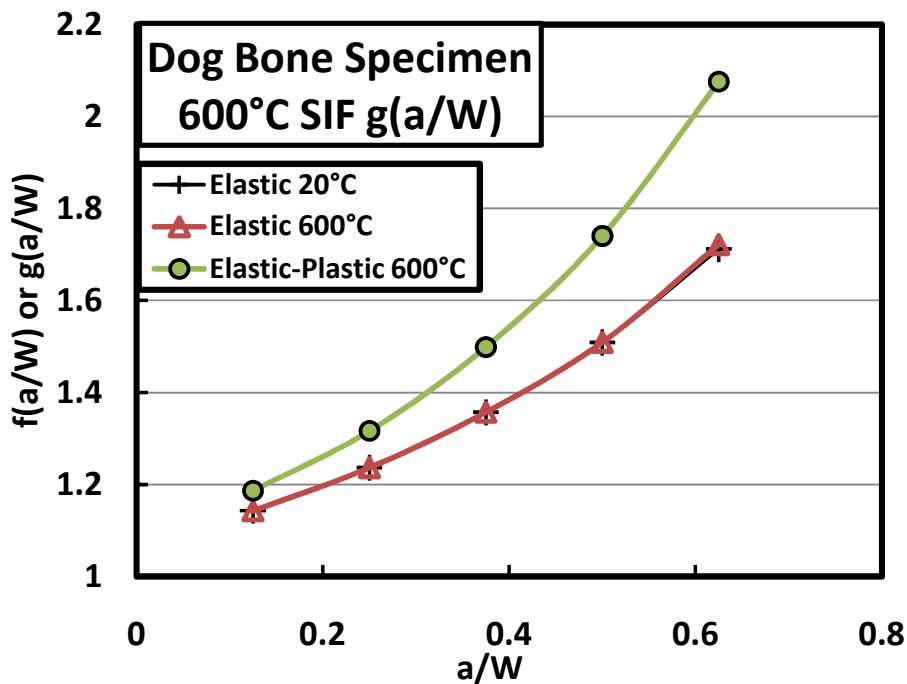


Fig 17. Comparison of correction factors of dog bone specimen for elastic and elastic-plastic material model at 20°C and 600°C

As can be seen in the figure 17, the elastic correction factor $f(a/W)$ at 20°C and $g(a/W)$ at 600°C coincide completely. Different values of J – Integral are obtained at different temperatures for the same amount of applied load. The correction factors ($f(a/W)$ and $g(a/W)$) calculated for elastic model from these different J values are found to be the same. This provides some verification for the procedure of J -Integral calculation and its path independence, that under different Young's modulus materials (with different J values for the same applied load), the correction factor for K_I has a constant value. However, the effects of plasticity are visible at 600°C, $g(a/W)$ values increase considerably.

III.3.3 Sensitivity analysis of the specimen grip position variation

The justification of sensitivity study has been presented in the section II.2.4 of this chapter. The sensitivity of grip installation position is studied for crack lengths corresponding to $0.125 \leq a/W \leq 0.625$. The analysis is carried out for 0 mm to 12 mm grip position, measured as shown in the figure 12. The results of the sensitivity analysis are shown in the figure 18. A maximum variation of 3% can be observed at the extreme positions. It should however be noted that this value in itself is very low, coupled with the fact that the sensitivity analysis is carried out for extreme position of the grips, whereas in reality only the half range of these conditions is encountered. To get an idea of acceptable limits of error, one needs to look at the comparison of different

methods of calculation, analytical and numerical by Courtin et al. [3] for standard C(T) specimens, showing up to 8% variation for the calculated values by different authors. Thus an error of 3% is considered to be acceptable.

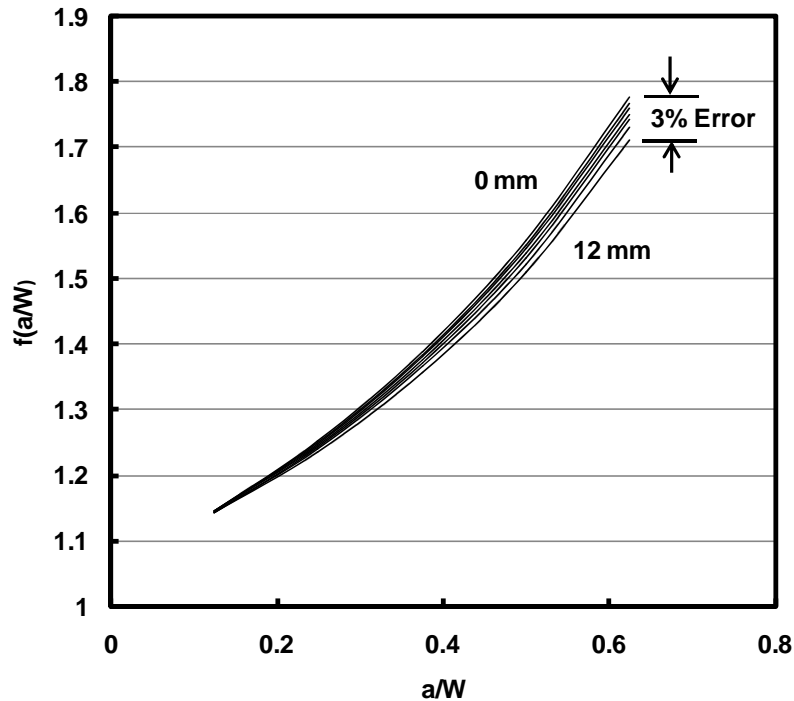


Fig 18. Sensitivity analysis of variation of specimen position in the grips on $f(a/W)$

The configuration of the test specimen and the experiment was not considered to be highly dependent on the variation of H/W in a dog bone specimen. This seems to be in contradiction to the H/W sensitivity seen in rectangular specimens, where much more sensitivity is observed. The difference in sensitivities can be explained by the extra rigidity provided by the large ends of the dog bone specimen (figure 19). The H/W sensitivity in rectangular specimens is in fact the effect of in plane rotation in an $SE(T)_C$ specimen [10]. The specimens with higher value of H , being less rigid, will show a higher K_I value. It follows from the in plane rotation of the specimen and the beam theory that the resistance to the bending moment, produced by the non symmetric loading, would be proportional to the moment of inertia or $B.W^3$, where W is the width of the specimen and B is its thickness as shown in figure 19.

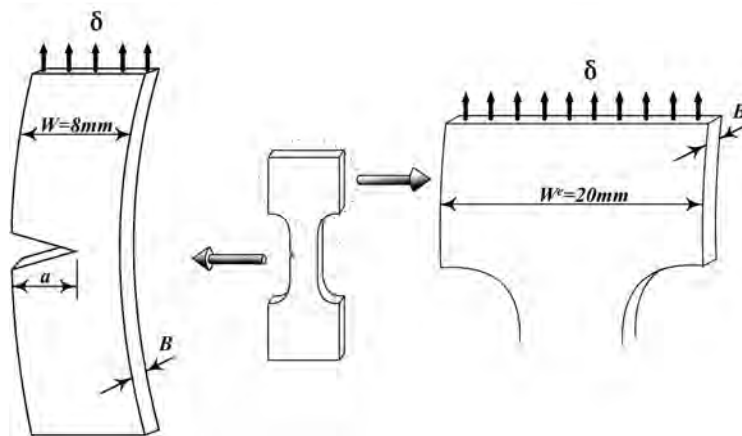


Fig 19. Asymmetric loading due to side cracking produces in plane bending or rotation which is more pronounced in the gauge length as compared to the specimen ends

Applying the above explanation to our specimen with $W = 8\text{mm}$ inside the gauge length and $W^e = 20\text{mm}$ at the ends (W^e being the width of the ends) the ratio of resistance to bending by the non symmetric loading in the gauge length to the specimen grip ends would be:

$$\phi = \left(\frac{W^e}{W} \right)^3 \cong 15.6$$

This shows that the specimen ends that are gripped by the machine are almost 16 times as rigid as the gauge length as regards to the in plane bending, hence the apparent non sensitivity of the position of the grips on the values of K_I of the specimens.

In light of the above discussion it can be safely said that the minor changes in the installation position of the specimens will not show a marked error on the results of the experiments that were performed on these specimens.

IV. CONCLUSION

In this chapter the numerical analysis carried out for clamped $SE(T)_c$ specimens is presented. A literature survey is initially presented detailing the different common strategies used for determining the stress intensity factors for this type of specimen. These include the displacement extrapolation method, the singular elements method and the energetic J-Integral method. It is shown that the J-Integral method can give satisfactory results with fairly coarse element mesh.

The method used in this study is based on the energetic J-Integral method, using the software ABAQUS/Standard™. Different boundary conditions are tested for the simulation of the specimens: applied uniform force and applied uniform displacement. The simulation results are verified using standard rectangular $SE(T)_c$ specimens of different H/W ratio, by comparing with the work of other researchers, using different methods. It is concluded that the procedure followed for the numerical simulation in this study gives satisfactory results for applied uniform displacement.

After verification, the numerical analysis procedure is applied on the real specimen, which has a “Dog Bone” profile. Mainly four types of analyses are carried out on the specimens viz:

- 1) Elastic analysis at 20°C
- 2) Elastic – Plastic analysis at 20°C
- 3) Elastic analysis at 600°C
- 4) Elastic – Plastic analysis at 600°C

It is shown that the analyses at ambient temperature for elastic and elastic-plastic models are almost the same and there is very little effect of plasticity on the J-Integral values. However, for the numerical simulation at elevated temperatures the elastic analysis results give the same values as for ambient temperature, whereas for the elastic-plastic analysis, there is a strong effect of the plasticity on the J-Integral values.

Due to the effect of plasticity at elevated temperature, the stress intensity factor may no longer be valid as a crack propagation criterion. Another criterion that takes into account the plasticity effects $\sqrt{J_{el,pl}E'}$ is also introduced. The K_I and the $\sqrt{J_{el,pl}E'}$ criterion are used in the chapter 4.

A sensitivity study has been carried out to determine the effect of specimen position in the grips. There can be slight variation in the way the specimens are installed in the grips; this variation is inherent to the experimental setup. It is found that this variation has a negligible effect on the stress intensity factor measurements.

V. REFERENCES

1. Shah, M., et al., *Crack propagation in tool steel X38CrMoV5 (AISI H11) in SET specimens*. Advanced Engineering Materials, 2009. **11**(9): p. 746-749.
2. Shah, M., C. Mabru, and F. Rezaï-Aria, *Investigation of crack propagation in X38CrMoV5 (AISI H11) tool steel at elevated temperatures*. Procedia Engineering. **2**(1): p. 2045-2054.
3. Courtin, S., et al., *Advantages of the J-integral approach for calculating stress intensity factors when using the commercial finite element software ABAQUS*. Engineering Fracture Mechanics, 2005. **72**(14): p. 2174-2185.
4. Owen, D.R.J. and A.J. Fawkes, *Engineering fracture mechanics: numerical methods and applications*. Pineridge Press Ltd, 91 West Cross Lane, West Cross, Swansea, UK, 1983. 305, 1983.
5. Barsoum, R., *On the use of isoparametric finite elements in linear fracture mechanics*. International Journal for Numerical Methods in Engineering, 1976. **10**: p. 25-37.
6. Lin, X.B. and R.A. Smith, *Fatigue growth simulation for cracks in notched and unnotched round bars*. International Journal of Mechanical Sciences, 1998. **40**(5): p. 405-419.
7. Rice, J.R., *A path independent integral and the approximate analysis of strain concentration by notches and cracks*. Journal of applied mechanics, 1968. **35**(2): p. 379-386.
8. Chiodo, M.S., S. Cravero, and C. Ruggieri, *Stress Intensity Factors for SE (T) Specimens*, Technical Report BT-PNV-68, Faculty of Engineering, University of Sao Paulo 2006.
9. John, R. and B. Rigling, *Effect of height to width ratio on K and CMOD solutions for a single edge cracked geometry with clamped ends*. Engineering Fracture Mechanics, 1998. **60**(2): p. 147-156.
10. Cravero, S. and C. Ruggieri, *Estimation procedure of J-resistance curves for SE (T) fracture specimens using unloading compliance*. Engineering Fracture Mechanics, 2007. **74**(17): p. 2735-2757.
11. Hibbit, K. and I. Sorensen, *ABAQUS users' manual, version 6.5*. Pawtucket, RI. 2002.
12. Sadanada, S. and P. Shahinian, *Elastic-plastic fracture mechanics for high temperature fatigue crack growth*, in *Fracture Mechanics: Twelfth Conference, ASTM STP 700*. 1980. p. 152-163.
13. Dowling, N.E. *Geometry effects and J integral approach to elastic-plastic fatigue crack growth*. 1976: ASTM International.

Chapter 4: Experimental Results

Résumé en Français	81
A. Propagation de Fissure en Fatigue à Température Ambiante	81
B. Détermination de K_c à la Température Ambiante	82
C. Propagation de Fissure en Fatigue à 600 °C.....	82
I. Fatigue Crack Propagation at Room Temperature.....	83
II. Determination of K_c at Room Temperature	99
III. Fatigue Crack Propagation at 600°C.	101
IV. Conclusion	120
V. References.....	121

RESUME EN FRANÇAIS

Ce chapitre est consacré aux résultats expérimentaux. Deux types d'essais sont réalisés ; la propagation de fissure en fatigue, et la propagation de fissure monotone pour obtenir les valeurs de K_C . Les essais sont réalisés sur des éprouvettes d'épaisseurs différentes ainsi que dans des conditions d'essais variables. Les faciès de rupture ainsi que le chemin de propagation par rapport à la microstructure ont été caractérisés en analyse post mortem. Trois grands groupes d'essais sont réalisés :

- 1) propagation de fissure en fatigue à température ambiante,
- 2) détermination du facteur d'intensité de contrainte critique K_C à température ambiante,
- 3) propagation de fissure en fatigue à 600 °C.

A. PROPAGATION DE FISSURE EN FATIGUE A TEMPERATURE AMBIANTE

Ce groupe d'essai représente le plus grand nombre d'essais réalisés au cours de cette étude. Toutes les calibrations et les étalonnages d'essais et du banc d'essais ont été réalisés sous ces conditions. Les buts principaux des ces essais sont :

- 1) déterminer les courbes de propagation de fissure de base, nécessaire pour comparer les courbes de propagation sous d'autres conditions,
- 2) étudier l'effet du rapport de charge R sur la propagation de fissure en fatigue,
- 3) étudier l'effet de l'épaisseur des éprouvettes sur la propagation de fissure en fatigue,
- 4) observer la morphologie des faciès de rupture dans les différentes conditions de chargement,
- 5) étudier les mécanismes de fissuration (inter-granulaire ou intra-granulaire), et le branchement de fissure dans les différentes conditions expérimentales,
- 6) mesurer l'ouverture de fissure (COD) qui est utilisée comme un paramètre de propagation de fissure.

L'effet de la variation de R sur la propagation de fissure est étudié pour plusieurs épaisseurs d'éprouvette. Les essais sont conduits principalement avec $R = 0,1$ et $0,7$. On constate que l'augmentation de la valeur de R augmente la vitesse de propagation de fissure à la température ambiante. Cela peut être expliqué par l'effet de la fermeture de fissure pour des basses valeurs de R qui augmente la valeur apparente de ΔK .

L'effet de la variation de l'épaisseur des éprouvettes sur la propagation de fissure est que plus l'éprouvette est fine, plus la vitesse de propagation diminue pour les mêmes valeurs de ΔK . Cela semble dû à l'augmentation de la zone plastique en pointe de fissure qui augmente la fermeture de fissure.

B. DETERMINATION DE K_C A LA TEMPERATURE AMBIANTE

Les objectifs de la détermination des valeurs de K_C dans les éprouvettes minces sont :

- 1) déterminer la dépendance de K_C en fonction du rapport a/W ,
- 2) déterminer la dépendance de K_C en fonction de l'épaisseur de l'éprouvette.

K_C est indépendant de a/W pour l'épaisseur de 2,5 mm, alors qu'il est fortement dépendant pour les éprouvettes de 1,0 et 0,6 mm d'épaisseur. La valeur de K_C augmente avec l'augmentation de a/W . L'évolution de K_C dans les éprouvettes de faible épaisseur semble suivre une loi quadratique de forme :

$$K_C = C_1 \left(\frac{a}{W}\right)^2 + C_2 \left(\frac{a}{W}\right) + C_3 \quad (3)$$

où C_1 , C_2 et C_3 sont des constantes déterminées par les essais.

K_C est aussi dépendant de l'épaisseur pour toutes les valeurs de a/W . En général la valeur de K_C augmente avec une réduction de l'épaisseur.

C. PROPAGATION DE FISSURE EN FATIGUE A 600 °C

La propagation de fissure à 600°C dépend de plusieurs phénomènes comme le facteur d'intensité de contrainte en mode I, l'oxydation, la plasticité, le fluage, etc. Puisque la plasticité est élevée à cette température, le critère de propagation de fissure $\sqrt{J_{el,pl}E'}$ a été utilisé en plus de K_I . Le premier critère est basé sur un calcul énergétique et rend compte de la plasticité alors que le deuxième est basé sur un calcul purement élastique.

L'effet de la variation de R est étudié pour plusieurs épaisseurs d'éprouvette. Généralement, il n'y a pas d'effet du rapport de charge sur la propagation de fissure dans le régime de propagation de Paris, alors qu'il existe un effet sur le seuil de propagation de fissure. Une augmentation du rapport de charge diminue la valeur de ΔK seuil de la propagation de fissure.

Le seuil de propagation de fissure à 600°C a été également étudié. La valeur du seuil de propagation de fissure à 600 °C est beaucoup plus élevée que celle des essais à température ambiante. Un essai a été spécialement réalisé pour confirmer l'augmentation du seuil de propagation de fissure à 600°C en augmentant la température en cours d'essai. Un arrêt de fissure a été démontré à 500°C ce qui confirme cette augmentation.

L'effet de la variation de l'épaisseur d'éprouvette est la diminution de la vitesse de propagation de fissure avec une diminution de l'épaisseur à l'instar des essais à l'ambiante.

This chapter is dedicated to the results of all the experimental work carried out during the research. Mainly two types of tests are carried out; fatigue crack propagation and monotonic crack propagation under tearing (determination of critical stress intensity). The tests are performed on different specimen configurations and under different testing conditions. Post mortem analysis of crack surface and crack path with respect to microstructure is also studied. There are mainly three groups of experiments:

- 1) Fatigue crack propagation at room temperature
- 2) Critical stress intensity factor, K_c at room temperature
- 3) Fatigue crack propagation at 600°C
- 4) Effect of oxidation on fatigue crack propagation (See appendix B)

I. FATIGUE CRACK PROPAGATION AT ROOM TEMPERATURE.

This makes up the bulk of the work carried out during the study. The machine and experimental calibrations are also done under the same conditions. There are many aims of experimental testing at room temperature:

- 1) Create base line crack propagation curves for comparison with other experimental conditions and specimen thicknesses (See appendix B for standard C(T) test).
- 2) Study the effects of load ratio R on the crack propagation behaviour.
- 3) Determine and study the effects, if any, of specimen thickness on the crack propagation curves.
- 4) Observation of morphology of crack face under different conditions of crack propagation.
- 5) Study the crack mode (inter or trans granular) and branching under different experimental conditions and thicknesses.
- 6) Measure the crack opening displacement (COD) and if possible use it as a fatigue crack propagation criterion.

The data for the fatigue crack propagation is presented as Paris[1] curves using the power law:

$$da/dN = C. \Delta K^m \quad (1)$$

I.1 Effect of R ratio on fatigue crack propagation

The R ratio is defined as the ratio of the minimum stress to the maximum applied stress during a fatigue crack propagation experiment:

$$R = \sigma_{min}/\sigma_{max} \quad (2)$$

The details of the experimental procedures are given under paragraph III.1-Chap 2. The results are shown below.

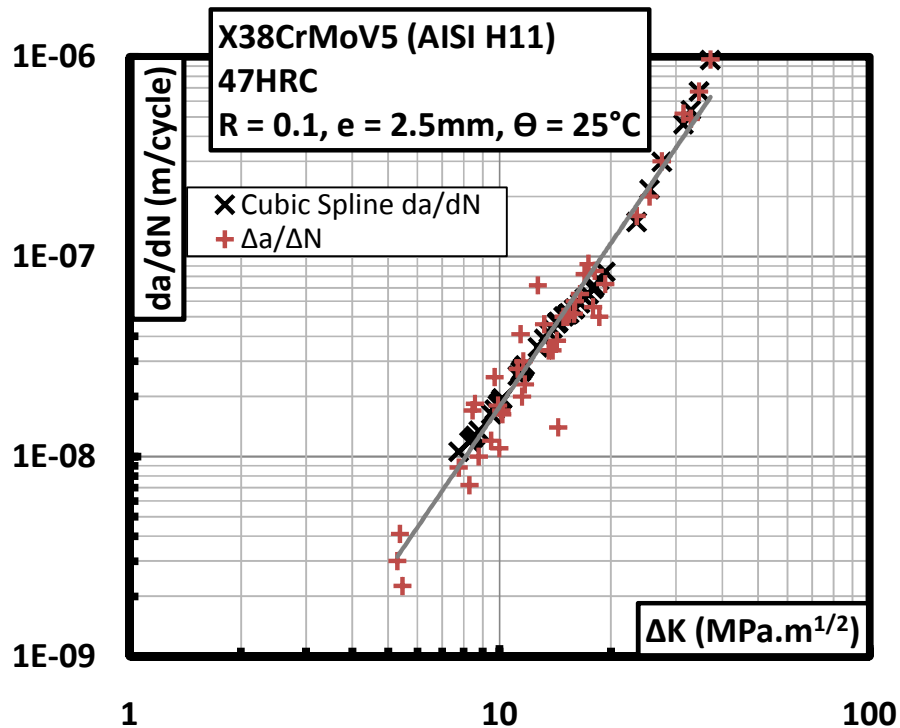


Fig 1. Paris curve for 2.5mm thickness specimen at $R=0.1$ at Ambient Temperature

Figure 1 presents the fatigue crack propagation curve for 2.5mm at $R = 0.1$ with different data smoothing techniques. The smooth curve has been obtained by cubic spline curve fitting, while the $\Delta a/\Delta N$ presents the full data scatter without any smoothing technique. All the data presented is smoothed using the cubic spline curve fitting unless specified otherwise.

It is noted that at room temperature the increase in R , causes an increase in the crack propagation speed by up to 2 times while the slope of the Paris curve remains the same, as shown in the comparison figure 2.

A more complete picture of the R effect appears in the figure 3. Here a specimen of 0.6mm thickness is tested at R 0.1 and 0.7. The specimen tested at $R = 0.7$ gives a simple log-linear fatigue crack growth curve, that may be characterised by the Paris law with a slope of $m = 3.6$. However, the specimen tested at $R = 0.1$ shows two distinct slopes on the fatigue crack propagation curve. It has the same slope as that of $R = 0.7$ ($m = 3.6$) for a certain value of ΔK . For higher values of ΔK the crack propagation curve follows a different slope of $m = 2.5$. This effect of slope change is related to the thickness and is discussed in the section 1.2 of this chapter. As compared to the test carried out at 2.5mm the increase in crack propagation speed may be up to 5 times. The effect of increase of crack propagation speed with the increase in R ratio seems to increase with a decrease in thickness of the specimen.

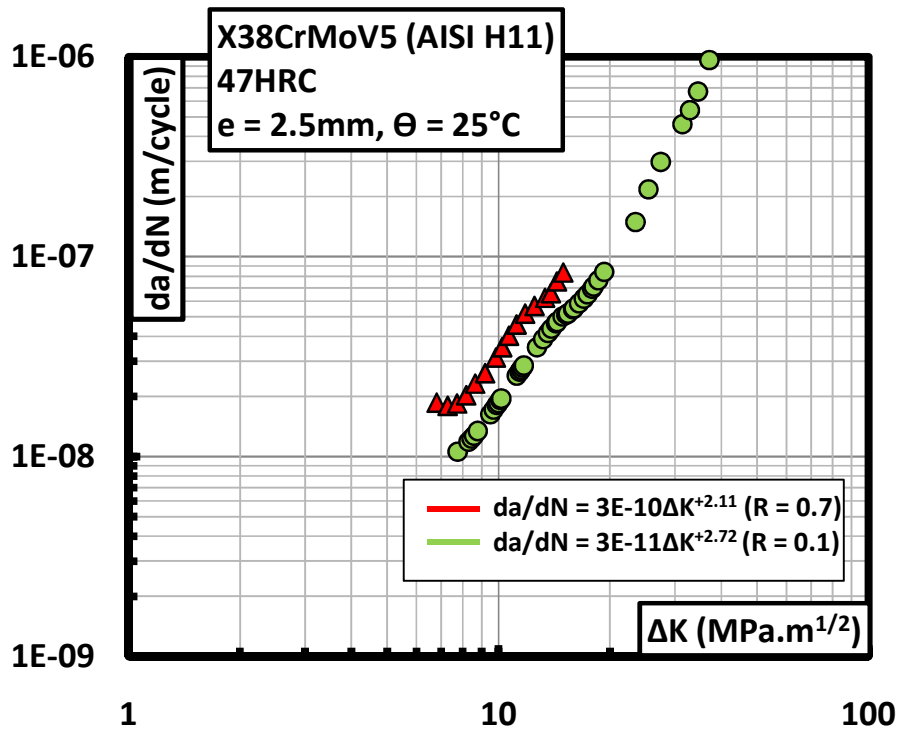


Fig 2. Effect of R ratio, comparison for 2.5mm thickness

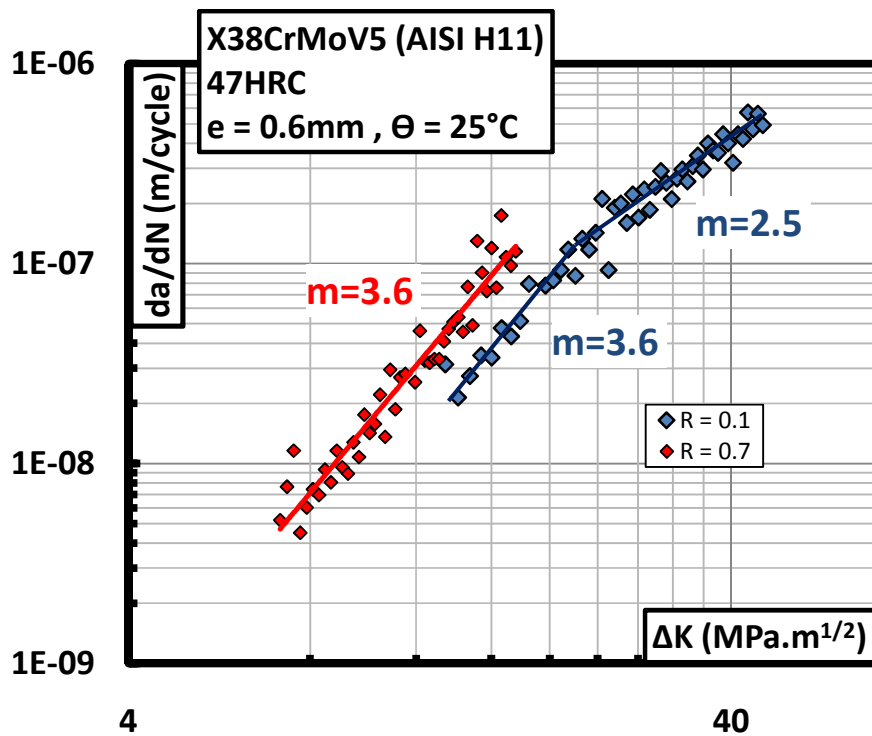


Fig 3. Effect of R ratio, comparison for 0.60mm thickness

The crack propagation curves for specimens of 0.12 mm show an effect of the R ratio as well, figure 4. The used R ratios for this experiment are 0.6 and 0.1. The need to use the R value of 0.6 is due to the difficulty of testing such thin specimens for R=0.7 on the equipment used.

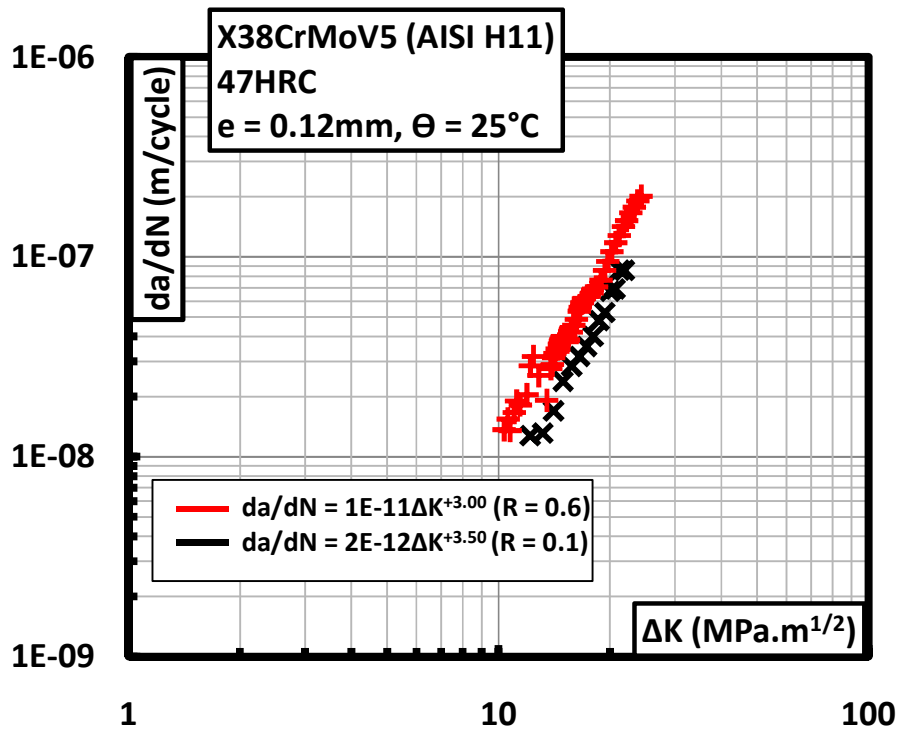


Fig. 4. Effect of R ratio, comparison for 0.12mm thickness

As noted in literature, the variation in R values may increase the crack propagation rate [2-4] or it may remain the same under vacuum [5-7]. The apparent increase in the propagation rate may be explained by the crack closure phenomenon [3] which may be caused by crack face roughness, oxide or crack front plasticity effects [8].

I.2 Effect of thickness “e” on fatigue crack propagation

The state of stress and strain (plane stress or plane strain) is dependent on the thickness of a cracked plate type material. The ASTM E647 “Standard Test Method for Measurement of Fatigue Crack Growth Rate” [9] and E399 “Standard Test Method for Plane-Strain Fracture Toughness of Metallic Materials” [10] dictate that the thickness of the material should be: $e \geq 2.5 (K_{Ic}/\sigma_{ys})^2$. This condition is to ensure the validity of the linear elastic fracture mechanics small scale yielding condition (SSY) as well as a plane deformation condition at the crack tip. For the material used in this study the specimen thickness according to this rule would be around 15mm. However this study deals with the surface and subsurface damage of tool steels which requires the testing of thin layers of material (a reduced thickness of the specimens).

In general plane strain conditions are dominant in thicker plate materials. At the surface (ends of crack) a plane stress condition prevails. If the thickness of a specimen has to be reduced the plane stress conditions become dominant. The effect of this change in the stress – strain state, due to a change of the thickness, on fatigue crack propagation is studied here.

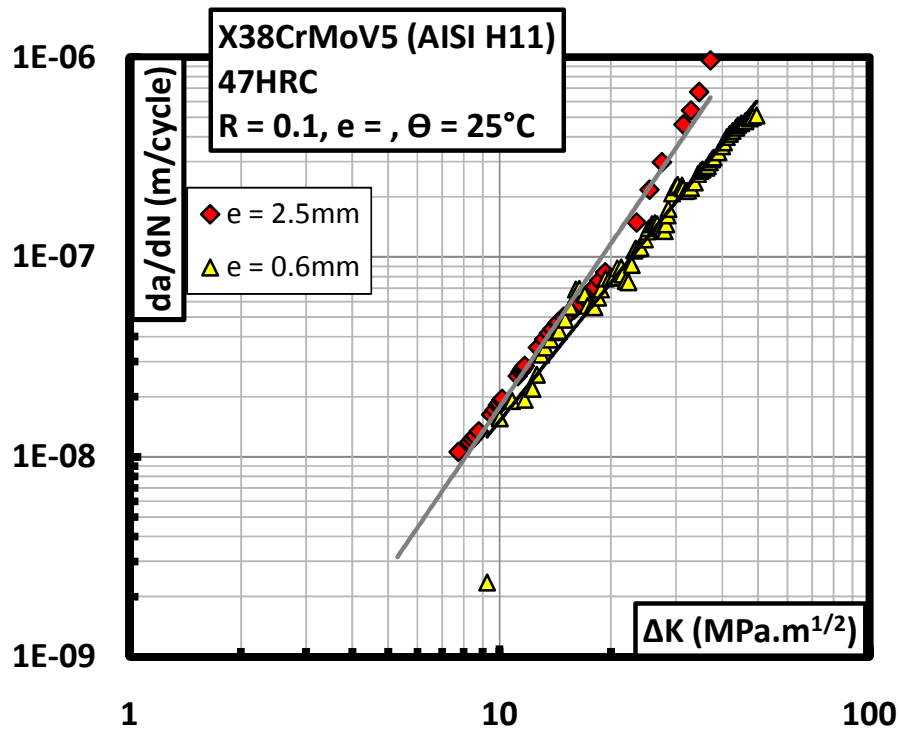


Fig 5 . Effect of specimen thickness $e = 2.50$ & 0.60 mm

The figure 5 shows the effect of the thickness of the specimen on the crack propagation curve. The effect of the reduction of the specimen thickness seems to be the reduction of rate of fatigue crack propagation. In the comparison between 2.5mm and 0.6mm thickness specimens, figure 5, the two curves have the same propagation characteristics for lower ΔK values, whereas the rate of crack propagation of $e = 0.6$ mm seems to diminish for higher ΔK values. In the comparison between the 2.5mm, 0.25mm and 0.12mm specimens the thinner specimens have lower crack propagation rates for all values of ΔK , figure 6. The 0.6mm thickness specimen presents a transition curve between thick specimens and the thinner specimens, whereas for the 0.25mm and 0.12mm specimens the crack propagation curve is identical. It is due to this transition that two slopes seem to exist in the crack propagation curve as shown in figure 3. This behaviour is probably linked to the fact that for higher ΔK , plane stress conditions become dominant in the specimen of $e = 0.6$ mm. For the specimens of $e < 0.6$ mm, this conditions exists for all crack lengths.

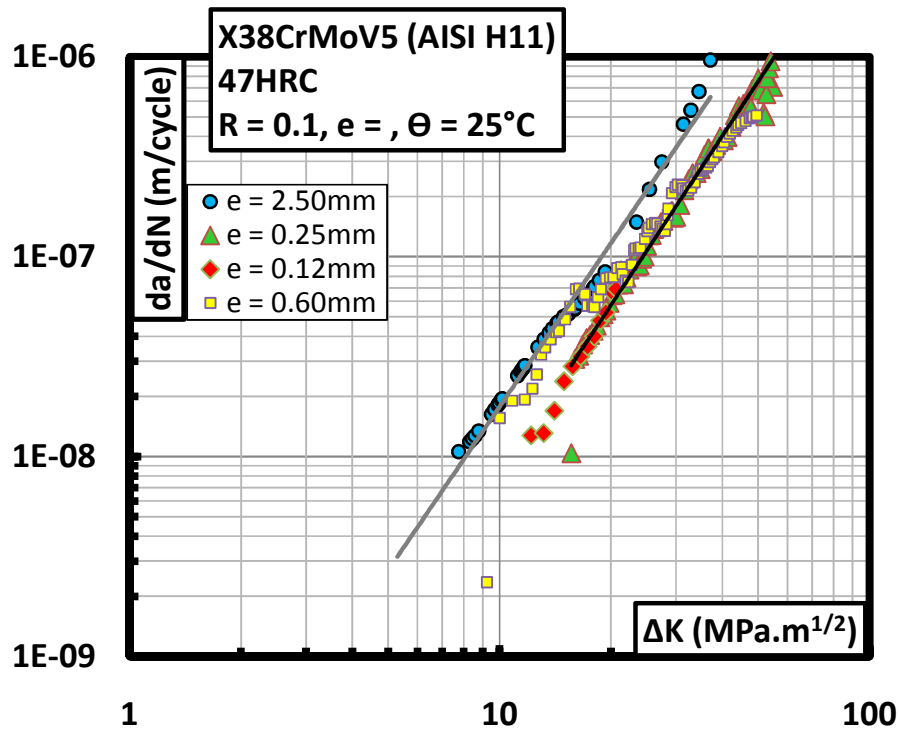


Fig 6. Effect of specimen thickness $e = 2.50, 0.60, 0.25$ & 0.12mm

I.3 Observation of fracture surface

Following the tests all the specimens are observed under a scanning electron microscope. The crack surface morphology and profile forms are observed. The arrow in all the micrographs indicates the direction of crack propagation.

I.3.1 Mechanism of fatigue crack propagation

A notch is machined in all the specimens used. Multiple zones of crack initiation are observed on the notch root figure 7.

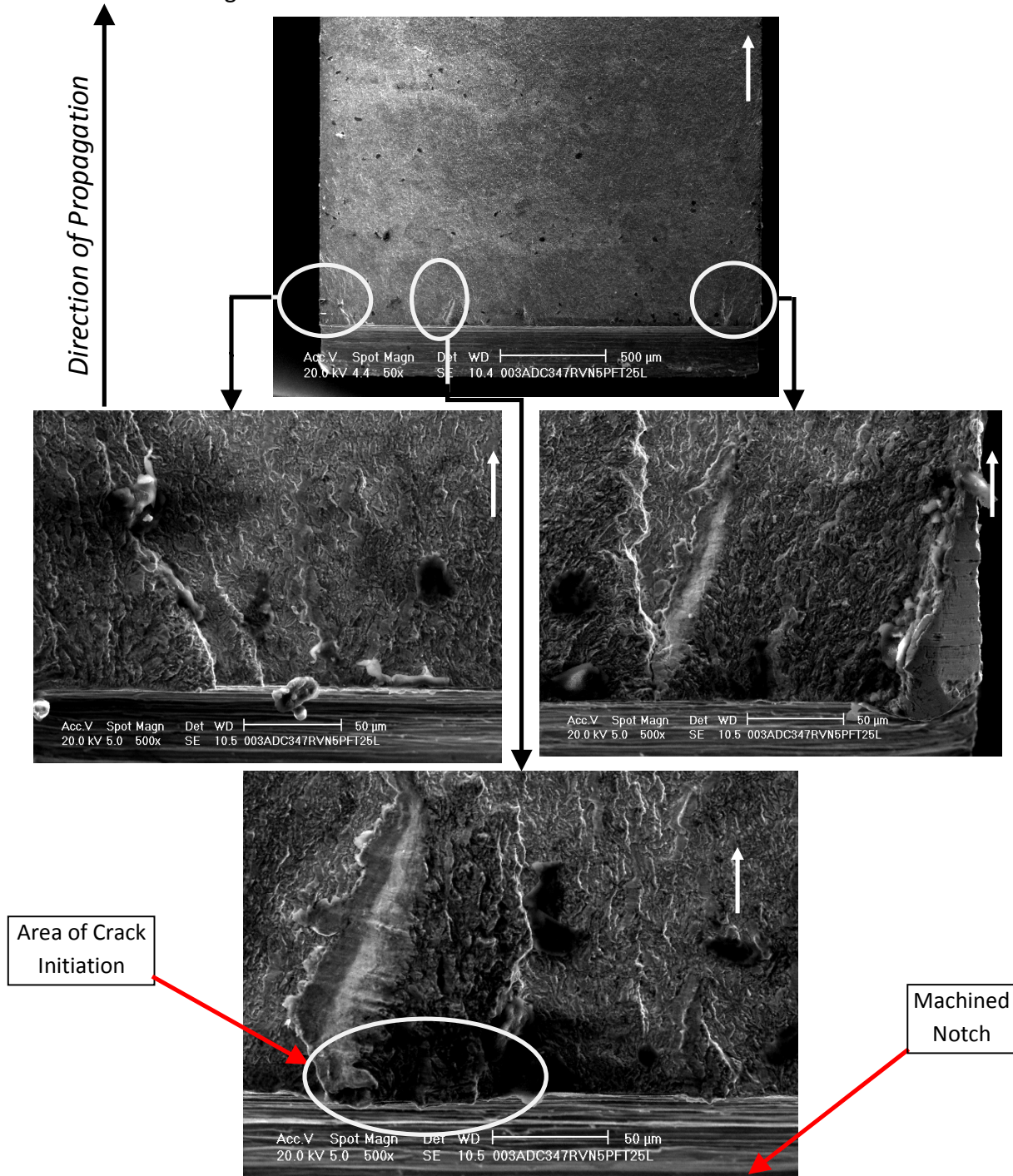


Fig 7. Crack initiation at the specimen notch root

A certain length of fatigue crack propagation is required for these multicracks to coalesce and present a unique crack front. This length is found to be about 600 μm in 2.5mm specimens. Any crack seen at the surface of the specimen below this length should not be considered as representative of a continuous crack front.

Fatigue striations can usually be seen in regions of high ΔK values or in a zone of strong plastic deformation ahead of the crack tip, figure 8. In the specimens of 2.5mm thickness, fatigue striations are detectable near the end of the crack propagation, figure 9. Also it can be seen that the fatigue striation correspond well to the speed of crack propagation of 1×10^{-6} m/cycle at this position where each striation measures 1 micrometer in width, figure 9.

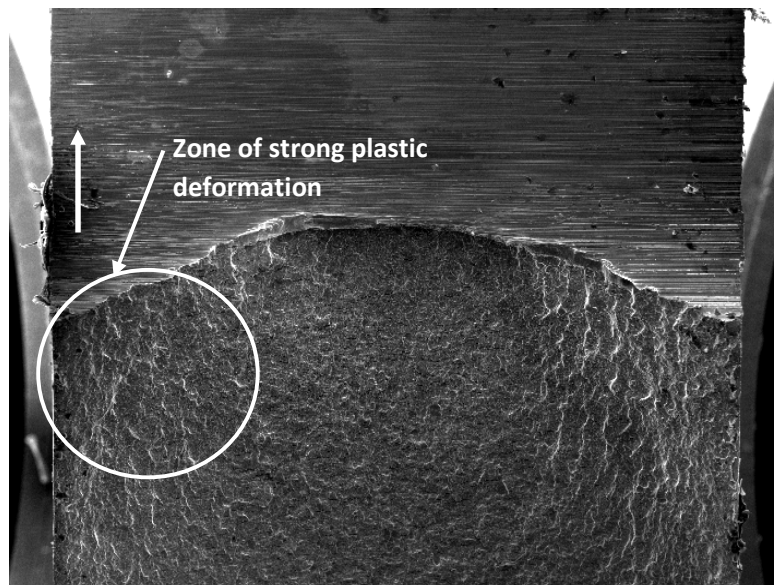


Fig 8. Zone of strong plastic deformation

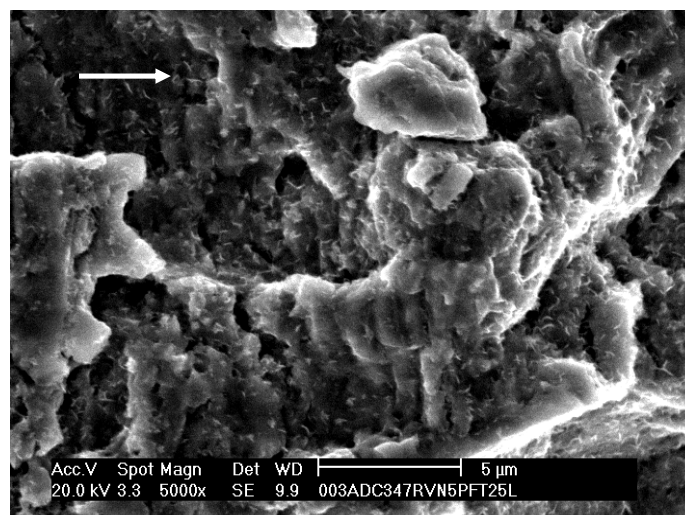


Fig 9. Fatigue striations corresponding to da/dN of 1×10^{-6} m/cycle $R=0.1$, 25°C

The observation of the fracture surface shows that in the 2.5mm thickness specimens, the crack surface is a flat plane for low ΔK . However, as the crack length increases, the crack starts to take a convex form (perpendicular to the plane of the crack). This convex form starts at the edges and later on covers the whole crack surface. This convex form is composed of flat planes separated by 45° inclined planes (blue) figure 10. This sort of tensile to shear mode transition was reviewed by Schijve [11], in the case of sheet metal (thin specimens).

It is to be noted that the creation of these planes depends on the K_{max} . On specimens of 2.5mm thickness they appear at around $38 \text{ MPa}\cdot\text{m}^{1/2}$, irrespective of the load ratio. The form of the crack surface may be related to the presence of increased plasticity, where the inclined planes form along the slip bands. The presence of slip bands alongside the convex or concave crack surface is demonstrated later in observations on thinner specimens.

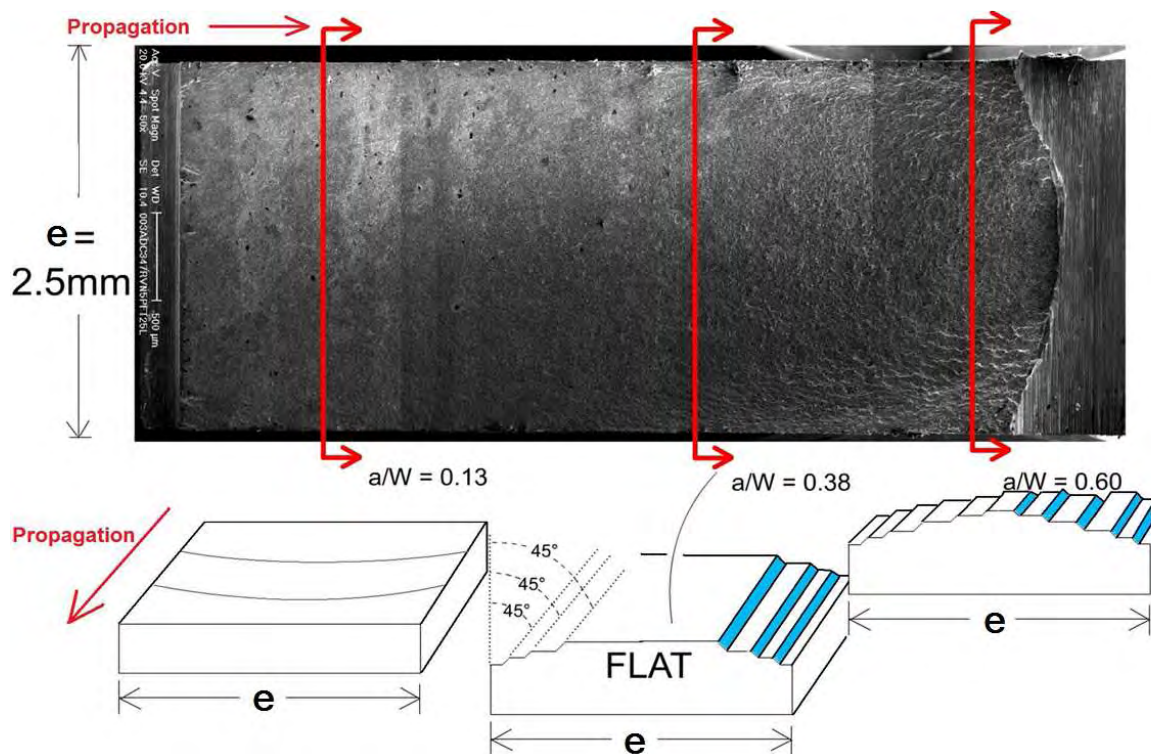


Fig 10. Creation of 45° inclined planes on the crack surface in a 2.5mm specimen

In specimens of 0.6mm thickness the flat zone is completely absent and these inclined planes appear right from the start. The only difference is that they are fine and more in number at the beginning, while they are larger in size and fewer in number as the crack advances as shown in figure 11.

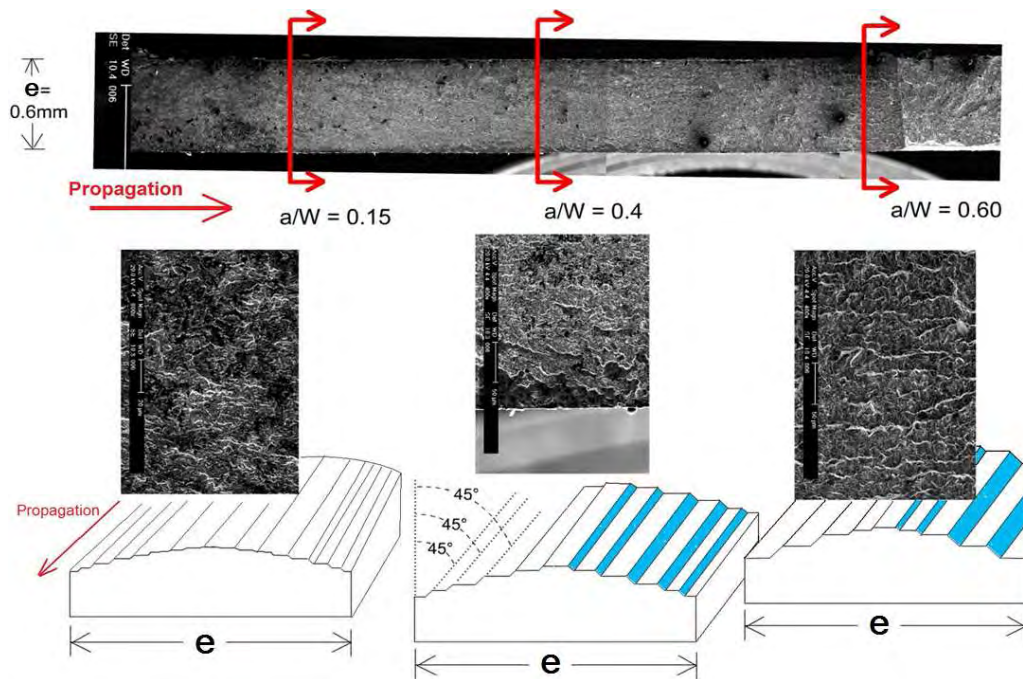


Fig 11. Creation of 45° inclined planes on the crack surface in a 0.6mm specimen

The presence of these inclined planes (shear mode transition) corresponds to the slip bands formed during crack propagation. This is very clearly observed in thinner specimens of 0.25mm thickness. The mechanism of formation of slip planes is much more evident in thinner specimens as shown in figure 12.

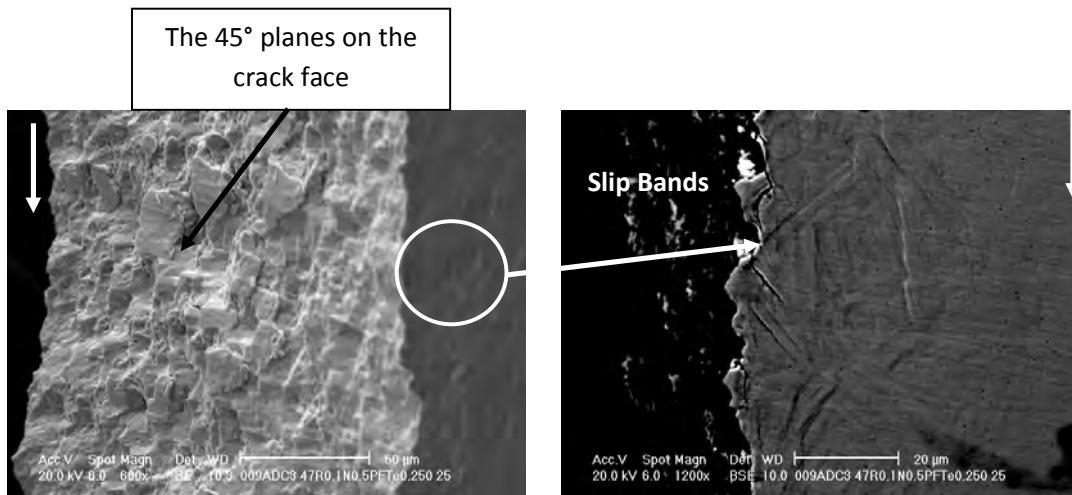


Fig 12 . Creation of 45° inclined planes on the crack surface in a 0.25mm specimen

Some micrographs are presented in figure 13 (a-d) to show the presence of slip bands in the material near the crack tip on the path of fatigue crack propagation. These micrographs show

the complex crack propagation mechanism with a mixed (normal and shear) mode of propagation.

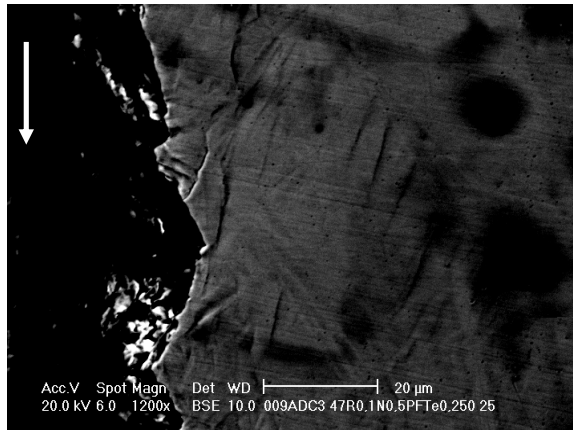


Fig 13(a). Presence of parallel slip bands, larger than the grain size (10µm)

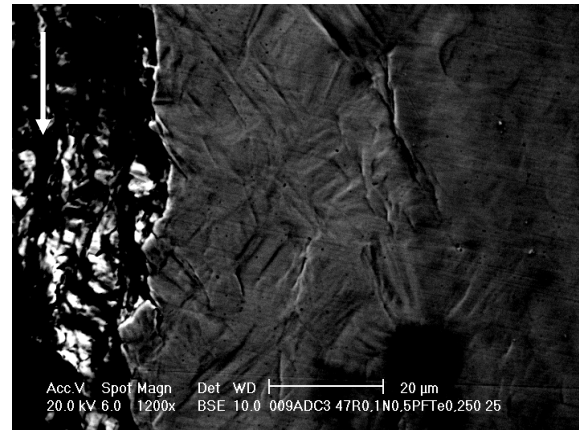


Fig 13(b). Presence of slip bands, mostly at 45° to the crack plane

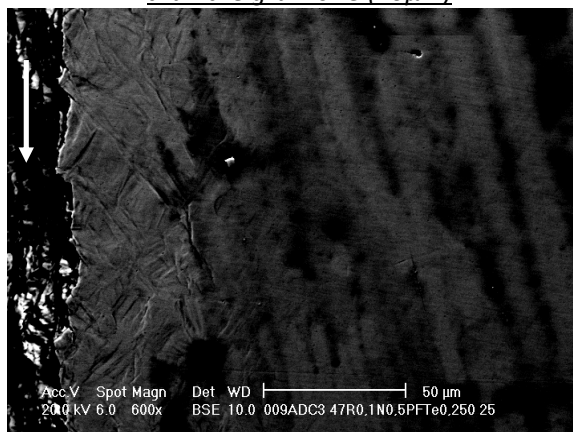


Fig 13(c). Presence of slip bands at 45°. Intrusions and extrusions are evident

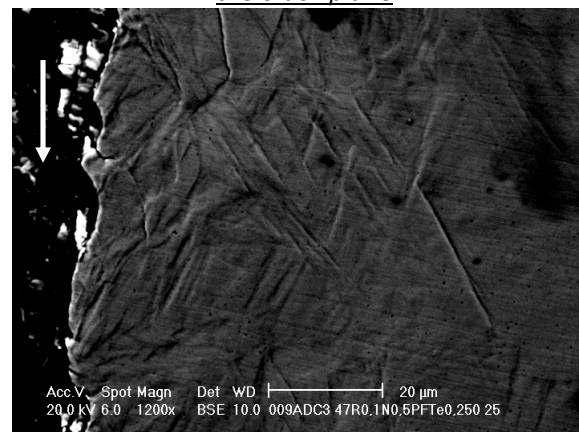


Fig 13(d). Extrusions and intrusions in slip bands

I.3.2 Specimens of 2.5mm thickness

For short crack lengths ; crack propagation is mostly trans granular figure 14(a-d). The fatigue crack propagates through the grains without much deviation. With the increase in length and subsequently the value of K_{max} the mode of propagation becomes mixed; intergranular and transgranular with the presence of shear propagation planes. The change in mode is related to the maximum value of the stress intensity factor K_{max} . This value corresponds to almost $38 \text{ MPa}\cdot\text{m}^{1/2}$. It is also observed that the appearance of the mode of inter granular propagation corresponds exactly to the presence of the 45° planes on the crack faces. The figures 14(b,c) show the transgranular propagation. The micrograph in fig 14(d) is treated with an edge detection filter in Matlab®, in order to visualize the grain boundaries and path of crack

propagation. The grain boundaries have a higher contrast when viewed under the SEM as compared to the martensite laths and carbides. The edge detection filter in Matlab® uses this contrast to trace a path. All the martensite laths and carbides seen as randomly dispersed lines inside the grains are deleted. This leaves only the grain boundaries and the crack path (also high contrast). The visualisation of the crack path thus becomes easier.

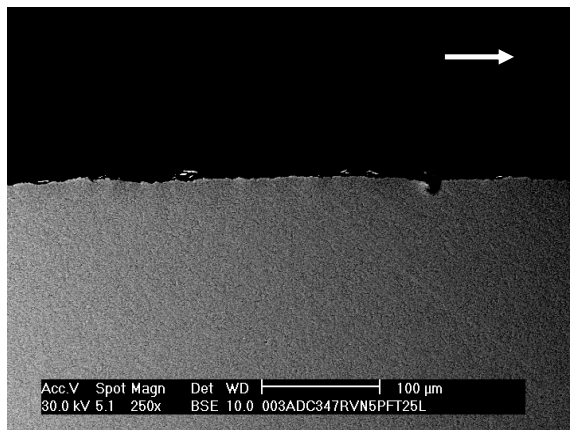


Fig 14(a). Zone of transgranular fatigue crack propagation 250X

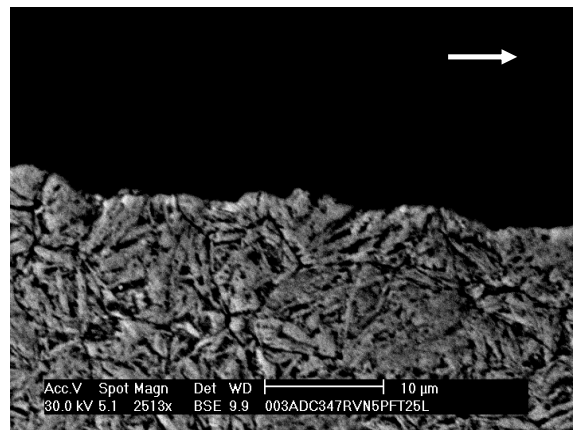


Fig 14(b). Previous austenitic grain network and martensite lattes. X2500. Nital 4%

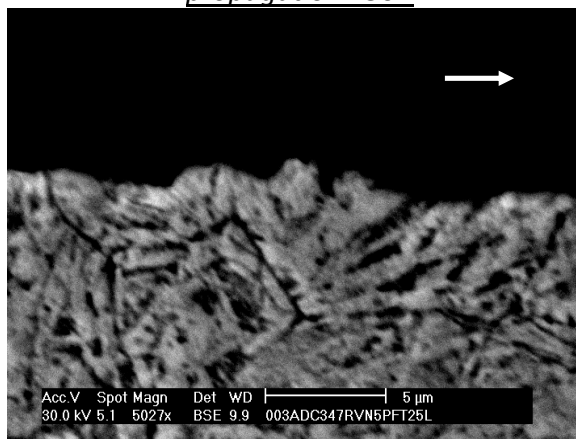


Fig 14(c). Previous austenitic grain network and martensite lattes. X5000. Nital 4%



Fig 14(d). Previous austenitic grain network crack path. Edge detection on micrograph with Matlab®

At a value of $a = 2.77\text{mm}$ which corresponds to $K_{\text{max}} = 38 \text{ MPa}\cdot\text{m}^{1/2}$ the mode of crack propagation transforms into the mixed trans granular and inter granular propagation figure 15(a-d). Some micrographs are added to show the mode of crack propagation in 3D figure 15(e, f).

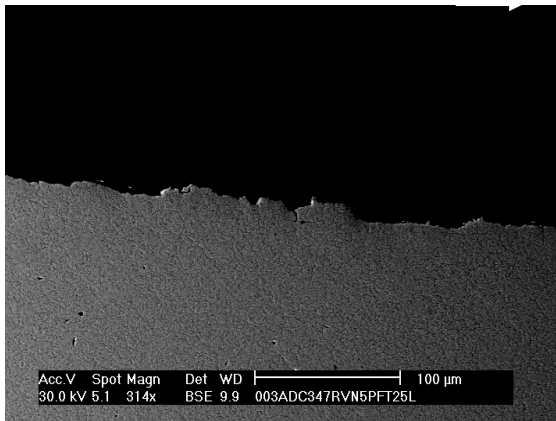


Fig 15(a). Zone of intergranular fatigue crack propaagation 250X

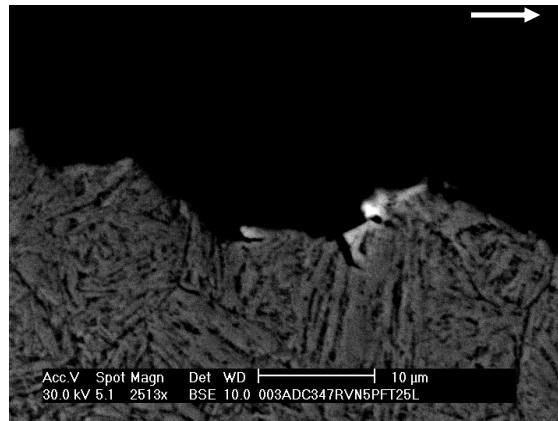


Fig 15(b). Previous austenitic grain network and martensite lattes. X2500. Nital 4%

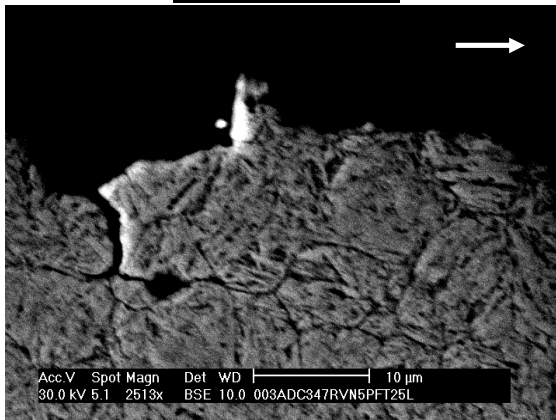


Fig 15(c). Previous austenitic grain network and martensite lattes. X2500. Nital 4%

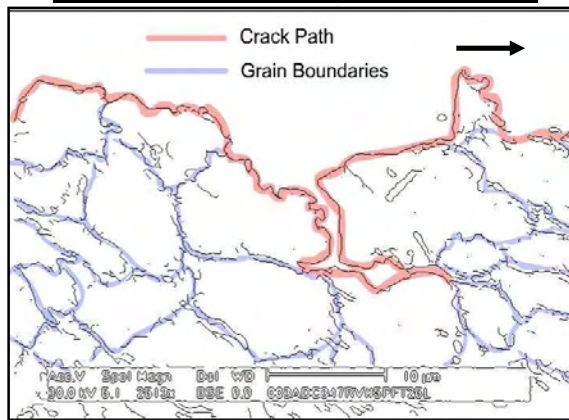


Fig 15(d). Previous austenitic grain network crack path. Edge detection on micrograph with Matlab®

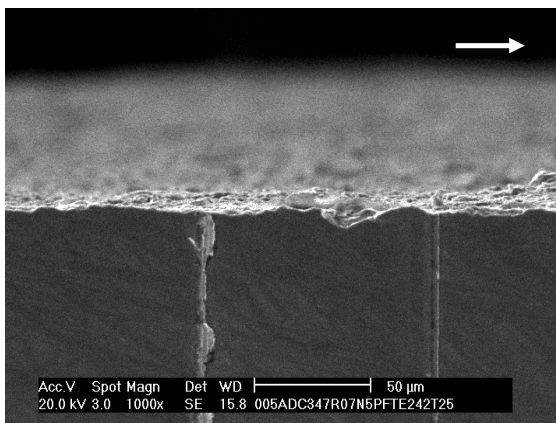


Fig 15(e). Combined view of crack profile and crack faces in trans granular propagation

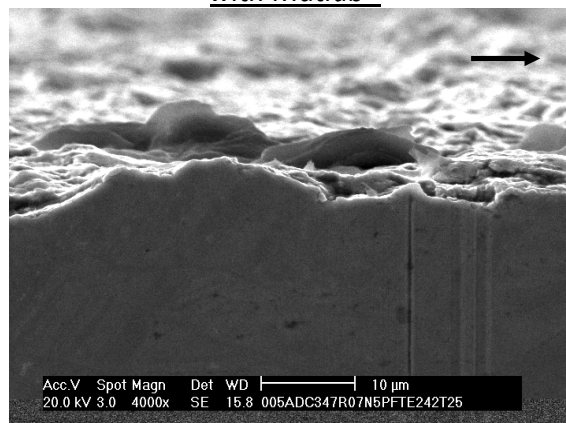


Fig 15(f). Combined view of crack profile and crack faces in inter granular propagation

Branching and decohesion of grain boundaries may also be viewed on the fracture surface figure 16(a,b). The distance between the crack branching is approximately of the same order of magnitude as the grain size.

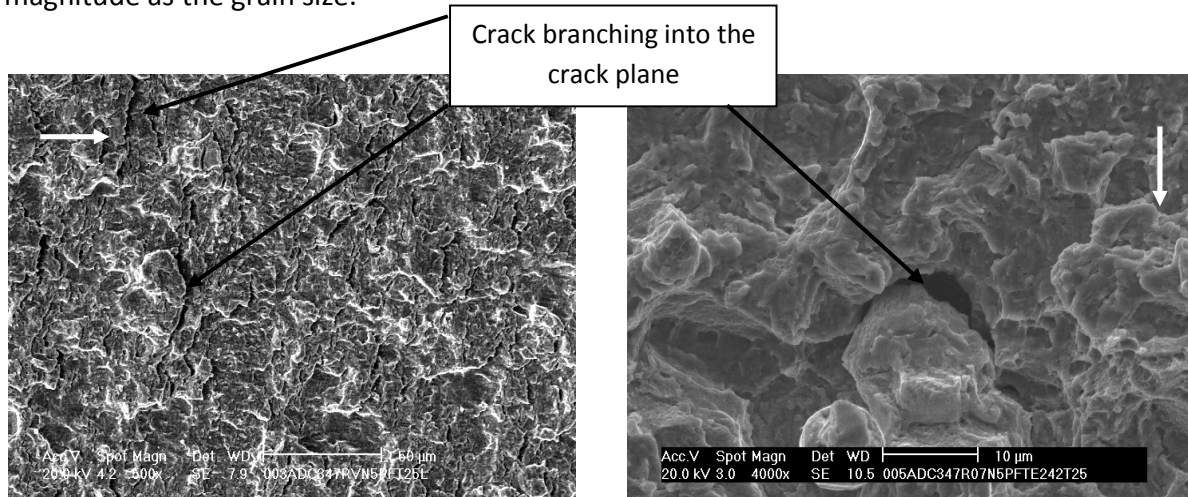


Fig 16(a). Branching and grain boundary decohesion seen on the crack surface. 2.5mm specimen. 250X

Fig 16(b). Branching and grain boundary decohesion seen on the crack surface. 2.5mm specimen. 4000X

I.3.3 Specimens of 1.0mm, 0.60mm and 0.250mm thickness

Most of these specimens show mixed trans granular-inter granular propagation and presence of shear mode planes right from low K_{max} values or shorter crack lengths, figure 11. One of the specimens of thickness 1.0mm was electrolytically attacked in a solution of chromic acid in order to reveal the austenite grain network before testing, figure 17.

The inter granular propagation that is seen cannot be regarded as the natural propagation mode since the specimen was attacked before testing, which causes the crack to follow the grains uniquely on the surface. This type of attack weakens and etches the grain boundaries (sites of chromium concentration). However, crack closure due to coupling of fracture surface roughness and mis-alignment of crack faces is evident, figure 19. This is observed in specimens without chemical etching as well. Some segregation banding (due to uneven precipitation during solidification) is also seen in the material figure 18.

All the observations presented here are post mortem using a scanning electron microscope.

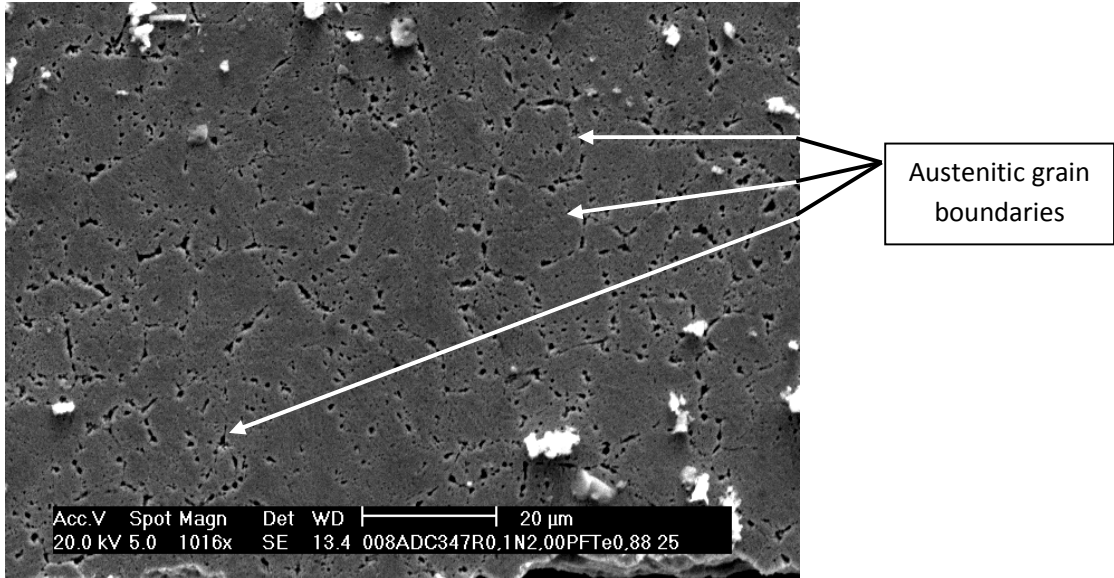


Fig 17. Austenitic grain network revealed by chromic acid 10% W/W

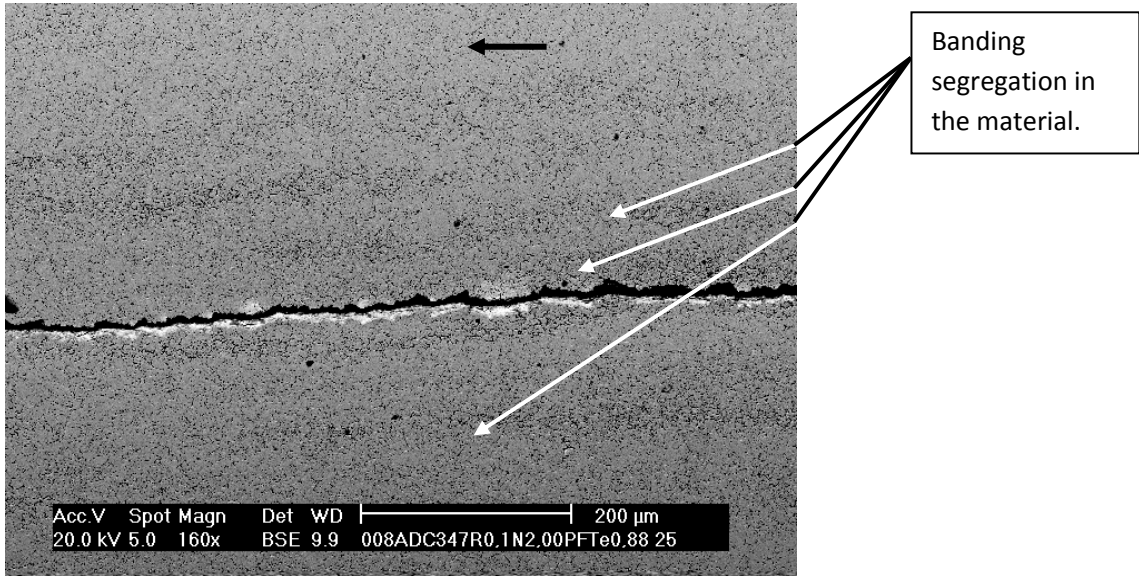


Fig 18. Banding segregation and crack propagation following the band

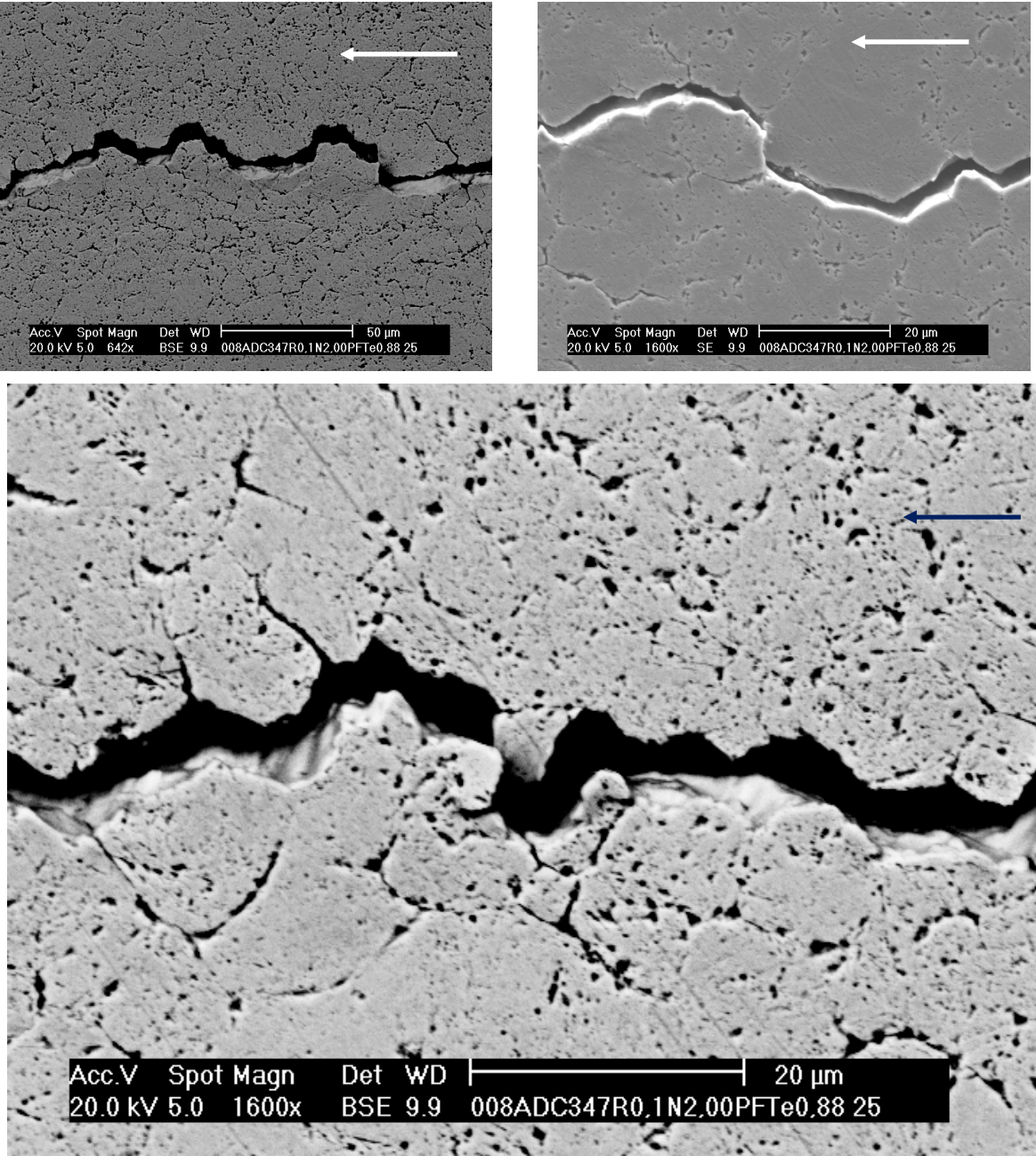


Fig 19. Crack closure due to misalignment of crack faces and roughness of the crack faces in inter granular propagation

II. DETERMINATION OF K_c AT ROOM TEMPERATURE

The values of critical stress intensity factor K_c are obtained in different specimens. The procedure for evaluation of K_c is presented in appendix D. Since the specimens are not made to standard ASTM E399 [10] parameters some conditions of the standard, like thickness sufficient for plane strain deformation and SSY condition etc. are not strictly followed. These experiments are carried out in order to:

- 1) Find dependence of K_c on a/W ratio.
- 2) Find dependence of K_c on specimen thickness.

II.1 Dependence of K_c on a/W

K_c is found to be completely independent on the value of a/W for the 2.5mm specimens as shown in the figure 20. However for specimens of 1.0mm and 0.6mm thickness the K_c values show a marked dependence on the crack length to width ratio a/W in the range of $0.3 < a/W < 0.6$, generally recommended by ASTM standards. The value of K_c increases with a corresponding increase in a/W as shown in figure 20.

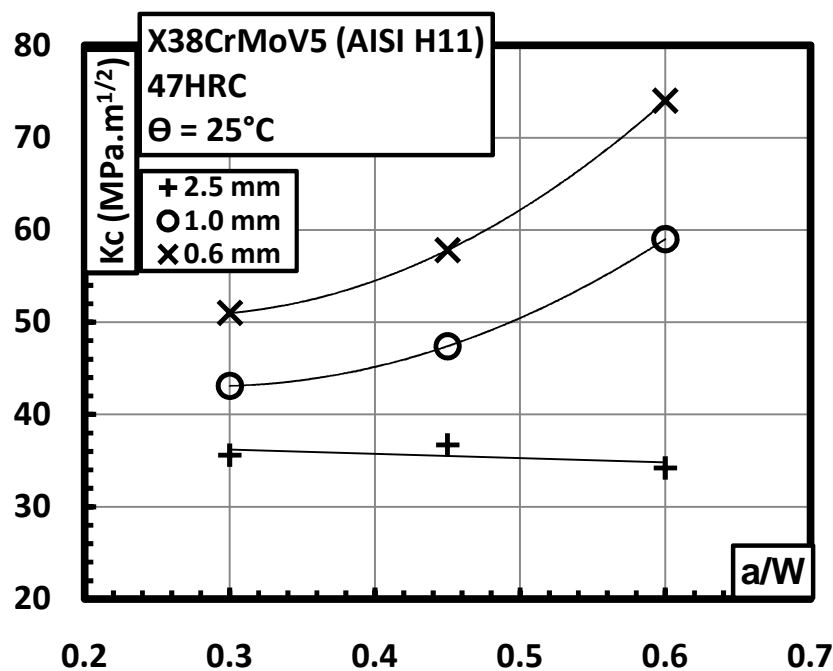


Fig 20. Dependence of critical stress intensity factor K_c on a/W ratios for different thicknesses

The increase in K_c values for thinner specimens seems to follow a quadratic law of the form:

$$K_c = C_1 \left(\frac{a}{W}\right)^2 + C_2 \left(\frac{a}{W}\right) + C_3 \quad (3)$$

Where, C_1 , C_2 and C_3 are constants dependant on the thickness of the material. The values are given in the table 1.

Table 1: Constant of equation 3, to determine K_C dependant on a/W in thin specimens

Specimen Thickness mm	a/W	C_1	C_2	C_3
2.5	0.30	-	-	-
1.0	0.45	162	-93	56.4
0.6	0.60	208	-111	65.5

II.2 Dependence of K_C on the specimen thickness e

The values of K_C for this configuration of specimen are dependent on the specimen thickness. The decrease in the specimen thickness causes a corresponding increase in the K_C values figure 21. This is to be expected as the decrease in the specimen thickness causes an increase in the monotonic plastic zone size, which in turn increases the ability of the material to absorb energy before unstable crack propagation, consequently increasing the K_C value [12].

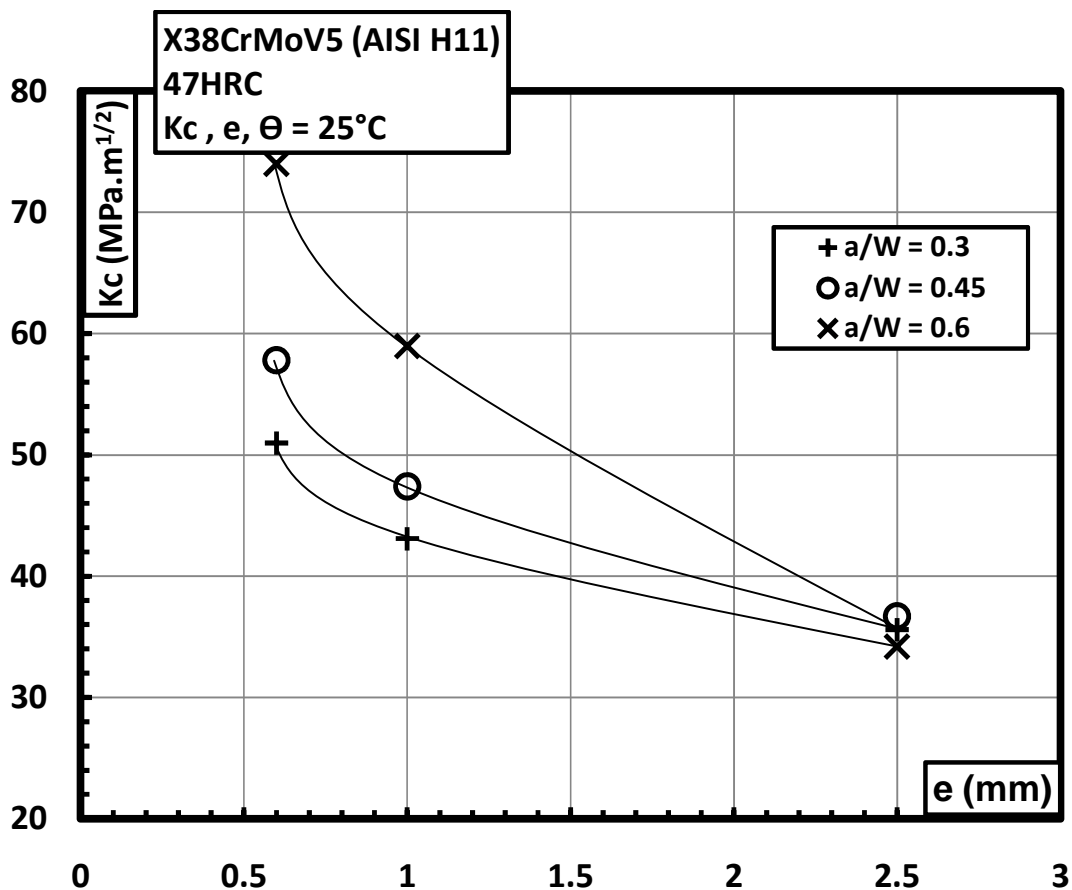


Fig 21. Dependence of critical stress intensity factor K_C on specimen thickness e for different a/W

III. FATIGUE CRACK PROPAGATION AT 600°C.

As mentioned in chapter 2 (Experimental Procedures), the fatigue crack propagation at elevated temperatures depends on numerous parameters. Therefore the question arises: what to use as a crack propagation criterion for the specimens tested at 600°C. Any one of K_I , $J_{el,pl}$, or J^δ can be used as a fatigue crack propagation criterion.

III.1 Effect of R ratio on fatigue crack propagation and comparison with ambient temperature results.

The experiments are carried out at $R = 0.1$ and $R = 0.5$ for specimens of 2.5mm thickness and $R = 0.1, 0.3$ and 0.7 for specimens of 0.6mm thickness. All the results of fatigue crack propagation are shown as a function of ΔK or $\Delta\sqrt{J_{el,pl}E'}$. The first criterion is most commonly used to represent the fatigue crack propagation data. The advantage of the second criterion is that it presents a better correlation between tests at 600°C and at ambient temperature. Also, the $\Delta\sqrt{J_{el,pl}E'}$ criterion takes into account the effects of crack tip plasticity at 600°C. Thus all the figures are presented as pairs of the two criteria.

Fatigue crack propagation at 600°C in specimens of $e = 2.5$ mm at different R values seems to show absolutely no effect in the Paris region, figures 22, 23. However, there seems to be a marked difference in the threshold values of specimens tested at different R ratios. The threshold ΔK value for $R = 0.1$ is found to be $11.9 \text{ MPa}\cdot\text{m}^{1/2}$, whereas for the specimen tested at $R = 0.5$ has a lower threshold value of $7.8 \text{ MPa}\cdot\text{m}^{1/2}$. Higher crack closure in the threshold region, for $R = 0.1$ may be the cause of this difference.

The specimens of 0.6mm thickness have also been compared in the same manner with $R = 0.1, 0.3$ and 0.7 in figures 24 and 25. The effect on the threshold value is more pronounced for 0.6mm specimens. The threshold ΔK values are 12.8, 10.6, $7.8 \text{ MPa}\cdot\text{m}^{1/2}$ for the R ratios of 0.1, 0.3 and 0.7 respectively. The increase in the threshold value especially for $R = 0.1$ may be due to increased plasticity in the thinner specimens, or may be an effect of reduced K_{max} . The reduction in K_{max} is inevitable to search for threshold values in thin specimens. This effect is graphically presented in the figure 26.

Contrary to ambient temperature where no threshold value was detected, ΔK_{th} clearly exists for specimens tested at 600°C. This could be attributed to crack tip plasticity and blunting.

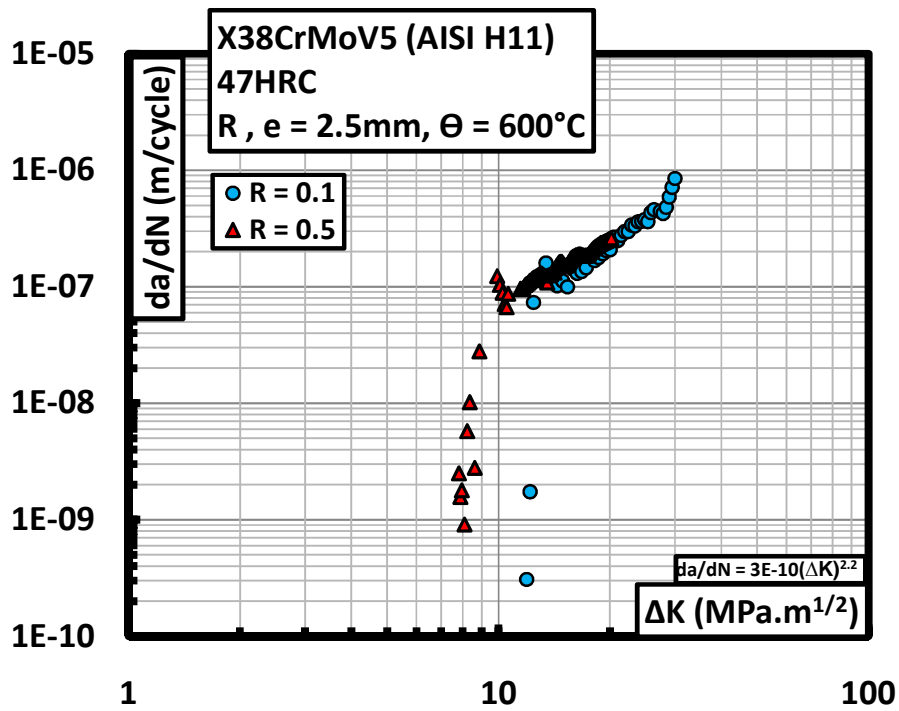


Fig 22. Effect of R ratio in 2.5mm specimen on fatigue crack propagation at 600°C ΔK

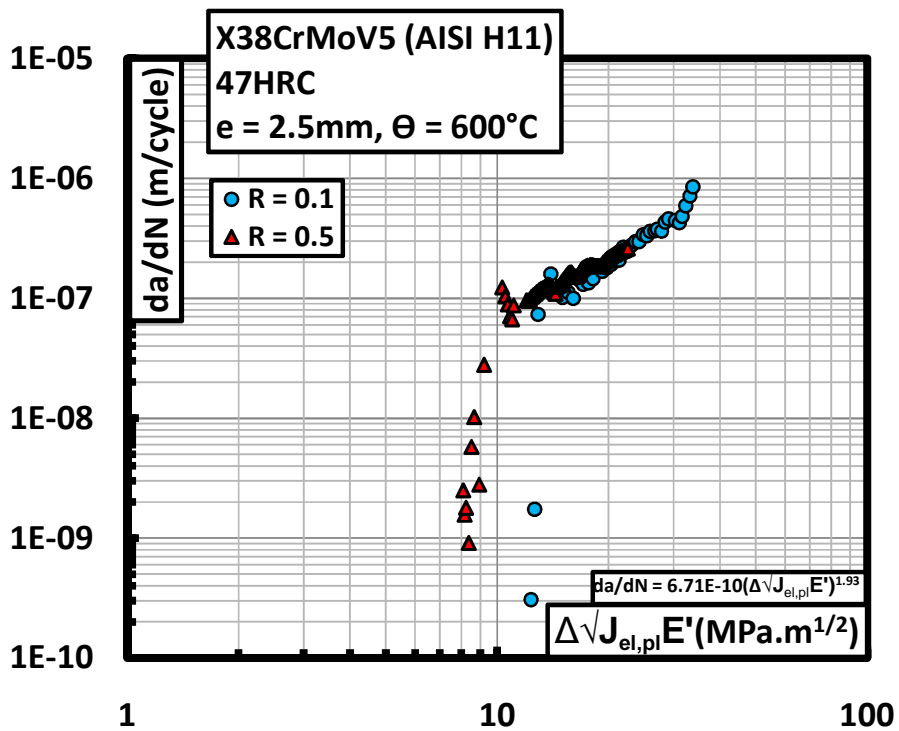


Fig 23. Effect of R ratio in 2.5mm specimen on fatigue crack propagation at 600°C $\Delta\sqrt{J_{el,pl}E'}$

Fatigue crack propagation curves for 600°C are compared with those at ambient temperature. Figures 27 and 28 show this comparison for 2.5mm specimens with elastic and elastic-plastic crack propagation criteria respectively. The crack propagation rate for the specimens at 600°C is higher for low values of ΔK or $\Delta\sqrt{J_{el,pl}E'}$. However this difference diminishes for higher ΔK or $\Delta\sqrt{J_{el,pl}E'}$.

Specimens of 0.6mm tested at these temperatures as shown in figures 29 and 30 show the same behaviour. The difference of fatigue crack propagation rate can be described for low, intermediate and high ΔK or $\Delta\sqrt{J_{el,pl}E'}$ values as explained below.

It is observed that in general the material at 600°C has higher crack propagation rate for low ΔK or $\Delta\sqrt{J_{el,pl}E'}$ values. The slope of the Paris curve “m” is lower at 600°C; the consequence is that the curves intersect at some intermediate value of ΔK or $\Delta\sqrt{J_{el,pl}E'}$.

The K_c at 600°C seems to be lower than at 25°C, which again forces the curves to separate for higher ΔK or $\Delta\sqrt{J_{el,pl}E'}$ values. It is pertinent to mention here that due to large number of points measured in experiments carried out on specimens of 0.6mm thickness, the raw data is presented without cubic spline smoothing techniques.

At higher R ratio, the situation is different. The curves seem to follow a more or less parallel path in the Paris regime, with the specimen at high temperature having higher fatigue crack propagation rate, figures 33 and 34.

The threshold values for high temperature specimens are explored in an experiment performed specifically for this purpose in a 0.6mm thickness specimen for $R = 0.1$. Under normal conditions of ascending ΔK fatigue crack propagation, there is a possibility of confusing the threshold value with the notch effect. This is because at low ΔK values the crack length is low as well and thus there is the risk that the crack tip is still in the large residual plastic zone of the precracking. The small amount of uncracked ligament (small specimen size) renders the exit of crack tip from the plastic zone difficult. The threshold values are thus tested at different crack lengths, while keeping the evolution of ΔK_{max} limited.

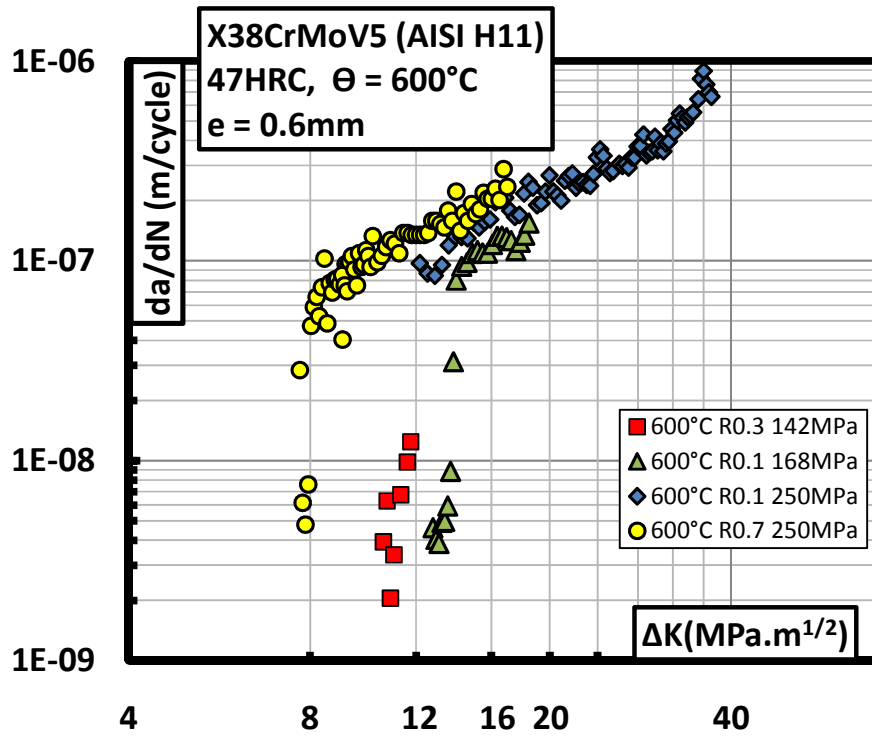


Fig 24. Effect of R ratio in 0.6mm specimen on fatigue crack propagation at 600°C ΔK

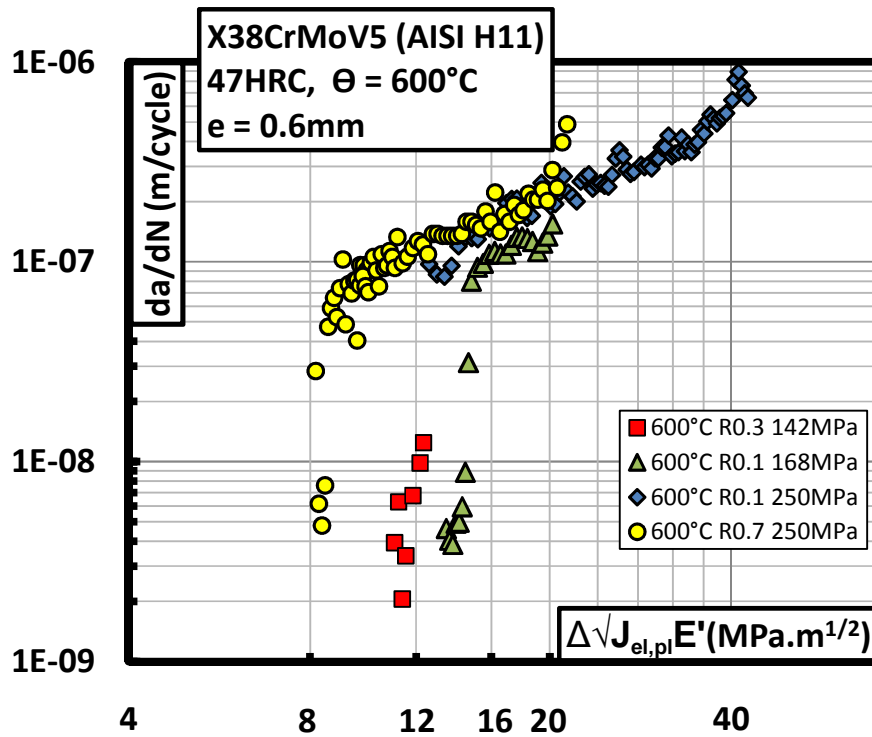


Fig 25. Effect of R ratio in 2.5mm specimen on fatigue crack propagation at 600°C $\Delta\sqrt{J_{el,pl}E'}$

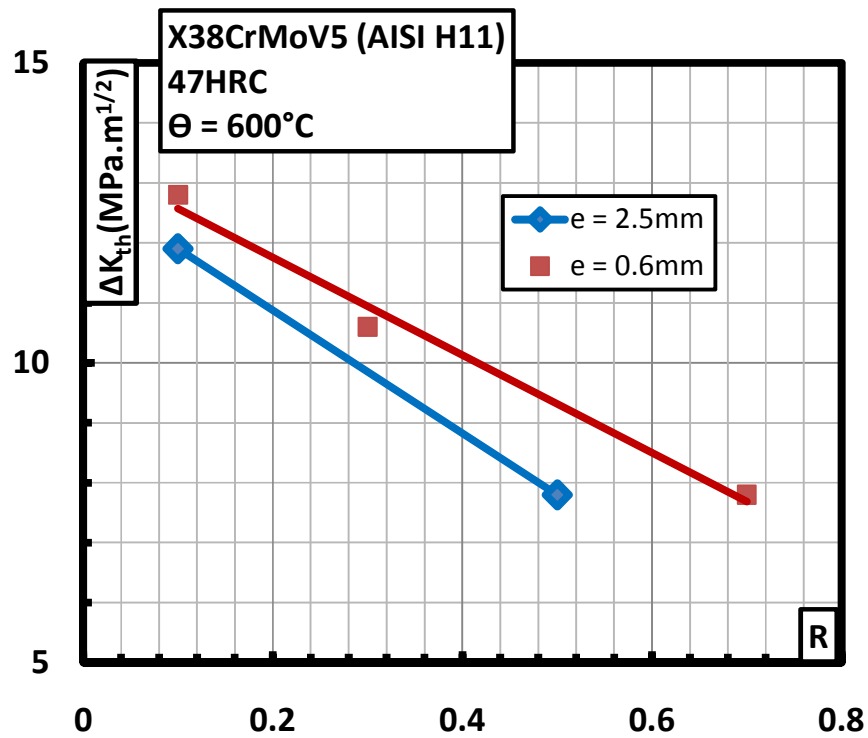


Fig 26. ΔK_{th} as a function of load ratio R for different specimen thicknesses tested at 600°C

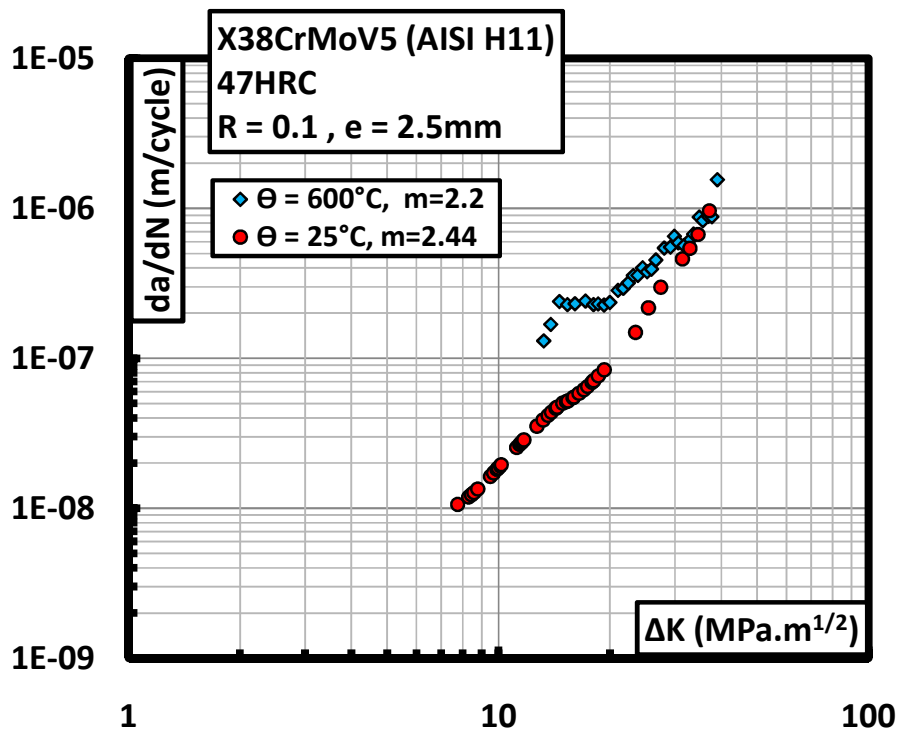


Fig 27. Fatigue crack propagation at ambient temperature and 600°C, $R=0.1$, $e=2.5mm$, ΔK

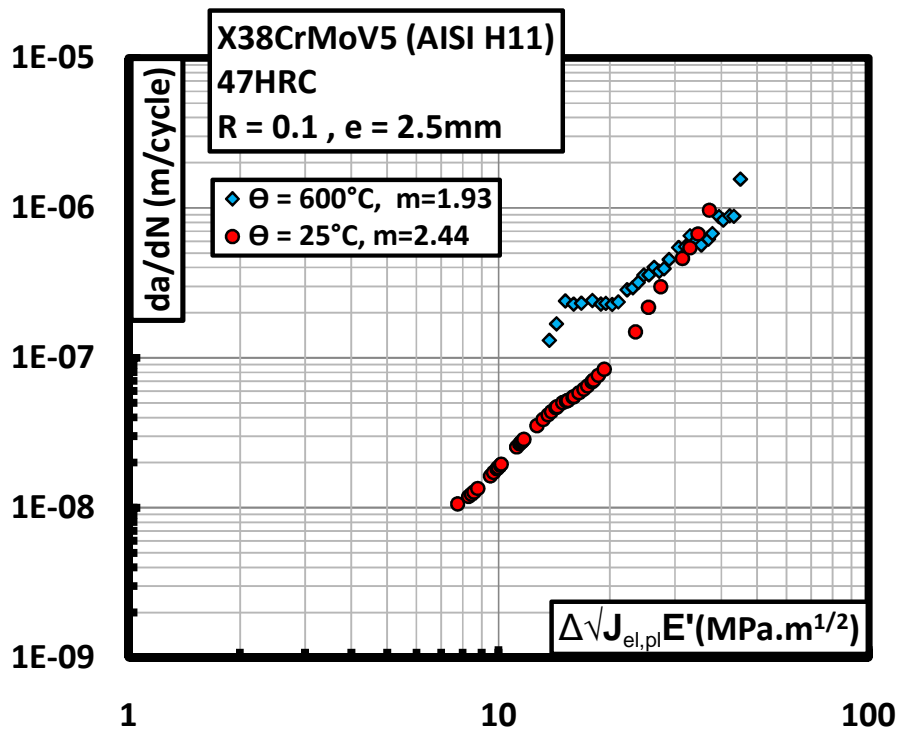


Fig 28. Fatigue crack propagation at ambient temperature and 600°C, e=2.5mm, R=0.1,

$$\Delta\sqrt{J_{el,pl}} E'$$

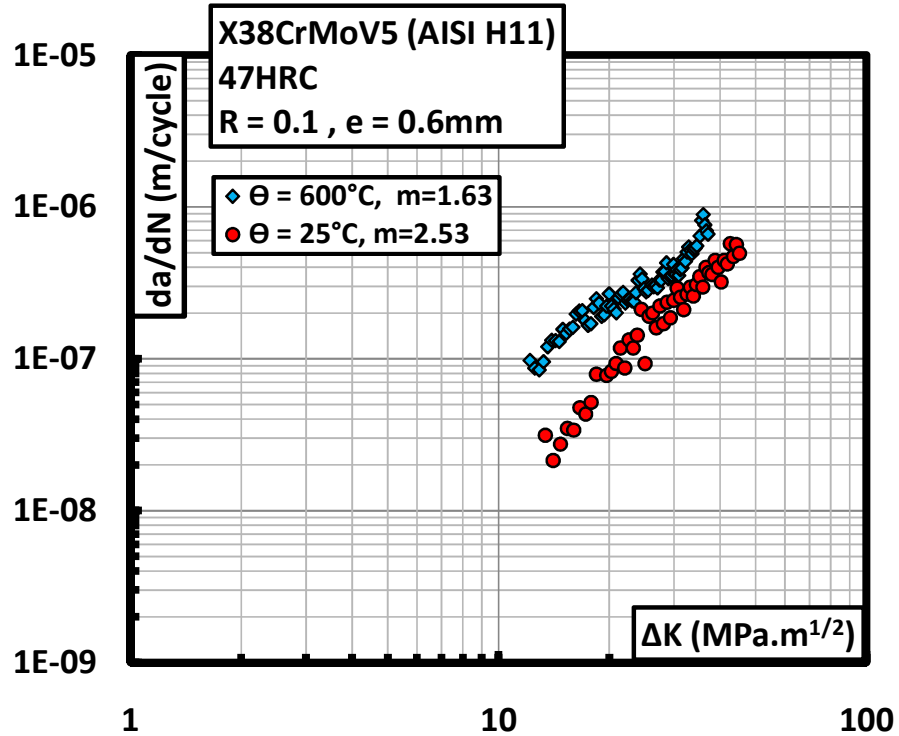


Fig 29. Fatigue crack propagation at ambient temperature and 600°C, e=0.6mm, R=0.1, ΔK

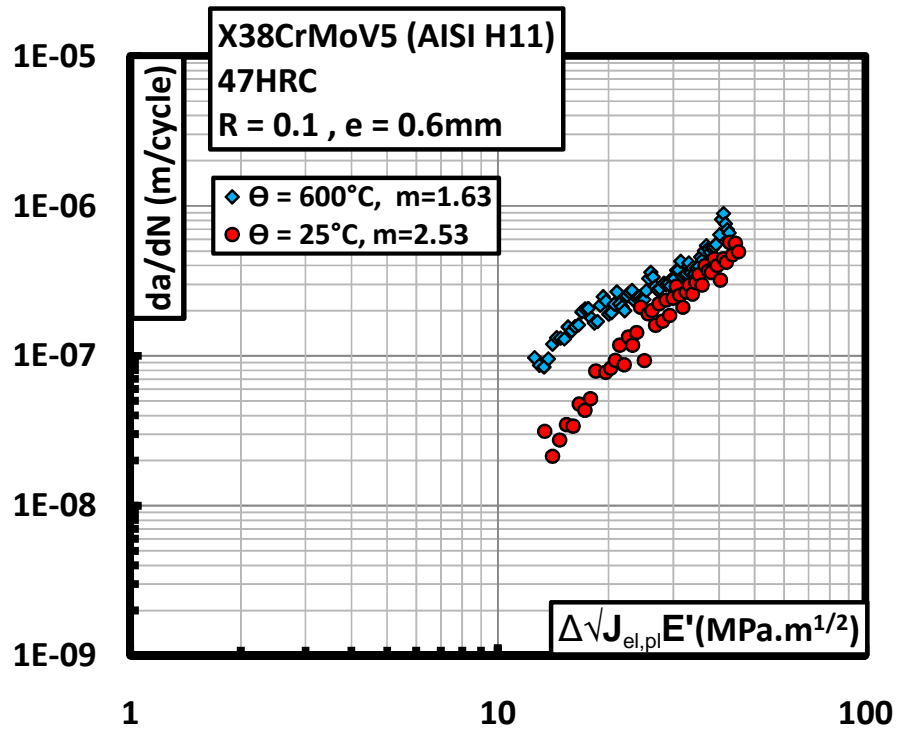


Fig 30. Fatigue crack propagation at ambient temperature and 600°C, e=0.6mm, R=0.1,

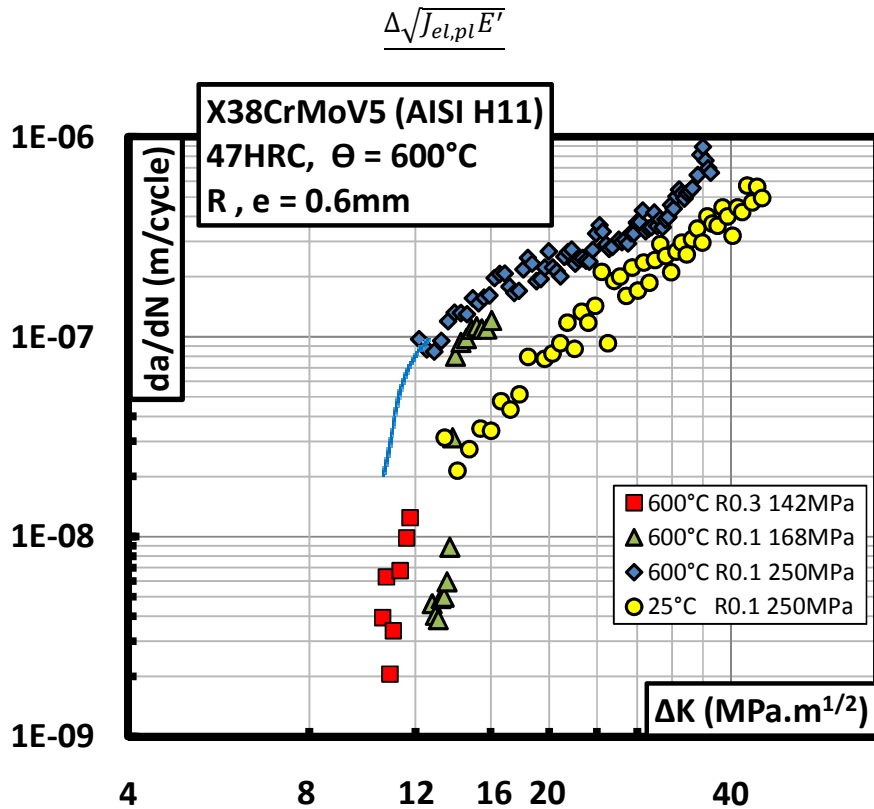


Fig 31. Determination of threshold value at 600°C, ΔK

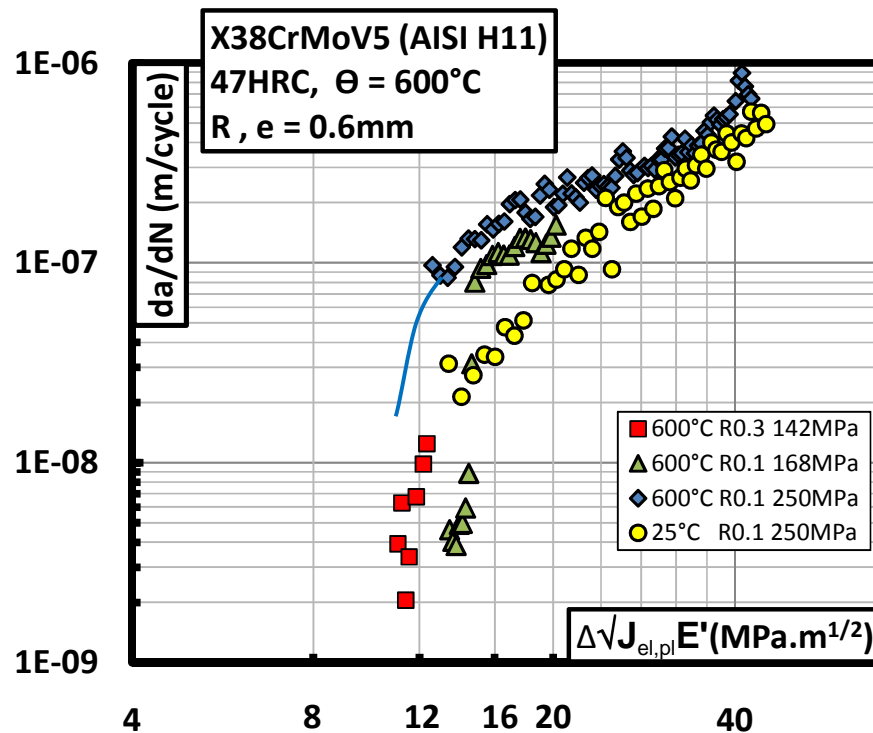


Fig 32. Determination of threshold value at elevated temperature $\Delta\sqrt{J_{el,pl}E'}$

The figures 31 and 32 show the experiment performed to determine ΔK_{th} and its comparison with a normal ascending ΔK crack propagation experiment.

The figures 31 and 32 provide an insight into the crack propagation behaviour, especially in the threshold region. The stress values indicated are the maximum stress values applied at the specimens. The effects are summarised below as:

- The threshold value in the region of 8 to 12 $\text{MPa}\cdot\text{m}^{1/2}$ is not an artefact of the notch, but is reproducible at different crack lengths.
- Increase in the R ratio tends to decrease ΔK_{th} . This indicates a presence of crack closure at threshold region.
- Increase in the maximum stress at 600°C seems to increase the crack propagation rate and reduce the threshold value slightly. This increase could be due to the reduction of the effect of crack closure at higher stresses which might also explain the apparent insensitivity of this material to R ratio when tested at 600°C at 250MPa.
- When compared to the specimen tested at 25°C, it seems that the threshold values for the specimen at 600°C is higher. In fact no ΔK_{th} was determined for specimens at ambient temperature.

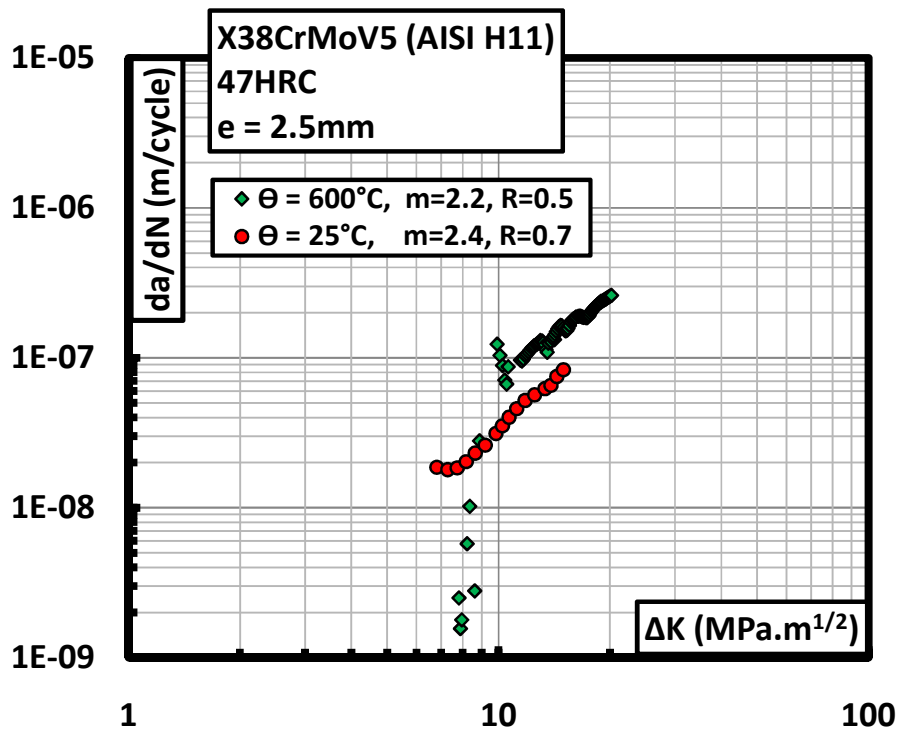


Fig 33. Fatigue crack propagation at 25°C (R=0.7) and 600°C (R=0.5), ΔK

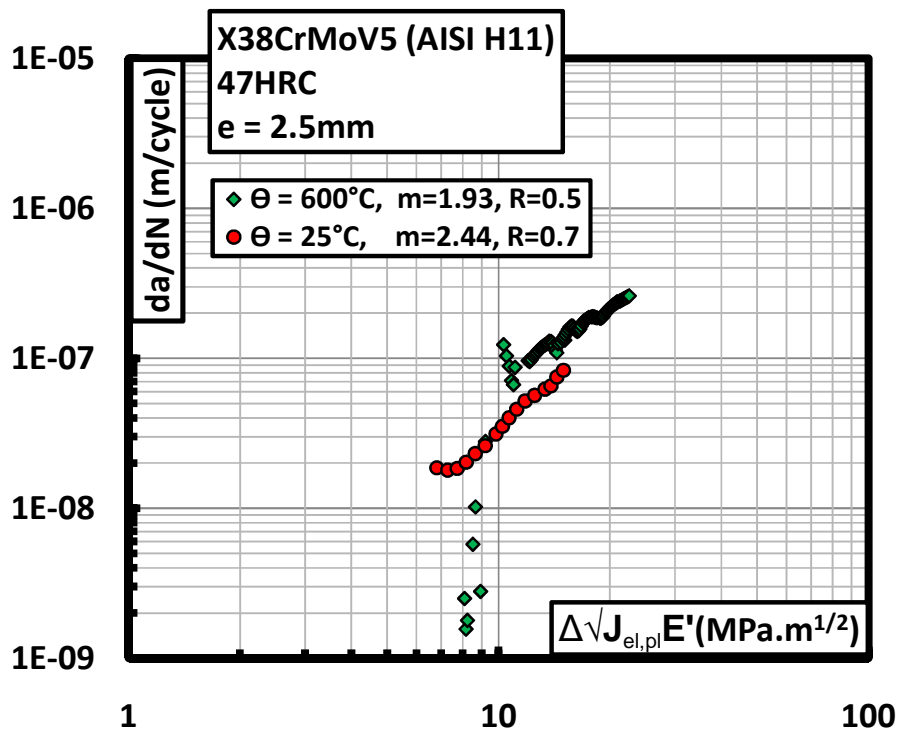


Fig 34. Fatigue crack propagation at 25°C (R=0.7) and 600°C (R=0.5) $\Delta\sqrt{J_{el,pl} E'}$

The effect of higher threshold values at 600°C is also shown in the figures 33 and 34 in specimens of 2.5mm thickness. The R ratios are different but it is believed that no crack closure exists for either of these R ratios in the stable crack propagation region.

In all the comparisons between the specimens tested at 600°C, it is observed that the ΔK threshold values at 600°C seem higher than ambient temperature. The experiment shown in figures 31 and 32 is carried out to confirm this. The experiment does confirm that the threshold values obtained are not notch or loading history artefacts. However, to confirm the increase in the threshold values with an increase in temperature another experiment is carried out with increasing temperatures during the crack propagation.

The results are shown in figure 35. In this experiment fatigue crack propagation at 25°C is carried out in a specimen of 0.6mm with $R = 0.7$. An increased R gives an inherent advantage to be able to apply low ΔK values in thinner specimens more conveniently from the testing machine control standpoint. The different steps followed during the experiment and the results are listed as follows:

- **Fatigue crack propagation at 25°C R=0.7.** This gives a crack propagation curve which is parallel to the other FCGR curve obtained for higher ΔK values with the same loading conditions. The curve follows the simple Paris regime of propagation between 4.4 and 5.0 MPa.m^{1/2}. However for this level of ΔK there is fair amount of scattering in the FCGR data. This is shown as the yellow data in figure 35.
- **Specimen heated to intermediate temperature at 300°C R=0.7.** All the other testing conditions like maximum load, frequency, load ratio etc are kept the same. The heating is done rapidly. The fatigue crack propagation experiment is continued at 300°C. Two distinct observations are made. One is that the FCGR increases three times, however the curve remains parallel to the FCGR curve at 25°C (Data in red in figure 35). This may be explained by the increase in material damage with a subsequent increase in the temperature. The second observation is a strong reduction in the scattering of the FCGR data. Due to an increase in temperature the Young's modulus decreases. This effect increases the crack opening displacement, which in turn may reduce the effects of crack face roughness and misalignment on the scattering of FCGR data. The propagation is carried out up to 5.7 MPa.m^{1/2}.
- **Specimen heated to 500°C R = 0.7.** This temperature is 50°C below the first tempering temperature of the material and is thus expected that no rapid phase transformation will occur at this temperature (in particular precipitation). The effects on the FCGR curve would be in principle related to mechanical properties more than metallurgical changes. However at this temperature we find a crack arrest. It is shown as the data in brown colour in the figure 35. To restart the propagation, the stress level is increased. The FCGR curve for 500°C follows closely that of 600°C. It should be emphasized that

oxidation measurements carried out at 550°C show a very slow oxidation rate [13] (even negligible). Therefore it can be assumed that this crack arrest effect is not related to environmental effects, but to the mechanical behaviour of the material at this temperature. The dashed black line shows the path followed upto this step.

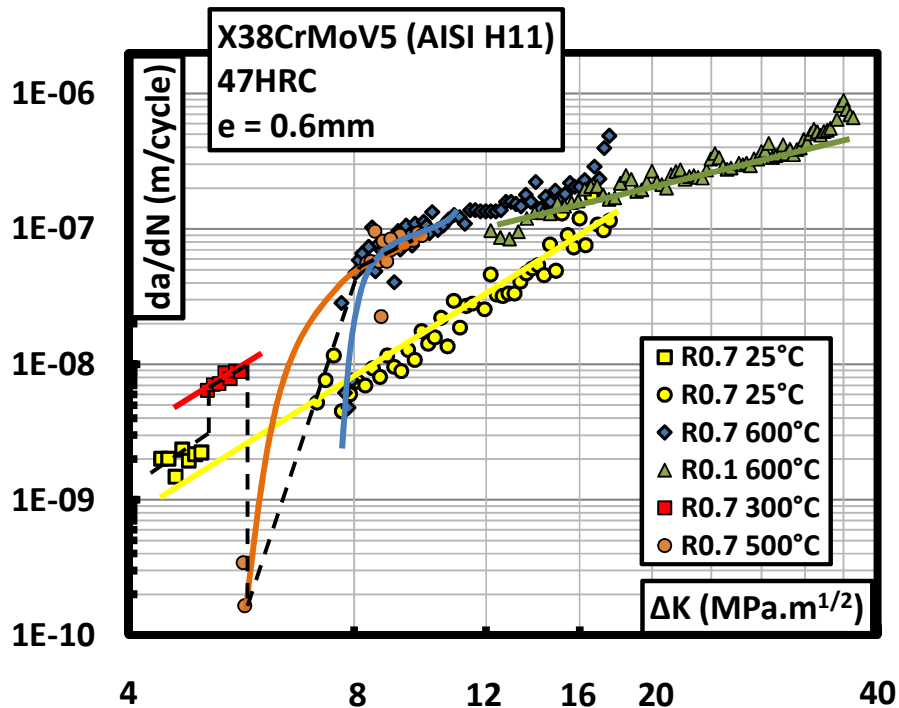


Fig 35. Effect of temperature variation during fatigue crack propagation. Propagation at 25°C, 300°C, 500°C, 600°C at R = 0.7, ΔK

- **Specimen heated to 600°C R = 0.7.** Not much effect is observed on the FCGR curve and it continues to follow the 500°C curve. This temperature approaches the second tempering temperature of the material so over tempering and the reduction dislocation density by thermal effects and mechanical cycling may be expected. The experiment is continued for some increase in the crack length. Then the ΔK is reduced to try to search for the threshold value, which was the principal goal. This value is found to be near 8 $\text{MPa.m}^{1/2}$ which agrees to threshold values obtained in other experiments for these experimental conditions (figures 31 and 33). The test is then continued up to rupture.

The results in this experiment are presented only as a function of ΔK , because the $\Delta\sqrt{J_{el,pl}E'}$ for 400°C and 500°C are not available (numerical simulations not performed for intermediate values). This experiment has established beyond any doubt that the material at high temperature of 600°C has a higher crack propagation threshold value. It has also been established that fatigue crack propagation curve for 600°C may cross over the curve for 25°C

near the threshold values. The same observation was made by Makhlof et al. [14] in FCGR experiments on 18%CrNb ferritic stainless steels tested at 500°C. They have explained this effect due to plasticity induced crack closure at 500°C as opposed to roughness induced crack closure at room temperature. Here the phenomenon may be explained by an increase in the crack tip plastic zone size due to reduced yield stress and drastic cyclic softening at elevated temperature. This plastic zone is large enough to cause a complete crack arrest. The evidence of crack arrest due to increased crack tip plastic zone is presented in the appendix C.

III.2 Effect of specimen thickness on the fatigue crack propagation rate at 600°C and comparison with ambient temperature

As explained in the section I.2, decrease in thickness favours the plane stress state condition, whereas in thick specimens the plane strain condition prevails. This difference may have an effect on the fatigue crack propagation behaviour of the material. In this section are presented the fatigue crack propagation curves for specimens of different thicknesses all tested at 600°C.

There seems to be a trend of reduction in crack propagation rate in the Paris region with a subsequent decrease in the specimen thickness figure 36 and 37. This behaviour is less pronounced than tests carried out at ambient temperature.

The main effect however is seen at the threshold values, with those of the 0.4mm specimen being $20.8 \text{ MPa.m}^{1/2}$, which is almost twice that of the 1.0mm and 0.6mm specimen figure 36. The effect on the ΔK_{th} is explored in detail in the previous section. The evolution of ΔK_{th} with respect to thickness for $R=0.1$ in specimens tested at 600°C is summarized in table 2 and shown in figure 38.

Table 2: Evolution of ΔK_{th} with reduction in thickness

	Thickness of specimens "e" (mm)			
	2.5	1.0	0.6	0.4
$\Delta K_{th} \text{ (MPa.m}^{1/2}\text{)}$	11.9	12.4	12.8	20.8

The sharp increase in the ΔK_{th} of the 0.4mm specimen may be attributed to the increased crack closure. Observations of the fracture surface of this specimen (figure 39) show the presence of a sort of tearing at the crack edges. Although this tearing is not seen for short crack lengths, its presence on the crack surface indicates a presence of large deformations as well as a possibility mismatch of the two crack surfaces even for short crack lengths, which may be the source of increased crack closure.

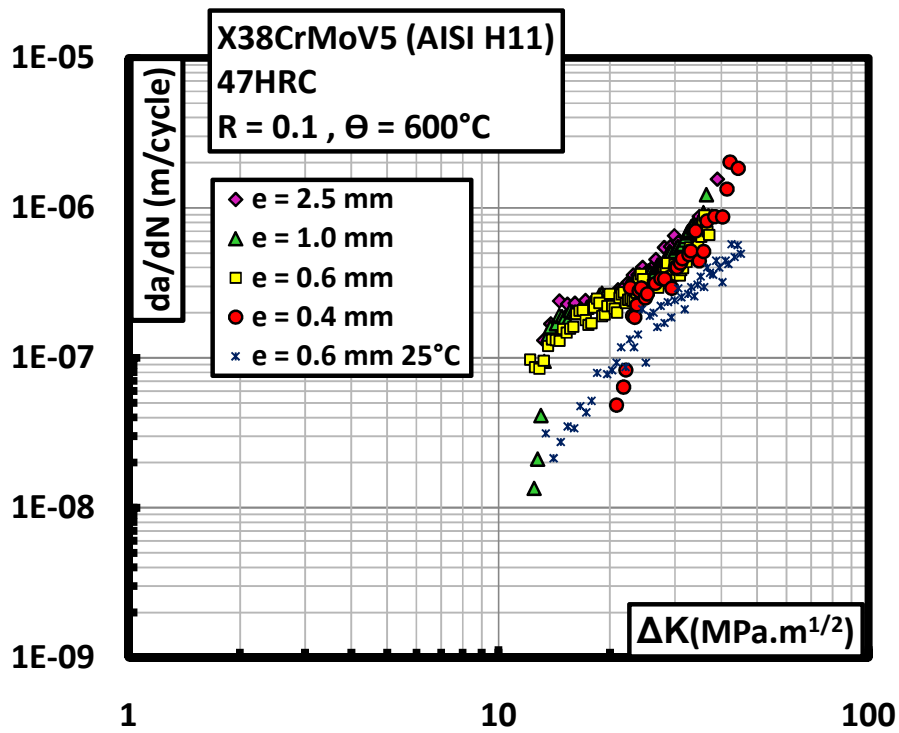


Fig 36. Effect of specimen thickness $e = 2.50, 1.0, 0.60$ & 0.40mm à 600°C , ΔK

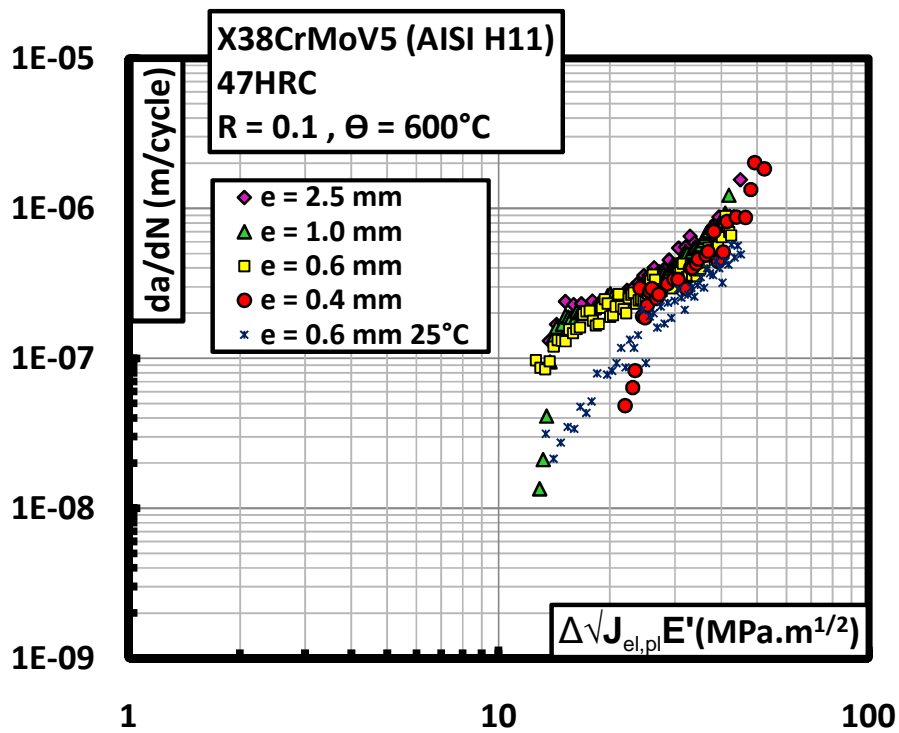


Fig 37. Effect of specimen thickness $e = 2.50, 1.0, 0.60$ & 0.40mm à 600°C , $\Delta\sqrt{J_{el,pl}}E'$

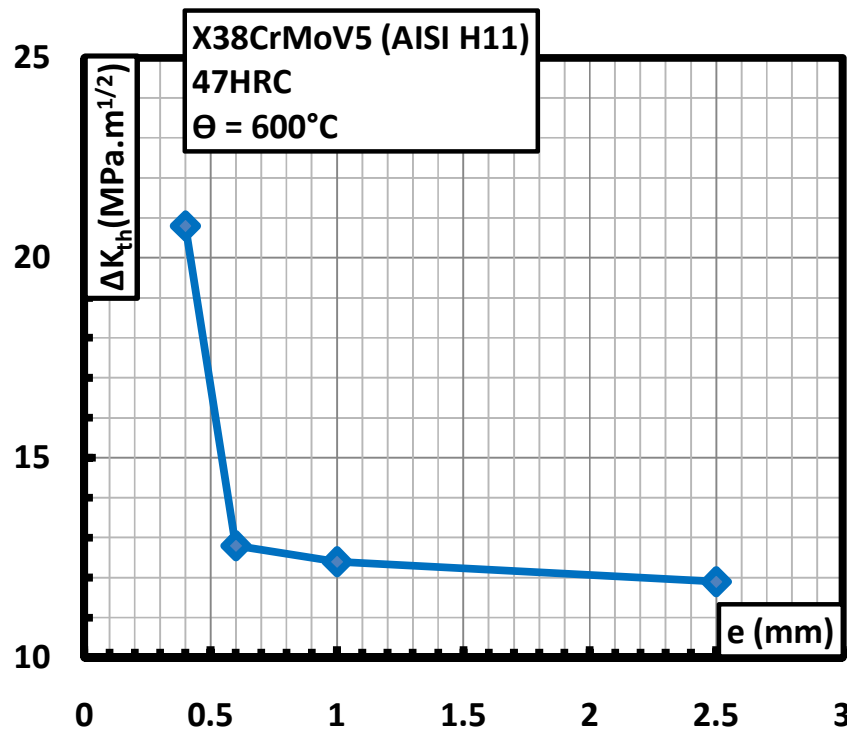


Fig 38. ΔK_{th} as a function of specimen thickness "e" for R=0.1 tested at 600°C

III.3 Observation of fracture surface

In this section the fractography is presented for specimens tested at 600°C.

The fractographic analysis is presented for a specimen of 0.4mm thickness, tested at R=0.1.

At a certain value of crack length ($a > 3.2$ mm) the fracture surface shows distinct morphology near the crack edges (free surface of the specimen). We can see distinct saw tooth type morphology with extrusion appearing on the specimen free surface as well as the crack surface as shown in figure 39. This type of morphology mainly gives an indication to the large plastic deformation as well as a mixed mode of crack propagation with mode II type mechanism near the edges. The thicker specimens do not show this effect. The arrow indicates the direction of propagation in the micrographs.

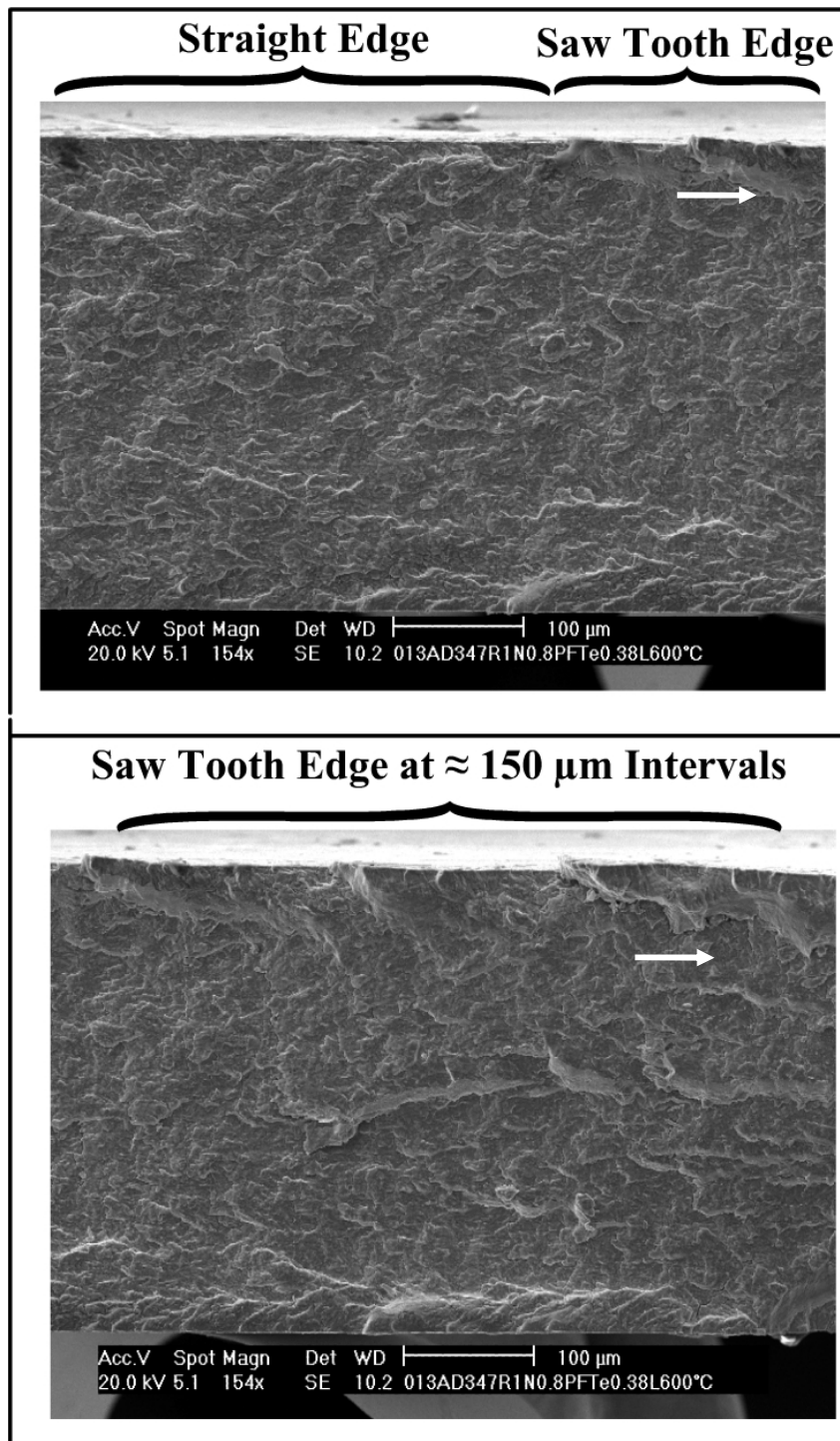


Fig 39. Creation of saw tooth morphology at the edges of the crack (free surface) in fatigue crack propagation in a specimen of 0.4mm thickness tested at R=0.1, 600°C

The fracture surface is made up of flat planes separated by flat inclined planes at almost 45° as in the specimens tested at room temperature. These inclined planes are probably shear mode propagation planes figure 40. Different types of oxide layers were found on these planes. The oxide layer on the flat plane figure 40, is of grey colour and has an approximate composition of FeO where the point X shows the position of the analysis, Table 3. In BSE it shows as the darker fracture surface.

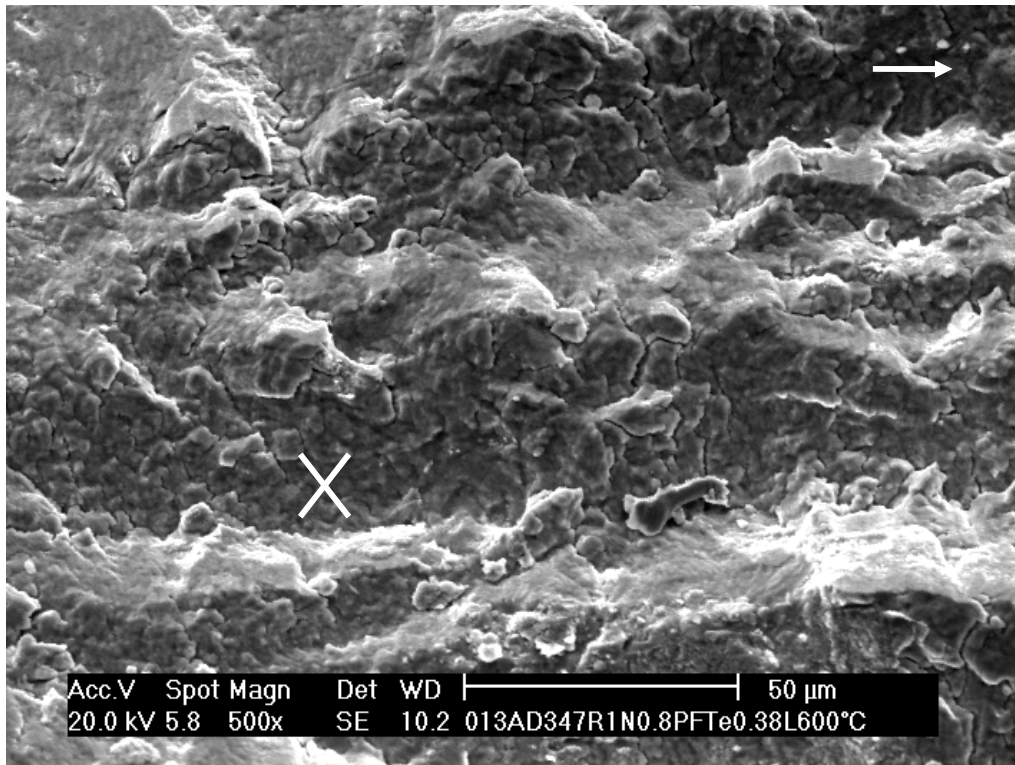


Fig 40. Analysis of oxide layer on the flat surface of fracture surface

Table 3: Chemical analysis of the oxide layer on the flat fracture surface

Element	K Ratio	Weight %	Atomic %
O K	0.1533	24.989	53.769
SiK	0.0031	0.510	0.626
MoL	0.0168	1.863	0.668
CrK	0.0483	3.497	2.315
MnK	0.0031	0.281	0.176
FeK	0.7753	68.860	42.447
Total		100.000	100.000

The oxide layer on the shear planes is richer in oxygen with an approximate composition of Fe₂O₃, Table 4. It appears as a red coloured oxide layer in the optical microscopy and as a lighter colour on the BSE detector of the SEM figure 41.

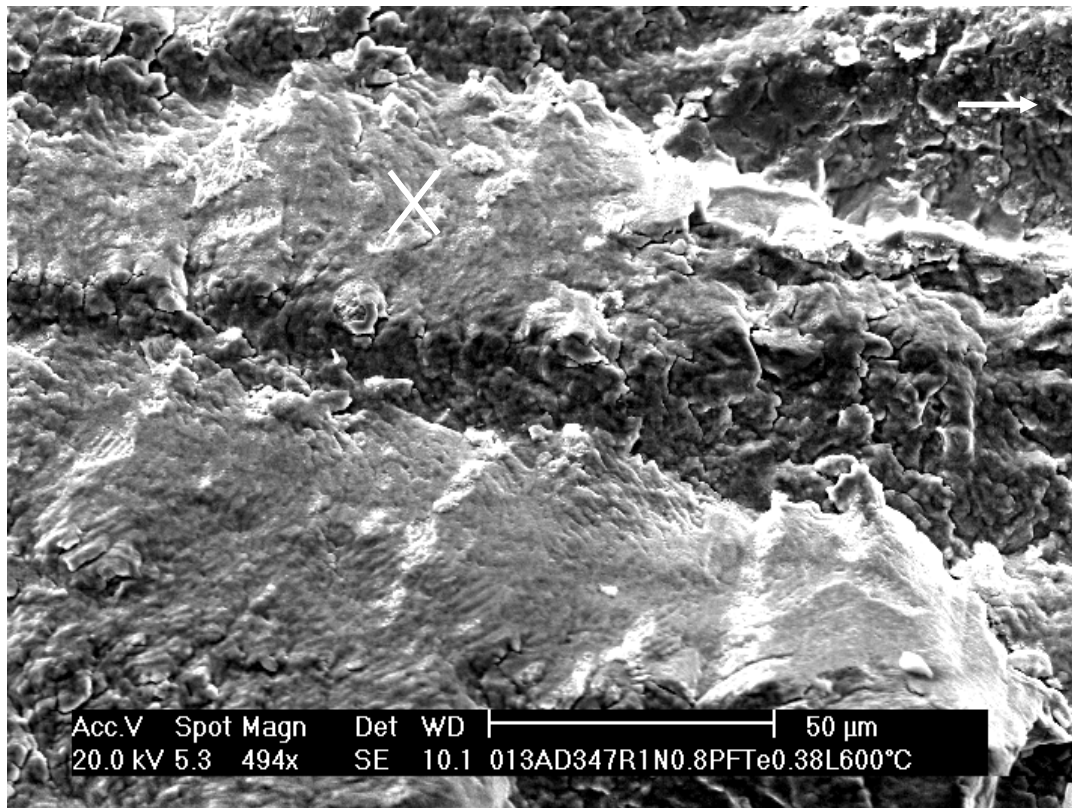


Fig 41. Analysis of oxide layer on the shear planes of fracture surface

Table 4: Chemical analysis of the oxide layer on the flat fracture surface

Element	K Ratio	Weight %	Atomic %
O K	0.2915	40.554	70.391
SiK	0.0051	0.720	0.712
MoL	0.0194	1.940	0.562
CrK	0.0382	2.662	1.422
MnK	0.0017	0.140	0.071
FeK	0.6441	53.983	26.843
Total		100.000	100.000

It may also be noted that fatigue striations can be seen only on the shear planes of the fracture surface, figure 42. These striations exist only in the oxide layer. Their size corresponds to the propagation per cycle in the FCGR curves. However each shear plane defines a fully developed crack front instead of a continuous single crack tip over the whole fracture surface. The crack front is composed of many smaller fully developed crack fronts that cover each inclined plane. Since we cannot detect striations on the flat planes, the exact shape of the crack front is difficult to interpret.

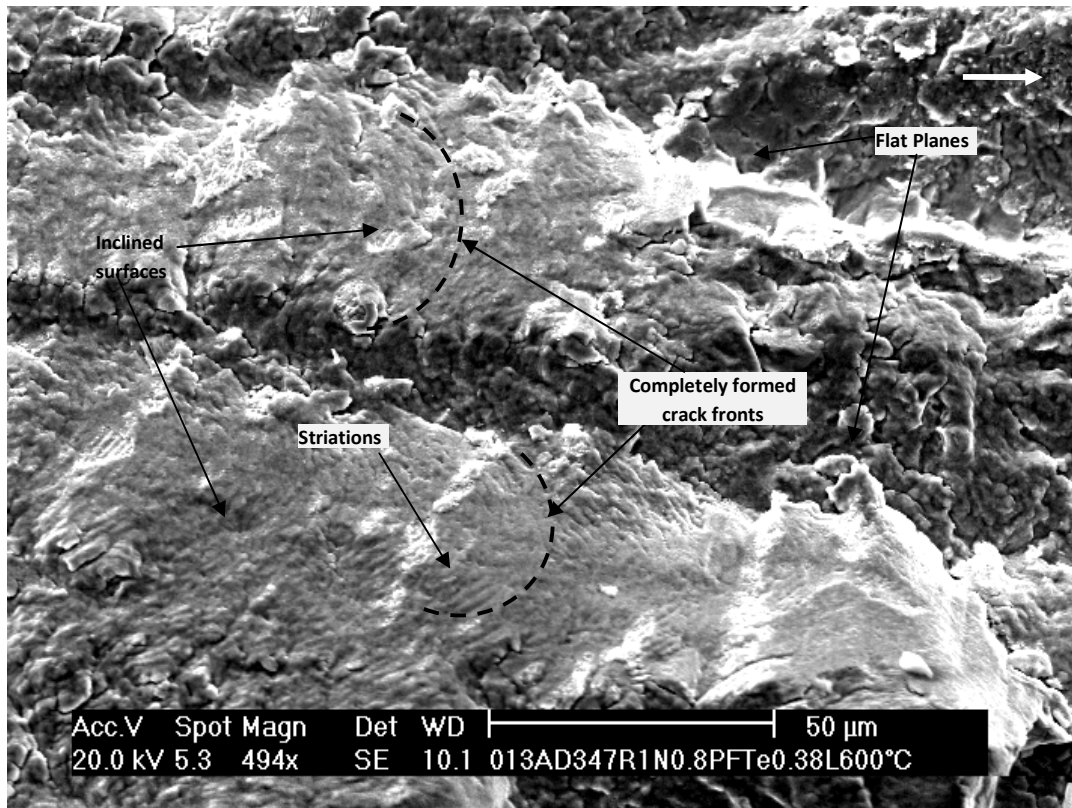


Fig 42. Multiple fully developed crack fronts in specimen tested at 600°C

During fatigue crack propagation there is considerable branching out of the plane of crack propagation. However most of this branching seems to stop at a grain boundary or a martensite lath boundary figure 43.

The crack branching is generally believed to be beneficial in reducing the fatigue crack propagation rate. The branching absorbs a part of the energy received by the main crack tip. This amount of branching was not found in specimens tested at ambient temperature. Most of the branched cracks are seen to be completely filled with an oxide layer.

At the end of the test in a 1mm specimen at 600°C a constant load was applied to determine qualitatively any presence of creep deformation. Effectively, creep deformation was observed, which created inter lath porosities. These porosities are elongated in the direction of the martensite laths, figure 44.

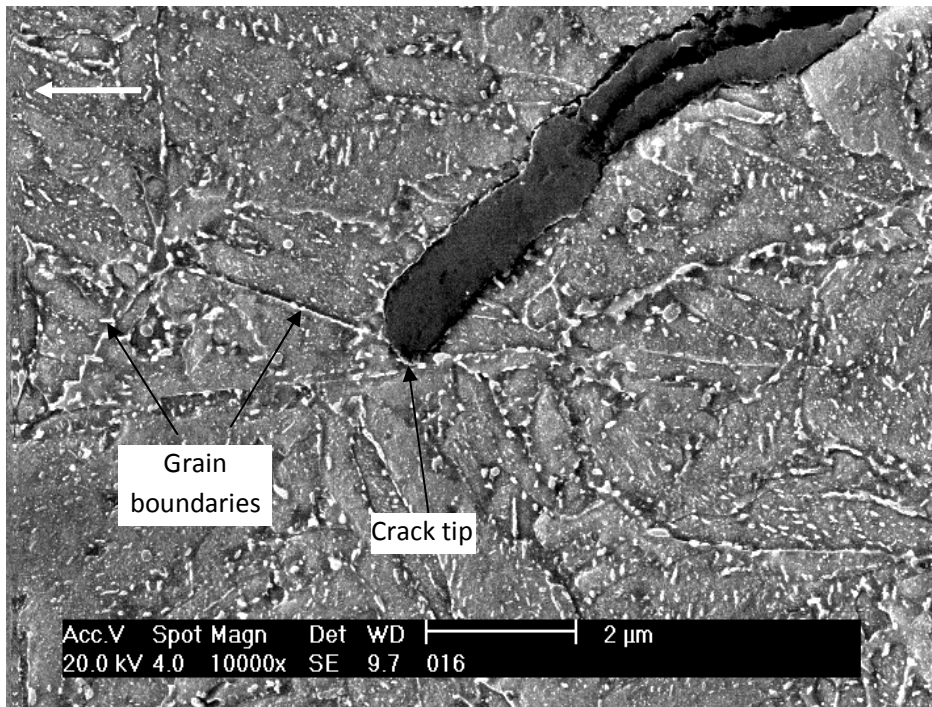


Fig 43. Crack arrest on branched crack fronts at grain boundaries in specimen tested at 600°C

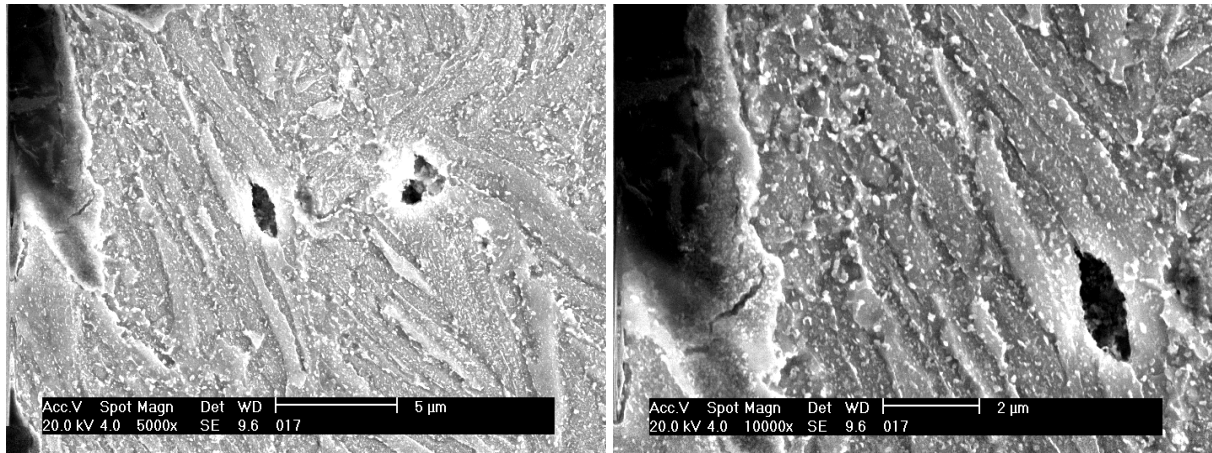


Fig 44. Evidence of porosities created by creep deformation ahead of crack tip at 600°C

IV. CONCLUSION

In this section the results of fatigue crack propagation experiments are presented. The specimens have been tested at ambient temperature and at 600°C. In addition to fatigue crack propagation some experiments of critical stress intensity factor are carried out at ambient temperature. Fractographic analysis of specimens tested at ambient temperature and 600°C are been presented.

The effect of R ratio on fatigue crack propagation is studied. It is seen that at room temperature the increase in R ratio causes an increase in the speed of crack propagation. This is usually explained by the presence of crack closure at lower R ratios. The effect of crack closure is more thoroughly discussed in chapter 5. At higher temperatures the effect of R ratio on crack propagation is different in the threshold region and the Paris region. In the stable crack regime there is almost no effect of R ratio. This is due to the absence of crack closure at elevated temperatures in this regime of propagation. However, there is a strong effect on the threshold values. At higher R ratios the threshold values are reduced. It shows that in the threshold regime a strong crack closure effects exist. The threshold values are found to be around 12 MPa.m^{1/2} for R = 0.1 and 8 MPa.m^{1/2} for R = 0.7 at 600°C. This effect of variation in threshold values seems to increase with a decrease in the specimen thickness. Intermediate temperature of 300°C simply causes an increase in the crack propagation rate, but no effect on the threshold value is observed under the experimental conditions investigated. The threshold values for ambient temperature have not been established. Crack propagation is seen at SIF values as low as 3.5 MPa.m^{1/2}.

The effect of thickness on fatigue crack propagation has been studied. In general it is found that the crack propagation speed is reduced with a subsequent reduction in the specimen thickness. This effect exists for both ambient temperature and elevated temperature. However at ambient temperature it seems that below 0.6mm thickness this effect diminishes. The threshold values at 600°C seem to increase with the decrease in thickness especially for R = 0.1. The reduction of specimen thickness from 0.6mm to 0.4mm causes a very sharp increase in ΔK_{th} .

Experiments carried out at ambient temperature to determine the K_c have yielded some interesting results. The specimens of 2.5mm thickness tested at ambient temperature show a constant K_c independent of the crack length to width ratio. However with a reduction in thickness to 1.0mm the K_c value increases sharply and becomes dependent on the crack length to width ratio. This may indicate that the SSY conditions that may have existed in 2.5mm thickness no longer exists and the plastic zone evolves with an increase in the crack length, causing an increase in K_c . For the 0.6mm thickness specimen the a/W dependence is even stronger and the increase in the K_c value is even more pronounced.

V. REFERENCES

1. Paris, P.C. and F. Erdogan, *A critical analysis of crack propagation laws*. Journal of basic engineering, 1963. **85**: p. 528-34.
2. Bergner, F. and G. Zouhar, *On the factors affecting the propagation of long fatigue cracks in thin-sheet wrought aluminium alloys*. International Journal of Fatigue. **25**(9-11): p. 885-889.
3. Elber, W., *Fatigue crack closure under cyclic tension*. Engineering Fracture Mechanics, 1970. **2**(1): p. 37-44, in3-in4, 45.
4. Skorupa, M. and A. Skorupa, *Experimental results and predictions on fatigue crack growth in structural steel*. International Journal of Fatigue, 2005. **27**(8): p. 1016-1028.
5. Kujawski, D., *Enhanced model of partial crack closure for correlation of R-ratio effects in aluminum alloys*. International Journal of Fatigue, 2001. **23**(2): p. 95-102.
6. Kirby, B.R. and C.J. Beevers, *Slow fatigue crack growth and threshold behaviour in air and vacuum of commercial aluminium alloys*. Fatigue & Fracture of Engineering Materials & Structures, 2007. **1**(2): p. 203-215.
7. King, J.E., *Surface damage and near-threshold fatigue crack growth in a Ni-base superalloy in vacuum*. Fatigue & Fracture of Engineering Materials & Structures, 2007. **5**(2): p. 177-188.
8. Suresh, S., *Fatigue of materials*. 1998: Cambridge Univ Pr.
9. Standard, A., *E647, Standard Test Method for Measurement of Fatigue Crack Growth Rates*. Annual Book of ASTM Standards: p. 615–657.
10. Standard, A., *E399-90*. Standard test method for plane strain fracture toughness of metallic materials. Annual book of ASTM Standards. **3**.
11. Schijve, J., *Fatigue of structures and materials in the 20th century and the state of the art*. Materials Science, 2003. **39**(3): p. 307-333.
12. Shahani, A.R., et al., *Experimental and numerical investigation of thickness effect on ductile fracture toughness of steel alloy sheets*. Engineering Fracture Mechanics.
13. Bruckel, P., *Oxydation de l'Acier à Outils X38CrMoV5 à 600-700°C et en présence de vapeur d'eau*. 2003, Thesis Ecole des Mines de Paris.
14. Makhlouf, K. and J.W. Jones, *Near-threshold fatigue crack growth behaviour of a ferritic stainless steel at elevated temperatures*. International Journal of Fatigue, 1992. **14**(2): p. 97-104.

Chapter 5: Modelling of Fatigue Crack Propagation Criteria

Résumé en Français	125
I. Introduction.....	127
II. Effect Of R Ratio.....	129
III. Damage Parameter: Crack Opening Displacement	139
IV. Application of Δ CTOD Criterion on Fatigue Crack Propagation	147
V. Critical Analysis Of The Crack Driving Force Models	162
VI. Conclusion	167
VII. References.....	168

RESUME EN FRANÇAIS

Ce chapitre présente la modélisation empirique et analytique réalisée pour établir un critère de propagation de fissure. La durée de vie d'un matériau sollicité par un chargement en fatigue comprend plusieurs étapes :

1) Amorçage

- évolution de la microstructure entraînant l'endommagement permanent,
- formation de microfissures,
- croissance et coalescence des microfissures,

2) La propagation

- propagation stable des macrofissures,
- rupture brutale ou propagation instable.

L'initiation de l'endommagement par fatigue est principalement traitée par « l'approche de durée de vie totale ». Cette dernière peut être basée sur la contrainte cyclique appliquée (Courbes S-N utilisées en HCF) ou la déformation cyclique appliquée (Fatigue oligocyclique).

La partie « propagation » de la durée de vie est très souvent traitée par « l'approche de tolérance au défaut » pendant laquelle, le matériau est considéré comme endommagé ou contenant un défaut de petite taille (en général la résolution minimum du moyen de détection de défaut est considérée comme la taille de ce défaut). Les contraintes cycliques appliquées pour caractériser la propagation sont souvent inférieures à la limite élastique du matériau. Quand la fissure atteint une longueur prédéterminée (longueur critique de la fissure a_c ou la ténacité K_{IC}), on considère alors que le matériau a atteint sa durée de vie.

La prédiction de la propagation de fissure est faite avec des lois empiriques décrivant la croissance de fissure basées sur la mécanique linéaire de la rupture (LEFM). Ces lois sont en général appliquées dans les conditions de SSY ou « Small Scale Yielding ». Dans ces conditions la zone plastique autour de la pointe de fissure est relativement petite (par rapport à la longueur de la fissure ou à la taille de la structure qui contient la fissure) et est bien confinée par une zone du matériau élastiquement déformée.

Lorsque les charges appliquées sont assez fortes pour déformer plastiquement le matériau, les critères utilisés pour prédire la propagation se basent plutôt sur la mécanique élasto-plastique de la rupture (EPFM). Le critère utilisant l'intégrale J est très souvent utilisé à cet effet. Bien que l'intégrale J ait été développée pour un matériau élastique non linéaire, son application pour caractériser la propagation de fissure dans un matériau élasto-plastique a été réalisée avec succès dans de nombreux travaux.

La dernière étape dans la durée de vie d'un matériau est la rupture brutale ou la propagation instable qui se caractérise par la ténacité K_{IC} ou J_{IC} .

Dans la durée de vie d'un outillage de mise en forme à chaud toutes les étapes précédentes peuvent exister. Les matériaux massifs sont très souvent caractérisés sous fatigue oligocyclique. Par contre, comme il a été indiqué dans le chapitre 1, l'approche développée pour caractériser l'endommagement des surfaces des outillages requiert des éprouvettes de faible épaisseur. Il est difficile de caractériser les matériaux minces en contraintes de compression (fatigue oligocyclique) à cause des problèmes de flambage. Nous avons donc décidé de caractériser les matériaux minces en se basant sur la mécanique linéaire et la mécanique élasto-plastique de la rupture. Dans un premier temps, seule la partie propagation de durée de vie en fatigue des surfaces des outillages sera étudiée.

Les paramètres de l'étude de l'endommagement sont :

- échelle
 - effet de l'épaisseur,
- conditions d'essais
 - effet du rapport de charge R ,
 - effet de la température.

Le but de la modélisation de la propagation peut consister à :

- trouver un critère d'endommagement en fatigue indépendant de l'échelle ou des conditions d'essais,
- trouver un critère (ou paramètre) qui soit utile pour rationaliser les courbes de propagation des différents essais par une fonction unique qui tient compte de l'échelle ou/et des conditions d'essai.

La rationalisation de l'effet de R a été réalisée par la correction de la fermeture de fissure à $R = 0,1$. Une méthode de rationalisation mathématique est aussi présentée en considérant que la propagation est un effet combiné de ΔK et de K_{max} . Il a été démontré que l'ouverture de la fissure est un critère efficace permettant de rationaliser l'effet de R .

L'effet de la variation de température sur la propagation de fissure a été analysé en utilisant le critère de l'ouverture en pointe de la fissure (CTOD) et l'intégrale J déterminée à partir de l'ouverture en pointe de fissure.

Le développement mathématique d'un critère (indépendant de R) basé sur l'ouverture de fissure est exposé. Ce critère a servi pour modéliser la propagation de fissure à chaud.

Une analyse critique des différents critères utilisés est reportée à la fin de ce paragraphe.

I. INTRODUCTION

This chapter presents the empirical and analytical modelling used for establishing damage criteria. The total fatigue life of materials is considered to consist of several stages [1]:

1) Initiation

- Microstructural changes which cause permanent damage.
- Microscopic crack formation.
- Coalescence and growth of microscopic cracks into macroscopic cracks also called 'dominant' cracks.

2) Propagation

- Stable crack propagation of the dominant crack(s).
- Complete failure or structural instability.

The fatigue damage initiation is mainly dealt with the "total-life approaches", which are based on the cyclic stress range (S-N curve generally applied in High Cycle Fatigue or HCF) method or the applied strain range (Low Cycle Fatigue or LCF) methods. Generally, the LCF testing has an appreciable amount of plastic deformation, tensile and compressive, applied on smooth specimens. The LCF testing is very often used to characterise in many circumstances the damage properties of hot work tool steels at different temperatures[2, 3]. The life of the tool material is represented (number of fatigue cycles) as a function of a fixed cyclic deformation.

The propagation mode of the fatigue damage is dealt under the "defect-tolerant approach". In this approach the material is either always inherently flawed or a small size defect has been detected in the material. Cyclic stresses are applied on the material, usually but not always within the elastic limits of the material [1]. Whenever the crack propagation of the material under study reaches a certain predetermined length (may be defined by critical crack length a_c or fracture toughness K_{IC}) the material or component is said to have achieved the service life N_f .

The prediction of crack propagation is based on empirical crack growth laws based on the fracture mechanics approach. The linear elastic fracture mechanics approach or LEFM is used in crack propagation laws applicable in the small scale yielding (SSY) conditions where the crack length and the component size is much larger than the crack tip plastic zone, and where predominantly elastic loading condition prevails. The elastic plastic fracture mechanics or EPFM approach is used when there is crack propagation under considerable plastic deformation. The approach in general involves the use of the J-Integral [4]. Even though the J-Integral is derived using the monotonic non linear elastic model it has been experimentally successfully applied to elastic-plastic fatigue crack growth [1, 5, 6] and the parameter itself has been proved to be mathematically viable (path independent) for Dugdale type crack where extensive plastic deformation occurs [7-9].

The final stage of the material damage is the unstable rupture of the material which is often characterised by a critical value of fracture toughness K_{IC} or J_{IC} .

In the life of a hot-work tool steel all the stages described above exist. The bulk materials are most often characterised using the low cycle fatigue damage criterion. This however, involves the use of large compressive stresses and strains applied on the specimen. As described in chapter I, the approach used in the modelling of the surface damage of tool steels was to use a very thin layer of un-deformed material taken from the tool material, which is to be considered characteristic of the material exposed to damaging conditions. The characterisation of a very thin material by LCF is very difficult from a practical standpoint, as high compressive stresses in such a material cause buckling of the specimen. It was thus decided to consider using the fracture mechanics approach to characterise, as a first measure, only the crack propagation component of the fatigue life of the tools surface.

Two main variables have been studied for the fatigue crack propagation characterisation:

- Scale
 - Effect of thickness.
- Testing conditions
 - Effect of R ratio.
 - Effect of temperature.

The goal of modelling the fatigue crack propagation parameter may involve several approaches:

- Find a fatigue crack propagation criterion independent of scale or testing conditions.
- Determine a criterion that consolidates all the test results onto a single function taking into account scale or testing conditions or both.

The parameter modelling in this study is mainly carried out for the testing conditions like load ratio R and temperature. Whereas the effect of scale has been limited to its effect on FCGR results and is discussed in detail in chapter 4.

II. EFFECT OF R RATIO

The increase in R ratio is in general considered to increase the crack propagation rate for a given ΔK value. Two methods have been identified to consolidate the different crack propagation curves.

One method is based on the physical aspects of the effect of R ratio [10]. This involves the effect of crack closure which is higher at lower values of R (typically $R=0.1$) and diminishes to no closure at higher R values (typically $R=0.7$). Due to the closure effects the crack is shielded from the applied load during a part of the loading cycle even under tensile loads. This shielding causes a reduction in the applied ΔK . A reduction in the applied ΔK causes an apparent decrease in the crack propagation rate. The ΔK for which the crack is shielded may be subtracted from the applied total ΔK to consolidate the results.

The other method is principally empirical and mathematical proposed by Kujawski et al [11]. It is considered that the crack propagation rate is no longer a unique function of the stress intensity factor range ΔK , but a combined function of the ΔK and K_{max} . The author has explored many possible data consolidation techniques [11-14] of which the generalized form seems to be the most adapted to our work [11].

II.1 Data consolidation of R ratio effect based on crack closure

The effect of R ratio on the fatigue crack growth rate in the Paris regime is an apparent decrease in the crack propagation rate with a decrease in the R ratio, figure 1.

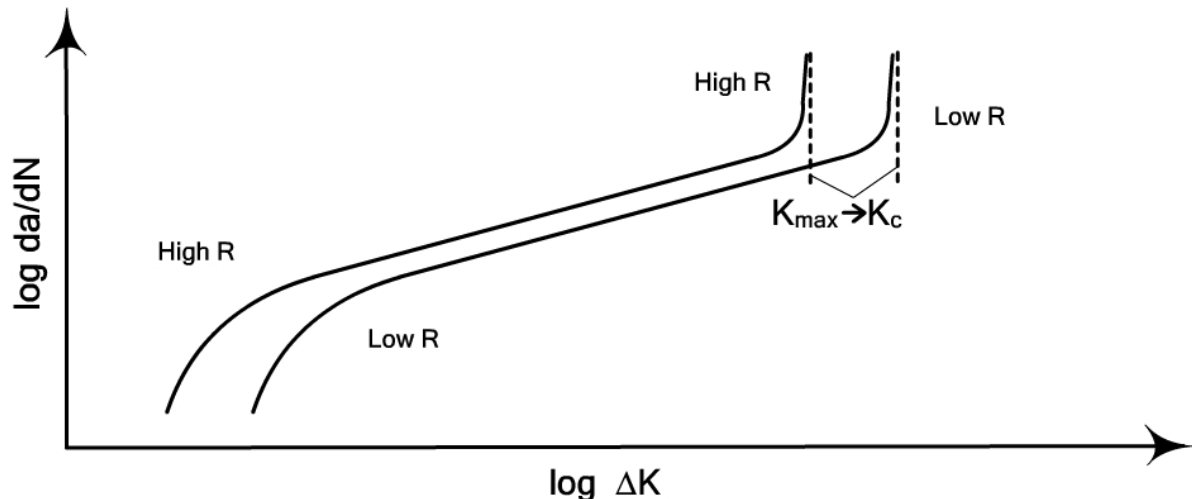


Fig 1. Effect of R ratio on the crack propagation speed of ductile materials, after Suresh [1]

This reduction in the crack propagation speed may be explained by the reduction in the applied stress intensity factor range (ΔK) due to crack closure. Figure 2 represents the relationship between applied load and the COD measured by strain gauges. Here the line OE represents the

strain gauge response if there was no crack in the specimen. The response is elastic depending on the Young's modulus of the material. However when there is a presence of the crack, the region A-B represents a constant slope on a σ - δ plot. At point B the crack starts to close, which increases the specimen's stiffness. Approaching C, the stiffness keeps on increasing due to increase in the length of the closed crack. At point C it is considered to be completely closed and region C-D behaves like a solid specimen without crack. It could be noted that traditionally the σ - δ plot is presented as a P- δ plot (load-displacement plot instead of stress displacement plot). However, in this study different thickness specimens are used and the use of σ allows us to normalise all the data on a common base.

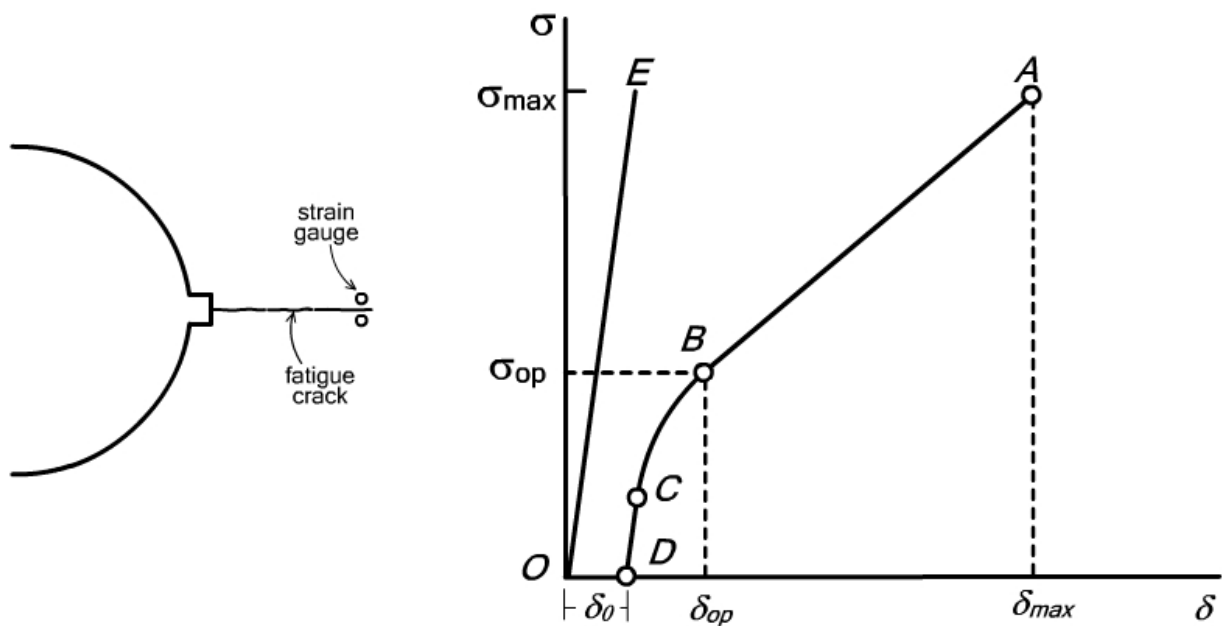


Fig 2. Relationship between applied stress and crack opening displacement measured by strain gauges [1, 10]

The stress at point B is to be considered the crack opening stress σ_{op} . Any stress range below σ_{op} has no effect on the crack tip, because the material in front of the crack tip is completely shielded. The compliance plot in figure 2 may be represented as a function of K instead of σ .

The shielding of the crack tip by closure has a direct effect on the applied stress intensity factor range ΔK . Without closure, ΔK is given by:

$$\Delta K = \Delta\sigma\sqrt{\pi a} \cdot f(a/W); \quad \Delta\sigma = \sigma_{max} - \sigma_{min} \quad (1)$$

Where, σ_{min} corresponds to the stress at point D. But as explained above the crack tip is shielded for all stresses between point B and D. An effective stress range is defined for which the crack tip is "exposed" to the loading cycle, which can be used to define an effective stress intensity factor range [10], equation 2:

$$\Delta K_{eff} = \Delta \sigma_{eff} \sqrt{\pi a} \cdot f(a/W); \quad \Delta \sigma_{eff} = \sigma_{max} - \sigma_{op} \quad (2)$$

In practice it is observed that tests carried out at $R = 0.1$ show the effects of closure while those carried out at $R = 0.7$ show no crack closure, in which case $\Delta \sigma_{eff} = \Delta \sigma$. The value of K corresponding to σ_{op} is called K_{op} . Using the K_{op} and K_{max} an effective R may be defined or R_{eff} defined as:

$$R_{eff} = K_{op}/K_{max} \quad (3)$$

The results applied on the tests carried out on specimens of 0.6mm thickness at 20°C are presented here. However, the complete procedure and the symbols used are explained first.

$\Delta \delta_{eff}$ is the actual crack opening displacement range (COD) measured by the virtual extensometer. In case there is crack closure then it is taken as the displacement for the completely open crack only. Figure 3 and 4 explain this concept.

$\Delta \delta_{max}$ is maximum possible crack opening displacement (COD) measured by the virtual extensometer if no crack closure exists. In the case where there is no crack closure $\Delta \delta_{max}$ is the same as $\Delta \delta_{eff}$, see figure 5. In case crack closure does exist then the linear part of the unloading curve is extended (linearly) to the point of minimum stress, figure 3 and 4. The total linear + extrapolated linear crack opening displacement is defined as $\Delta \delta_{max}$.

The figure 3 presents the crack opening displacement (COD) for a crack length of 4.8mm in a specimen of 8.0mm width. The virtual extensometer here is placed 0.6mm behind the crack tip. The COD measurements are experimentally carried out between σ_{max} and σ_{min} (so as not to disturb the fatigue experiment). The value of COD at zero load is not accessible, thus the absolute value of δ_0 is arbitrary. However, the difference values like; $\Delta \delta_{eff}$, $\Delta \delta_{max}$, etc have physical sense and represent the real displacement of the virtual extensometer as a response to stress range $\Delta \sigma = \sigma_{max} - \sigma_{min}$. The crack opening data for other crack lengths and specimens is given in appendix E.

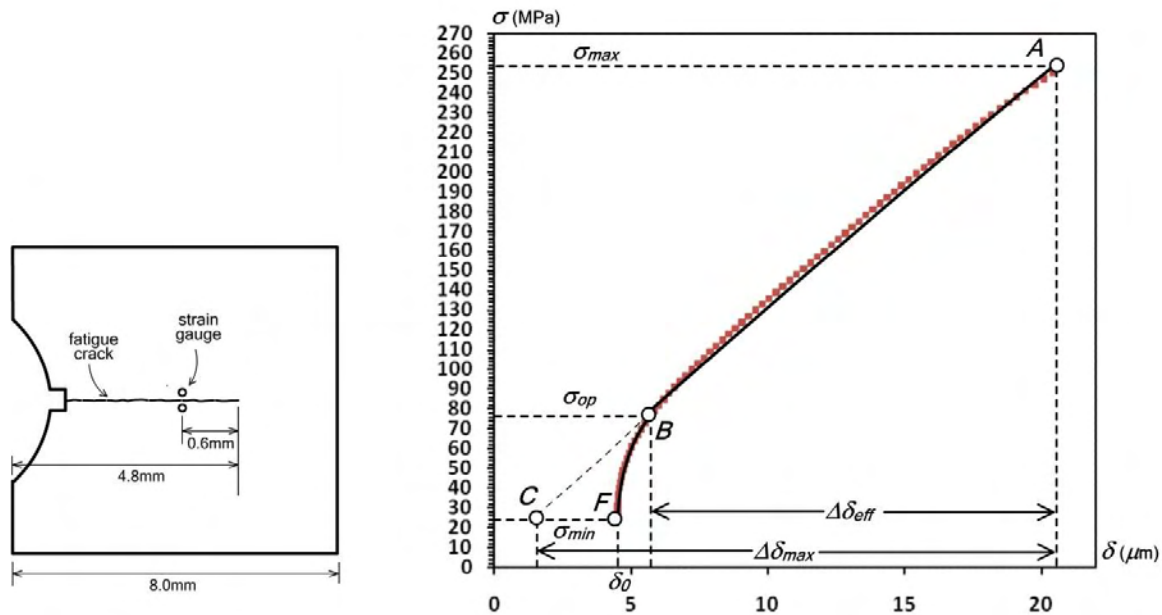


Fig 3. Relationship between applied stress and crack opening displacement measured by a virtual extensometer

In figure 3 the region A-B represents the linear variation of the COD with respect to applied stress. It is an unloading curve. From point B we can see the crack closure begins to appear, right upto point F. The crack opening displacement corresponding to A-B is given by $\Delta\delta_{\text{eff}}$. This is a tension-tension test with $R = 0.1$ the $\sigma_{\text{max}} = 250$ MPa and $\sigma_{\text{min}} = 25$ MPa. From the figure 3 (Point B) the $\sigma_{\text{op}} = 75$ MPa. From here we can calculate the ΔK_{eff} or R_{eff} [10] from equations 2 and 3. For this specific case R_{eff} is found out to be 0.3. In practice it is easier to present the crack opening displacement as a function of time or number of images if a triangular load signal is used figure 4. In reality the figure 4 is the same as figure 3 rotated 90° counter-clockwise. The advantage is that the untreated values measured by the machine and the extensometer may be used directly to calculate the $\Delta\delta_{\text{eff}}$, δ_{op} and $\Delta\delta_{\text{max}}$. If there were no closure present then the straight line A-B would continue to point C corresponding to σ_{min} , figure 3. Thus the line A-B-C represents the extrapolated crack opening for no closure the magnitude of which is given by $\Delta\delta_{\text{max}}$.

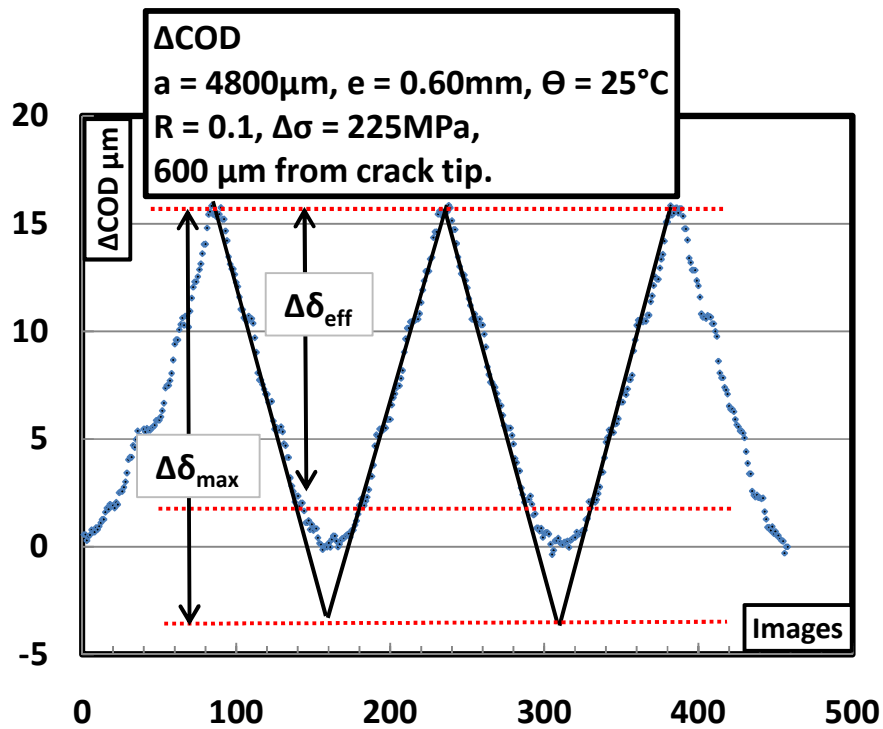


Fig 4. Variation of δ (COD) as a function of a number of images during fatigue cycles in a specimen of 0.6mm tested at $R=0.1$ showing crack closure

This same procedure of COD measurement is applied on the same type of specimen tested at $R = 0.7$. Under $R = 0.7$ no crack closure is detected as shown in figure 5. In most of the cases 5 virtual extensometers are placed at 200 μm intervals behind the crack tip. However according to the conditions of the experiment more extensometers (further from or nearer to crack tip) may be added. The effect of using ΔK_{eff} as a fatigue crack propagation criterion is shown in figure 6. The specimens are of 0.6mm thickness tested at 25°C at two different R values of 0.7 and 0.1. The crack closure measurements were carried out throughout the crack propagation (for all crack lengths, see appendix E).

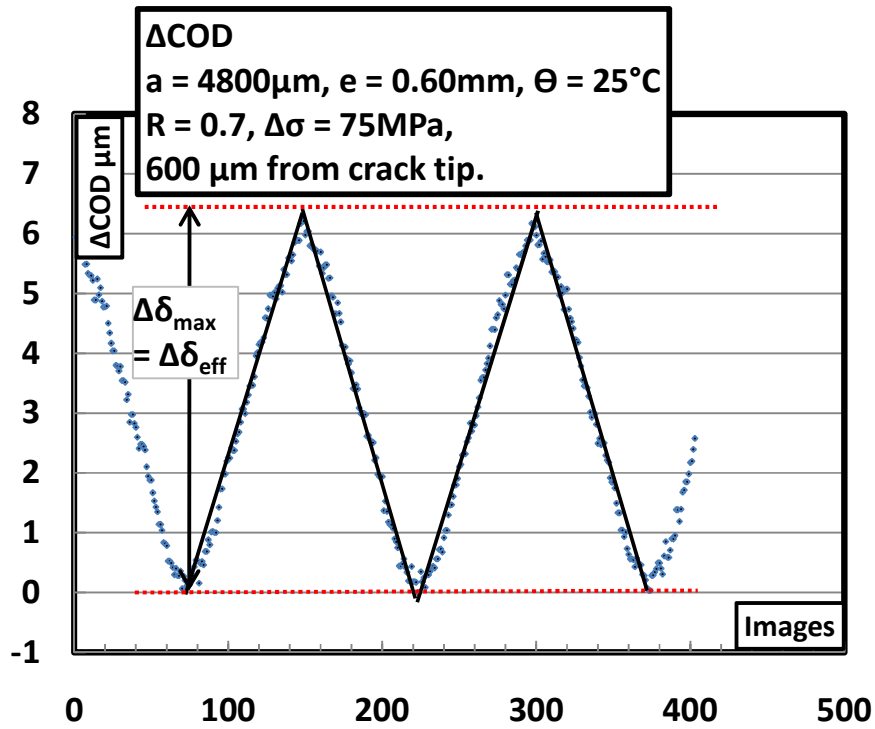


Fig 5. Variation of δ (COD) as a function of a number of images during fatigue cycles in a specimen of 0.6mm tested at $R=0.7$ showing no crack closure

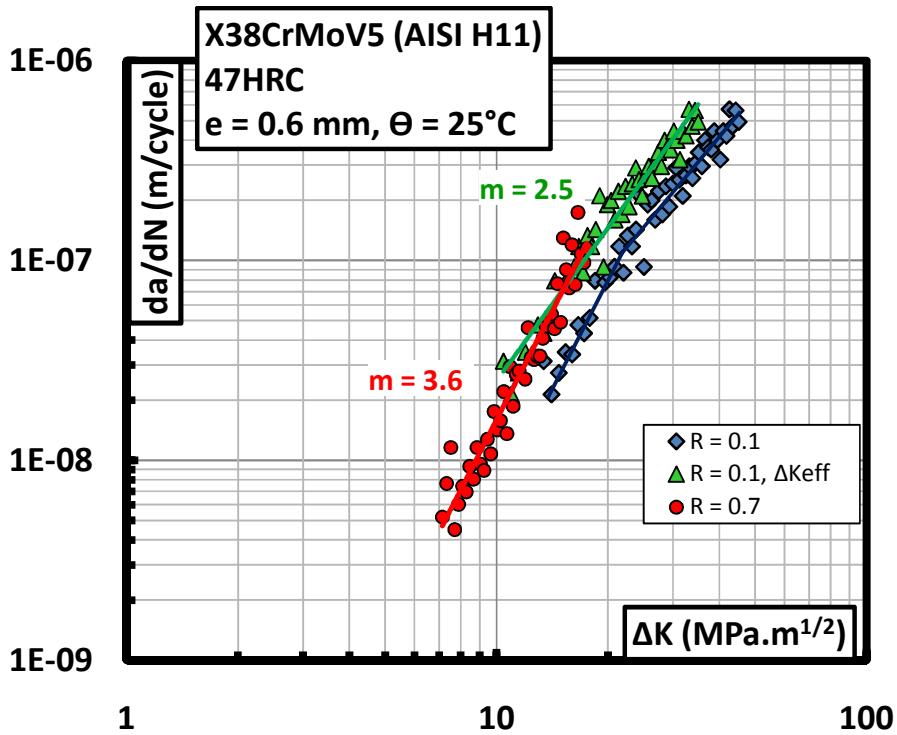


Fig 6. Effect of using ΔK_{eff} of Paris curve for $R=0.1$ in a 0.6mm specimen at 25°C

ΔK_{eff} correction makes the two curves overlap, however, the slope of the two curves is distinctly different with:

$$R = 0.1; \quad m = 2.5$$

$$R = 0.7; \quad m = 3.6$$

Here it is pertinent to note that the FCGR curve at $R=0.1$ using ΔK as crack driving force parameter shows two distinct slopes (Discussed in more detail in the section 1.2 Chapter 4). For lower ΔK it is parallel to the FCGR curve of $R = 0.7$ i.e. $m = 3.6$ however, for higher ΔK the slope reduces to $m = 2.2$. The final slope after application of the ΔK_{eff} criterion gives an averaged slope of $m = 2.5$.

II.2 Consolidation of R ratio effect based on a “two parameter crack driving force”

In a propagating fatigue crack, the crack closure phenomenon may be present due to many reasons. They include but are not limited to, plasticity, crack wake roughness, oxide formation on crack faces, debris [1] etc. Any correction for the effects of variation in R based on the crack closure mechanism assumes that as soon as the crack begins to close it is fully shielded from the applied load. However this is not always true in reality. In practice the crack closure does not always account for the difference in crack propagation curves due to variation in R ratio[13].

Problems associated with the crack closure based models have been reviewed by Kujawski et al. [13]. To account for the R ratio effects, many different models have been presented based on closure, residual compressive stresses, environmental influence and the partial crack closure [1, 13].

The data consolidation model presented here removes the need for taking into account the crack closure phenomenon. The model is based on the proposition made by Walker [15] reviewed by Kujawski [11] according to which there is a close similarity between fatigue life corresponding to crack initiation and that of fatigue crack propagation behaviour. He showed that an effective stress based on maximum stress and the applied varying stress range:

$$\bar{\sigma} = \sigma_{\text{max}}^{(1-m)} \Delta\sigma^m \quad (4)$$

was able to correlate the effects of R ratio on fatigue life (crack initiation) in 7075-T6 and 2024-T3 aluminium alloys. In this approach m is considered to be a material property. The equation 4 may be modified and adapted to the fatigue crack growth correlation:

$$\bar{K} = K_{\text{max}}^{(1-m)} \Delta K^m = (1 - R)^m K_{\text{max}} \quad (5)$$

Where, \bar{K} is an effective stress intensity range used to demonstrate the consolidation of fatigue crack propagation data for positive R ratios:

As discussed above the effect of R ratio may be due to many different reasons which are not necessarily dependent on the material properties. Thus the m in equation 5 may be replaced by α . The α is used to normalise the crack propagation curves at different R values. The equation 5 then takes the form [11]:

$$\bar{K}^* = (K_{max})^\alpha (\Delta K)^{1-\alpha} \quad (6)$$

Where $0 \leq \alpha \leq 1$ is a parameter that characterises the apparent sensitivity of \bar{K}^* to the applied K_{max} value. The value of α may depend on the material, temperature, environment and the dimensions of the specimen (thin or thick). The definition of \bar{K}^* is based on the assumption that:

- The damage at the crack tip is due to two simultaneous damage mechanisms based on monotonic damage due to K_{max} and cyclic damage due to ΔK .
- Existence of tensile stresses in the process zone ($K_{max} > 0$) is a necessary condition for fatigue crack propagation.

There are some interesting properties of α that may be mentioned here. In a case of very brittle material the value of $\alpha \rightarrow 1$ which shows the damage is based on K_{max} only. In the case of ductile materials with no effect of charge ratio R (like under vacuum for some materials) $\alpha \rightarrow 0$. For ductile metallic materials an intermediate value is generally found.

II.2.1 Determining α for fatigue crack

FCG data obtained on two positive load ratios, namely $R_2 \geq R_1 \geq 0$ is presented schematically in the figure 7. Now from the explanation in the preceding paragraphs we know that α is the sensitivity of the FCGR curve on K_{max} .

We know:

$$\begin{aligned} K_{max} &= \Delta K / (1 - R) \\ \bar{K}^* &= (K_{max})^\alpha (\Delta K)^{1-\alpha} \\ &= \{\Delta K / (1 - R)\}^\alpha (\Delta K)^{1-\alpha} \\ &= \Delta K / (1 - R)^\alpha \end{aligned} \quad (7)$$

For consolidating the two curves any da/dN value should lie on the same crack driving force parameter \bar{K}^* , thus:

$$\bar{K}_1^* = \bar{K}_2^*$$

$$\frac{\Delta K_1}{(1 - R_1)^\alpha} = \frac{\Delta K_2}{(1 - R_2)^\alpha} \quad (8)$$

Rearranging and taking log on both sides of equation 8 we get:

$$\alpha = \frac{\log(\Delta K_1/\Delta K_2)}{\log(1 - R_1/1 - R_2)} \quad (9)$$

An average α_{avg} may be obtained at different da/dN values along the curve and collapse the FCG data onto a thin band.

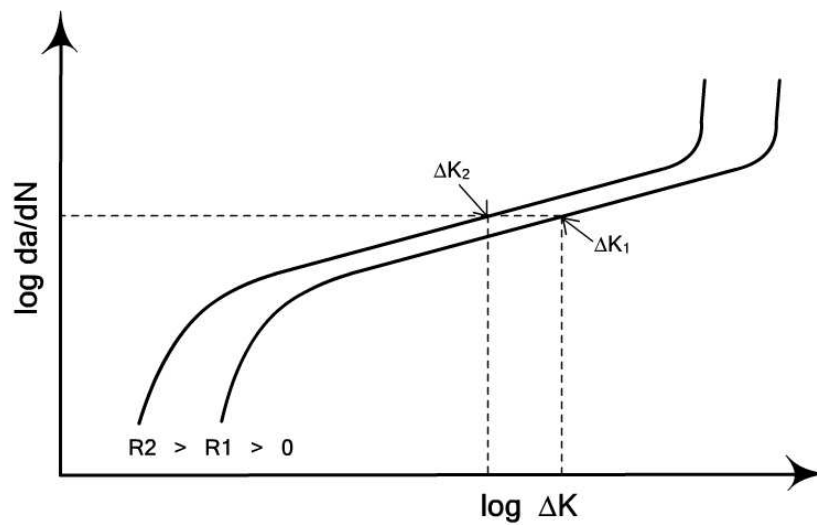


Fig 7. Schematic representation of fatigue crack growth rates at two stress ratios

II.2.2 Application on experimental data

This method of fatigue crack growth rate consolidation is applied on a specimen of 0.6mm thickness tested at $R=0.1$ and 0.7 , figure 8. The FCGR curve without consolidation is presented in figure 6. We have chosen three crack propagation rates of $da/dN = 2e-8$, $6e-8$ and $2e-7$ to determine the value of α the values of which are summarised in table 1. The two curves overlap for $2e^{-8} \leq da/dN \leq 2e^{-7}$ (m/cycle).

Table 1: Summary of α values determined for specimen 0.6mm tested at $R = 0.1$ and 0.7

da/dN	ΔK_1	ΔK_2	R_1	R_2	α
$2e^{-8}$	11.6	10.5	0.1	0.7	0.1
$6e^{-8}$	17.8	14.2			0.2
$2e^{-7}$	28.6	19.9			0.3
α_{avg}					0.2

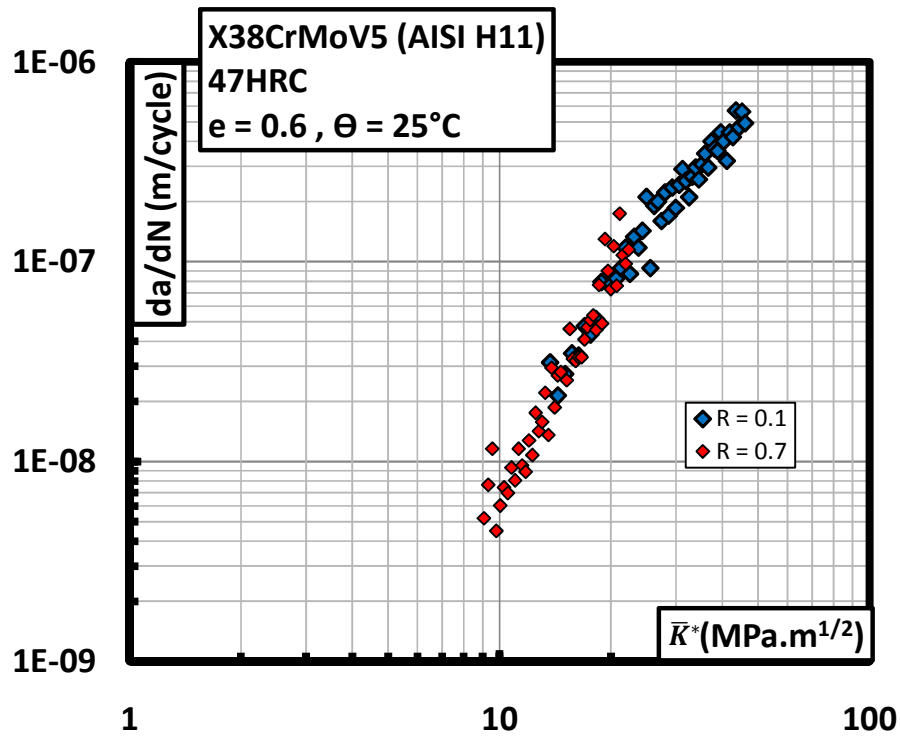


Fig 8. Consolidation of fatigue crack growth data for $R = 0.1$ and $R = 0.7$, using the \bar{K}^ parameter. Value of $\alpha = 0.2$*

Results are then similar to what was obtained after crack closure correction.

III. DAMAGE PARAMETER: CRACK OPENING DISPLACEMENT

III.1 Use of J Integral as a damage parameter

Different testing conditions like change in temperature, dimensions, charge ratio etc. may cause a change in the fatigue crack propagation behaviour of the material tested. Taking all of these into account by calculations alone is difficult and many approximations have to be made. At high temperatures, especially, the fatigue crack propagation can no more be treated using the LFM assumptions of SSY, and needs to be treated using the EPFM criterion. Dowling [5, 6] initially proposed using the J-Integral of Rice[16] as a parameter for characterising elastic-plastic fatigue crack growth.

In this procedure hysteresis curves were plotted between crack opening displacement δ and applied force in C(T) specimens. The same was done for centre crack panels by calculating the elastic component J_{el} (based on load and geometry) and adding the plastic component J_{pl} (based on load displacement curve). The methods are schematically represented in figure 9.

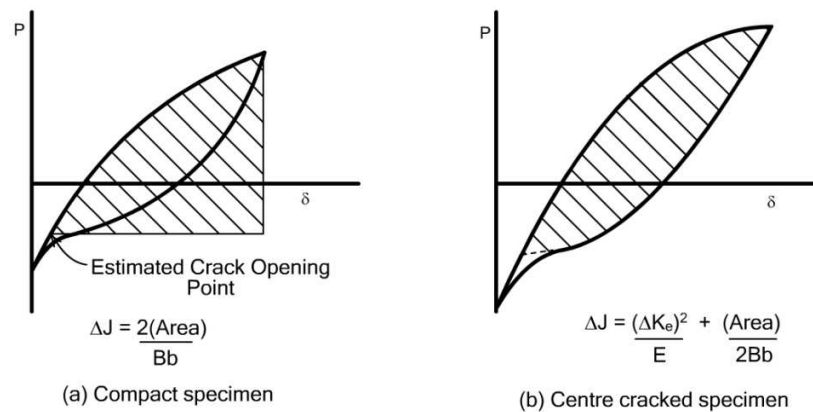


Fig 9. Definition of cyclic J calculated by using load displacement curves [6]

The method and definitions of cyclic J integral were then reviewed and analysed extensively by Chow [7]. The J – Integral used as a fatigue crack growth parameter was also presented by Sadanada [17, 18] as:

$$\frac{da}{dN} = A_1 \left(\sqrt{\Delta J_{cycl} E^*} \right)^{m_1} \quad (10)$$

This law has been extensively used in this study to characterise the fatigue crack propagation of specimens at high temperature.

III.2 Use of CTOD as a damage parameter

The J-Integral calculated by Dowling[5, 6] and Chow[7] is based on load displacement curves dependent on the geometry of the specimen. Another parameter that may be used to calculate the J-Integral is the Crack Tip Opening Displacement or CTOD which will henceforth be denoted as δ_t .

III.2.1 Bibliography: Relationship between J-integral and δ_t

The relationship between crack tip opening displacement and the J-Integral proposed by Rice[4] is extensively reviewed and treated by Shih [19] among others principally Hutchinson[20], Tracey[21], McClintock[22] and McMeeking[23]. However the model used in this study is mostly adapted from Shih[19]. The calculations are based on monotonic loading of the crack tip.

In a power law hardening material the monotonic plastic strain is related to the stress σ through the relationship:

$$\varepsilon_p = \alpha \left(\frac{\sigma}{\sigma_0} \right)^{n-1} \frac{\sigma}{E} \quad (11)$$

Where E is the young's modulus, α is a material constant, n is the hardening exponent and σ_0 is the yield stress. The equation 11 can be generalised to multiaxial stress states according to the J_2 deformation theory of plasticity which gives:

$$\varepsilon_{ij} = \frac{3}{2} \alpha \left(\frac{\sigma_e}{\sigma_0} \right)^{n-1} \frac{S_{ij}}{E} \quad (12)$$

Where S_{ij} is the stress deviator and the equivalent stress is given by:

$$\sigma_e^2 = \frac{3}{2} S_{ij} S_{ij} \quad (13)$$

Based on the power-law description Hutchinson[20] and Rice and Rosengren[4] showed that the stress and strain fields in the vicinity of the crack are:

$$\begin{aligned} \sigma_{ij} &= \sigma_0 \left(\frac{EJ}{\alpha \sigma_0^2 I_n r} \right)^{\frac{1}{n+1}} \tilde{\sigma}_{ij}(\theta, n) \\ \varepsilon_{ij} &= \frac{\alpha \sigma_0}{E} \left(\frac{EJ}{\alpha \sigma_0^2 I_n r} \right)^{\frac{n}{n+1}} \tilde{\varepsilon}_{ij}(\theta, n) \end{aligned} \quad (14)$$

Where r, θ are polar coordinates centred at crack tip, I_n is an integration constant and $\tilde{\sigma}_{ij}$ and $\tilde{\varepsilon}_{ij}$ are dimensionless functions of the hardening exponent n, polar coordinate θ and

the state of stress i.e. plane stress or plane strain[1]. The J-Integral represents the amplitude of the HRR singularity described by equation 14.

The crack opening profile $\delta(x)$ may be presented in a similar fashion. Thus the displacements along the edge of the crack ($\theta = \pm\pi$, figure 10) are given by:

$$\frac{\delta}{2} = \frac{\alpha\sigma_0}{E} \left(\frac{E}{\alpha\sigma_0^2} \frac{J}{I_n} \right)^{\frac{n}{n+1}} \frac{1}{r^{n+1}} \tilde{u}_y(n)$$

$$u_x = \frac{\alpha\sigma_0}{E} \left(\frac{E}{\alpha\sigma_0^2} \frac{J}{I_n} \right)^{\frac{n}{n+1}} \frac{1}{r^{n+1}} \tilde{u}_x(n)$$
(14)

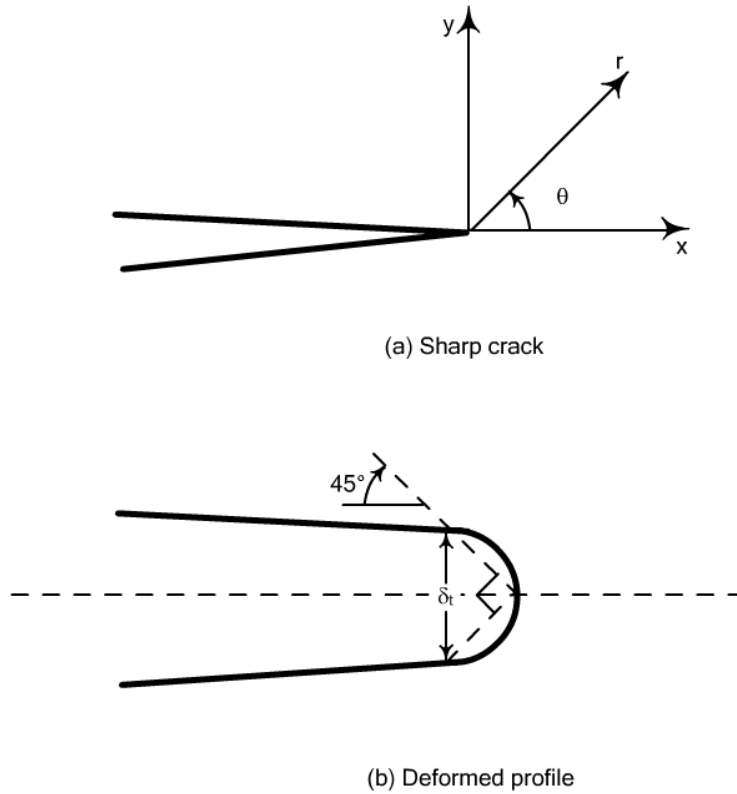


Fig 10. Sharp and deformed crack showing the 45° procedure for defining δ_t .

Where u_x and u_y are displacements in the x and y directions respectively, while $\delta = 2u_y$. The definition of δ_t suggested by Rice and reviewed by Tracey is shown in figure 10(b) [21] with two 45° lines drawn back from the crack tip with the deformed profile. Thus at the intercept:

$$r - u_x = \delta/2$$
(15)

The value of δ that satisfies equations 14 and 15 is given by [19]:

$$\delta_t = d_n \frac{J}{\sigma_0} \quad (16)$$

Where:

$$d_n = \left(\frac{\alpha \sigma_0}{E} \right)^{\frac{1}{n}} (\tilde{u}_x + \tilde{u}_y)^{\frac{1}{n}} \frac{\tilde{\delta}}{I_n} \quad (17)$$

$$\tilde{\delta} = 2\tilde{u}_y$$

Rice and Schwalbe have also presented the relation in a similar fashion, reviewed by Shih[19]:

$$\delta_t = 2Y \frac{K^2}{E\sigma_0} \left[\frac{\gamma_0(X+Y)}{0.0116} \right]^{\frac{1}{n}} \quad (18)$$

Where X and Y are values of u_x and $\delta/2$ at $r = 0.0077K^2/\sigma_0^2$ and γ_0 is the shear yield strain. Another relation, suggested by Tracey [21] is:

$$\delta_t = 0.49 \frac{K^2}{E\sigma_0} \lambda [(n+1)\gamma_0]^{\frac{1}{n}} \quad (19)$$

Where, $\lambda = (n+1)/n$.

This study is based principally on the use of equation 16 as a damage parameter for fatigue crack propagation. The factor d_n is a function of material properties:

$$d_n = f\left(\frac{\sigma_0}{E}, n\right) \quad (19)$$

This parameter varies slightly with σ_0/E but significantly with n . For elastic-perfectly plastic materials the value of d_n approaches 1. The evolution of d_n with respect to n and σ_0/E is shown in the figure 11.

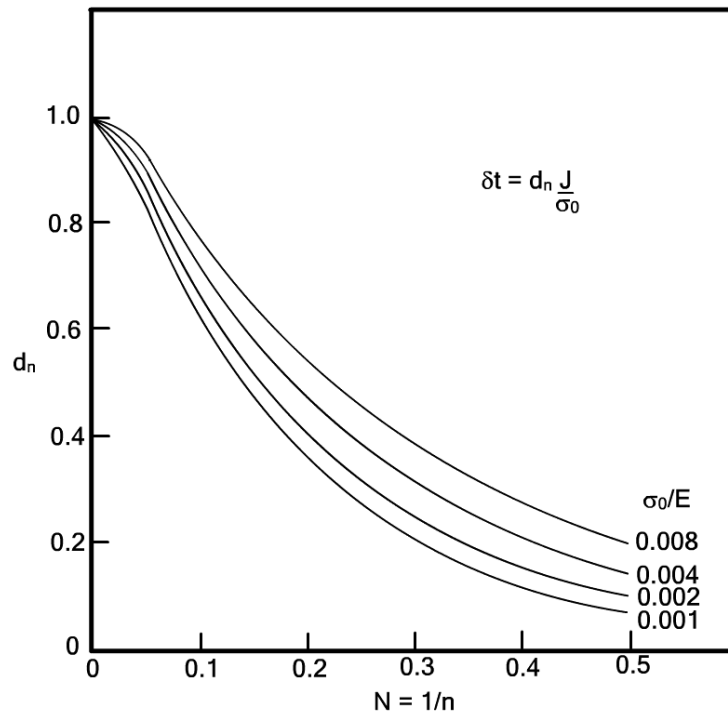


Fig 11. Variation of d_n with n and σ_0/E for plane stress [19]

III.2.2 Determination of parameters of $\delta_f = d_n(J/\sigma_0)$ for X38CrMoV5 at 20°C and 600°C

III.2.2.1 Test conditions

The model is applied on thin specimens of thicknesses of 1.0mm and 0.6mm. Some assumptions that have been made as regards to the state of stress and strain in these specimens are

- Plane stress state exists in material at 20°C and 600°C.
- There is a possibility of generalised yielding in high temperature specimens, but this is considered to be a narrow strip of material ahead of the crack tip. This configuration allows the Dugdale model to be invoked, which represents a particular condition for J-integral path independence (under Large Scale Yielding) and validity for large plastic deformations[8, 9, 19].
- All material properties used are obtained by monotonic tensile tests. The material in reality presents different properties under cyclic loading (like cyclic softening).
- At 600°C the material properties are considered to be constant. This temperature is very near the tempering temperature of this material, so tempering of the metal will occur during the test. This temperature was chosen because it is often achieved during real working conditions.

III.2.2.2 Determination of d_n

The results of monotonic tensile tests are presented in figure 12.

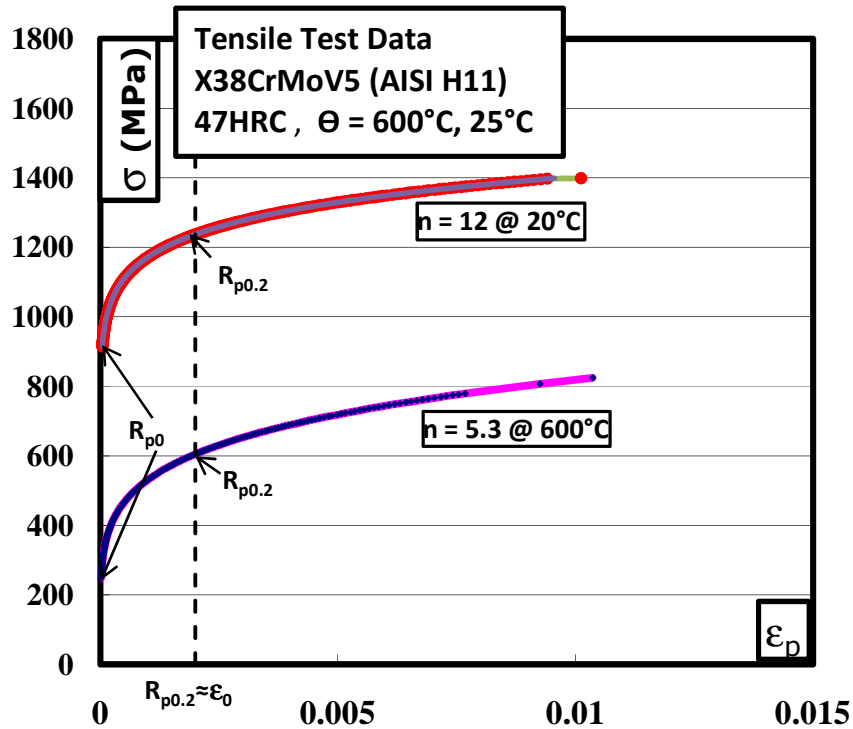


Fig 12. Monotonic tensile test stress-deformation curve for X38CrMoV5 – 47 HRC

The results are summarised in table 2. Using the values of E , $R_{p0.2} = \sigma_0$ and n one can calculate the value for d_n .

Table 2: Tensile test data for X38CrMoV5 – 47HRC

Temperature	R_{p0} (MPa)	$R_{p0.2}$ (MPa)	E (MPa)	n	d_n
20°C	913	1200	208000	12	0.8
600°C	213	600	147000	5.3	0.5

III.2.3 Adaptation of $\delta_t = d_n(J/\sigma_0)$ for fatigue crack propagation

The model presented above is basically used for the monotonic loading of the cracked specimen. However, the study has been carried out for the fatigue crack propagation. The model has to be modified in such a manner that it can deal with the following parameters:

1. Ability to calculate crack driving force from $\Delta\delta_t$. In fatigue experiments the loading is cyclic. It is in general preferable not to disturb the loading conditions during the experiment. Thus the $\Delta CTOD$ is determined for the stress range $\Delta\sigma = \sigma_{max} - \sigma_{min}$. We thus

do not have the CTOD value at unloaded specimen. The form of the crack driving force parameter becomes:

$$\Delta\delta_t = d_n \frac{\Delta J}{\sigma_0} \text{ where } \Delta\delta_t = \delta_t^{\sigma_{max}} - \delta_t^{\sigma_{min}} \quad (20)$$

2. Find a unique law that shows the $\Delta\delta_t$ to be a function of R. This is necessary to be able to compare results of crack propagation experiments at different R values.
3. Ideally be able to correlate test results of specimens tested at cold and hot temperatures.
4. Data obtained by $\Delta\delta_t$ should be comparable to some extent with the numerical simulations carried out for these specimens.

Some of the mathematical derivation will be carried out using LFM assumptions, especially for the effect of R on the crack driving force.

Under linear elastic conditions:

$$J = \frac{K_I^2}{E'} \quad (21)$$

Where E' is E for plane stress and $E/(1-\nu^2)$ for plane strain.

The definition of K_I dictates that it is linearly proportional to the applied stress, thus from equation 1:

$$\Delta K = \Delta\sigma\sqrt{\pi a} \cdot f(a/W); \quad \Delta\sigma = \sigma_{max} - \sigma_{min} \quad (1)$$

From equation 20:

$$\begin{aligned} \delta_t^{\sigma_{max}} &= d_n \frac{J_{max}}{\sigma_0} = d_n \left(\frac{K_{I_{max}}^2}{E' \sigma_0} \right) \\ \delta_t^{\sigma_{min}} &= d_n \frac{J_{min}}{\sigma_0} = d_n \left(\frac{K_{I_{min}}^2}{E' \sigma_0} \right) \end{aligned} \quad (22)$$

The expressions 22 show that ΔK depends on the square root of the $\Delta\delta_t$. Also if the charge ratio is to be taken into account (necessary to present a coherent fatigue crack propagation law):

$$R = \frac{K_{min}}{K_{max}}$$

$$\Delta K_I = K_{max} - K_{min}$$

$$\begin{aligned}
\Delta\delta_t &= d_n \left(\frac{K_{I_{max}}^2}{E' \sigma_0} \right) - d_n \left(\frac{K_{I_{min}}^2}{E' \sigma_0} \right) \\
\Delta\delta_t &= d_n \left(\frac{K_{I_{max}}^2}{E' \sigma_0} \right) - \frac{d_n}{E' \sigma_0} (RK_{I_{max}})^2 \\
\Delta\delta_t &= \frac{d_n}{E' \sigma_0} K_{I_{max}}^2 (1 - R^2)
\end{aligned} \tag{23}$$

Inversely the equation 23 may be used to calculate the stress intensity factor range from Δ CTOD denoted ΔK^δ :

$$K_{max}^\delta = \sqrt{\frac{E' \sigma_0 \Delta\delta_t}{d_n (1 - R^2)}} \tag{24}$$

$$\Delta K^\delta = (1 - R_{app}) \sqrt{\frac{E' \sigma_0 \Delta\delta_t}{d_n (1 - R^2)}} \tag{25}$$

Where,

R used to calculate the K_{max}^δ parameter
 R_{app} is any value of applied stress ratio

The interest in calculating expression 24 is that if LFM conditions prevail, K_{max}^δ can be calculated through an experiment carried out at R and then use these values to determine the ΔK^δ for any other R_{app} , where $R \neq$ or $= R_{app}$.

Now in cases where the plasticity cannot be ignored, we will replace $K_{I_{max}}^2/E'$ by J_{max} . Thus from equations 24 and 25:

$$J_{max}^\delta = \frac{\sigma_0 \Delta\delta_t}{d_n (1 - R^2)} \tag{26}$$

$$\Delta J = J_{max} - J_{min}$$

$$\Delta J^\delta = (1 - R_{app}^2) \left(\frac{\sigma_0 \Delta\delta_t}{d_n (1 - R^2)} \right) \tag{27}$$

The ΔJ^δ calculated in this manner may be used directly as a fatigue crack propagation criterion. Comparisons of this parameter measured experimentally and calculated by numerical simulations are presented in the following section.

IV. APPLICATION OF Δ CTOD CRITERION ON FATIGUE CRACK PROPAGATION

This section deals with two main aspects of the application of Δ CTOD criterion on fatigue crack propagation:

1. The method of measurement of the crack tip opening displacement.
2. Use of the measured Δ CTOD in fatigue crack propagation.

IV.1 Measurement of Δ CTOD

IV.1.1 Definition of terms

Some additional terms are defined for establishing the Δ CTOD as a criterion for fatigue crack propagation:

$\Delta\delta_t$ or crack tip opening displacement (Δ CTOD) is calculated from $\Delta\delta_{eff}$. Taking the crack tip as origin, a number of virtual extensometers at specified distances are placed around the crack. Each extensometer gives a $\Delta\delta_{eff}$ reading. Obviously the extensometer which is further away will show higher Δ CTOD values. Of interest is the Δ CTOD value. Thus all the $\Delta\delta_{eff}$ values are plotted against the position of the extensometer and extrapolated to the crack tip. The procedure is explained in figure 13.

$\Delta\delta_{th}$ is calculated from $\Delta\delta_{max}$. The exact same procedure used for the calculation of $\Delta\delta_t$ is followed while using the extrapolated $\Delta\delta_{max}$ readings from the extensometers. The procedure is explained in figure 13.

$\Delta\delta_{calc}$ is calculated via J-Integral using equations 20 and 22. The numerically calculated values of J or K_I are used directly to calculate this parameter. It is used in validating the hypothesis used in this modelling. This parameter is calculated through J-Integral obtained by numerical simulations. It is not related to the measurement procedure using virtual extensometers.

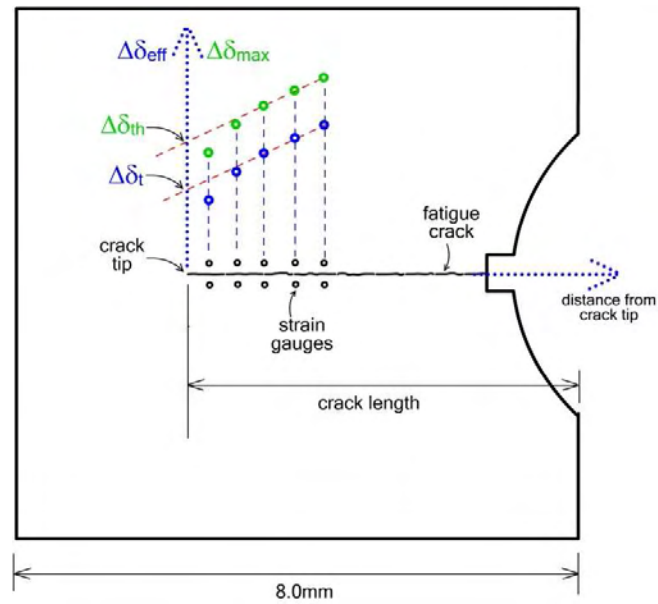


Fig. 13: Definition of terms used for CTOD criterion $\Delta\delta_{eff}$, $\Delta\delta_{max}$, $\Delta\delta_t$ and $\Delta\delta_{th}$

IV.1.2 Δ CTOD and Δ CTOD measurement

In this section the real Δ CTOD measurements for 0.6mm specimens are described for a crack length of 4.8mm in a specimen of 0.6mm thickness. The specimen is tested at a maximum stress of 250MPa with a charge ratio of 0.1. Here five extensometers are placed separated by a distance of 200 μ m. The first extensometer is also placed at a distance of 200 μ m from the crack tip. The $\Delta\delta_{eff}$ and $\Delta\delta_{max}$ measurements are made from data as presented in the figure 4. These δ values measured for the five extensometers are then extrapolated by linear fitting up to the crack tip as shown in the figure 14. The extrapolation of $\Delta\delta_{eff}$ gives $\Delta\delta_t$ and the extrapolation of $\Delta\delta_{max}$ gives $\Delta\delta_{th}$.

This procedure is further used to determine the $\Delta\delta_t$ and $\Delta\delta_{th}$ for the whole length of the crack during the crack propagation experiments.

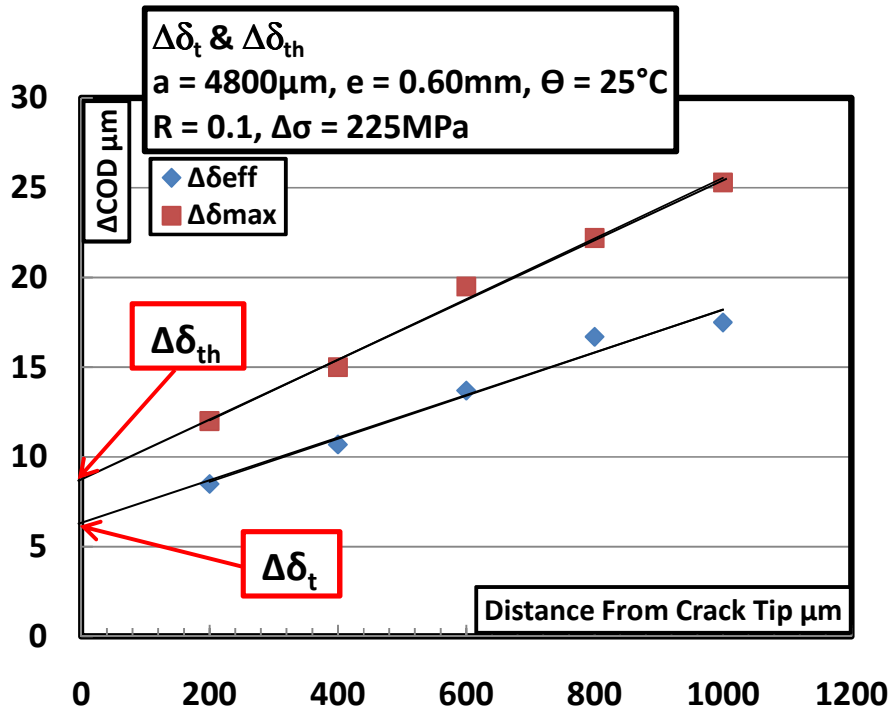


Fig. 14: Estimation of $\Delta\delta_t$ and $\Delta\delta_{th}$ with the help of $\Delta\delta_{eff}$ and $\Delta\delta_{max}$ respectively. The specimen is of 0.6mm thickness, tested at $R=0.1$ and 25°C

IV.2 $\Delta\delta_t$ and $\Delta\delta_{th}$ for specimens under different conditions

In this section are presented the CTOD values for specimens tested under conditions as given in table 3. The data presented is for the complete crack propagation from the start to the end of the experiment.

Table 3: Experimental conditions for the $\Delta\delta_t$ and $\Delta\delta_{th}$ determination

Thickness (e mm)	Temperature	R	σ_{max} (MPa)	Figures
0.6	20°C	0.1	250	15, 16
		0.7	250	17,18
0.6	600°C	0.1	250	19,2

In each the graphs presented are as follows:

1. One extensometer reading to determine presence or absence of closure
2. One graph presents $\Delta\delta_t$, $\Delta\delta_{th}$ and $\Delta\delta_{calc}$ and their corresponding mathematical function along the length of the crack during propagation.

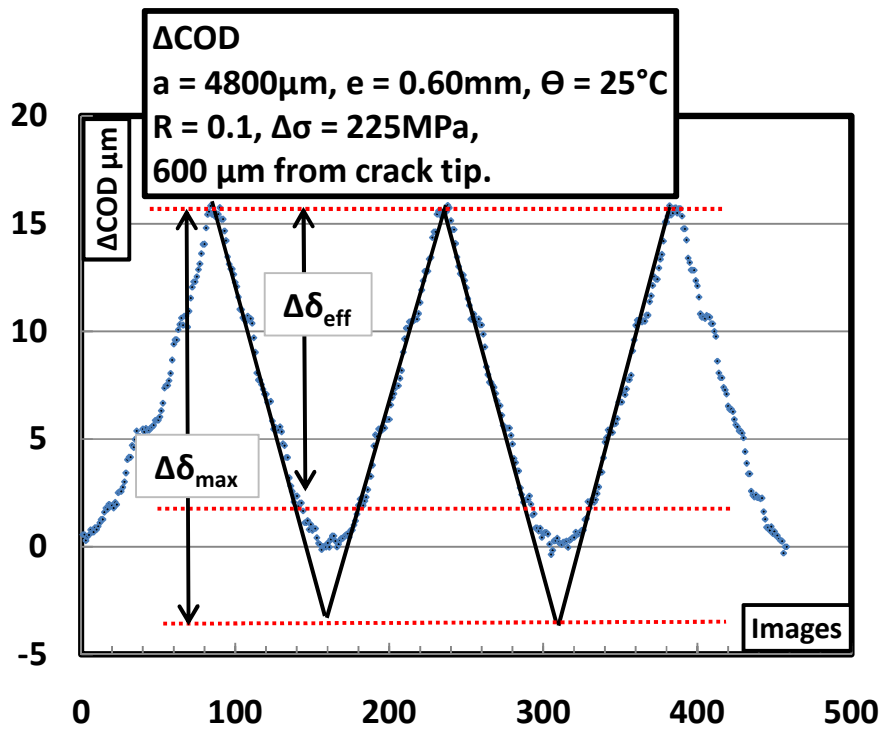


Fig 15. Crack closure detected by extensometer in a specimen of 0.6mm tested at R=0.1 at 25°C

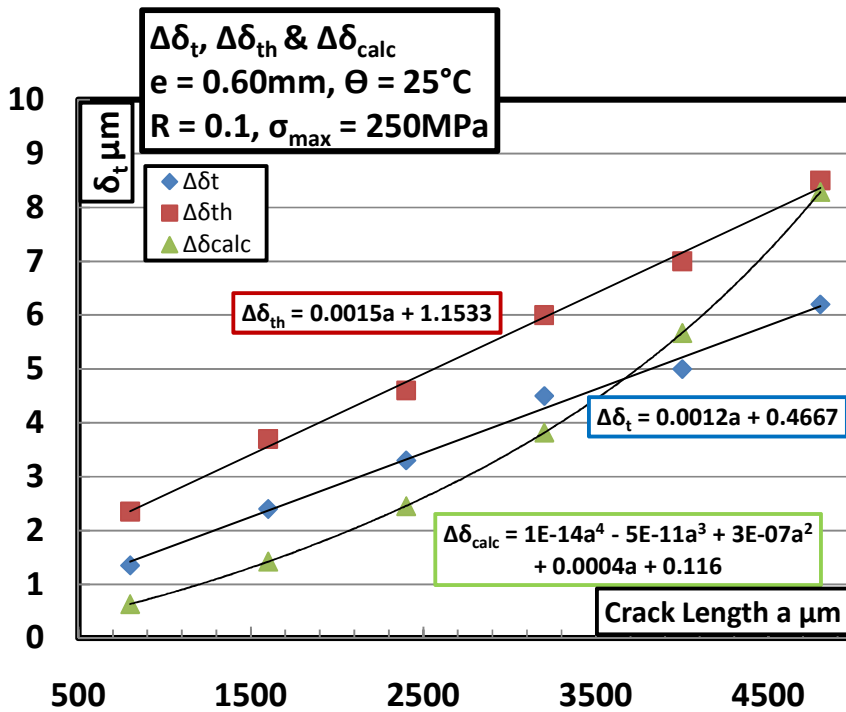


Fig 16. Evolution of $\Delta\delta_t$, $\Delta\delta_{th}$ and $\Delta\delta_{calc}$ with increase in crack length R=0.1 at 25°C

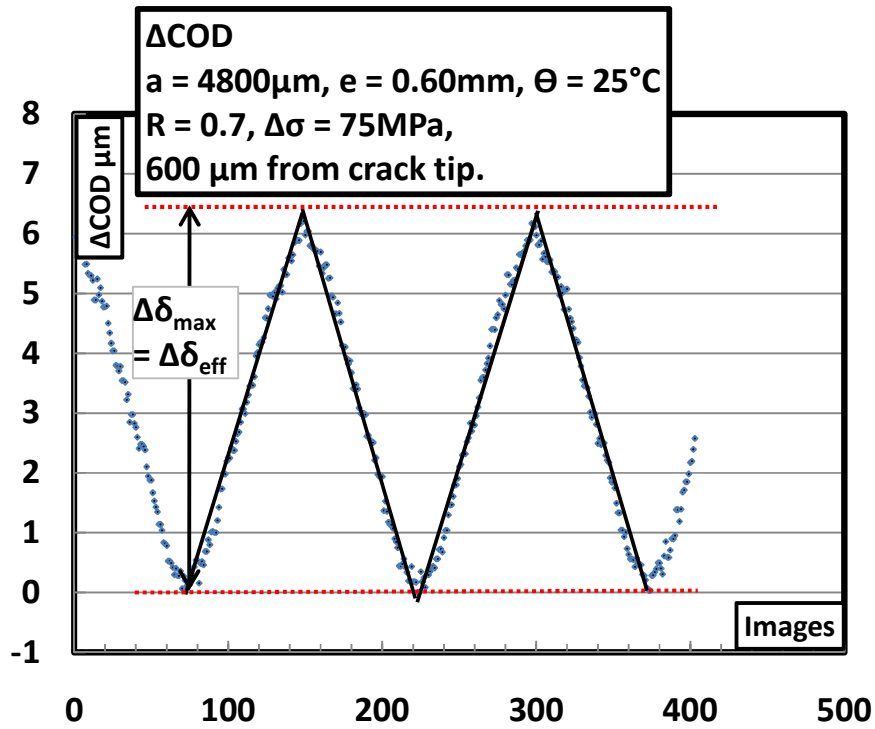


Fig 17. No crack closure in a specimen of 0.6mm tested at R=0.7, 25°C

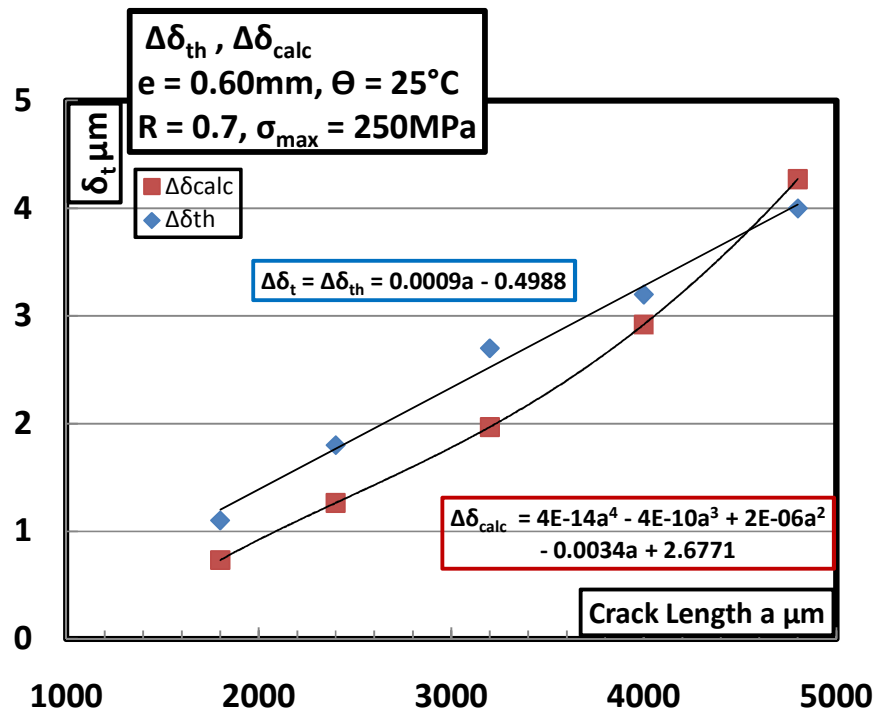


Fig 18. Evolution of $\Delta\delta_t$, $\Delta\delta_{\text{th}}$ and $\Delta\delta_{\text{calc}}$ with increase in crack length R=0.7 at 25°C

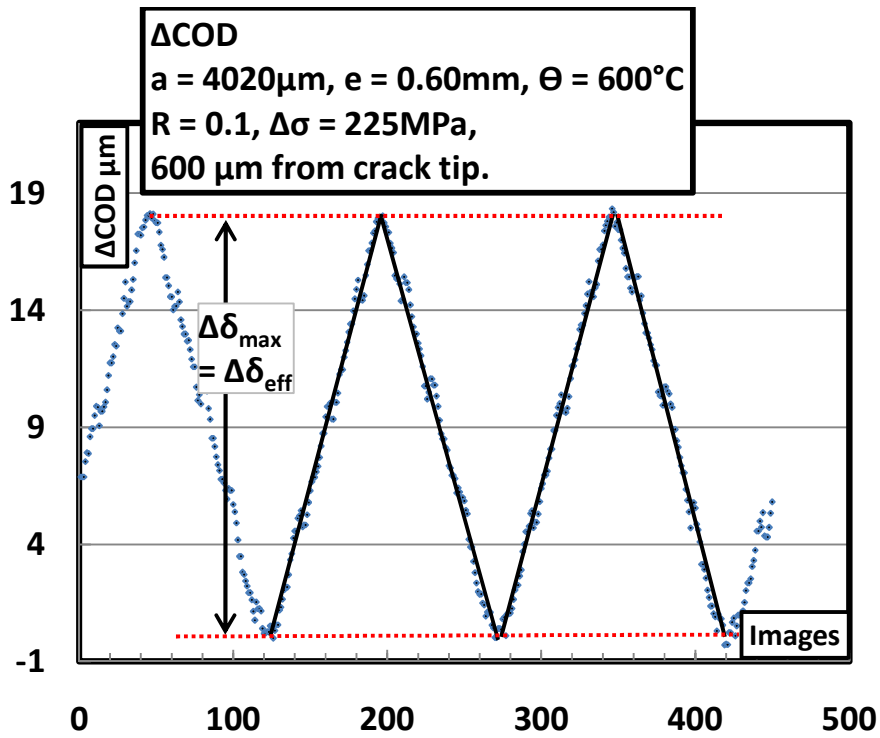


Fig 19. No crack closure in a specimen of 0.6mm tested at $R=0.1$, 600°C

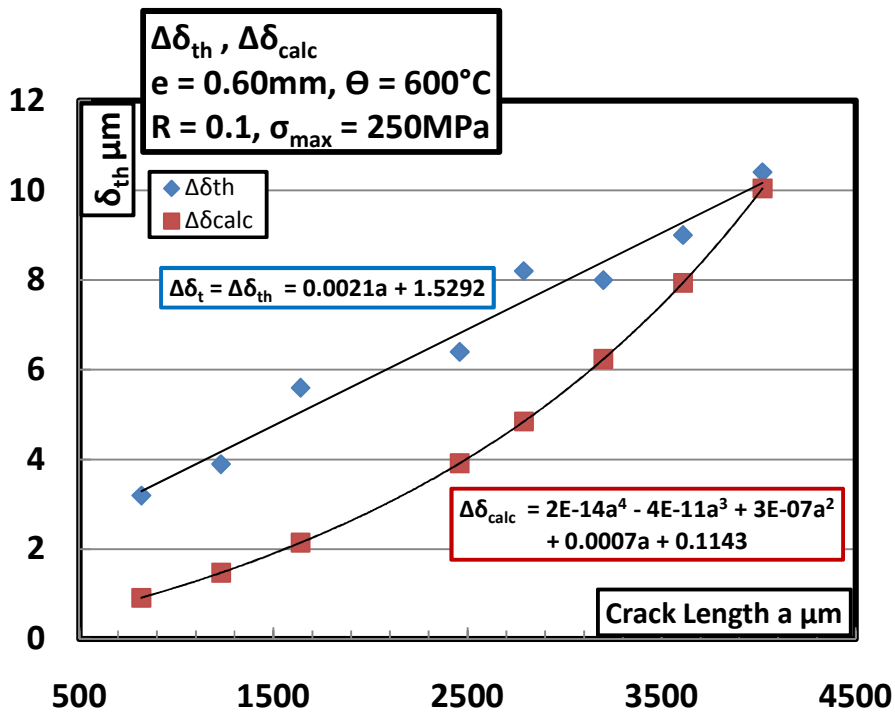


Fig 20. Evolution of $\Delta\delta_{\text{t}}$, $\Delta\delta_{\text{th}}$, and $\Delta\delta_{\text{calc}}$ with increase in crack length $R=0.1$ at 600°C

0.6mm R=0.1 25°C specimen Δ COD data is presented in the figures 15 and 16. The figure 15 is the virtual extensometer response during fatigue cycling. In this case the extensometer is placed 600 μ m behind the crack tip. The total crack length for this measurement is 4.8mm, which represents the end of the fatigue crack propagation ($a/W \leq 0.6$). Crack closure is detected in this specimen throughout the fatigue experiment. The whole crack closure procedure is defined in the section II.1 of this chapter.

The figure 16 gives the values of the crack tip opening displacements in this specimen for the full length of the crack during crack propagation. Due to crack closure there is a difference between the values of the $\Delta\delta_t$ and $\Delta\delta_{th}$. The evolution of these quantities follows a linear law. The $\Delta\delta_{calc}$ is calculated using the elastic-plastic J values calculated by numerical simulation under the same test conditions. $\Delta\delta_{calc}$ shows smaller values as compared to the $\Delta\delta_t$ and $\Delta\delta_{th}$ especially for lower crack lengths. This is probably due to cyclic softening in the material which changes the material constants given in table 2. This phenomenon is further discussed in section V.3.1 of this chapter.

0.6mm R=0.7 25°C specimen Δ COD data is presented in the figures 17 and 18. The figure 17 is the virtual extensometer response during cycling. It is clear from the response that no discernible crack closure exists under these conditions. Due to absence of crack closure the $\Delta\delta_t$ and $\Delta\delta_{th}$ have the same value (figure 18). However as for test at R=0.1 25°C, the $\Delta\delta_{calc}$ also shows smaller values especially for lower crack lengths.

0.6mm R=0.1 600°C specimen Δ COD data is presented in the figure 19 and 20. The figure 19 is the virtual extensometer response during cycling at 600°C. The crack length taken here is 4.05mm. This is because the experiment ends at this crack length at 600°C. From this response crack closure is not detected. As for tests at ambient temperature $\Delta\delta_{calc}$ is smaller than $\Delta\delta_t$ and $\Delta\delta_{th}$. The comparison of $\Delta\delta_{th}$ and $\Delta\delta_{calc}$ for this test is similar to the test with the same loading conditions at 25°C.

The absence of crack closure is confirmed by tests on specimens of 2.5mm and 0.6mm thickness specimens tested at different R ratios at 600°C as shown in chapter 4. There we can see that the variation in R has no effect on the FCGR curve. This is only possible if there were no shielding of the crack tip at R=0.1 or no crack closure. The absence of crack closure may be due to greater cyclic softening in specimens tested at 600°C. The cyclic softening is known to reduce the effect of crack closure.

IV.3 Calculation of FCGR criterion based on $\Delta\delta_t$ and $\Delta\delta_{th}$

The interest of using the $\Delta\delta_t$ or $\Delta\delta_{th}$ as damage parameters is that they are measured on the specimen. They are dependent on material properties and also reflect any changes in the

material properties during experimentation. According to equation 10 above, an FCGR criterion based on the J – Integral is defined as [17, 18]:

$$\frac{da}{dN} = A_1 \left(\sqrt{\Delta J_{cycl} E^*} \right)^{m_1} \quad (10)$$

In this equation the ΔJ_{cycl} may be replaced by the ΔJ^δ as defined in the equation 27. The Young's modulus used is for plane stress. Thus the equation 10 becomes:

$$\frac{da}{dN} = A_1 \left(\sqrt{\Delta J^\delta E} \right)^{m_1} \quad (29)$$

The $\sqrt{\Delta J^\delta E}$ parameter is especially adapted for the high temperature fatigue crack growth; however it approaches the K_I values for materials tested at ambient temperature or small scale yielding condition. Its use has the added advantage that the tests carried out at high temperature may be compared directly with those carried out at ambient temperature.

The specimens showing crack closure have different values for $\Delta\delta_t$ or $\Delta\delta_{th}$. Both of them were tested to find the FCGR criterion that gives the best data consolidation. It is observed practically that the $\Delta\delta_{th}$ gives better data consolidation for FCGR curves at different values of R. An added advantage of using $\Delta\delta_{th}$ is the simplicity in its use and calculations, because crack closure is not taken into account, and an R independent criterion may be defined. Equation 29 thus will be modified to:

$$\frac{da}{dN} = A_1 \left(\sqrt{\Delta J^{\delta_{th}} E} \right)^{m_1} \quad (30)$$

In addition to the criterion in equation 30, the FCGR curves may be obtained by using the $\Delta J^{\delta_{th}}$ directly. This is especially adapted when large scale plasticity exists. In this case the crack propagation law takes the form:

$$\frac{da}{dN} = A_2 (\Delta J^{\delta_{th}})^{m_2} \quad (31)$$

IV.3.1 Application of $\sqrt{\Delta J^{\delta_{th}} E}$ and $\Delta J^{\delta_{th}}$ on specimens tested at 25°C at R = 0.1 and 0.7

The evolution of $\sqrt{\Delta J^{\delta_{th}} E}$ measured by using $\Delta\delta_{th}$ for two conditions of crack propagation of R = 0.1 and 0.7 are compared in the figure 21. As expected the values of the $\sqrt{\Delta J^{\delta_{th}} E}$ are higher for the specimen tested at R = 0.1.

The FCGR curves based on this criterion are plotted in the figure 22. Here we can see that the curves are completely superposed. Also the effect of multiple slopes seen while using ΔK (section I.1 figure 6) has completely disappeared for the specimen tested at R = 0.1. One should take care however in the interpretation of this data, since we know that crack closure exists, but when applying this criterion the data is only consolidated if this crack closure is neglected.

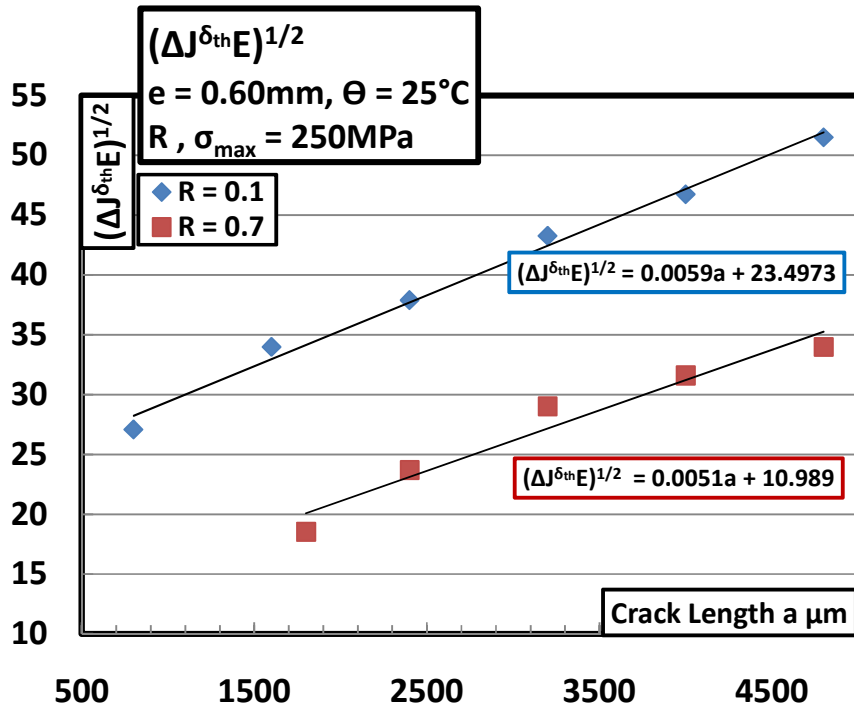


Fig 21. Evolution of $\sqrt{\Delta J^{\delta_{th}} E}$ with increase in crack length for different R

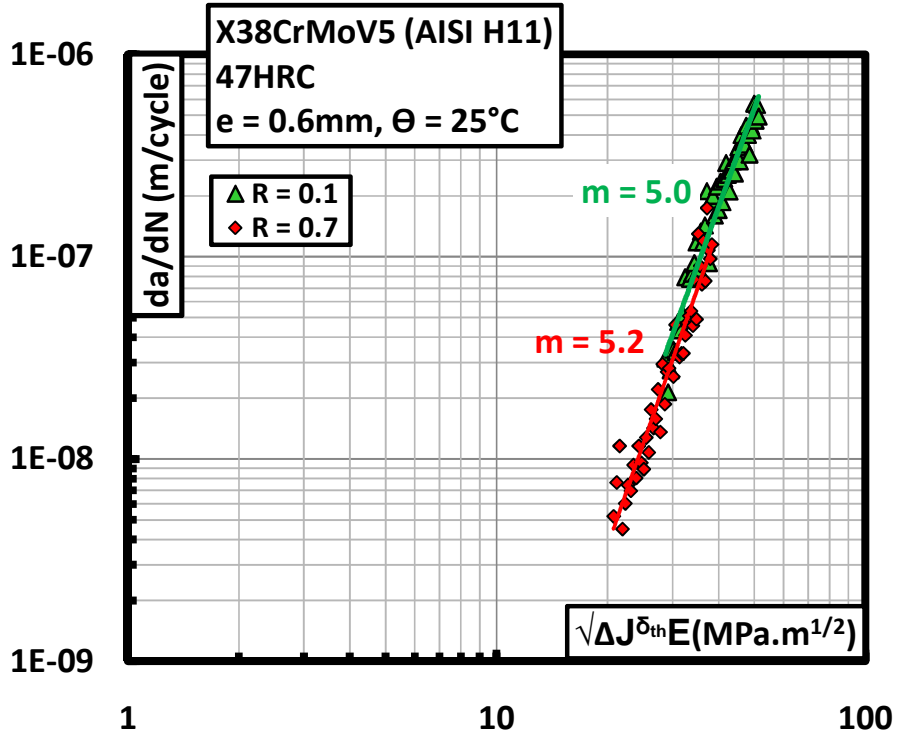


Fig 22. $\sqrt{\Delta J^{\delta_{th}} E}$ as a FCGR parameter at $R = 0.7$ and 0.1 in a 0.6mm specimen at 25°C

Since the Young's modulus is the same for the two specimens, the FCGR curves as a function of the crack driving force parameter $\Delta J^{\delta_{th}}$ will also be parallel as for figure 22. The comparison is presented in figure 23.

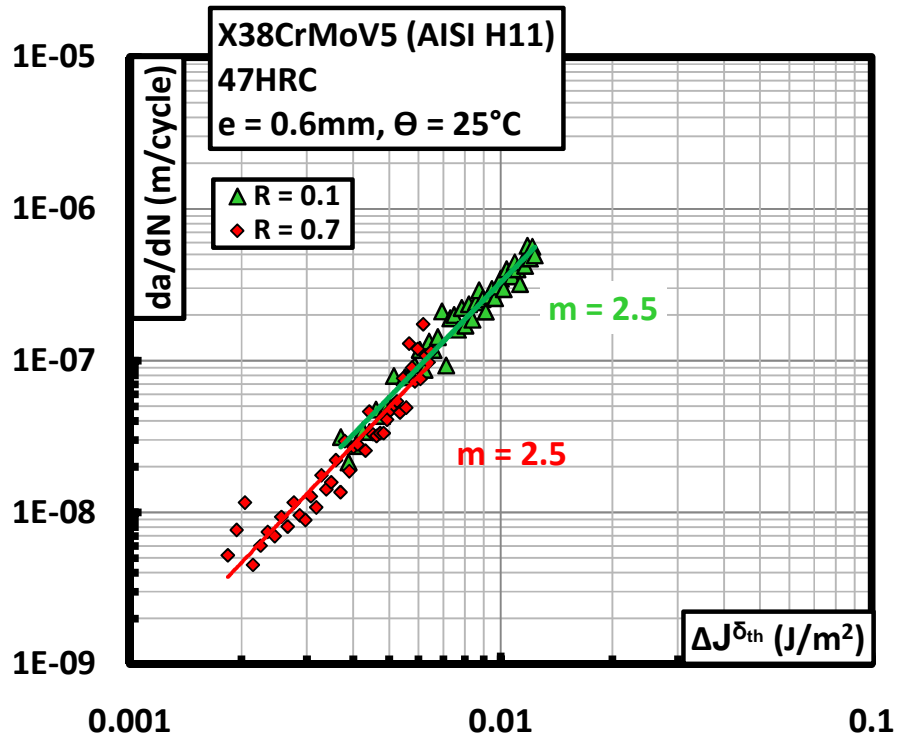


Fig 23. $\Delta J^{\delta_{th}}$ as a FCGR parameter at R = 0.7 and 0.1 in a 0.6mm specimen at 25°C

IV.3.2 Comparison of $\sqrt{\Delta J^{\delta_{th}} E}$ and $\Delta J^{\delta_{th}}$ FCGR curve at 600°C and 25°C tested at R = 0.1

The use of the $\Delta\delta_t$ or $\Delta\delta_{th}$ has the advantage of reflecting any changes in the material properties, since they are measured directly on the specimen being tested. The $\sqrt{\Delta J^{\delta_{th}} E}$ parameter values at same loading conditions and different temperatures are shown in the figure 24.

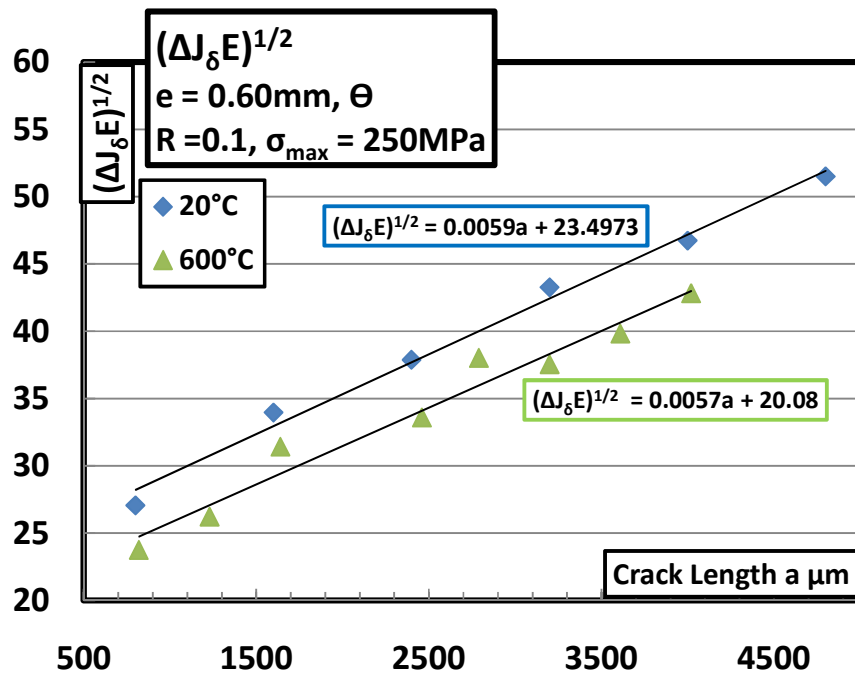


Fig 24. Evolution of $\sqrt{\Delta J^{\delta_{th}} E}$ with increase in crack length for different 25°C and 600°C at $R = 0.1$

An interesting thing to note is that although the $\Delta \delta_{th}$ values of the specimen tested at higher temperatures is higher, its corresponding $\sqrt{\Delta J^{\delta_{th}} E}$ gives a curve with lower values. This effect is the result of the definition of $\Delta J^{\delta_{th}}$ which is dependent on the yield stress and the Young's modulus value, both of which are lower for the specimen tested at 600°C. These curves can be used to get the FCGR curves with $\sqrt{\Delta J^{\delta_{th}} E}$ as crack driving force parameter. Using this parameter the FCGR curve for higher temperature gives elevated crack propagation speeds for the same $\sqrt{\Delta J^{\delta_{th}} E}$ as shown in figure 25. However, the two curves follow an almost log linear form instead of the S-shape shown when $\Delta J^{\delta_{th}}$ parameter is used, figure 26

The same comparison can be made using only the $\Delta J^{\delta_{th}}$ as FCGR parameter. Thus no correction for the elastic modulus is applied, figure 26. The curve shows better correlation between the curves as compared to $\sqrt{\Delta J^{\delta_{th}} E}$ as regards to superposition, however the 600°C specimen still shows faster FCGR for the same value of $\Delta J^{\delta_{th}}$.

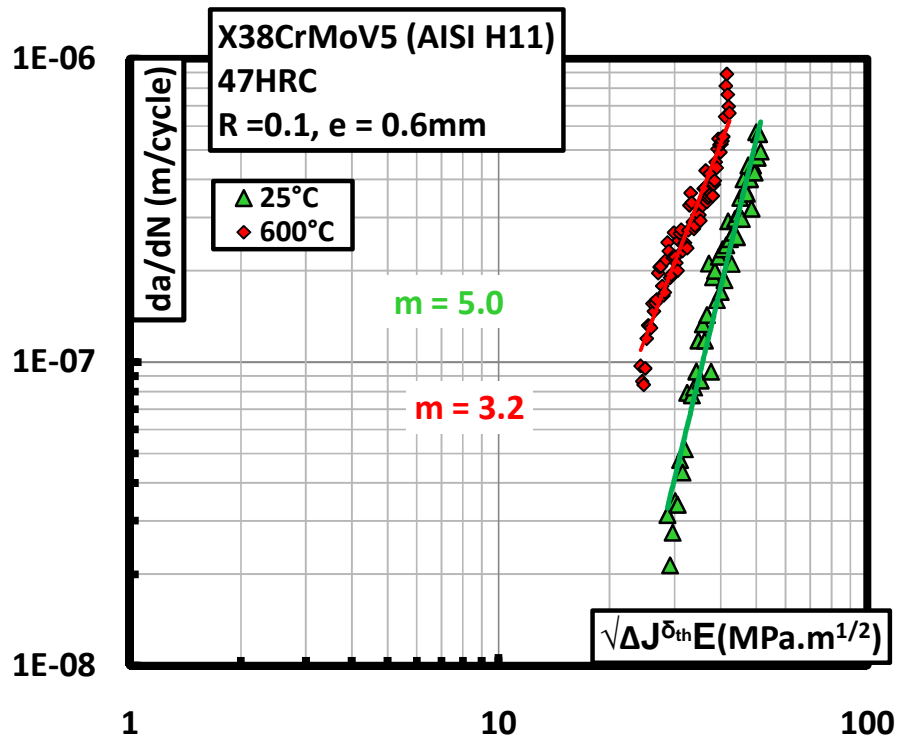


Fig 25. $\sqrt{\Delta J^{\delta_{th}} E}$ as a FCGR parameter at R = 0.1 in a 0.6mm specimen at 25°C and 600°C

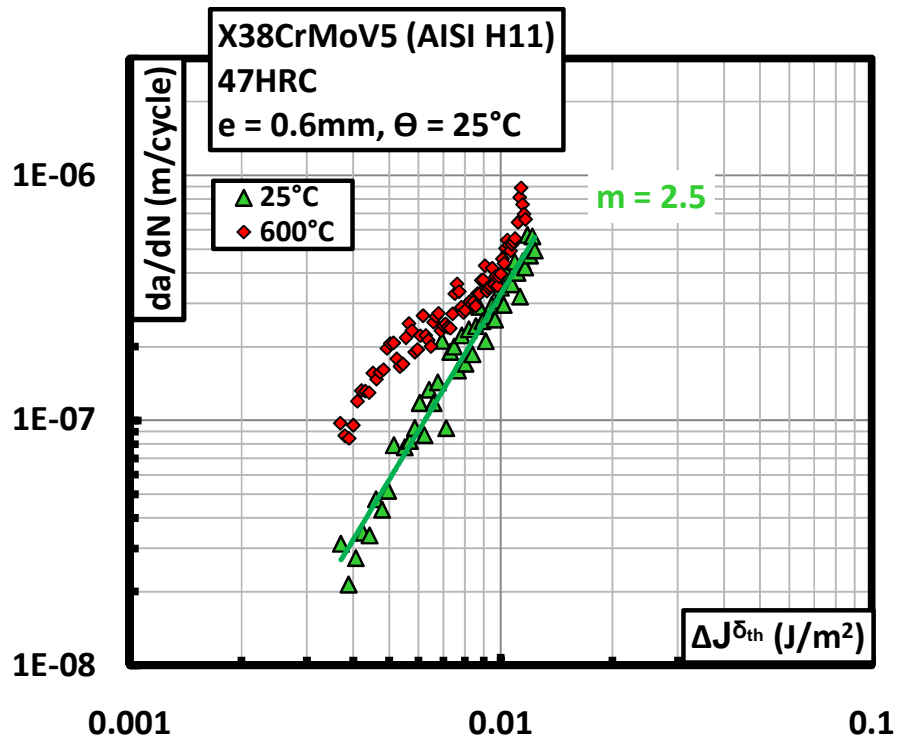


Fig 26. $\Delta J^{\delta_{th}}$ as a FCGR parameter at R = 0.1 in a 0.6mm specimen at 25°C and 600°C

IV.3.3 Use of $\sqrt{\Delta J^{\delta_{th}} E}$ and $\Delta J^{\delta_{th}}$ as an R independent FCGR criterion

We have presented in equation 27 above an R independent criterion of fatigue crack propagation based on the $\Delta\delta_{th}$ parameter. The validity of this criterion is explored in this section.

$$\Delta J^{\delta} = (1 - R_{app}^2) \left(\frac{\sigma_0 \Delta \delta_t}{d_n (1 - R^2)} \right) \quad (27)$$

For simplicity of calculations, it was decided to use FCGR data under such experimental conditions for which no crack closure is observed. It was also decided to use the criterion calculated for 0.6mm specimens directly on specimens of 2.5mm thickness. The temperature chosen is 600°C because of an absence of crack closure in a test of R=0.1. The FCGR curves for ΔK are reproduced in figure 27. The specimens are 2.5mm thickness specimens tested at 600°C at R = 0.1 and 0.5.

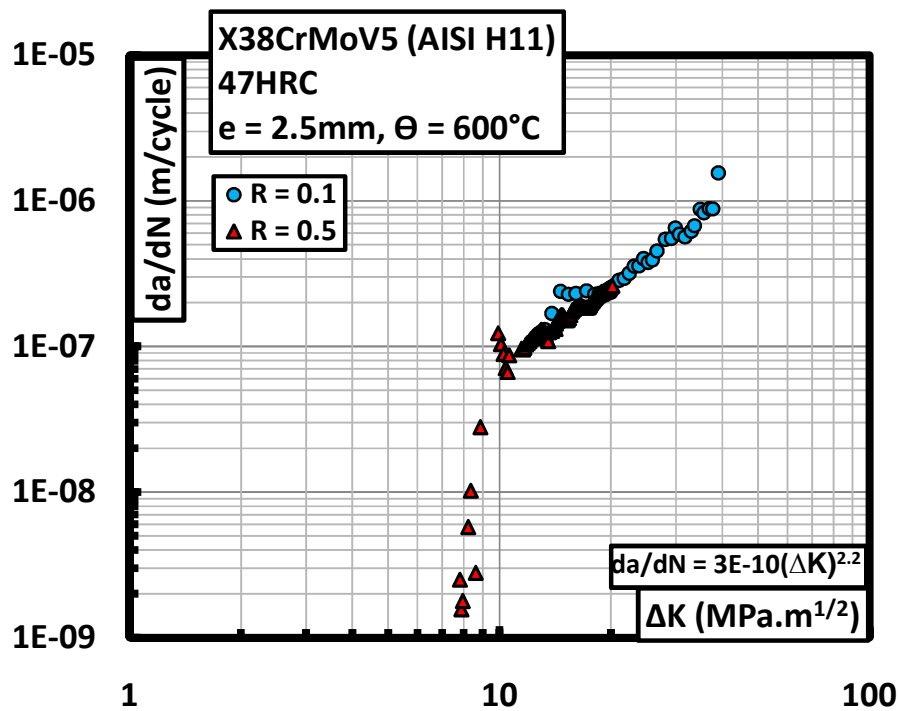


Fig 27. Effect of R ratio on fatigue crack propagation at 600°C ΔK

Some observations about these FCGR curves can be made here. The two curves are superposed. This basically means that there is no presence of crack closure (or crack shielding) in the specimen tested at either R ratio.

To validate the criterion presented in the equation 27, one should be able to find the crack propagation law for $R = 0.1$, then be able to apply it on the specimen tested at $R = 0.5$ and find the same superposed FCGR curves. This is demonstrated in the equation below:

$$\Delta J^\delta = (1 - R_{app}^2) \left(\frac{\sigma_0 \Delta \delta_t}{d_n (1 - R^2)} \right) \quad (27)$$

$$R = 0.1$$

$$R_{app} = 0.5 \text{ or } 0.1$$

$$\sigma_0 = 600 \text{ MPa}$$

$$d_n = 0.5$$

Now for $R = 0.1$ the equation 27 has been determined to be:

$$\begin{aligned} \Delta J_{R=0.1}^\delta &= \left(\frac{\sigma_0 \Delta \delta_t}{d_n} \right) \frac{(1 - 0.1^2)}{(1 - 0.1^2)} \\ &= \left(\frac{600}{0.5} \right) (0.0021a + 1.5292) \times 10^{-6} \text{ J/m}^2 \end{aligned} \quad (32)$$

Where, "a" is the crack length. The equation 32 can be used to interpret the FCGR criterion for the specimen tested at $R = 0.5$:

$$\begin{aligned} \Delta J_{R=0.5}^\delta &= \left(\frac{\sigma_0 \Delta \delta_t}{d_n} \right) \frac{(1 - 0.5^2)}{(1 - 0.1^2)} \\ &= \left(\frac{600}{0.5} \right) \times 0.758 \times (0.0021a + 1.5292) \times 10^{-6} \text{ J/m}^2 \end{aligned} \quad (33)$$

From the equations 32 and 33 the FCGR curves may be plotted using the $\sqrt{\Delta J^{\delta th} E}$ or $\Delta J^{\delta th}$ parameter. Both of these parameters will give the same FCGR characteristics because the two specimens have been tested at the same temperature and the value of the young's modulus is constant. For simplicity of comparison of units with figure 27, the comparison is presented for the $\sqrt{\Delta J^{\delta th} E}$ in figure 28.

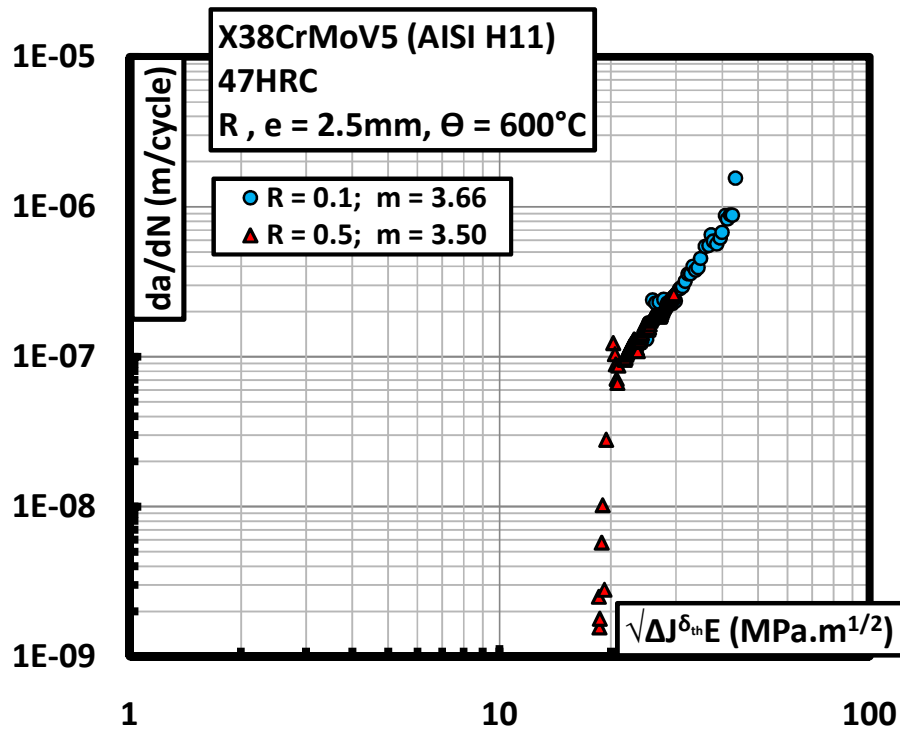


Fig 28. Effect of R ratio on fatigue crack propagation at 600°C . $\sqrt{\Delta J^{\delta_{th}} E}$

From figure 28 we can see that the definition of ΔJ^{δ} as presented in equation 27 is able to reproduce the FCGR curve characteristics of two experiments carried out at different R values. The FCGR curves in figure 28 are superposed as for the parameter ΔK . One thing interesting to note is that the ΔK parameter is dependent on R whereas the $\sqrt{\Delta J^{\delta_{th}} E}$ and ΔJ^{δ} parameters are dependent on R^2 . The source of this difference is explained in the section II of this chapter.

V. CRITICAL ANALYSIS OF THE CRACK DRIVING FORCE MODELS

All the crack driving force models presented above may have some limitations. The limitations may be related but not limited to

- The physical phenomena associated with the fatigue crack driving force
- Mathematical justifications of the model
- Assumptions or hypotheses made in the definition of the crack driving force parameter
- Material properties
- Utilisation of monotonic damage criteria on cyclic loading

V.1 Rationalisation of R ratio: $\bar{K}^* = (K_{max})^\alpha (\Delta K)^{1-\alpha}$

There are certain physical and practical limitations associated with this model. This model uses an empirical mathematical adjustment to rationalise the FCGR data. Its physical interpretation is somewhat vague. The model assumes that the fatigue damage is a function of ΔK and K_{max} . It however, presents no real physical proof to this effect. The fact that the FCGR may be a function of the average stress intensity factor K_{av} is also a possibility, not explicitly defined in the model.

The model presents no real reference curve to which the data will collapse. FCGR data of different charge ratios is displaced by a factor proportional to α towards the left (lower K value) with respect to a simple ΔK based FCGR curve. The curves at different charge ratios will be displaced in the same direction, by different amounts to achieve superposition.

The model may represent false results for cases where there is no effect. For example: α is calculated as a unique value using FCGR data for $R = 0.1$ and 0.7 . The material tested shows no crack closure for $R \geq 0.3$. Thus all FCGR curves for $R \geq 0.3$ will coincide on a Paris curve based on simple ΔK . The correction applied by \bar{K}^* will make these curves non coincident and in some cases the FCG rate for lower R ratios will be higher than for higher R ratios (inverse R effect). This effect has been found to be very low because of low α values of this material and the \bar{K}^* model in general gives satisfactory results.

V.2 J-Integral as a damage parameter.

The J-integral Rice[16] on its own has been developed by assuming a non linear elastic material. This causes problems because the unloading of this material has to follow the same path as the loading curve. This is not the case because real metallic materials most often show an elastic-plastic behaviour, which while unloading simply follows a linear elastic path. Thus the definition of the cyclic J integral presents difficulties and is ambiguous. Chow[7] has performed a detail critical analysis of the cyclic J – integral, the use of which, for fatigue, was first proposed by

Dowling[6]. The main problem with the definition of the cyclic J – Integral arises when it is compared to the stress intensity factor for small scale yielding conditions. For a specific case of fatigue crack propagation when a material is cycled between σ_{max} and σ_{min} , the stress intensity factor range ΔK is given by:

$$\Delta K = (\sigma_{max} - \sigma_{min})\sqrt{\pi \cdot a} \cdot f(a/W) \quad (34)$$

The cyclic J-Integral may be presented as the difference of the monotonic J value at σ_{max} and σ_{min} , which we will call J_{max} and J_{min} respectively:

$$\Delta J = (J_{max} - J_{min}) \quad (35)$$

However for SSY conditions Suresh[1]:

$$J = K^2/E \quad (36)$$

Now the cyclic J-Integral may be defined as either:

$$\Delta J_{cycl} = (\Delta K)^2/E = (K_{max} - K_{min})^2/E \quad (37)$$

Or,

$$\Delta J = \Delta(K)^2/E = (K_{max}^2 - K_{min}^2)/E \quad (38)$$

Where,

$$(K_{max}^2 - K_{min}^2) > (K_{max} - K_{min})^2 \quad (39)$$

This difference presents difficulties in the operational definition of the cyclic J integral. According to the Griffith energy balance [24] reviewed by Chow[7], the crack driving force is the forward loading part of the cycle represented by ΔJ in equation 38.

In this study the stress intensity factor range has been calculated by calculating the K_{max} from J_{max} using $J_{max} = K_{max}^2/E$ and the simple LEFM relation $\Delta K = (1 - R)K_{max}$. J_{min} has not been explicitly calculated but assumed to be a linear function of applied σ as is the case in the LEFM problems. This calculation strategy gives a solution best represented by equation 38. However, ΔJ^δ is determined using $\Delta\delta$ and may be considered representative of ΔJ_{cycl} .

The same problem arises when using the $\Delta CTOD$ criterion as a parameter linearly proportional to loading. Since $\delta_t = d_n(J/\sigma_0)$ shows a linear relationship of δ_t with J, the same cannot be true for K, since K has a quadratic proportionality to J. Due to these difference care must be

taken while making calculations of $\Delta CTOD$, K and J especially, when they are being used as comparative fatigue crack driving force parameters.

V.3 Cyclic J – Integral calculated using $\delta_t = d_n(J/\sigma_0)$ as a damage parameter

V.3.1 Material properties

The basic expression $\delta_t = d_n(J/\sigma_0)$ [19] is defined for monotonic loading of a cracked specimen. In this study we have used $\Delta\delta_t$ in lieu of the monotonic δ_t . This presents two problems. One is the same as explained in the previous paragraph that by definition it is not linearly proportional to loading, whereas practically it is seen to be linearly variable with respect to applied load.

The other issue is that the material used for the study follows a power law hardening behaviour under monotonic tensile stress, and thus can be easily characterised by

$$\varepsilon_p = \alpha \left(\frac{\sigma}{\sigma_0} \right)^{n-1} \frac{\sigma}{E} \quad (11)$$

Where n and α represent monotonic material properties. The material used however shows cyclic softening under LCF tests figure 29. Thus in reality the cyclic plastic zone will have a lower σ_0^c and n^c as compared to the monotonic set of these material properties. Also these cyclic material constants will be dependent on the number of cycles and the magnitude of the plastic deformation seen in the cyclic plastic zone. This will in general give larger $\Delta CTOD$ values as compared to the ones determined by numerical analyses. This effect is shown schematically in figure 30. The softening is much more pronounced at higher temperatures.

V.3.2 Large scale yielding in front of crack tip

The expression of J Integral has been found to be valid and path independent in large scale yielding conditions for the unique case of Dugdale type thin strip yielding [7-9] even though the non linear elastic material assumption is invalidated. However this path independence has been studied extensively by Shih[19], McMeeking and Parks[25], Shih et al.[26], Shih and German[27] on centre cracked panels CCP, edge cracked panels ECP and cracked bend bars CBB. They have determined that the region dominated by the singularity fields (equation 14) is dependent on specimen geometry and material hardening behaviour. They have concluded that the size of HRR (equation 14) is greater for the CBB than for CCP. The dominating region for ECP (used in this study) lies in between the two. They suggest that the relationship between J and δ_t as expressed by equations 16 and 17 will continue to hold for hardening materials where the un

cracked ligament (under generalised plasticity) is subjected primarily to bending and may not be valid for ligaments under primarily tensile loading.

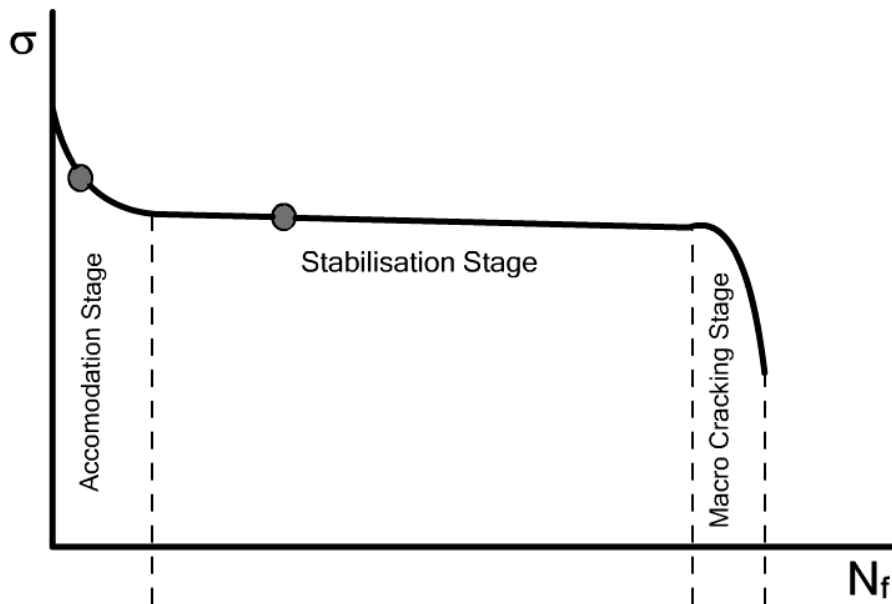


Fig. 29: Cyclic softening under imposed deformation isothermal LCF testing. The cyclic plastic zone may lie on any part of the curve (grey spots)

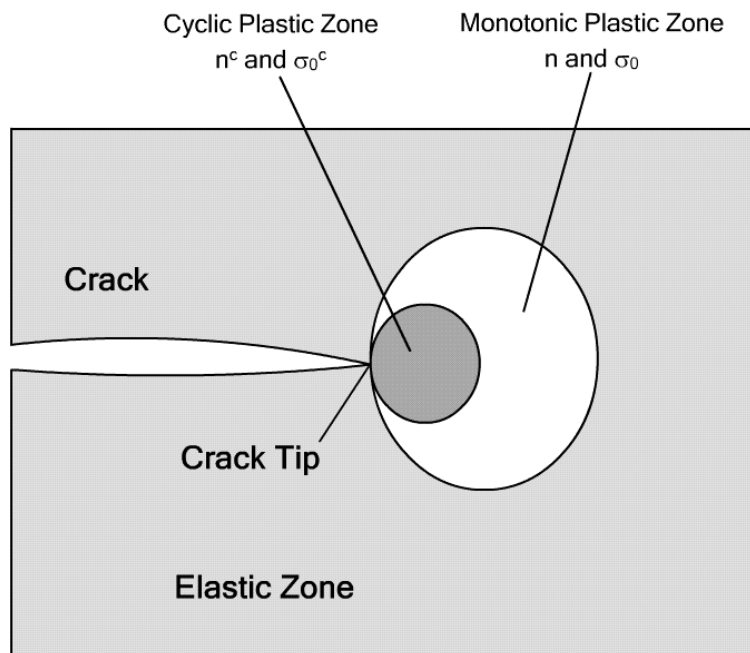


Fig 30: Variation of material constants with respect to the monotonic and cyclic plastic zone at the crack tip

Shih[28] has also presented the analysis of fully plastic edge cracked specimens where it is suggested that a deep crack in an edge cracked plate may give an important HRR dominant zone due to an important component of bending stresses. However the fact that the specimen in our experiments is fixed grip type, which may increase the tensile component of the crack tip stresses thus reducing the HRR dominant field.

Care must thus be taken when using the J and δ_t relations (equations 16 and 17) in fatigue crack propagation experiments in SENT specimens especially at elevated temperatures. At elevated temperatures the hardening exponent becomes low and there is a larger possibility of a generalised plastic deformation.

VI. CONCLUSION

In this section the different models for fatigue crack propagation developed during the research work are presented. Most of the models are developed to be able to consolidate the FCGR curve obtained at different experimental conditions. Of interest are the variations in the charge ratio, and the effects of temperature.

A model for the consolidation of the effects of the charge ratio R is presented. The model is mostly empirical in nature based on mathematical consolidation of FCGR curves by considering the fatigue crack propagation as a function of a two parameter law based on K_{\max} and K .

The use of the J-Integral [4] for fatigue crack propagation is presented. The J-Integral may be determined using measured ΔCTOD ($\Delta\delta_t$) values by optical observation of the crack faces during fatigue crack propagation experiments. Most of the parameters and the methodology used are discussed. The parameters defined are then used to create the FCGR curves and make comparisons. It is found that the use of ΔCTOD as an FCGR crack driving force parameter is interesting and presents an R independent alternative to the simulated ΔK parameter.

In the last section a critical analyses of all the proposed models is presented. All the models stated above are based on certain hypotheses and assumptions which may render them inaccurate in certain conditions. The problems have been discussed in the light of a detailed literature review based mostly on the works of Shih[19]. In spite of all the probable pitfalls associated with using these relations for fatigue loading it is shown that they may provide a good FCGR criterion. This has been confirmed mostly by experimental results of this study.

VII. REFERENCES

1. Suresh, S., *Fatigue of materials*. 1998: Cambridge Univ Pr.
2. Oudin, A., *Thermo-mechanical fatigue of hot work tool steels*. 2001, Thesis Ecole des Mines de Paris, work performed at Ecole des Mines d'Albi - Carmaux.
3. Delagnes, D., *Comportement et tenue en fatigue isotherme d'aciers à outils Z38CrMoV5 autour de la transition oligocyclique-endurance*. 1998, Thesis Ecole des Mines de Paris work performed at Ecole des Mines d'Albi - Carmaux.
4. Rice, J.R. and G.F. Rosengren, *Plane strain deformation near a crack tip in a power-law hardening material*. Journal of the Mechanics and Physics of Solids, 1968. **16**(1): p. 1-12.
5. Dowling, N.E. and J.A. Bagley, *Fatigue crack growth during gross plasticity and the J-integral*. Mechanics of crack growth, 1976: p. 82-103.
6. Dowling, N.E. *Geometry effects and J integral approach to elastic-plastic fatigue crack growth*. 1976: ASTM International.
7. Chow, C.L. and T.J. Lu, *Cyclic J-integral in relation to fatigue crack initiation and propagation*. Engineering Fracture Mechanics, 1991. **39**(1): p. 1-20.
8. Rice, J.R., *The path dependence of the J-contour integral*. International Journal of Fracture, 1975. **11**: p. 352-353.
9. Chell, G.G. and P.T. Heald, *The path dependence of the J-contour integral*. International Journal of Fracture, 1975. **11**(2): p. 349-351.
10. Elber, W., *Fatigue crack closure under cyclic tension*. Engineering Fracture Mechanics, 1970. **2**(1): p. 37-44, in3-in4, 45.
11. Kujawski, D., *A fatigue crack driving force parameter with load ratio effects*. International Journal of Fatigue, 2001. **23**: p. 239-246.
12. Kujawski, D., *Enhanced model of partial crack closure for correlation of R-ratio effects in aluminum alloys*. International Journal of Fatigue, 2001. **23**(2): p. 95-102.
13. Kujawski, D., *A new $[\Delta] K + K_{max}$ 0.5 driving force parameter for crack growth in aluminum alloys*. International Journal of Fatigue, 2001. **23**(8): p. 733-740.
14. Stoychev, S. and D. Kujawski, *Analysis of crack propagation using $[\Delta] K$ and K_{max}* . International Journal of Fatigue, 2005. **27**(10-12): p. 1425-1431.
15. Walker, K. and B. Lockheed-California Co. *THE EFFECT OF STRESS RATIO DURING CRACK PROPAGATION AND FATIGUE FOR 2024-T3 AND 7075-T6 ALUMINUM*. 1970: ASTM International.
16. Rice, J.R., *A path independent integral and the approximate analysis of strain concentration by notches and cracks*. Journal of applied mechanics, 1968. **35**(2): p. 379-386.
17. Sadanada, S. and P. Shahinian, *Elastic-plastic fracture mechanics for high temperature fatigue crack growth*, in *Fracture Mechanics: Twelfth Conference, ASTM STP 700*. 1980. p. 152-163.
18. Sadanada, S. and P. Shahinian, *A fracture mechanics approach to high temperature fatigue crack growth in Udimet 700*. Engineering Fracture Mechanics, 1979. **11**: p. 73-86.
19. Shih, C.F., *Relationships between the J-integral and the crack opening displacement for stationary and extending cracks*. Journal of the Mechanics and Physics of Solids, 1981. **29**(4): p. 305-326.
20. Hutchinson, J.W., *Plastic stress and strain fields at a crack tip*. Journal of the Mechanics and Physics of Solids, 1968. **16**(5): p. 337-342.
21. Tracey, D.M., *Finite element solutions for crack-tip behavior in small-scale yielding*. (American Society of Mechanical Engineers, 1976.) ASME, Transactions, Series H- Journal of Engineering Materials and Technology, 1976. **98**: p. 146-151.

22. McClintock, F.A., *Plasticity aspects of fracture*. Fracture: an advanced treatise, 1971. **3**: p. 47–225.
23. McMeeking, R.M., *Finite deformation analysis of crack-tip opening in elastic-plastic materials and implications for fracture*. Journal of the Mechanics and Physics of Solids, 1977. **25**(5): p. 357–381.
24. Griffith, A.A., *The phenomena of rupture and flow in solids*. Philosophical Transactions of the Royal Society of London. Series A, Containing Papers of a Mathematical or Physical Character, 1921: p. 163-198.
25. McMeeking, R.M. and D.M. Parks, *Elastic-Plastic Fracture*. ASTM STP, 1979. **668**: p. 175–194.
26. Shih, C.F., H.G. de Lorenzi, and W.R. Andrews, *Elastic-plastic fracture*. ASTM STP, 1979. **668**: p. 65-120.
27. Shih, C.F. and M.D. German, *Requirements for a one parameter characterization of crack tip fields by the HRR singularity*. International Journal of Fracture, 1981. **17**(1): p. 27-43.
28. Shih, C.F., *J-dominance under plane strain fully plastic conditions: the edge crack panel subject to combined tension and bending*. International Journal of Fracture, 1985. **29**(2): p. 73-84.

Chapter 6: Conclusions and Perspectives

Résumé en Français	173
A. Résumé	173
B. Principaux Résultats Obtenus.....	174
C. Perspectives	176
I. Resume	178
II. Principal results obtained	179
III. Future Perspectives.....	181

RESUME EN FRANÇAIS

Dans ce chapitre, un bref résumé de la stratégie poursuivie dans cette étude est donné. Ensuite, un rappel des principaux résultats obtenus est présenté. Quelques suggestions sont données pour les futurs travaux à la fin du document.

A. RESUME

Le travail réalisé est une contribution à la caractérisation de l'endommagement d'un acier à outils pour travailler à chaud « X38CrMoV5-47HRC ». Cette nuance a fait l'objet de nombreuses études menées dans le laboratoire. Toutefois, il s'agit de la première étude systématique sur la propagation de fissure de fatigue. La stratégie de la recherche se focalise sur la caractérisation de l'endommagement de la surface. Les cinq principales étapes suivies sont :

- Présentation d'une méthode de détermination de l'endommagement des surfaces des outillages. Il a été proposé que la propagation de fissure en fatigue dans des échantillons minces, ce qui représente la surface d'un outillage, soit comparée à celle déterminée à partir des échantillons massifs. Différentes conditions d'essais ont été réalisées pour déterminer une gamme complète des effets de l'épaisseur qui peuvent exister ;
- Un banc d'essai capable de tester des échantillons minces a été installé. Il se compose d'une machine d'essai universelle de capacité de chargement en fatigue à des fréquences élevées. Les échantillons sont testés à différentes températures. Le système de chauffage utilise l'induction à fréquence élevée. Les lignes d'amarrages ont été conçues et fabriquées dans le laboratoire pour réaliser des essais aux températures élevées ;
- Les données expérimentales ne peuvent être utilisées de façon fiable qu'avec un paramètre d'endommagement pertinent. Classiquement, les données de propagation de fissures en fatigue sont représentées en fonction du facteur d'intensité de contrainte (FIS). Ici, le FIS et l'intégrale J ont été calculés numériquement à l'aide du logiciel ABAQUS/Standard™. Les conditions aux limites et les erreurs liées à l'installation des échantillons ainsi que les effets de la température ont été étudiés pour déterminer les bonnes valeurs du FIS et de l'intégrale J ;
- Une série d'essais de propagation de fissure en fatigue a été effectuée. Différentes conditions de chargement et température ont été utilisées pour étudier la propagation de fissure en fatigue ;
- Différentes méthodes de consolidation des données de propagation de fissure ont été étudiées. L'effet du rapport de charge R à l'ambiante a été corrigé en utilisant la fermeture de fissure proposée par Elber. Les courbes de propagation déterminées à 20

et 600 °C ont été analysées en utilisant le critère de déplacement de l'ouverture en pointe de fissure qui est obtenue par des techniques de corrélation d'images.

B. PRINCIPAUX RESULTATS OBTENUS

Des simulations numériques sur des échantillons fissurés ont été réalisées au préalable dans le **chapitre 3**. Elles démontrent que le paramètre d'endommagement de fissure en fatigue ΔK dépend fortement des conditions aux limites ainsi que de la géométrie de l'éprouvette. Il a été démontré également, que l'usage de la condition aux limites basée sur le déplacement imposé simule les conditions d'essai de manière plus réaliste. La validité de ces conditions a également été vérifiée par rapport aux travaux de littérature. Il a été déterminé que le ΔK est fortement dépendant de la géométrie (rapport entre la hauteur et la largeur ou H/W). La structure des échantillons (profil en haltère) pose quelques difficultés pour déterminer le bon rapport H/W. Dans le cas étudié, on a déterminé que la longueur de l'épaulement d'échantillon en dehors de la zone utile doit être pris en compte dans la sélection de la hauteur H. Le problème lié au rapport H/W peut également être résolu en réalisant des simulations numériques pour chacune des formes d'éprouvette.

L'installation des échantillons varie d'un essai à l'autre, et peut parfois changer au cours du même essai. Cette variation est potentiellement problématique car le ΔK dépend du rapport H/W. L'effet de cette différence (entre les positions des mors) sur la valeur ΔK demeure toutefois insignifiant en raison de la rigidité des extrémités de l'échantillon.

La simulation numérique par le logiciel ABAQUS/Standard™ a permis d'autre part, de déterminer les valeurs de l'intégral J en se basant sur et les modèles élastique et élasto-plastique. Les deux modèles donnent des valeurs identiques de J à T = 20 °C en raison de la limite d'élasticité élevée du matériau à cette température. Les valeurs de J calculées à 600 °C sont toutefois différentes. Un critère de propagation de fissure $\Delta\sqrt{J.E}$ est utilisé afin de rationaliser les courbes de propagation pour les différentes températures. En effet, le ΔK est un paramètre qui correspond au concept de la mécanique de la rupture linéaire élastique. L'utilisation de ce paramètre est alors compromise quand on est en conditions de plasticité généralisée en pointe de fissure car il perd son sens physique.

Après avoir déterminé les ΔK et $\Delta\sqrt{J.E}$, nous avons procédé à la réalisation des essais de propagation qui sont décrits au **chapitre 4**. Comme nous l'avons indiqué précédemment, ces expériences sont indispensables dans l'approche développée pour caractériser l'endommagement de la surface des outillages, car ils permettent d'établir les courbes de propagation de fissure pour l'X38CrMoV5 à 47HRC. Les essais ont été réalisés dans différentes conditions. Les paramètres étudiés sont :

- 1) l'épaisseur d'éprouvette (0.12 – 2.5 mm),
- 2) le rapport de charge R (0.1, 0.3 et 0.7),
- 3) la température (T = 20 et 600 °C).

Il a été montré qu'à l'ambiante, la vitesse de propagation des fissures en fatigue (FCGR) augmente légèrement avec l'augmentation du rapport de charge R. Cet effet a été observé dans le cas des éprouvettes d'épaisseur différentes. Il est lié à la fermeture de fissure pour un rapport de charge égal à 0,1. Cet effet a été mis en évidence en utilisant les techniques de corrélation d'images qui ont permis de déterminer le déplacement de l'ouverture en pointe de fissure. Le seuil de propagation n'a jamais été établi dans le cas des essais effectués à la température ambiante.

Les fissures ne sont jamais complètement fermées dans le cas des essais qui sont réalisés avec un R = 0,7. L'effet du rapport de charge à T = 600 °C est observé plutôt dans le domaine des faibles vitesses de propagation où les valeurs du seuil de propagation diminuent avec l'augmentation de R. La fermeture de fissure (pas encore démontré) peut être à l'origine de ce décalage. Cependant, dans le domaine de Paris, le rapport de charge n'a pas d'effet sur la propagation. Cela peut être lié à la non-fermeture de la fissure. Ce comportement est à l'opposé des observations réalisées dans le cas des essais à chaud, car l'oxyde formé sur les faciès de rupture remplit la fissure et contribue donc à la fermeture de la fissure. De ce fait, l'absence de la fermeture de fissure à 600 °C peut être attribuée à l'effet de l'adoucissement cyclique. L'adoucissement en pointe de fissure élargit en effet la zone de propagation de fissure par rapport à la longueur de fissure. Par conséquent, ce cas peut être assimilé aux conditions des fissures courtes où la zone plastique est non négligeable par rapport à la longueur de fissure.

L'effet de l'épaisseur a les mêmes tendances quelle que soit la température. La réduction de l'épaisseur entraîne une diminution de la vitesse de propagation de la fissure. À la température ambiante, l'épaisseur n'a pas d'effet sur la propagation en dessous de 0.6 mm. Deux effets d'épaisseur ont été distingués à 600 °C ; il y a eu d'une part, une augmentation des valeurs du seuil de propagation lorsqu'on diminue l'épaisseur de l'éprouvette. Cette effet est probablement dû à la fermeture de fissure qui augmente à cause de la création d'une large zone plastique dans le cas des échantillons plus minces. D'autre part, il y a une légère diminution de la vitesse de propagation de fissure dans le domaine de Paris. On note également que les valeurs du seuil à 600°C sont beaucoup plus grandes qu'à la température ambiante. Cela peut aussi être lié à la formation d'une zone plastique très large devant la pointe de fissure qui entraîne l'arrêt de la fissure (voir annexe C). Cet effet a été démontré expérimentalement et nous avons pu observer l'arrêt de la fissure lorsque la température de l'essai a été élevée.

Nous avons tenté dans le **chapitre 5**, de rationaliser les différentes courbes de propagation déterminées par les différents essais. De nombreuses stratégies ont été testées. La première consiste à utiliser le facteur d'intensité de contrainte effective ΔK_{eff} en corrigeant l'effet de la fermeture de fissure dans le cas de l'éprouvette de 0,6 mm d'épaisseur testé avec $R = 0,1$. L'utilisation de K_{eff} conduit à la superposition des courbes de propagation pour $R = 0,1$ et $0,7$. La deuxième procédure est purement mathématique et est tirée des travaux de Kujawski et al. La loi de propagation est exprimée dans ce cas là, en fonction de K_{max} et de ΔK . Une fonction de poids est introduite pour rendre compte des effets de R et se distinguer de la loi de Paris.

$$\frac{da}{dN} = C. \left(\Delta K^\alpha \cdot K_{\text{max}}^{(1-\alpha)} \right)^m$$

où α est la fonction de poids déterminée directement à partir des courbes expérimentales de la propagation de fissure.

Une autre approche basée sur l'ouverture de fissure ΔCTOD a été utilisée pour tenir compte des effets de la température sur la propagation par fatigue. Les valeurs de l'intégrale J ont été estimées à partir des valeurs ΔCTOD qui sont déterminées par la méthode de corrélation d'images. Il a été démontré que l'intégrale J calculée à partir de ΔCTOD donne une bonne corrélation entre les courbes de propagation établies à différentes températures. Cette approche a permis également de rationaliser les courbes de propagation pour les différentes valeurs de R tout en ignorant l'effet de la fermeture de fissure.

Nous avons développé à partir des approches précédentes, un modèle indépendant de R mais utilisant le critère ΔCTOD . L'analyse critique des différents modèles utilisés a permis de discuter la validité de chaque critère de propagation.

C. PERSPECTIVES

Quelques suggestions sont présentées dans ce paragraphe en perspective.

Techniques expérimentales: Des possibilités d'amélioration ont été constatées dans les techniques de mesure utilisées dans les expériences. Nous avons utilisé un microscope à longue portée pour toutes les observations et les mesures de la longueur de la fissure. La mesure de la longueur de la fissure peut être améliorée en utilisant la technique de chute de potentiel en complément de la microscopie. Cela sera particulièrement utile pour déterminer la propagation de fissure par fatigue à des températures transitoires ou à des positions d'arrêt de la fissure, par exemple, chauffage pendant la propagation de fissure en fatigue.

Toutes les images sont stockées dans un film magnétique, qui est ensuite converti en images en utilisant un logiciel iMovie®. Des caméras vidéo rapides de résolution supérieure sont disponibles ces jours-ci. Elles permettent d'améliorer la précision de mesure ΔCTOD . Aussi

L'utilisation des caméras numériques avec enregistrement d'images de haute qualité au lieu de la vidéo peut également être avantageux notamment dans la détermination de la déformation plastique en pointe de la fissure.

Le chauffage et le signal de force peuvent être synchronisés pour réaliser des expériences de fatigue thermomécanique TMF. En réalité, la plupart des aciers de mise en forme à chaud sont utilisés dans des conditions TMF et rarement dans des conditions isothermes.

D'autres essais doivent être réalisés à des températures intermédiaires afin de déterminer l'effet de la température dans les domaines du seuil de propagation et de Paris. Des essais à des températures élevées pour déterminer le K_C doivent être également effectués.

L'effet de l'oxydation sur la vitesse de propagation de fissure en fatigue peut être établi. Pour ce faire, des éprouvettes d'épaisseur plus fine doivent être testées.

Simulations numériques: Toutes les simulations effectuées, ainsi que les modèles de matériaux utilisés sont monotones. En effet, les paramètres des modèles utilisés dans la simulation ont été déterminés à partir des essais de traction monotone à différentes températures. Les valeurs de l'intégrale J ont été également déterminées pour les conditions de chargement monotone. Les résultats seront plus pertinents en considérant les conditions cycliques. Par ailleurs, les valeurs de $\Delta CTOD$ calculées numériquement et déterminées expérimentalement doivent être comparées. Leur comparaison pourrait être utilisée comme un critère pour la validation des simulations numériques.

Modélisation: De même, la considération des conditions de chargements cycliques peut s'étendre aux cas de la modélisation de la propagation de fissure (modèle utilisant le critère $\Delta CTOD$). Cela peut en effet réduire l'écart entre les valeurs du $\Delta CTOD$ calculé numériquement et celles obtenues par la corrélation d'images.

In this chapter a short résumé of the strategy followed in this study is given followed by a brief recall of the principal results obtained. In the end some suggestions are given for future work on this subject.

I. RESUME

The work carried out is a contribution to the characterisation of the damage behaviour of a hot work tool steel X38CrMoV5-47HRC. Other studies have already been carried out on this material in the laboratory. However, this is the first systematic study carried out to determine the fatigue crack propagation characteristics of this material at different temperatures. The strategy of research follows the need to characterise the surface damage of tools steels. There are five principal stages followed during this thesis:

- Presentation of a method of determining surface damage of tool steels. It was proposed that the fatigue crack propagation characteristics in thin specimens, representing the surface of a tool, be compared with those of bulk material specimens. Different conditions of tests are used to determine the full range of thickness effects that may exist.
- A test bench capable of testing thin specimens was setup. It consists of a universal testing machine with a capacity of high speed fatigue testing. The specimens are tested at different temperatures. The heating system consists of high frequency induction heating. Special grips made of IN 718 and IN 100 were designed in house and fabricated to be used with these specimens.
- Experimental data can be reliably used only when there is a proper characterisation criterion available. Classically the fatigue crack propagation data is presented as a function of the stress intensity factor (SIF). Here, SIF and the J-Integral were determined using numerical simulations using the ABAQUS®/Standard software package. Different end conditions, imposed by the machine and errors in specimen installation and effects of temperature were extensively studied to determine the right values for fatigue crack propagation experiments.
- A series of fatigue crack propagation experiments was carried out. Different conditions of loading and temperature are imposed to fully characterise the FCGR behaviour.
- Different methods of consolidation of the FCGR data are established. The effect of load ratio R at ambient temperature was corrected using the classic crack closure correction of Elber. An attempt was made to consolidate the FCGR curves of the specimens tested at ambient temperature and at 600°C by using the Crack Tip Opening Displacement obtained by data correlation techniques.

II. PRINCIPAL RESULTS OBTAINED

Before carrying out any experiments on the specimens, numerical simulations of the cracked specimens are performed in **chapter 3**. It was determined that the fatigue crack driving force ΔK is strongly dependant on the end conditions imposed during simulation and the specimen geometry. It was determined that the use of fixed displacement boundary condition closely simulates the real test conditions. The validity of this conditions was also verified by comparing to work carried out by other researchers. It was also determined that the fatigue crack driving force is strongly dependent on the geometric parameter: height to width ratio or H/W. The structure of the specimens (dog bone profile) presents some difficulties in determining the correct H/W ratio. In the case studied here, it was determined that the shoulders of the specimen outside the gauge length should be included when selecting the height of the specimen. The other solution to the H/W problem is to carry out numerical simulations separately for every form of specimen.

From a practical standpoint, the specimen installation varies from one experiment to another, and it may vary during the test as well if ever the specimen is dismantled from the machine. Since ΔK seems to be dependent on the H/W ratio, this variation may cause some problems. It was shown that in reality this difference in grip position does not have an adverse effect on the ΔK values mainly because of the rigidity of the specimen ends.

The numerical simulation performed in ABAQUS/Standard gives us values of the J-integral. It was determined that for specimens tested at ambient temperature the J-integral has the same values for elastic or elastic-plastic material models due to the high yield limit of this material. At 600°C however, there is a large difference between the elastic and elastic-plastic material models. A different crack driving force parameter $\Delta\sqrt{J \cdot E}$ is introduced for comparison with the specimens at ambient temperature. The need for a new parameter arises from the fact that ΔK is a linear elastic fracture mechanics parameter and loses physical sense when there is generalised plasticity in front of the crack tip.

Having determined the crack driving force parameters ΔK and $\Delta\sqrt{J \cdot E}$, fatigue crack growth experiments were carried out, described in **chapter 4**. Here it may be recalled that the main goal of the experiments was to determine a way to characterise the surface damage of hot work tool steels as well as to establish the fatigue crack propagation curves of X38CrMoV5-47HRC. For this purpose the specimens are tested at different experimental conditions. The parameters varied for the experimentation were the 1) Thickness of the specimens (0.12 – 2.5mm), 2) Load ratio R and 3) The testing temperature.

We have established that at ambient temperature the fatigue crack propagation rate (FCGR) increases slightly with a corresponding increase in the load ratio. This effect is seen in all the

different thicknesses tested. The effect is due to crack closure at $R = 0.1$. This effect was demonstrated using the image correlation techniques while determining the crack tip opening displacement. No discernible threshold ΔK was ever established in the experiments performed in the laboratory at ambient temperature.

Crack closure is completely absent in specimens tested at $R = 0.7$. At 600°C there seems to be no effect of the R ratio in the Paris zone of propagation. However, the threshold values seem to decrease with an increase in the R ratio. This effect may be due to crack closure but we have not yet been able to demonstrate this crack closure at the near threshold ΔK . No crack closure was observed in specimens tested at 600°C , in the Paris regime. This seems to be in accordance to the absence of the effect of R at 600°C . This behaviour is contrary to normal observations of high temperature FCG testing. The creating of oxides at the crack faces would normally increase the crack closure. In this case the absence of crack closure at 600°C may be attributed to the effect of stronger cyclic softening of the material in reducing the crack closure phenomenon at elevated temperatures. This changes the small scale yielding situation and extends the plastic zone with respect to the crack length. It can be claimed that under these conditions we are approaching the same conditions as short cracks where the plastic zone is non negligible as compared to the crack length.

The effect of thickness is found to have the same tendencies at ambient and elevated temperatures. A decrease in the thickness causes a decrease in the crack propagation rate. At ambient temperatures it seems that below 0.6mm thickness there is no effect of thickness. At 600°C however the effect of thickness is twofold. Reduction in thickness causes an increase in the threshold values. This may be due to increased crack closure because of a larger plastic zone in the thinner specimens. There is a very slight reduction in FCGR in the stable propagation zone. One thing to be noted is that the threshold values at 600°C are much greater than the ambient temperatures. We believe this is due to the creation of a very large plastic zone in front of the crack tip at 600°C which causes crack arrest (see appendix C). This effect was demonstrated by a special FCGR test done under slowly increasing temperature.

With all the different effects of the variation in experimental conditions on FCGR, an attempt was made to consolidate all the different data onto a single curve in [chapter 5](#). Different strategies were adopted for this purpose. The first is to use the effective stress intensity factor or ΔK_{eff} by correcting for crack closure in a specimen of 0.6mm thickness tested at $R = 0.1$. The results show that by correcting for crack closure, the curves of the two experiments i.e., $R = 0.1$ and 0.7 collapse onto the same path. The second procedure is purely mathematical and is taken from the works of Kujawski et al. [1] The FCGR is considered in this case to be a function of K_{max} and ΔK . A weight function is introduced to take into account the effects of the load ratio giving the Paris law the form:

$$\frac{da}{dN} = C. \left(\Delta K^\alpha \cdot K_{max}^{(1-\alpha)} \right)^m$$

Where α is the weight function determined directly from experimental FCGR curves.

An approach based on the Crack Tip Opening Displacement or Δ CTOD criterion was used for the effect of temperature on FCGR. J-Integral values were estimated from the Δ CTOD values. The Δ CTOD itself was determined by image correlation at ambient temperature as well as at 600°C. It was demonstrated that the J-integral calculated through Δ CTOD provides good correlation between the experiments carried out at different temperatures. It has also proved to be of use in consolidating the experiments at different R values, without taking into account the crack closure phenomenon.

In the end some mathematical development is presented and subsequently applied on FCGR curves of an R independent fatigue crack propagation criterion based on the Δ CTOD. A critical analysis of all the FCGR criteria and correction used therein is also presented to discuss the assumptions made in determining these criteria and the possible problems that may arise due to their use.

III. FUTURE PERSPECTIVES

Some suggestions are presented here for the possible line of research or improvement in the methodology followed in this work.

Experimental techniques: Some room for improvement has been found in the measurement techniques used in the experiments. We have used a long distance microscope for all the observations and the crack length calculations. Improvements may be made in the crack length calculations by using the potential drop technique in addition to the microscope. This will be especially useful in determining the FCGR at transient temperatures or at positions of crack arrest, e.g. heating during fatigue crack growth.

All the images are stored in on analogue film, which is then converted to images using software. Higher video speed and resolution cameras are available these days, which may greatly improve the Δ CTOD measurement accuracy. Also the use of digital cameras, saving high quality images instead of video may also be used to determine the plastic deformation ahead of the crack tip.

The machine heating and force signals may be synchronised, in order to be able to do TMF experiments. In reality most of these tools steels are used under TMF conditions and rarely under isothermal conditions.

Further experiments need to be carried out at intermediate temperatures to determine the effect of temperature on threshold as well stable fatigue crack growth. Experiments for K_c determination at elevated temperatures should also be performed.

The effect of oxidation may be established on fatigue crack growth rate. For this specimens of even lesser thickness may be used with experiments carried out at low frequencies.

Numerical simulations: All the simulations carried out as well as the material models used are monotonic. That means that the tensile test data used is obtained by monotonic tensile tests at different temperatures. The J-integral values obtained are also under monotonic tensile loads. All of these results will be more pertinent if they are obtained under cyclic conditions as for the experimental conditions. In addition to that the $\Delta CTOD$ values obtained by numerical simulations and by experimental conditions should be compared. Their proper correlation could be used as a criterion for validation of the numerical simulations.

Modelling: The same comment regarding the use of cyclic properties made in the numerical simulation section may be used in the FCGR modelling and data consolidation techniques. All the material properties for $\Delta CTOD$ and J-Integral based criteria follows the monotonic tensile tests. Cyclic properties may for example reduce the difference between $\Delta CTOD$ calculated numerically and that obtained by image correlation.

Appendices

Appendix A : Thermal Gradient In Specimens	185
Appendix B : Supplementary Paris Curves.....	187
I. Comparison of Paris curves of different specimen configurations SE(T) _c and C(T) at R = 0.1	187
II. Study of the effect of crack front oxidation on fatigue crack propagation.....	188
III. Effect of multicracking.....	189
Appendix C : Temperature Dependent Evolution of Crack Tip Plastic Zone.....	191
Appendix D : Procedure of K_c Determination	193
Appendix E : ΔCOD Measurements	195
Appendix F : ΔCTOD Measurements.....	199
Appendix G: Symbols and Abbreviations.....	203
Appendix H: Material Properties Used in Numerical Simulations	205

Appendices

APPENDIX A : THERMAL GRADIENT IN SPECIMENS

The heating system used in these experiments is based on induction heating with a rectangular helix surrounding the specimens. There are advantages and disadvantages to the induction heating system.

Advantages: Quick heating and cooling of the specimens is possible with a high frequency induction heating system. The interest of this is for doing TMF experiments (for future work) at high frequency. Also for cooling, the power can be simply cutoff, and there is no “furnace type” thermal inertia. The other advantage is easy visual access to the specimen which is necessary for measuring the crack length and the crack opening displacement.

Disadvantages: The main disadvantage of an induction heating system is in managing the thermal gradients. Very fine adjustments need to be made to be able to get a reasonable thermal gradient. There are two main sources of the thermal gradient. One is the uneven distribution of the eddy currents in the specimen causing hot and cold zones. The other source is the conduction of heat by the grips of the machine. Normally only the specimen is heated while the grips act as heat sinks. Even if the grips are heated, they have a higher thermal inertia (heavy construction) so they heat up much more slowly than the specimens.

In this experiment the thermal gradient is controlled with the help of three type K thermocouples. Their distribution on the specimen is shown in the figure 1-A. The two distributions are used in different experiments and give the same gradient.

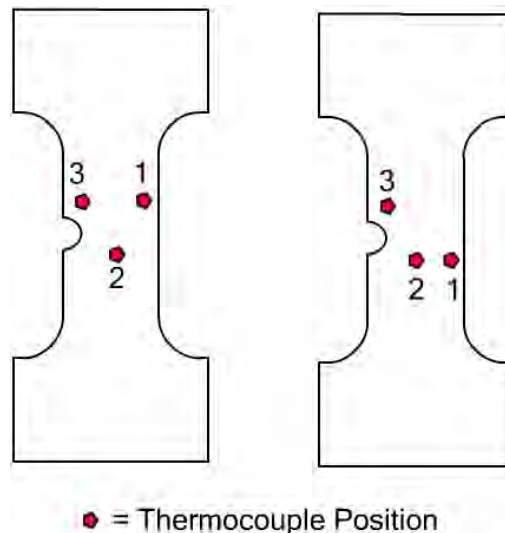


Fig 1-A. Thermocouples on the specimen to control the thermal gradient 1) Generator pilot, 2) Overheat security and 3) Thermal gradient surveillance

The three thermocouples are used as 1) Pilot of the induction generator, 2) Overheat security and 3) General temperature surveillance. Since the specimens are thin no real thermal gradient was observed across the flat faces. The pilot thermocouple is always the furthest from the notch. This is because the presence of the crack can perturb the heating of the specimen and there is lesser danger of thermocouple coming off on the uncracked material.

At the stabilised regime a thermal gradient of no more than 5°C is obtained, which is considered to be fairly accurate for an induction heating setup. The low thickness of the specimens also helps in maintaining a low thermal gradient throughout the experiment.

APPENDIX B : SUPPLEMENTARY PARIS CURVES

Certain experimental results of fatigue crack propagation are presented here. These comparisons and tests are carried out as a means for verification or to gain better insight into the results presented in the manuscript.

I. Comparison of Paris curves of different specimen configurations SE(T)_c and C(T) at R = 0.1

Paris curve of X38CrMoV5 47HRC steel at R=0.1 is established using CT25B12mm thickness specimens by Souki (Thesis in progress at ICAA). The specimen is prepared respecting all the dimensional parameters imposed by ASTM E647 standard. This curve is compared with the 2.5mm SE(T)_c [side edge cracked clamped tension] specimen in figure 1-B.

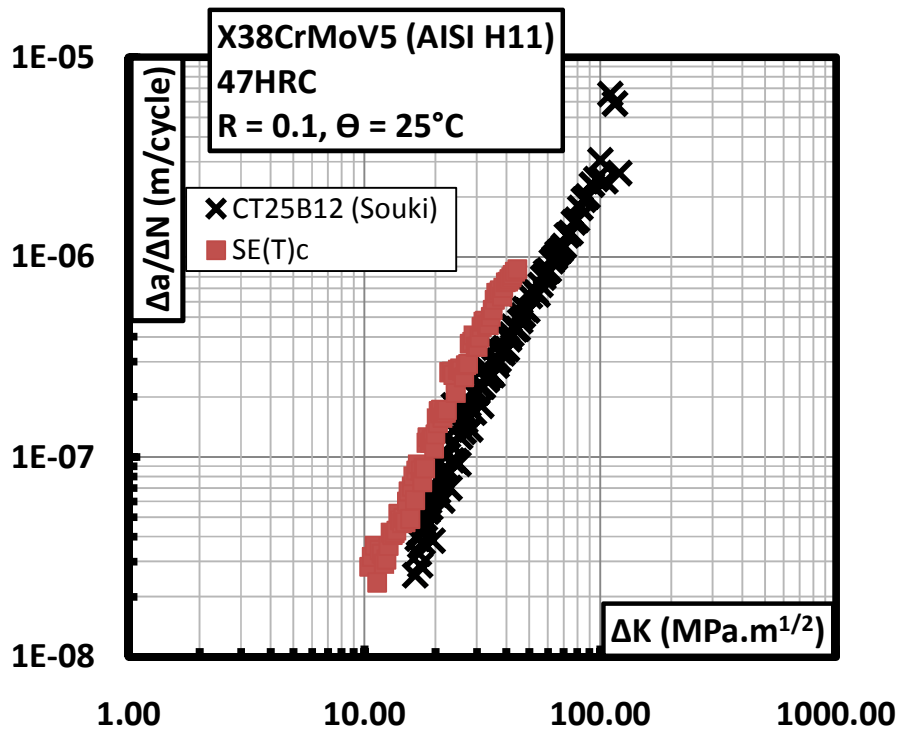


Fig 1-B. Comparison of FCGR in C(T) and SE(T)_c specimen configuration, R=0.1, 25°C

The figure 1-B shows the same slope of Paris law for the two specimens. However the curves are slightly offset resulting in lower FCGR for SE(T)_c specimen. This is in contradiction with the findings of this study where a reduction in thickness is causes a reduction in FCGR. However this error may be from one of the following sources.

1) Difference in configuration may introduce errors in the calculation of ΔK . Numerical simulation is carried out (chapter 3) to try to reduce this effect as much as possible.

2) The C(T) specimen crack length is measured mainly by the compliance method, whereas the SE(T)C specimen crack length is measured optically. This may introduce a difference in the measured crack lengths.

3) The two curves are established on the same grade of material, however these are completely different lots from foundry. Also the thermomechanical history of the two materials may be different. In addition to this, the orientation of the specimens inside the material is not the same. These metallurgical differences may be responsible for this offsetting of the curves.

II. Study of the effect of crack front oxidation on fatigue crack propagation

This test is described in the section III.4 of Chapter 2. The results are shown in the figure 2-B.

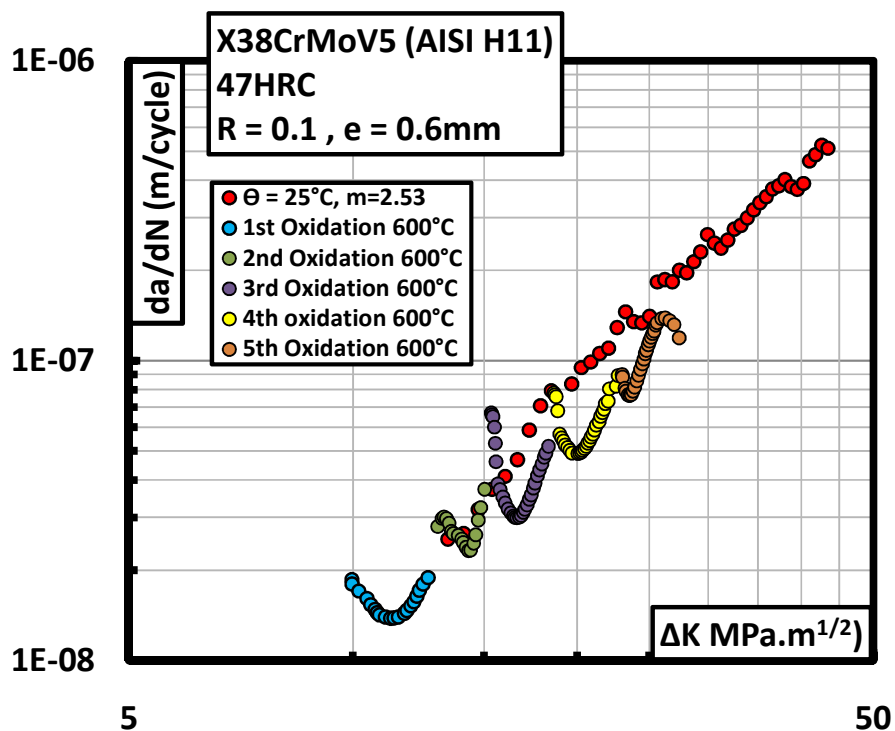


Fig 2-B. Effect of cyclic oxidation of crack tip on the FCGR at 25°C.

The main idea was to explore the effect of oxidation of the material at 600°C on FCGR at ambient temperature. It is seen that by heating the specimen at 600°C and then cooling in ambient air a jump in the FCGR is witnessed. The length material perturbed in front of the crack tip that causes this jump is much larger (100µm app.) than the oxide layer built up on the specimen surface (5µm). This shows that the oxygen weakens the damaged material in front of the crack tip. After each jump the FCGR slow down to a rate below the FCGR curve at ambient temperature. However with further propagation the FCGR curve has a tendency to rejoin the undisturbed ambient temperature curve.

III. Effect of multicracking

In one of the tests on a specimen of 0.6mm thickness at 600°C, in addition to the crack at notch root, another crack initiated at the specimen shoulder. This crack was not seen until the end of the experiment. The effect of this crack was to decrease the bending resistance of the material, consequently increasing the effective ΔK . This in turn is seen as an increase in the FCGR. The cracked specimen as well as the FCGR curve are shown in the figure 3-B.

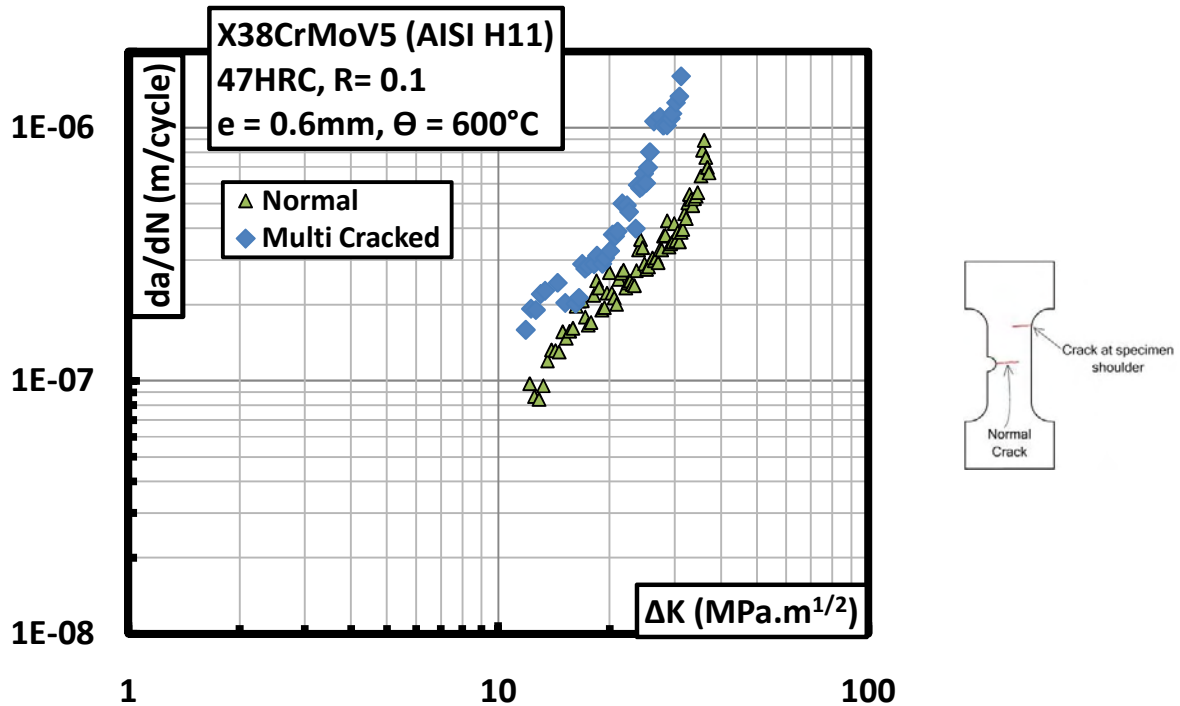


Fig 3-B. Increase in FCGR due to multicracking in the specimen of $e=0.6\text{mm}$ tested at $R=0.1$ and 600°C

The reason of crack initiation in the specimen shoulder was uneven machining, which created a stress concentration. The shoulders were subsequently polished for all other experiments carried out at 600°C.

APPENDIX C : TEMPERATURE DEPENDENT EVOLUTION OF CRACK TIP PLASTIC ZONE

This section is in complement to the paragraph III.1 of Chapter 4, figure 35. The experiment deals with the heating of the specimen during crack propagation in order to study the effect of material behavior modification on FCGR. It is seen that the FCGR of a specimen when heated to 300°C increases whereas heating to 500°C may completely stop the fatigue crack advance (crack arrest). The reason of this effect is the large crack tip plastic zone created at 500°C that causes crack arrest as shown in figure 1-C.

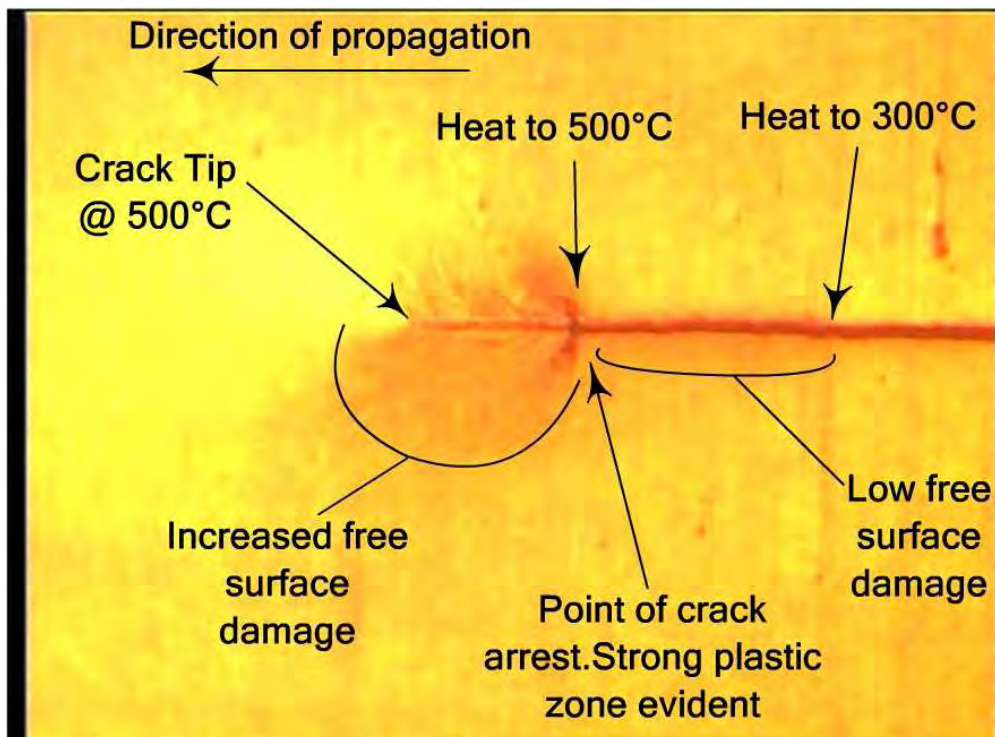


Fig 1-C. Effect of heating on the crack tip plastic zone size.

It can be seen in the figure 1-C that heating the specimen to 300°C does not create a large crack tip plastic zone. Also the surface damage along the path of propagation is larger than that at ambient temperature. Heating to 500°C causes a drastic softening in the material and the subsequent severe crack tip plastic zone is evident in the figure 1-C. During propagation at 500°C a much larger surface damage along the path of propagation is seen also indicating high amount of material deformation. The point of crack arrest is clearly shown as the black spot. Once the crack tip leaves the point of crack arrest (which corresponds to ΔK_{th} at this temperature) stable fatigue crack propagation resumes.

APPENDIX D : PROCEDURE OF K_c DETERMINATION

The standard procedure of K_c evaluation ASTM E399 should be followed to obtain the K_c value by the 5% reduction in compliance method.

Usually specimens can be tested by using the 5% compliance drop method, if the crack length is sufficiently long ($a/W = 0.6$). One such measurement is shown for a 2.5mm specimen with $a/W = 0.6$, figure 1-D. The point of intersection of the actual load displacement curve and the slope representing 5% compliance drop is called P_5 . The corresponding load (P_5) is used to calculate the K_c which in this case is $35.2 \text{ MPa}\cdot\text{m}^{1/2}$.

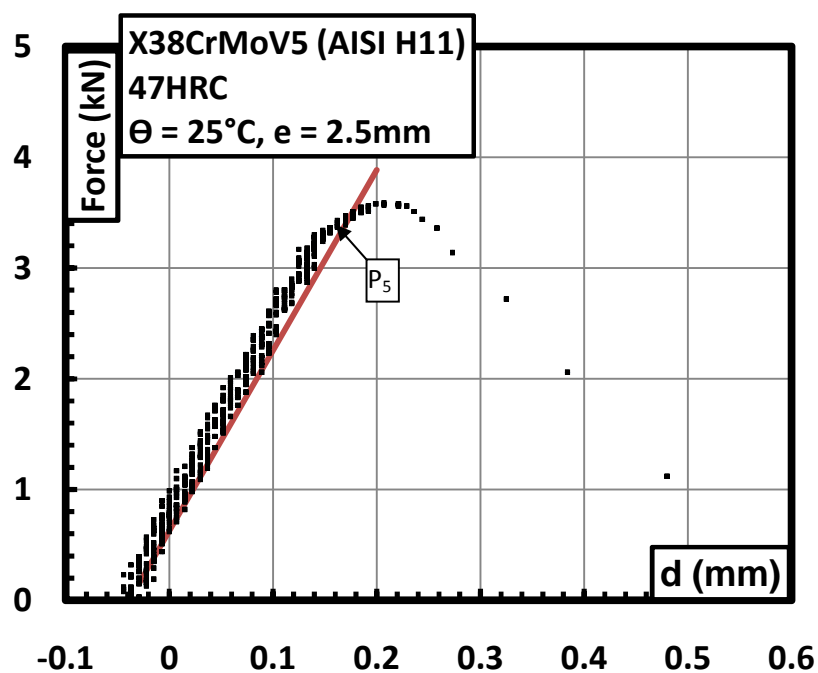


Fig 1-D. Force displacement curve for K_c measurement by 5% drop in compliance method 2.5mm specimen, $a/W = 0.6$.

In the 2.5mm specimen when the crack length is low ($a/W = 0.3$), the specimen shows fragile behaviour and compliance drop cannot be detected as shown in figure 2-D. In this case the maximum force before rupture is used as $P_Q = P_5$ to calculate K_c .

In general the specimens of 0.6mm thickness show a compliance drop throughout the crack length, whereas the specimens of 1.0mm thickness show a behaviour similar to that of the 2.5mm specimens, i.e. fragile for low a/W and ductile behaviour for high a/W .

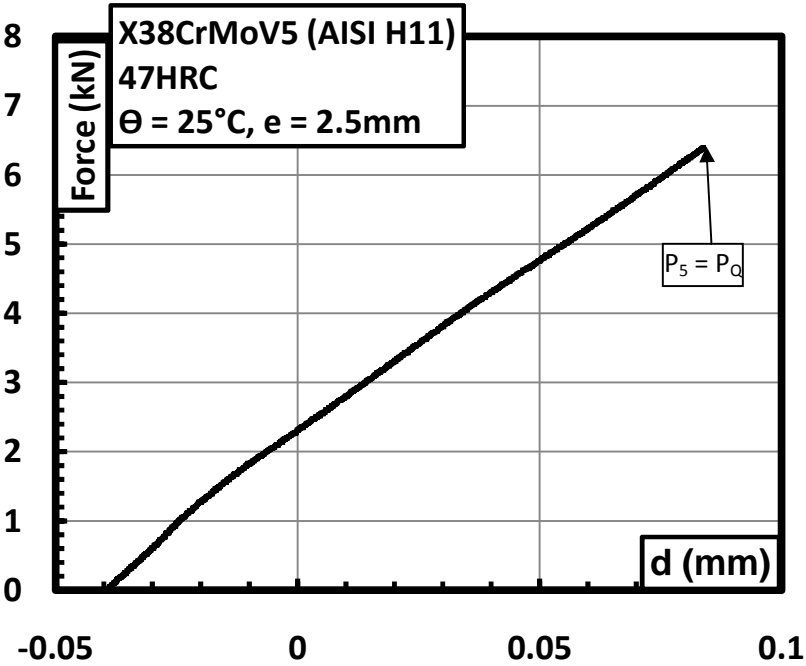


Fig 2-D. Force displacement curve for Kc measurement by 5% drop in compliance method 2.5mm specimen, $a/W = 0.6$

APPENDIX E : Δ COD MEASUREMENTS

Crack opening readings in specimens of 0.6mm thickness are presented. In all cases the virtual extensometer is placed 600 μ m behind the crack tip. The choice of the extensometer position is from a practical standpoint, this distance is found to give the best compromise between camera resolution and proximity to crack tip. All data has undergone cubic spline smoothing. All the curves are unloading curves. The maximum applied stress in all the cases is $\sigma_{\max} = 250$ MPa, while the minimum stress depends on R.

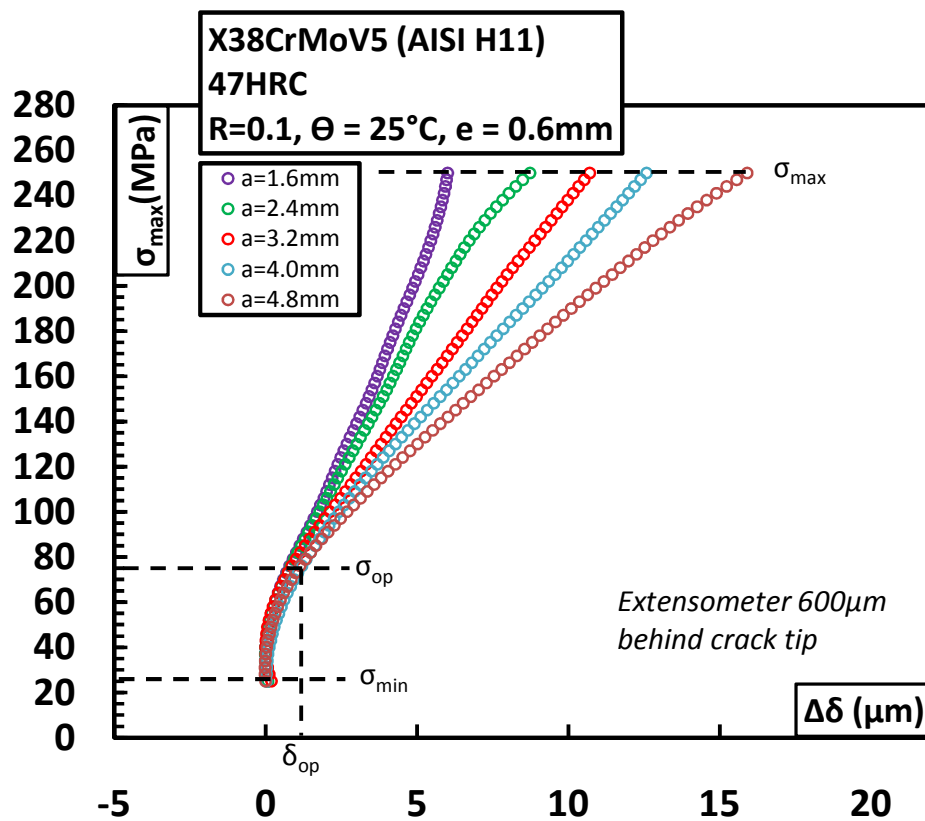


Fig 1-E. COD measurements 600 μ m behind the crack tip for different crack lengths in 0.6mm thickness specimen tested at R = 0.1, 25°C.

The figure 1-E shows the crack opening displacement (Δ COD or $\Delta\delta$) measured in a specimen of 0.6mm thickness tested at R=0.1 and 25°C. Crack closure at 75 MPa is obvious in this experiment.

The figure 2-E shows the Δ COD for a specimen tested at R = 0.7 and 25°C. The displacement values at this length become very small. This causes the noise of image acquisition system (camera + video recorder) and the machine vibrations to introduce an error in the readings as

shown in the figure 2-E. Cubic spline smoothing techniques give erroneous results, thus a linear interpolation is used to measure the crack opening displacements figure 2-E.

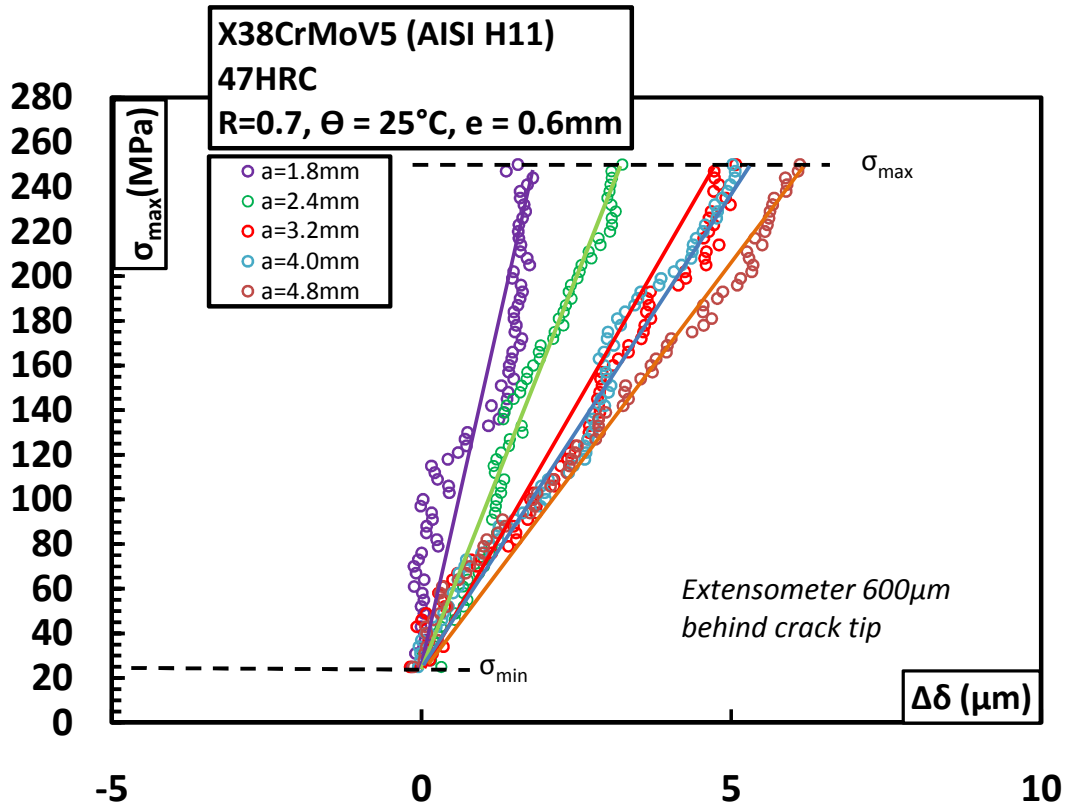


Fig 2-E. COD measurements 600μm behind the crack tip for different crack lengths in 0.6mm thickness specimen tested at R = 0.1, 25°C.

It should be noted that this noise error exists in all measurements of Δ COD. However, when the Δ COD readings are small, the effect of the noise amplifies. The values of Δ COD for this test are in the range of 1.6 – 6 microns. The maximum resolution of an optical system is considered to be $1\mu\text{m}$ (1.6λ , λ = maximum wavelength of visible light $\approx 600\text{nm}$). Thus this measurement is at the physical limitation of the optical measurement system causing large scattering in measured Δ COD.

The figure 3-E shows the Δ COD values for a specimen tested at $R=0.1$ and 600°C . The data is presented with cubic spline smoothing. The quality of the Δ COD measurement is very good mainly due to two reasons:

1. The magnitude of the displacements is large due to reduced E as well as reduced σ_0 at 600°C . Thus the noise as seen as figure 2-E does not have a large effect on the measured data.
2. The texture necessary for the image correlation is created automatically by the oxide layer at 600°C . The polishing marks are preferentially oxidized giving a very fine, high contrast texture on the specimens. This greatly increases the quality of correlation.

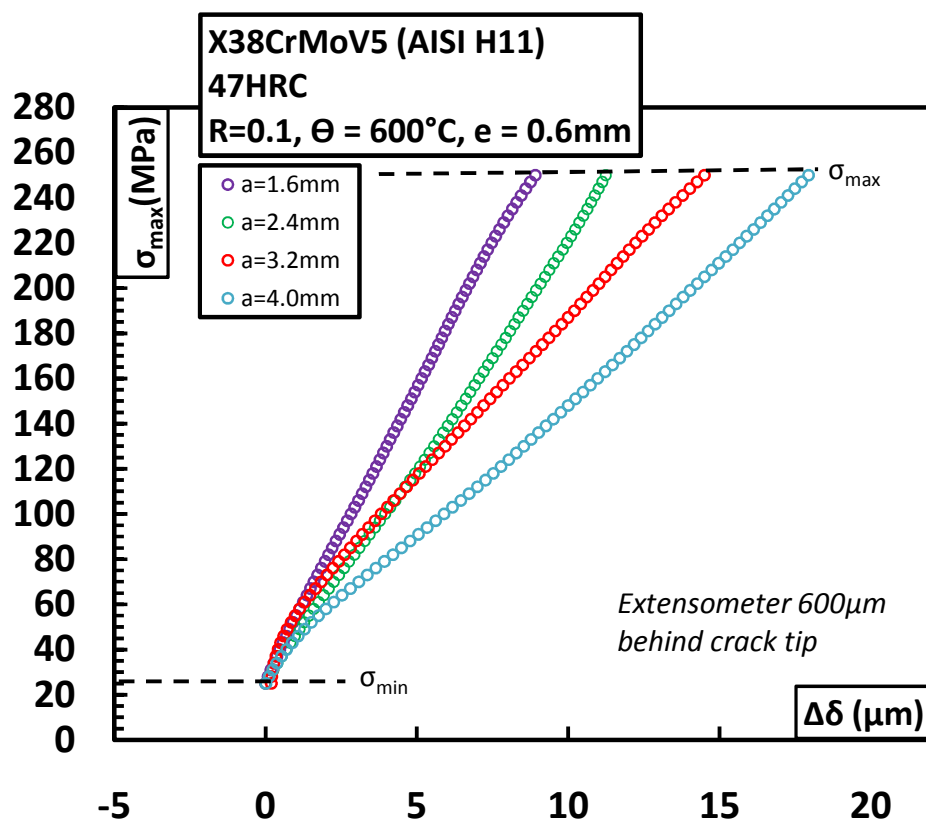


Fig 3-E. Δ COD measurements $600\mu\text{m}$ behind the crack tip for different crack lengths in 0.6mm thickness specimen tested at $R = 0.1, 600^\circ\text{C}$

No discernible crack closure is seen. For the 3.2mm , and 4.0mm crack lengths there seems to be a crack closure like effect, but this is an artefact of measurement errors and cubic spline smoothing.

APPENDIX F : Δ CTOD MEASUREMENTS

The procedure of Δ CTOD measurements is given in chapter 5 (Section III, Figure 13). Here the actual measurements for 0.6mm thickness specimens tested at R=0.1 and 0.7 at 25°C and at R=0.1 at 600°C are presented. Figure 1-F presents the $\Delta\delta_{max}$ as a function of the placement of the extensometers. The data is extrapolated to the crack tip to get $\Delta\delta_{th}$ values. Here λ is the distance of the extensometers from the crack tip.

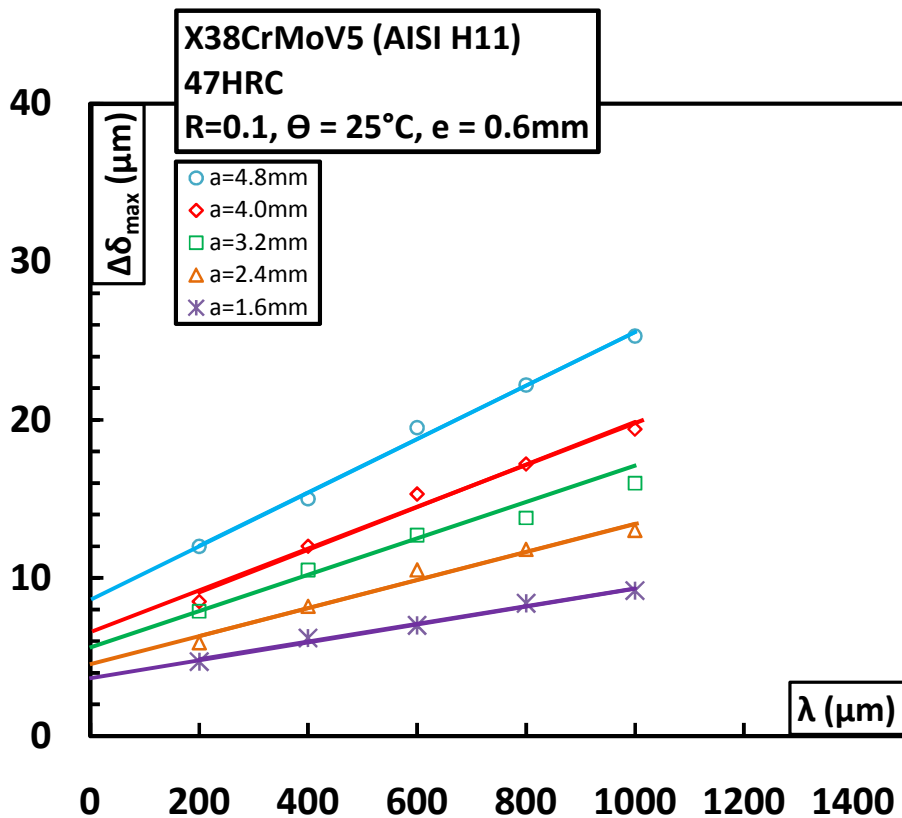


Fig 1-F. $\Delta\delta_{max}$ as a function of extensometer position behind crack tip λ . The extrapolation to crack tip ($\lambda=0$) gives $\Delta\delta_{th}$. Specimen $e=0.6\text{mm}$, $R=0.1$ and 25°C

For R = 0.1 at 25°C there is an effect of crack closure which is seen in the lower $\Delta\delta_t$ as compared to $\Delta\delta_{th}$ for the same conditions, figure 2-F. The figure 3-F shows the same plot for R = 0.7. No crack closure is detected at R=0.7, thus $\Delta\delta_{th} = \Delta\delta_t$. The extensometer near the crack tip ($\lambda=200\mu\text{m}$) shows erroneous results. This is a problem of resolution as the displacements at R = 0.7 are very small. This extensometer reading is thus not used in the extrapolation of $\Delta\delta_{th}$.

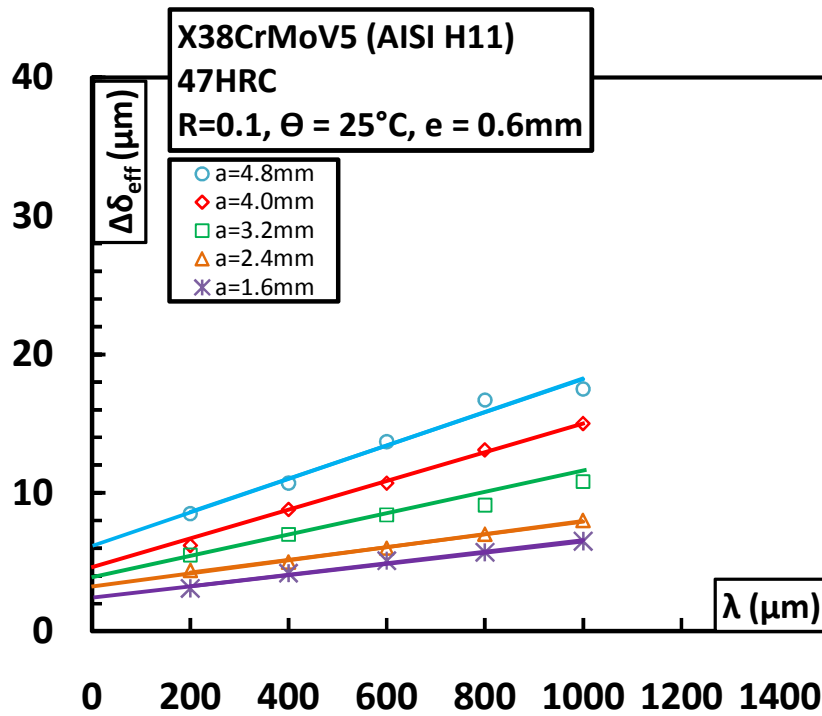


Fig 2-F. $\Delta\delta_{\text{eff}}$ as a function of extensometer position behind crack tip λ . The extrapolation to crack tip ($\lambda=0$) gives $\Delta\delta_t$. Specimen $e=0.6\text{mm}$, $R=0.1$ and 25°C

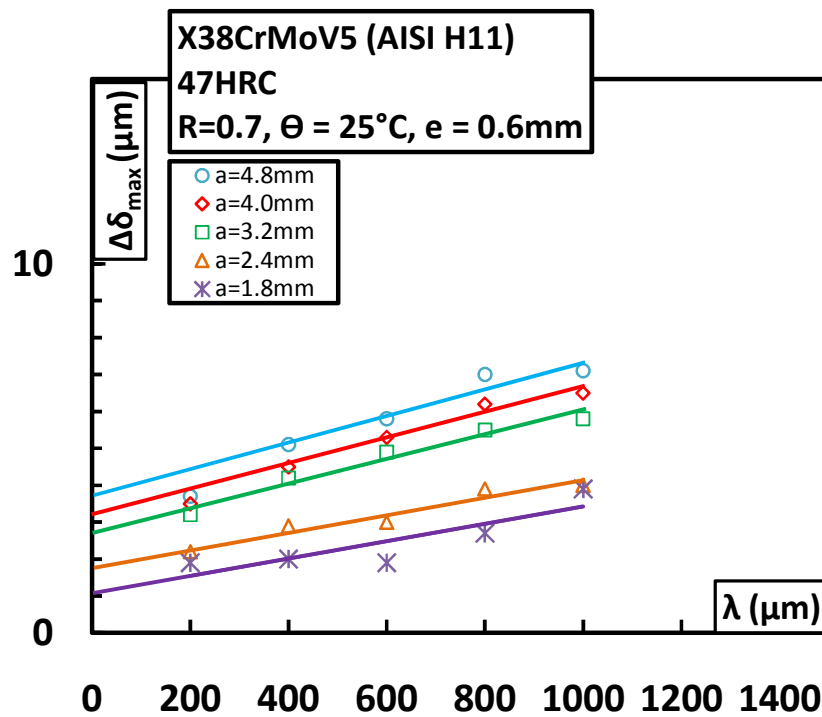


Fig 3-F. $\Delta\delta_{\text{max}}$ as a function of extensometer position behind crack tip λ . The extrapolation to crack tip ($\lambda=0$) gives $\Delta\delta_{\text{th}}$. Specimen $e=0.6\text{mm}$, $R=0.7$ and 25°C

Figure 4-F presents the $\Delta\delta_{max}$ as a function of λ for a specimen of 0.6mm thickness tested at $R = 0.1$ and 600°C . An attempt was made to find out the Δ COD very close to the crack tip for short and long crack lengths. Extra virtual extensometers were placed at $\lambda = 50\mu\text{m}$, $100\mu\text{m}$ and $150\mu\text{m}$ from the crack tip. It is observed that these extensometers are useful for short crack lengths where there is not much deformation of the near crack tip material. However, for longer crack lengths as can be seen in the figure 4-F, the near tip Δ COD values drop sharply. Image correlation requires the presence of a window for correlation as shown in chapter 2, figure 11 . If there is large deformation near the crack tip, the correlation results will give an average of the uncracked and cracked displacement. Any rotary displacement (due to presence of crack tip) will not be detected. This effect manifests as a non linear drop in the measured Δ COD, figure 4-F. This effect will not exist for small cracks due to low deformation of near crack tip material. For long cracks the near tip extensometers are not taken into account.

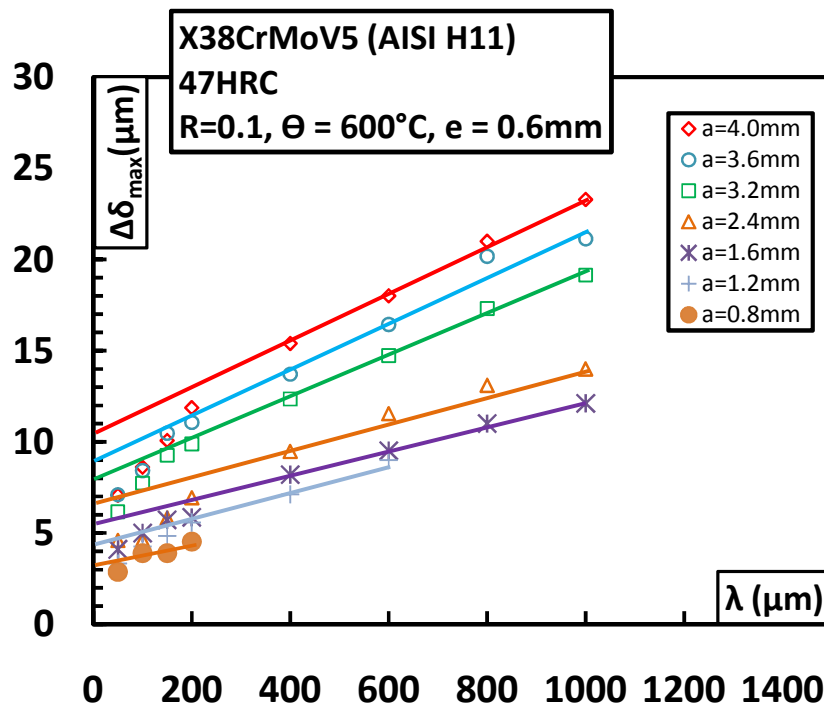


Fig 4-F. $\Delta\delta_{max}$ as a function of extensometer position behind crack tip λ . The extrapolation to crack tip ($\lambda=0$) gives $\Delta\delta_{th}$. Specimen $e=0.6\text{mm}$, $R=0.1$ and 600°C

APPENDIX G: SYMBOLS AND ABBREVIATIONS

<u>Symbols</u>	
da/dN	Crack propagation rate with cubic spline smoothing
$\Delta a/\Delta N$	Crack propagation rate without smoothing
C	Intercept of Paris law
m	Slope of Paris law
e	Thickness of specimen
a/W	Crack length to width ratio
H/W	Specimen height to width ratio
K_I	Mode I stress intensity factor
K_{IC}	Plane strain critical stress intensity factor
K_C	Critical stress intensity factor
ΔK	Stress intensity factor range
ΔK_{eff}	Effective stress intensity factor range
R	Load ratio
R_{eff}	Effective load ratio
R_{app}	Applied load ratio
$J_{el,pl}$	Elastic-Plastic J Integral
J_{el}	Elastic J Integral
J^δ	J Integral calculated through $\Delta CTOD$
δ_0	Crack opening displacement at zero load
δ_{op}	Crack opening displacement at the point of crack opening
$\Delta \delta_{eff}$	Effective crack opening displacement range
$\Delta \delta_{max}$	Extrapolated crack opening displacement range assuming no crack closure
$\Delta \delta_t$	CTOD range
$\Delta \delta_{th}$	CTOD range extrapolated to no crack closure
α	Stress intensity factor weight function
r_p	Crack tip plastic zone size
λ	Distance of extensometer from crack tip in opposite direction of propagation
θ	Specimen temperature °C
<u>Abbreviations</u>	
LEFM	Linear elastic fracture mechanics
EPFM	Elastic plastic fracture mechanics
FCG	Fatigue crack growth
FCGR	Fatigue crack growth rate
LSY	Large scale yielding
SSY	Small scale yielding
SIF	Stress intensity factor
PID	Proportional, Integral, Differential control parameter of hydraulic systems

APPENDIX H: MATERIAL PROPERTIES USED IN NUMERICAL SIMULATIONS

In this section the material properties used to carry out numerical simulations to determine the values of the J Integral are presented. The table 1 presents the R_{p0} , $R_{p0.2}$, E, n, and v. These mechanical properties are determined through tensile tests carried out on X38CrMoV5-47HRC steel.

Table 1: Tensile test data for X38CrMoV5 – 47HRC

Temperature	R_{p0} (MPa)	$R_{p0.2}$ (MPa)	E (MPa)	n	v
20°C	913	1100	208000	12	0.3
600°C	213	600	147000	5.3	0.3

Since the material model used is an incremental plasticity model, the table 2 and 3 present the tensile test data of deformation vs stress increments for 600°C and 25°C respectively.

Table 2: Incremental plasticity data for X38CrMoV5 – 47HRC at 600°C

Strain	Stress	Strain	Stress	Strain	Stress	Strain	Stress
0	247	7.2446E-05	323.707952	0.00022587	401.012536	0.00057503	478.172686
1.8032E-05	249.121701	7.578E-05	326.462742	0.00023322	403.437454	0.00059068	480.596376
1.9117E-05	251.877113	7.8805E-05	328.878245	0.0002402	405.68213	0.00060665	483.016861
1.9894E-05	253.773776	8.1925E-05	331.291672	0.00024789	408.098973	0.00062311	485.45748
2.1067E-05	256.527731	8.4451E-05	333.191736	0.00025694	410.862808	0.00064094	488.043721
2.206E-05	258.762834	8.8232E-05	335.951464	0.00026449	413.110609	0.00065805	490.471301
2.3174E-05	261.175151	9.1644E-05	338.360563	0.00027222	415.358593	0.00067428	492.726874
2.4333E-05	263.585826	9.4918E-05	340.604748	0.00028074	417.775844	0.00069211	495.154788
2.5538E-05	265.99657	9.828E-05	342.844359	0.00029012	420.368139	0.00071029	497.579441
2.6793E-05	268.409281	0.00010256	345.607007	0.00029912	422.794366	0.00072756	499.835472
2.7907E-05	270.476572	0.00010642	348.018725	0.00030766	425.042816	0.00074925	502.608349
2.9448E-05	273.229409	0.00011011	350.263435	0.00031707	427.460576	0.00076871	505.040413
3.0852E-05	275.636756	0.0001139	352.500924	0.00032603	429.709292	0.00078706	507.289878
3.242E-05	278.221695	0.00011812	354.925098	0.0003366	432.299346	0.00080734	509.725782
3.3719E-05	280.287461	0.00012275	357.506663	0.0003475	434.90147	0.00082943	512.323587
3.5518E-05	283.044469	0.00012722	359.921278	0.00035788	437.319654	0.0008505	514.749312
3.7273E-05	285.627832	0.00013216	362.510428	0.00036778	439.571922	0.00087049	517.00635
3.8726E-05	287.691838	0.00013656	364.753334	0.00037865	441.990404	0.00089086	519.263733
4.0359E-05	289.937669	0.00014177	367.337688	0.00038981	444.415053	0.00091803	522.2102
4.2433E-05	292.68715	0.00014681	369.760362	0.00040121	446.833767	0.00093763	524.291939
4.4191E-05	294.933279	0.00015197	372.172927	0.00041374	449.427744	0.00096091	526.71831
4.6139E-05	297.339206	0.0001569	374.418776	0.00042659	452.024939	0.00098646	529.328028
4.831E-05	299.925172	0.00016235	376.834166	0.00043799	454.275032	0.00101086	531.769438
5.0108E-05	301.995762	0.00016837	379.424206	0.00044965	456.528325	0.00103552	534.188986
5.2427E-05	304.579931	0.00017373	381.670423	0.00046338	459.122856	0.0010609	536.630706
5.467E-05	306.992378	0.00017923	383.919433	0.00047554	461.366974	0.00108291	538.709668
5.6988E-05	309.402755	0.00018529	386.32993	0.00048897	463.792815	0.00111295	541.492755
5.939E-05	311.817499	0.00019154	388.751192	0.0005027	466.218862	0.00113591	543.579359
6.1871E-05	314.230203	0.00019935	391.688567	0.00051774	468.813972	0.00116315	546.010721
6.4622E-05	316.814931	0.00020501	393.760699	0.00053209	471.233834	0.00119486	548.78318
6.6703E-05	318.712184	0.00021178	396.177013	0.00054682	473.663578	0.00122126	551.046457
7.002E-05	321.638641	0.00021824	398.424089	0.00056184	476.086929	0.00125236	553.662057

Appendix H : Material Properties Used in Numerical Simulations

Strain	Stress	Strain	Stress
0.0012819	556.098018	0.00374344	680.456945
0.00130551	558.013194	0.00382177	683.11605
0.0013383	560.625725	0.00389609	685.598113
0.00137393	563.407053	0.00396657	687.916888
0.00140578	565.843748	0.00404333	690.40449
0.00143586	568.104439	0.00412722	693.079728
0.00146652	570.369135	0.00421224	695.746069
0.00150267	572.990636	0.00428205	697.903321
0.00153453	575.259707	0.00436379	700.392893
0.00157187	577.8699	0.00445327	703.07524
0.00160741	580.3079	0.00452603	705.224386
0.00164371	582.754081	0.00461224	707.734753
0.00168571	585.529336	0.00470605	710.423669
0.00171535	587.454543	0.00480815	713.301005
0.00175648	590.082037	0.00487346	715.11568
0.00180107	592.874146	0.00498492	718.167675
0.00183215	594.787793	0.00507215	720.517759
0.00187836	597.584482	0.00516064	722.868469
0.00191373	599.687409	0.005271	725.754585
0.00195558	602.13561	0.00535596	727.943233
0.00199198	604.230727	0.00546286	730.657542
0.00204755	607.369488	0.00555077	732.85758
0.00208564	609.481724	0.00565379	735.400029
0.00212727	611.754201	0.005766	738.12681
0.00217629	614.384651	0.00585857	740.344186
0.00221955	616.666133	0.00596652	742.894057
0.00227014	619.288714	0.0060772	745.470174
0.00231133	621.389597	0.006197	748.215689
0.00236379	624.021371	0.00630348	750.620066
0.0024173	626.657662	0.00643507	753.546364
0.00246784	629.104567	0.0065379	755.799588
0.0025124	631.227979	0.00665781	758.390893
0.00256836	633.852431	0.0067793	760.977984
0.00261788	636.136141	0.00690363	763.586907
0.00267566	638.756725	0.00703037	766.20739
0.00273487	641.395258	0.00716765	769.002883
0.00278353	643.529012	0.00728202	771.298909
0.00283652	645.818419	0.00741534	773.938767
0.00289841	648.449083	0.00754282	776.427004
0.00296151	651.084594	0.00768097	779.085416
0.00302182	653.561029	0.00925389	806.904299
0.00307893	655.869653	0.01036438	824.311141
0.0031495	658.674613		
0.00320812	660.965916		
0.00326774	663.262186		
0.00332876	665.576941		
0.00339954	668.219505		
0.00346706	670.698926		
0.00353072	673.001164		

Table 3: Incremental plasticity data for X38CrMoV5 – 47HRC at 20°C

Strain	Stress	Strain	Stress	Strain	Stress	Strain	Stress
0	913	0.00011302	986.637842	0.00028347	1061.08103	0.00067013	1134.90061
4.30E-05	914.25781	0.00011506	988.208612	0.00028821	1062.29488	0.00068216	1136.63303
4.38E-05	915.992405	0.00011738	989.600392	0.00029247	1063.68094	0.00069421	1138.2245
4.47E-05	917.210463	0.00011998	991.157667	0.00029855	1064.90934	0.00070645	1139.79223
4.58E-05	918.760357	0.00012161	992.866819	0.00030475	1066.6332	0.00071627	1141.3603
4.67E-05	920.482418	0.00012433	993.921005	0.00030865	1068.35677	0.00073027	1142.59897
4.7705E-05	921.879126	0.00012713	995.650634	0.00031507	1069.42777	0.0007402	1144.33966
4.8733E-05	923.422579	0.00012883	997.393979	0.00032098	1071.15875	0.00075608	1145.5549
4.9682E-05	924.972494	0.0001317	998.43454	0.00032702	1072.72471	0.00076793	1147.46797
5.063E-05	926.375604	0.00013434	1000.16427	0.00033305	1074.29839	0.00077988	1148.87163
5.1965E-05	927.753316	0.00013672	1001.72863	0.00033858	1075.8423	0.00079365	1150.26725
5.2723E-05	929.654017	0.00013947	1003.11383	0.0003456	1077.23617	0.00080597	1151.85143
5.3846E-05	930.71293	0.00014286	1004.68504	0.00035206	1078.97458	0.00081847	1153.24715
5.5001E-05	932.256529	0.00014506	1006.5804	0.0003564	1080.54845	0.00083452	1154.64321
5.6179E-05	933.81282	0.00014795	1007.79323	0.00036376	1081.59011	0.00085042	1156.40785
5.7245E-05	935.369244	0.00015057	1009.35783	0.00037051	1083.32885	0.000862	1158.12498
5.8472E-05	936.753445	0.00015353	1010.74996	0.00037737	1084.89513	0.00087703	1159.35647
5.944E-05	938.316352	0.00015588	1012.30076	0.00038435	1086.46165	0.00089077	1160.9331
6.0846E-05	939.528345	0.00015967	1013.50681	0.00039063	1088.02811	0.00090781	1162.35298
6.2144E-05	941.257059	0.00016211	1015.42305	0.00039947	1089.41472	0.00092176	1164.08624
6.3615E-05	942.820081	0.00016531	1016.63621	0.00040435	1091.33358	0.00093607	1165.48252
6.4655E-05	944.555338	0.00016854	1018.20082	0.00041341	1092.37541	0.00095042	1166.89483
6.6181E-05	945.760989	0.0001715	1019.75168	0.00042023	1094.27937	0.00096868	1168.291
6.7416E-05	947.49625	0.00017487	1021.14412	0.00042794	1095.68863	0.00098551	1170.04055
6.8689E-05	948.874183	0.00017792	1022.70894	0.00043483	1097.25534	0.00100243	1171.62543
7.029E-05	950.271559	0.0001818	1024.10156	0.00044286	1098.6347	0.0010197	1173.19442
7.1443E-05	951.993938	0.00018536	1025.8387	0.00045095	1100.21647	0.00103348	1174.77151
7.3103E-05	953.21271	0.00018932	1027.40365	0.00045811	1101.78341	0.00105116	1176.01146
7.4456E-05	954.935112	0.00019303	1029.11273	0.00046561	1103.14758	0.0010693	1177.5808
7.6032E-05	956.312962	0.00019598	1030.68479	0.00047412	1104.55708	0.00108773	1179.16615
7.7435E-05	957.889521	0.00019976	1031.91222	0.00048274	1106.1317	0.00110617	1180.75148
7.9056E-05	959.267469	0.00020362	1033.46303	0.00049247	1107.6988	0.00112738	1182.3128
8.0524E-05	960.830775	0.00020717	1035.02124	0.0004995	1109.43819	0.00114451	1184.07908
8.1997E-05	962.221955	0.00021111	1036.42816	0.00050946	1110.6756	0.00115964	1185.48403
8.4277E-05	963.593395	0.00021527	1037.96508	0.00051764	1112.40004	0.00118148	1186.7084
8.6037E-05	965.673629	0.00021985	1039.55872	0.00052707	1113.79475	0.00120169	1188.45051
8.7601E-05	967.243768	0.00022359	1041.28208	0.00053552	1115.37715	0.00122211	1190.03628
8.9014E-05	968.615152	0.0002274	1042.66072	0.00054404	1116.77196	0.00123602	1191.61406
9.1054E-05	969.834268	0.00023226	1044.04663	0.00055387	1118.15934	0.00125962	1192.67426
9.2711E-05	971.563484	0.00023624	1045.78436	0.00056266	1119.73426	0.00128073	1194.44913
9.4632E-05	972.941477	0.00023971	1047.18449	0.00057382	1121.12159	0.0013	1196.01085
9.6574E-05	974.511878	0.00024434	1048.38384	0.00058311	1122.85358	0.00131736	1197.41616
9.8339E-05	976.069011	0.00024904	1049.96371	0.00059459	1124.2719	0.00134697	1198.66563
0.00010034	977.460451	0.00025373	1051.53635	0.0006028	1125.99646	0.00136728	1200.76163
0.00010242	979.010796	0.00025804	1053.08026	0.0006148	1127.21133	0.00139053	1202.17548
0.00010426	980.588116	0.00026407	1054.47358	0.00062586	1128.95893	0.00141145	1203.7704
0.00010686	981.966263	0.0002668	1056.39111	0.0006357	1130.54227	0.00143764	1205.18441
0.00010831	983.867994	0.00027356	1057.24563	0.0006483	1131.92972	0.00145656	1206.92739
0.00011075	984.90837	0.00027938	1059.32845	0.00065725	1133.67761	0.00148391	1208.16869

Appendix H : Material Properties Used in Numerical Simulations

Strain	Stress	Strain	Stress	Strain	Stress
0.001503	1209.93674	0.00326572	1285.73417	0.0069139	1364.19085
0.00153128	1211.1535	0.00331295	1287.34341	0.0070375	1365.53618
0.00155683	1212.92963	0.00336656	1288.79752	0.00713947	1367.4398
0.00158277	1214.50866	0.00341485	1290.42487	0.00724219	1368.98711
0.0016036	1216.08756	0.00346998	1291.87046	0.00736936	1370.5255
0.00163348	1217.33782	0.00352563	1293.49803	0.00746639	1372.40224
0.00166075	1219.10605	0.00357603	1295.11703	0.00759855	1373.81432
0.00168554	1220.69373	0.0036342	1296.56304	0.00769641	1375.71063
0.00171332	1222.11687	0.00369261	1298.20884	0.00780864	1377.09532
0.00174181	1223.68797	0.00374522	1299.83718	0.00794645	1378.66348
0.00176772	1225.2756	0.00381138	1301.28365	0.00806279	1380.56093
0.00179736	1226.69909	0.00386724	1303.07628	0.00819379	1382.13934
0.00182373	1228.30382	0.00393506	1304.56749	0.00832607	1383.89167
0.00185391	1229.71078	0.00397179	1306.35177	0.00844908	1385.63521
0.00188137	1231.29886	0.00404236	1307.30644	0.0085867	1387.23367
0.00191227	1232.72272	0.00410029	1309.11764	0.00871255	1388.99691
0.00194069	1234.30243	0.00417298	1310.58302	0.00885419	1390.58666
0.001976	1235.73503	0.00423301	1312.39473	0.00898528	1392.35068
0.00200851	1237.48775	0.0043003	1313.86934	0.00911739	1393.96039
0.00204186	1239.07626	0.00436934	1315.49933	0.0092668	1395.56086
0.00207555	1240.68174	0.00444018	1317.14758	0.00940442	1397.34539
0.00210585	1242.27904	0.00450299	1318.81385	0.01011824	1398.96574
0.00213711	1243.69507	0.00457584	1320.27122		
0.00216862	1245.13694	0.00464125	1321.93805		
0.00221182	1246.5702	0.00472321	1323.41394		
0.00224434	1248.50469	0.00478221	1325.23628		
0.00227711	1249.93828	0.00486689	1326.53028		
0.00231032	1251.36343	0.00493659	1328.36211		
0.002352	1252.78857	0.00500765	1329.84798		
0.002395	1254.55086	0.00508806	1331.34294		
0.00243001	1256.33904	0.00516071	1333.01131		
0.00246979	1257.7731	0.00526028	1334.49784		
0.00250538	1259.38002	0.00531903	1336.50422		
0.00254631	1260.79716	0.005413	1337.67182		
0.00259236	1262.40441	0.00549137	1339.51464		
0.0026257	1264.18465	0.00558865	1341.02931		
0.00265896	1265.45508	0.0056684	1342.88186		
0.0027116	1266.70829	0.00575867	1344.37865		
0.00275087	1268.66179	0.00585125	1346.04937		
0.00280034	1270.09688	0.0059345	1347.73833		
0.0028359	1271.87768	0.00602973	1349.23595		
0.00287684	1273.1401	0.00614695	1350.92567		
0.00291356	1274.57544	0.0062149	1352.97197		
0.00296572	1275.8468	0.00631377	1354.14185		
0.00301384	1277.62812	0.00642567	1355.82312		
0.00306873	1279.24559	0.00649762	1357.697		
0.00311786	1281.06224	0.00658998	1358.88612		
0.00316797	1282.66262	0.00669732	1360.39468		
0.00321417	1284.27157	0.00682775	1362.12377		

TITLE : Investigation of crack propagation in X38CrMoV5 tool steel at room temperature and 600°C on small scale specimens

Forging and high pressure die casting processes impose heavy mechanical loads on die materials and tools damaging their surface during production. This study proposes a novel method of characterisation of the surface damage of tool steels using thin specimens. Fatigue crack propagation experiments are carried out on the tool steel X38CrMoV5 at ambient temperature as well as at 600°C. The effect of specimen thickness, load ratio and temperature on the fatigue crack propagation is studied.

Different fatigue crack propagation parameters are established using numerical simulations. A method of crack tip opening displacement measurement is developed. This method is based on image acquisition with the help of a digital camera and a long distance microscope followed by an image correlation procedure, to measure the crack opening displacements. A fatigue crack propagation model based on crack opening displacement is developed and compared with traditional propagation models.

AUTEUR : Sayyid Masoodur Rahman SHAH

TITRE : Etude de la propagation de fissures de l'acier à l'outil X38CrMoV5 à la température ambiante et à 600°C dans le cas d'éprouvettes de dimensions réduites

DIRECTEUR DE THESE : Farhad REZAÏ-ARIA

LIEU ET DATE DE SOUTENANCE : Albi, le 9 Novembre 2010

Les outillages de mise en forme à chaud, sont soumis à des chargements thermomécaniques sévères, qui endommagent leur surface. Une nouvelle méthode de caractérisation de l'endommagement par fatigue est proposée. Des éprouvettes de dimensions réduites, représentatives de la surface, ont été utilisées. Les essais de propagation de fissure en fatigue sur l'acier à outil X38CrMoV5 traité à 47 HRC sont réalisés à la température ambiante et à 600°C. Les effets de l'épaisseur de l'éprouvette, du rapport de charge et de la température ont été étudiés.

Différents paramètres de propagation de fissure ont été établis à l'aide de la simulation numérique. Une méthode de mesure de l'ouverture en fond de fissure, utilisant une caméra numérique et un microscope à longue portée, a été développée. Les images acquises sont ensuite traitées par corrélation d'images pour mesurer l'ouverture de fissure. Un modèle de propagation de fissure basé sur l'ouverture en fond de fissure a été développé.

MOTS CLES : Propagation de fissure – Fatigue – Aciers à outil – CTOD – Corrélation d'images – Intégrale J – Facteur d'intensité de contrainte – Rupture

DISCIPLINE ADMINISTRATIVE : Génie Mécanique, Mécanique des Matériaux

INTITULE ET ADRESSE DE LABORATOIRE : Université de Toulouse ; INSA, UPS, Mines Albi, ISAE ; ICA (Institut Clément Ader), Campus Jarlard, Route de Teillet, F-81013 Albi – France.